

TOWARD CARBON-NEUTRAL HYDROGENATION USING A PALLADIUM
MEMBRANE REACTOR

by

RYAN JANSONIUS

B.Sc. (Hons), The University of Calgary, 2016

A DISSERTATION SUBMITTED IN PARTIAL FULFILLMENT OF THE REQUIREMENTS
FOR THE DEGREE OF

DOCTOR OF PHILOSOPHY

in

THE FACULTY OF GRADUATE AND POSTDOCTORAL STUDIES

(Chemistry)

THE UNIVERSITY OF BRITISH COLUMBIA

(Vancouver)

June 2021

© Ryan Jansonius, 2021

The following individuals certify that they have read, and recommend to the Faculty of Graduate and Postdoctoral Studies for acceptance, the dissertation entitled:

Toward carbon-neutral hydrogenation using a palladium membrane reactor

submitted by Ryan Jansonius in partial fulfilment of the requirements for

the degree of Doctor of Philosophy

in Chemistry

Examining Committee:

Dr. Curtis Berlinguette, Professor, Chemistry and Chemical & Biological Engineering, UBC

Supervisor

Dr. Dan Bizzotto, Professor, Chemistry, UBC

Supervisory Committee Member

Dr. David Perrin, Professor, Chemistry, UBC

University Examiner

Dr. Martin Ordonez, Professor, Chemistry, UBC

University Examiner

Additional Supervisory Committee Members:

Dr. Gren Patey, Professor, Chemistry, UBC

Supervisory Committee Member

Dr. Pierre Kennepohl, Professor, Chemistry, University of Calgary

Supervisory Committee Member

Abstract

Organic chemicals are the building blocks for plastics, clothing, fertilizers, pharmaceuticals and fuels. Nearly all these materials are manufactured at high temperatures, using fossil fuels to heat the reactors. These processes are resultantly carbon intensive. This thesis presents a technology, called an electrocatalytic palladium membrane reactor (ePMR), that can reduce the carbon impact of chemical manufacturing by using only water and electricity to produce hydrogenated chemicals. This reactor generates reactive hydrogen atoms from water electrolysis, the hydrogen atoms then pass through a palladium membrane to react with an unsaturated feedstock at the opposite surface of the metal. By using an electrochemical driving force, the ePMR can perform hydrogenation without any fossil-derived inputs or high temperatures or pressures.

I first focused on the palladium electrode at the center of the ePMR. I investigated how the spacing between palladium atoms influences the rate that hydrogen is produced during electrolysis, and also the amount of hydrogen that absorbs into the palladium electrode. I designed an electrochemical cell that applies mechanical strain to the palladium lattice and used electrochemical measurements to show that tensile strain increases the hydrogen production rate, and decreases the amount of hydrogen that absorbs into the lattice.

I then focused on increasing the rate of hydrogenation in an ePMR through electrochemical flow cell design. I developed a flow reactor to enable up to 15-fold faster hydrogenation rates than can be achieved in a conventional palladium membrane reactor. This flow cell also enabled me to study how hydrogen in the membrane influences reaction rate and selectivity. Hydrogenation rate is proportional to the hydrogen loading in the membrane, while selectivity for the alkene intermediate is inversely proportional to hydrogen content.

Finally, I show that hydrogenation reactivity can be influenced by depositing secondary metals on the hydrogenation surface of the palladium membrane. This approach was designed to increase reactivity for harder-to-reduce C=O functionalities. I found that thin films of iridium, gold and platinum all increase hydrogenation rates for carbonyl groups, while only platinum increases hydrogenation rates for C=C unsaturations. This work provides a new catalyst design strategy for tailoring reactivity in the ePMR.

Lay Summary

Many chemical building blocks used to produce biofuels, plastics, cosmetics, pharmaceuticals and food are manufactured through a process called hydrogenation. This simple, but ubiquitous chemical reaction adds hydrogen to a chemical feedstock to make useful products. A key challenge with hydrogenation is that methods used today require high temperatures and pressures, and use flammable H₂ gas. The combustion and reforming of natural gas is required to generate this heat and H₂ and results in a large carbon footprint. This thesis presents an attractive alternative – the “electrocatalytic palladium membrane reactor” produces the same useful chemicals, but uses only water and electricity as inputs for the reaction. If paired to a renewable electricity source, this device can drive carbon-neutral hydrogenation. Discoveries presented in this work improve the understanding of this nascent technology, and provide strategies to enhance the efficiency and versatility of this reactor.

Preface

Portions of **Chapters 1, 2 and 6** were adapted from a Perspective article entitled “Efficient organic electrosynthesis using a membrane reactor” submitted for publication. This work was supervised by Prof. Curtis Berlinguette. The article was conceptualized by myself, in collaboration with Dr. Rebecca Sherbo at Harvard University and Dr. Camden Hunt in the Berlinguette group. Dr. Aiko Kurimoto and I designed the figures. The manuscript was written by myself, with contributions by all authors.

Chapter 3 was adapted from a research article entitled “Strain influences the hydrogen evolution activity and absorption capacity of palladium” published in *Angewandte Chemie International Edition* in 2020 [Jansonius, R. P.; Schauer, P. A.; Dvorak, D. J.; MacLeod, B. P.; Fork, D. K.; Berlinguette, C. P. Strain Influences the Hydrogen Evolution Activity and Absorption Capacity of Palladium. *Angew. Chem. Int. Ed.* **2020**, *59* (29), 12192–12198.]. This work was supervised by Prof. Curtis Berlinguette. I designed the unique instrumentation reported in the work with input from Dr. Phil Schauer and Ben Macleod. The instruments were built by Doug Yuen, Graham Liebelt and Tobias Donaldson in the Department of Chemical and Biological Engineering. I designed the study and carried out all experiments with feedback from my co-authors. The manuscript was written by Dr. Berlinguette and I, with contributions from all authors. Graham Entwistle at the School of Architecture and Landscape Architecture at UBC and Bernhard Zender in the department of Physics and Astronomy at UBC supervised laser micromachining. I collected electron microscopy images at the Centre for High-Throughput Phenogenomics (CHTP) under the supervision of Dr. Gethin Owen. A portion of the introduction was adapted from a Perspective article entitled “Strain engineering electrocatalysts for selective CO₂ reduction” published in ACS

Energy Letters in 2019. This work was supervised by Dr. Curtis Berlinguette and the manuscript was written with equal contributions from myself and Dr. Lacey Reid. Dr. Carolyn Virca also contributed to the construction of the manuscript.

Chapter 4 was adapted from a research article entitled “Hydrogenation without H₂ using a palladium membrane flow cell” published in Cell Reports Physical Science in 2020 [Jansonius, R. P.; Kurimoto, A.; Marelli, A. M.; Huang, A.; Sherbo, R. S.; Berlinguette, C. P. Hydrogenation without H₂ Using a Palladium Membrane Flow Cell. *Cell Rep. Phy. Sci.* **2020**, *1* (7), 100105.]. This work was supervised by Prof. Curtis Berlinguette. I designed the flow cell reported in the work, which was fabricated by Tobias Donaldson, a machinist in the Department of Chemical and Biological Engineering at UBC. I designed the study and carried out all flow cell hydrogenation experiments with help from Antonio Marelli. Dr. Aiko Kurimoto conducted a hydrogenation experiment in an H-cell for comparison. Aoxue Huang helped with palladium membrane characterization. I wrote the manuscript with contributions from Dr. Berlinguette.

Chapter 5 was adapted from a research article entitled “Physical separation of H₂ activation from hydrogenation chemistry reveals the specific role of secondary metal catalysts” published in Angewandte Chemie International Edition in 2021 [Kurimoto, A.; Jansonius, R. P.; Huang, A.; Marelli, A. M.; Dvorak, D. J.; Hunt, C.; Berlinguette, C. P. Physical Separation of H₂ Activation from Hydrogenation Chemistry Reveals the Specific Role of Secondary Metal Catalysts. *Angew. Chem. Int. Ed.* **2021**, *60* (21), 11937–11942.]. This work was supervised by Prof. Curtis Berlinguette. Dr. Aiko Kurimoto and I designed the study. Dr. Kurimoto carried out all hydrogenation experiments and mass spectrometry experiments. I fabricated the thin film

catalysts, and selected the metals investigated in the study. Dr. Kurimoto and I wrote the manuscript with contributions from Prof. Curtis Berlinguette.

Table of Contents

Abstract.....	iii
Lay Summary	v
Preface.....	vi
Table of Contents	ix
List of Figures.....	xiv
List of Abbreviations	xix
Acknowledgements	xxiii
Dedication	xxiv
Chapter 1: Introduction	1
1.1 Motivation.....	1
1.2 Electrocatalytic palladium membrane reactors	2
1.3 Structure of the thesis.....	4
Chapter 2: Literature review.....	7
2.1 The case for using electricity as a reagent in chemical synthesis.....	7
2.2 Hydrogenation in chemical manufacturing.....	8
2.2.1 Thermochemical hydrogenation	9
2.2.2 Chemical reduction	10
2.2.3 Electrochemical hydrogenation	11
2.2.4 Electrocatalytic palladium membrane reactors.....	12
2.3 Operation principles of electrocatalytic palladium membrane reactors	14

2.3.1	Hydrogen evolution and evolution at a palladium surface	14
2.3.2	Hydrogenation at a palladium surface	17
2.3.3	Advantages of using palladium as a membrane for catalysis	18
2.4	Hydrogenation in an ePMR	21
2.4.1	Variables that control reaction outcomes in an ePMR.....	21
2.4.2	Applications of the ePMR.....	25
2.5	Membrane and reactor design for ePMRs	27
2.5.1	Palladium membrane designs	28
2.5.2	Flow chemistry for organic transformations.....	29
Chapter 3: Strain Influences the Hydrogen Evolution Activity and Absorption Capacity of Palladium.....		33
3.1	Introduction.....	33
3.1.1	Strain engineering in electrocatalysis	33
3.1.2	Strain engineering palladium electrodes.....	36
3.2	Results.....	39
3.2.1	Design of a tensile testing electrochemical device (“TED”)	39
3.2.2	Measuring the effect of mechanical strain on HER and H:Pd at a palladium electrode	43
3.2.3	Correlation of applied mechanical strain to palladium lattice strain	45
3.3	Discussion.....	48
3.4	Conclusion	50
3.5	Experimental Methods	51

3.5.1	Materials	51
3.5.2	Thin film deposition.....	52
3.5.3	X-ray diffraction experiments.....	52
3.5.4	Fabrication of electrode assemblies	53
3.5.5	Tensile test experiments.....	54
3.5.6	Electrochemical measurements.....	55
3.5.7	Hydrogen absorption quantification	56
3.5.8	Calculation of uncertainty for electrochemical measurements.....	57
3.5.9	Scanning electron microscopy	57
Chapter 4: Electrocatalytic Hydrogenation Using a Palladium Membrane Flow Cell.....		58
4.1	Introduction.....	58
4.2	Results and Discussion	61
4.2.1	Design of an electrochemical palladium membrane flow cell.....	61
4.2.2	Benchmarking hydrogenation reaction performance in the flow cell.....	64
4.2.3	Palladium membrane properties determine hydrogenation reaction performance	67
4.3	Conclusions.....	71
4.4	Experimental Methods	72
4.4.1	Materials	72
4.4.2	Pd foil preparation.....	73
4.4.3	Electrochemistry	73
4.4.4	Catalyst preparation	74
4.4.5	Hydrogenation experiments in a flow cell	74

4.4.6	Gas chromatography–mass spectrometry	75
4.4.7	Atmospheric–mass spectrometry	76
4.4.8	Flow coulometry experiments.....	77
4.4.9	Kinetic modelling.....	77

Chapter 5: Physical Separation of H₂ Activation from Hydrogenation Chemistry Reveals

the Specific Role of Secondary Metal Catalysts79

5.1	Introduction.....	79
5.2	Results.....	82
5.3	Discussion.....	88
5.4	Conclusion	92
5.5	Experimental methods	92
5.5.1	Materials and instrumentation.....	92
5.5.2	Pd foil and Pd-black catalyst preparation	93
5.5.3	Catalyst-coated membrane preparation.....	94
5.5.4	Electrochemistry	94
5.5.5	Hydrogenation of acetophenone and styrene in a palladium membrane reactor ..	95
5.5.6	Product quantification.....	95
5.5.7	Hydrogen permeation.....	96
5.5.8	Temperature Programmed Desorption (TPD)	97
5.5.9	Hydrogenation of acetophenone with 1 atm H ₂ gas.....	97
5.5.10	Scanning electron microscope (SEM and transmission electron microscopy (TEM)	98

5.5.11	Electrochemical surface area (ECSA) determination	98
Chapter 6: Conclusions and Future Work		100
6.1	Conclusions.....	100
6.2	Future work: Advancing the ePMR towards applications in chemical synthesis.....	101
6.3	Research and development roadmap for the ePMR.....	103
6.3.1	Research direction 1: Increased substrate scope.....	104
6.3.2	Research direction 2: Palladium-free membranes	105
6.3.3	Research direction 3: Zero-gap reactor design	106
6.4	Outlook: How ePMRs can contribute to a future of carbon-neutral chemical manufacturing	107
References		109
Appendices		123
Appendix 1: Chapter 3		123
Appendix 2: Chapter 4		146
Appendix 3: Chapter 5		171

List of Figures

- Figure 1.1 a) Simplified illustration of an electrocatalytic palladium membrane reactor b) Illustration showing proton reduction, H absorption and permeation occurring in a palladium membrane during ePMR operation..... 3
- Figure 1.2 Graphical summary of research contributions presented in this thesis. 4
- Figure 2.1 Substrates are ranked from least to most challenging to reduce on a Pd catalyst surface. The substrate structure, solvent and use of co-catalysts affect the sequence of hydrogenation difficulty. This figure is a qualitative guide based on published reduction tables.⁶⁹ 9
- Figure 2.2 Comparison of the ePMR to TCH and ECH. a) Thermochemical hydrogenation requires fossil-derived H₂ and heat to drive hydrogenation of an organic feedstock at a nanoparticle catalyst. b) Chemical reduction (i.e., transfer hydrogenation or reduction with metal hydrides) uses stoichiometric reagents to reduce the feedstock, at low temperature, but generates undesired chemical waste. c) Electrochemical hydrogenation sources H atoms from water, then uses them to hydrogenate the feedstock dissolved in the electrolyte at an electrode. d) The electrochemical palladium membrane reactor (ePMR) separates reactive H formation from the hydrogenation process using a palladium membrane. This architecture solves the key challenges with both TCH and ECH setups..... 13
- Figure 2.3 Illustrations of the four processes that proceed during water electrolysis at a cathodic palladium surface: a) the Volmer step, b) the Tafel step, c) the Heyrovsky step, and d) hydrogen absorption..... 15
- Figure 2.4 a) Illustration depicting hydrogen permeation and evolution measurements performed on both sides of the membrane using a gas chromatograph (GC). b) Hydrogen evolution and permeation rates using H₂SO₄ and pentane on the permeation side of the membrane, with hydrogen permeation dominating when a non-polar, non-coordinating solvent is used. Data presented in panel b is adapted from ref. 91..... 17
- Figure 2.5 Illustrations summarizing the attributes of using electrolytic hydrogen driven through a membrane for hydrogenation. “C=X” refers a generic unsaturation with X referring to either a C, N, or O atom. R groups are not shown for simplicity..... 19
- Figure 2.6 a) Labelled image of an ePMR H-cell setup used for hydrogenation of alkynes. b) Plot of alkyne, alkene, and alkane relative concentration as a function of time during sustained electrolysis in an ePMR adapted from ref. 63..... 22

Figure 2.7 Reaction outcomes can be manipulated in an ePMR using current density, and electrolyte or catalyst composition. Catalyst data (leftmost plot) was reproduced from ref. 44,45 Current density and electrolyte data (rightmost plots) were adapted from ref. 31. 24

Figure 2.8 Membrane designs for ePMRs reported to date. The vast majority of studies use dense Pd foils as the electrocatalyst, membrane and hydrogenation catalyst. Pd membranes are prone to mechanical degradation due to lattice expansion and contraction during hydrogen absorption-desorption cycling which causes the foil to crinkle, embrittle and eventually crack. Delima *et al.* report a supported Pd membrane architecture (image reprinted from ref. 127) and Iwakura *et al.* provide proof of concept for using Pd-free hydrogen storage alloy membranes in this application. 28

Figure 2.9 Illustrations of a) H-cell and b) flow cell reactors used in organic electrosynthesis. Flow cells enable faster conversion by increasing c) mass transport kinetics and d) current density. Data presented in panels c and d adapted from ref. 81,137..... 31

Figure 3.1 a) Schematic of the tensile-testing electrochemical device (TED) designed for this study. b) Photograph of the TED in a support housing, which holds the data acquisition equipment (not shown for simplicity) and a stepper motor. c) Schematic of the completed sample assembly consisting of a flexible sample sandwiched between two polymethylmethacrylate (PMMA) sample holders. d) Photograph of a completed sample assembly with a flexible Pd|substrate electrode installed between the sample holders..... 38

Figure 3.2 a) A prototypical chronoamperometric plot illustrating the two stages of a hydrogen absorption measurement using coulometry.¹⁵⁴ Hydrogen is absorbed into the palladium lattice during electrolysis at -0.35 V vs Ag/AgCl. Hydrogen is then desorbed from the lattice by applying an oxidative potential of 0.30 V vs. Ag/AgCl to the electrode. b) Chronoamperometric curve highlighting the integrated region of the oxidative step used to calculate the amount of hydrogen absorbed into the palladium lattice (i.e., H:Pd ratio). 41

Figure 3.3 a) Plot of the H:Pd ratio as a function of electrolysis time (at -0.35 V vs Ag/AgCl in 1 M H₂SO₄) for a Pd|substrate electrode. H:Pd increases abruptly during the first 60 s of electrolysis, forming the β -hydride phase,¹⁷² then remains constant as the H:Pd ratio reaches equilibrium b) Chronoamperometric trace for a Pd|substrate electrode under sustained electrolysis (at -0.35 V vs Ag/AgCl in 1 M H₂SO₄). The initial decrease in current as a function of time is inferred to represent the completion of hydrogen absorption, that occurs concomitantly with HER. 42

Figure 3.4 a) Plot of the % change in the H:Pd ratio at a Pd|substrate electrode as a function of applied tensile strain ($\epsilon_{\text{applied}}$). This result was replicated four separate times, each at a fresh Pd|substrate sample. Data collected for every sample is overlaid and the entire dataset fit with a linear regression, shown in blue. b) Plot of the % change in HER activity as a function of $\epsilon_{\text{applied}}$ collected at four fresh β -PdH_x|substrate electrodes. The orange line is a second-order polynomial fit of the compiled data from all samples..... 44

Figure 3.5 a) Photograph of the custom x-ray diffraction strain stage fabricated to measure the effect of mechanical strain on the metal lattice using the $\ln(d)$ vs. $\sin^2\psi$ relationship. b) $\epsilon_{\text{macrostrain}}$ is proportional to the slope of $\ln(d)$ vs. $\sin^2\psi$ with each linear fit representing one $\epsilon_{\text{macrostrain}}$ data point c) $\epsilon_{\text{macrostrain}}$ in the 50-nm thick palladium film increases linearly up to $\epsilon_{\text{applied}} = 2.1\%$. The dotted line represents a linear fit ($R^2 = 0.97$) of the data over a $\epsilon_{\text{applied}}$ range of 0 to 2.1%. 46

Figure 3.6 Scanning electron microscope (SEM) images of (top) Pd|substrate samples mechanically strained to 2.0%, 4.7% and 10.3%, and (bottom) hydrided β -PdH_x|substrate electrodes strained to 4.7%, 5.4% and 7.8%. Fractures perpendicular to the direction of applied mechanical strain were observed for electrodes strained to levels greater than 2.0% and 5.4% for Pd|substrate and β -PdH_x|substrate, respectively. 47

Figure 4.1 Illustrations of a) the two-compartment H-cell reactor architecture used to date for electrocatalytic palladium membrane hydrogenation reactions,^{90,180} and b) the ePMR flow cell architecture reported here, wherein the organic reagent is delivered to the catalyst surface through a flow field plate. c) Rendering of the ePMR flow cell, which includes electrolysis and hydrogenation compartments partitioned by a palladium membrane. The electrolysis compartment houses a 3-electrode electrochemical setup, and the hydrogenation compartment includes a flow field plate with a triple serpentine flow pattern for efficient reagent delivery (see Figure A2.1 for an image of the complete setup). 60

Figure 4.2 a) Concentration profile of a hydrogenation reaction carried out at 250 mA/cm² in the ePMR flow cell. The inset scheme shows that hydrogenation of phenylacetylene (PA) may proceed via a styrene intermediate or directly to ethylbenzene (EB) in a single step. Kinetic fits (indicated by solid lines) are described by Equations A2.4 to A2.6. b) Bar chart comparing reaction performance in an H-cell and a flow cell (with an identical Pd surface area) using four reaction performance metrics: initial reaction rate; maximum styrene concentration; current efficiency (CE); and cell voltage (E_{cell}) at 100 mA/cm². This flow architecture enables higher performance in every metric than the H-cell..... 63

Figure 4.3 Plots showing the effect of current density on; a) the initial rate of phenylacetylene (PA) hydrogenation to styrene and ethylbenzene (EB) (reaction scheme inset), b) maximum styrene

concentration, and c) current efficiency, as a function of current density in an ePMR flow cell. Current density increases the hydrogenation reaction rate while concurrently decreasing selectivity and current efficiency. Each data point represents the average value from at least three reactions with error bars representing ± 1 standard deviation of the mean value. 66

Figure 4.4 Plots illustrating the effect of a) applied voltage and b) current density on the amount of hydrogen that absorbs into the palladium membrane, showing direct electrochemical control over the palladium membrane hydrogen content (expressed as the H:Pd ratio). Plots showing that higher membrane hydrogen content c) increases the initial reaction rate and d) decreases selectivity for the styrene intermediate. Error bars represent ± 1 standard deviation of the mean value for at least 3 reactions. 69

Figure 4.5 a) Illustration of the experiment setup used to measure the amount of hydrogen that permeates through the palladium membrane by tracking the $m/z = 2$ ion current using in situ atmospheric-mass spectrometry b) The amount of the hydrogen that permeates through the membrane increases with current density and is described by a polynomial fit. c) Plot showing that current efficiency decreases linearly with increasing hydrogen evolved at the side of the membrane where hydrogenation occurs. Error bars represent ± 1 standard deviation of the mean value for at least 3 reactions. 71

Figure 5.1 (a) Schematic diagram of the electrocatalytic palladium membrane reactor (ePMR) with a secondary metal catalyst (Pt, Au, Ir) deposited on the side of the palladium membrane exposed to the chemical compartment. (b) Illustration of the relevant processes occurring at the catalyst-coated membrane during hydrogenation: i) Proton reduction occurs on the Pd membrane to form H atoms; ii) H atoms diffuse through the Pd membrane to the secondary metal catalyst; iii) The substrate is hydrogenated on the secondary metal catalyst. The catalyst-coated membrane was prepared by depositing a 10 nm layer of the secondary metal catalyst layer (orange) over Pd black (grey), which was electrodeposited to increase the reaction surface area. 81

Figure 5.2 Photograph of the electrocatalytic Pd membrane reactor (ePMR) with a catalyst-coated membrane serving as proton reduction cathode, hydrogen-permeable membrane, and hydrogenation catalyst. The 3-compartment cell contains a divided electrochemical compartment filled with 1 M H₂SO₄ and one chemical compartment filled with organic solvent. The terminal electrochemical compartment contains a platinum mesh anode (where water oxidation occurs) and the middle electrochemical compartment contains a Ag/AgCl reference electrode, and the palladium cathode where protons are reduced then absorbed. The anode and cathode are separated by a Nafion membrane. Secondary metal catalysts are coated on the face of the membrane exposed to the chemical compartment. 83

Figure 5.3 Hydrogenation performance of catalyst-coated membranes. Cell setup and product conversion for hydrogenation of (a) C=O bonds (acetophenone) and (b) C=C bonds (styrene) on catalyst-coated membrane (Pt, Ir, Au) and Pd catalysts at an applied current of 200 mA. 86

Figure 5.4 (a) Ratio of H₂ gas evolved on the chemical/electrochemical side of the Pd membrane with different secondary metal catalysts in toluene (dark color) and ethanol (light color). (b) Cell setup used to determine hydrogen flux through catalyst-coated membranes. 87

Figure 5.5 Temperature programmed desorption spectra of H₂ (m/z = 2) from catalyst-coated membranes. Each sample was loaded with hydrogen in 0.1 M HCl at a reductive potential of -0.4 V (vs. Ag/AgCl) until a total charge of 10 C was passed. 88

Figure 5.6 (a) Ratio of H₂ gas evolved on the chemical/electrochemical side of the catalyst-coated membrane as a function of their hydrogen desorption temperature determined by TPD. (b) Schematic representation illustrating the influence of M–H binding strength on hydrogen flux. Weak M–H binding strength leads to higher hydrogen flux, whereas strong M–H binding strength results in lower hydrogen flux. 90

Figure 5.7 (a) Ratio of H₂ gas evolved on the chemical/electrochemical side of the catalyst-coated membrane as a function of hydrogen adsorption energy for the pure metal surface (ΔG_{H^*})²⁰⁹. Potential energy diagram for hydrogen permeation (diffusion then desorption) of absorbed hydrogen in the catalyst-coated membrane when the process is (b) desorption limited and (c) diffusion limited. 91

Figure 6.1 Summary of suggested future research directions for the ePMR. 104

List of Abbreviations

“	Inches
%	Percent
°	Degrees
°C	Degrees Celsius
<	Less than
>	Greater than
~	Approximately
∝	Proportional to
Å	Angstrom
ASTM	American society of testing and materials
CE	Counter electrode
cm	Centimeters
CO₂RR	Carbon dioxide reduction reaction
CR	Chemical reduction
DCM	Dichloromethane
e-PTFE	Expanded polytetrafluoroethylene
e.g.	For example
E_a_{desorption}	Activation energy of desorption
EB	Ethylbenzene
E_{cell}	Cell voltage
ECH	Electrocatalytic hydrogenation

ePMR	Electrocatalytic palladium membrane reactor
Eq.	Equation
g	Gas-phase
g	Grams
GC	Gas chromatography
GC-MS	Gas chromatography-mass spectrometry
h	Hour
H:Pd	Hydrogen to palladium angle
H₂	Diatomic hydrogen gas
H_{abs}	Absorbed hydrogen
HAR	Hydrogen absorption reaction
HER	Hydrogen evolution reaction
i.e.	In other words
ID	Internal diameter
k	Rate constant
kWh	Kilowatt hour
M	Moles per liter
m/z	Mass to charge ratio
mA	Milliamperes
mbar	Millibar
mg	Milligram
min	Minutes

mmol	Millimole
mV	Millivolt
N	Newtons
NIST	National Institute of Standards and Technology
nm	Nanometer
No.	Number
OD	Outer diameter
OER	Oxygen evolution reaction
ORR	Oxygen reduction reaction
PA	Phenylacetylene
pA	Picoamperes
PTFE	Polytetrafluoroethylene
QCM	Quartz crystal microbalance
RE	Reference electrode
rpm	Rotations per minute
s	Seconds
SEM	Scanning electron microscopy
ST	Styrene
TCH	Thermochemical hydrogenation
T_{desorp}	Desorption temperature
TED	Tensile testing electrochemical device
TPD	Temperature programmed desorption

USD	United states dollars
V	Volts
α	First phase of palladium hydride
β	Second phase of palladium hydride
δ	Chemical shift
ε	Strain
θ	Diffraction angle
μ	Micrometer
σ	Standard deviation
Ω	Resistance, ohms
ψ	Goniometer angle relative to sample normal

Acknowledgements

I would like to first thank Dr. Curtis Berlinguette for supporting the research directions I proposed, and my entrepreneurial pursuits during my PhD. I would also like to thank my committee, especially Dr. Dan Bizzotto for his thoughtful feedback on my thesis and manuscript drafts throughout my studies. Many of the projects I pursued involved custom instrumentation - Doug Yuen, Graham Liebelt, and Tobias Donaldson are the careful machinists who built it.

My experience in STEM is somewhat unique in that many of my mentors have been women. Dr. Ashley Crusch inspired me, a failing undergraduate at the time, to pursue a career in clean tech. Dorina Manolescu taught me the value of meticulous lab notes. Dr. Rebecca Sherbo forged the path for the technology that I chose to spend the last 3 years studying. Dr. Val Chiykowski has been a thoughtful guide in the world of entrepreneurship. Dr. Aiko Kurimoto showed me what creative research and a dedicated work ethic look like. These powerful women of science have played a key role in my growth over the last 5 years. I will be forever grateful.

In addition to those listed above, the support and friendship of Dave, Ben, Natalie, Angelica, Rebecka, and Camden helped me to manage the low points, and celebrate the highs. Morning runs with the Wednesday Crew were a source of balance and perspective, and are some of my fondest memories of the last 5 years. Thank you Warren, Natalie, Ben, Val, Tom, and Chris.

Kate, I couldn't have done this without your patience, support and kindness. Thank you.

For my family

Chapter 1: Introduction

1.1 Motivation

Chemical manufacturing consumes 10% of the energy produced worldwide and is responsible for 5.5% of all carbon emissions.¹ This large carbon footprint arises because nearly all chemicals are synthesized using thermal energy generated by fossil fuel combustion.² To reduce this footprint, chemical manufacturing methods must be developed that do not rely on fossil-derived heat.^{2,3} The electrosynthesis of organic products is an attractive strategy to circumvent carbon-intensive thermochemical methods by using electricity to drive the same chemistry, but at ambient temperature.⁴⁻⁷ If coupled to a renewable electricity source, electrosynthesis provides a pathway to decarbonize chemical manufacturing.²

Hydrogenation is an ideal electrosynthetic target.⁸ This reaction, in which hydrogen atoms are added to an unsaturated organic feedstock, is used in 20% of all fine chemical syntheses,⁹ and is widely used in pharmaceutical,¹⁰ food,¹¹ and (bio)fuel production.¹² The most common commercial method, thermochemical hydrogenation, requires methane-derived hydrogen gas (H_2)¹³ and operation at high temperatures and pressures. Other common hydrogenation methods, including transfer hydrogenation¹⁴ or chemical reduction,^{15,16} proceed at low temperatures but generate stoichiometric amounts of chemical waste. A carbon-efficient hydrogenation method must address both of these issues by mediating the reaction at low temperature without requiring heat or $H_2(g)$, and must also avoid producing chemical waste.

This thesis presents the electrocatalytic palladium membrane reactor (ePMR) as a disruptive technology capable of solving challenges with conventional hydrogenation methods. ePMRs hydrogenate organic molecules in ambient conditions, without using $H_2(g)$ or generating hazardous chemical waste.^{17,18} This device instead uses electricity and water as the only inputs to

hydrogenate the chemical feedstock.¹⁹⁻²² The ePMR is the only known reactor capable of using hydrogen generated from water to hydrogenate organic compounds in an organic medium. Despite these attributes, there are relatively few studies of ePMRs, and the full capabilities of this reactor are largely unknown. The opportunity to develop this nascent technology toward carbon-neutral, waste-free hydrogenation was the primary motivation for my work.

1.2 Electrocatalytic palladium membrane reactors

At the core of the ePMR is a hydrogen-permeable palladium membrane that physically separates an electrochemical reaction from a hydrogenation reaction (Figure 1.1a). Hydrogen is supplied to the reaction from water electrolysis in an electrochemical compartment. The protons formed at the anode (eq. 1.1) are reduced at the surface of the cathodic palladium foil (eq. 1.2). These H atoms then absorb into the palladium foil (eq. 1.3) and diffuse through octahedral (and to a lesser extent, tetrahedral) interstices in the metal lattice (Figure 1.1b).²³ H atoms transition from the bulk to (sub)surface at the opposite face of the membrane and react with an unsaturated substrate in the hydrogenation compartment (eq.1.4).^{17,18,24} This architecture enables the electrolysis to proceed in aqueous electrolyte while hydrogenation is mediated in organic solvent.



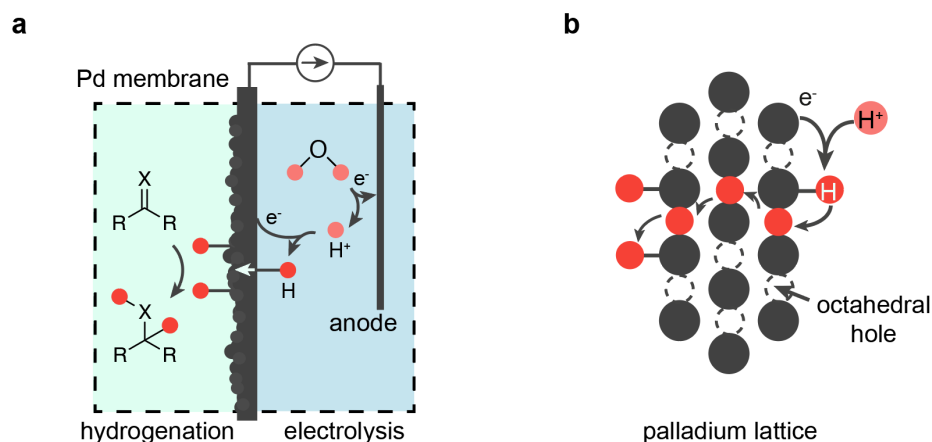


Figure 1.1 a) Simplified illustration of an electrocatalytic palladium membrane reactor b) Illustration showing proton reduction, H absorption and permeation occurring in a palladium membrane during ePMR operation.

The first iteration of ePMR was reported in 1996,¹⁸ but the Berlinguette group's studies of the palladium-hydrogen system²⁵ led Sherbo *et. al.* to independently develop this technology in 2018.¹⁷ To date, there are roughly 30 studies^{17–22,26–49} focused on this device showing that a variety of functionalities can be hydrogenated (or deuterated²¹), including: alkynes,^{17,19,26,27,32} alkenes;²⁷ aldehydes;³⁹ imines²¹ and ketones;⁴² quinones;⁴³ aromatic rings;⁴⁵ and CO₂.⁴⁹ These capabilities suggest that this device may eventually be used for chemical manufacturing across diverse industries. However, to compete with well-optimized thermochemical methods, high performing ePMRs must be developed that can operate at high current densities and energy efficiencies, and are capable of hydrogenating a broad scope of unsaturated feedstocks.⁶

1.3 Structure of the thesis

The discoveries presented in this thesis seek to advance our understanding of the ePMR and also provide strategies to improve the efficiency and versatility of this reactor. **Chapter 2** provides a literature review of the palladium-hydrogen system, hydrogenation reactions, and describes the advantages of the ePMR compared to established thermo- and electro- chemical methods. **Chapters 3-5** are based on published or submitted studies I authored on the palladium-hydrogen system and the ePMR.^{22,50} **Chapter 6** concludes the thesis by providing a development roadmap for this technology. The primary research findings are summarized in Figure 1.2.

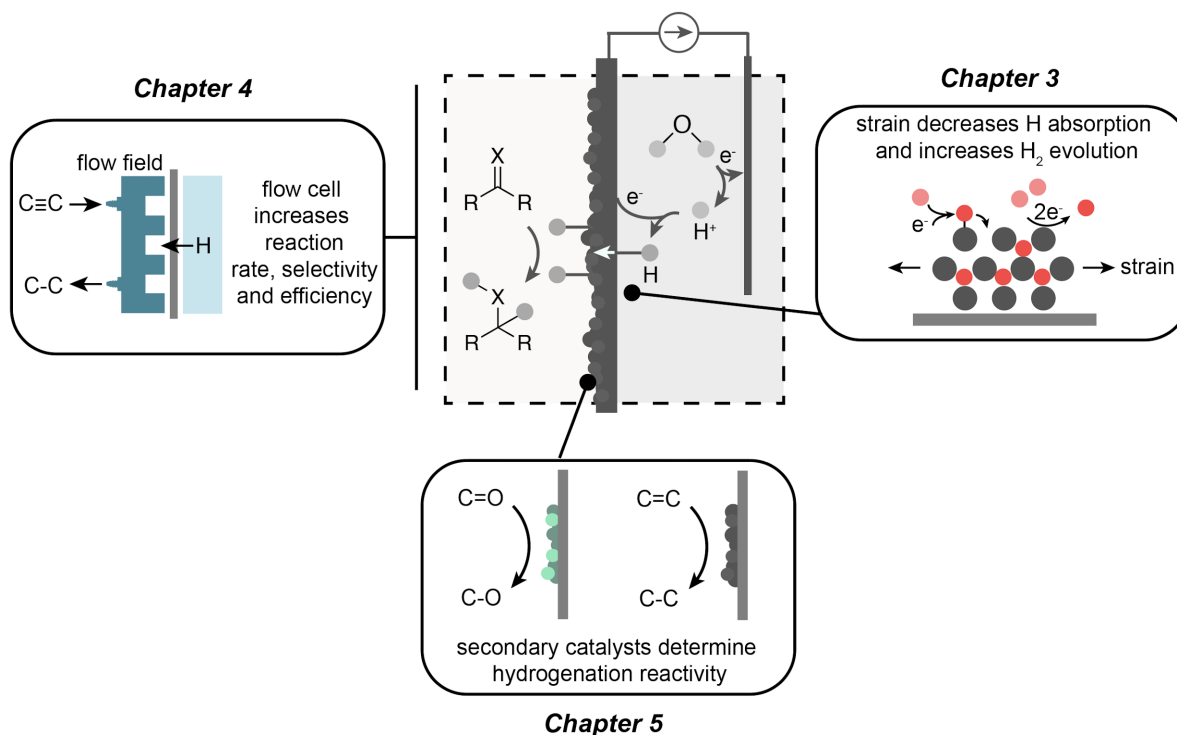


Figure 1.2 Graphical summary of research contributions presented in this thesis.

Chapter 3 focuses on understanding palladium-hydrogen interactions under reductive electrolysis. In this work, I analyzed how the spacing between palladium atoms influences the rate of the hydrogen evolution reaction (eq. 1.2) and hydrogen absorption (e.q., 1.3) at a palladium thin

film surface. I designed and constructed a unique electrochemical cell that can apply measured amounts of mechanical strain to a flexible palladium electrode during electrolysis. This work demonstrates that tensile strain increases HER activity, and decreases the amount of hydrogen that absorbs into the metal.

Chapter 4 describes an ePMR flow cell that enables faster, more selective, and more energy efficient hydrogenation. All previous studies of ePMRs were conducted in a common electrochemical cell architecture called an “H-cell”. While H-cells are convenient for proof-of-concept research, this architecture is not scalable and is hindered by poor reaction rates and low energy efficiencies. I show that cell design considerations alone (improving mass transport of the organic feedstock to the palladium surface, and increasing the maximum electrolysis current density) enables up to 15-fold faster hydrogenation rates compared to reaction rates in H-cells. I also used this flow cell as an analytical tool to relate the amount of hydrogen absorbed in the membrane to hydrogenation performance.

Chapter 5 discusses how secondary catalysts can be deposited on the surface of a palladium membrane to tailor reactivity for C=C and C=O bonds in an ePMR. Research to date on this device has largely focused on the reduction of C–C unsaturated bonds to alkenes and alkanes. While these reactions are required to make a multitude of industrial chemicals (e.g., vitamin and fragrance precursors, hydrogenated fats, ethylene, among many others), there are many applications in the pharmaceutical and specialty chemical applications that require the hydrogenation of C=O bonds.¹⁰ To enable C=O hydrogenation in an ePMR, we deposited a thin film of a secondary metal (i.e., Pt, Ir and Au) on the hydrogenation face of the palladium membrane and found that the thin co-catalytic films increased C=O hydrogenation rates, and decreased rates for C=C hydrogenation.

Chapter 6 concludes the thesis and provides a roadmap for future ePMR development. I envision this technology may eventually be a cost-competitive, and low-carbon alternative to conventional thermochemical hydrogenation methods. However, there remains important advances to be made before this device can be used to efficiently produce hydrogenated chemicals. This chapter highlights the importance of broadening the types of molecules that can be hydrogenated in this device, decreasing the amount of palladium used in the membrane, and decreasing the electrical voltages required to drive the reaction. The development goals I present within this chapter serve to inform the continued development of this useful technology.

Chapter 2: Literature review

This chapter reviews the role of hydrogenation in chemical synthesis, and introduces the electrocatalytic palladium membrane reactor (ePMR) as an enabling technology to decarbonize this chemical manufacturing process. I describe how the ePMR can address challenges with competing hydrogenation methods (Section 2.1). The reactions occurring at the centrally-located palladium are reviewed in Section 2.2. Finally, I detail how hydrogenation reactions are carried out in this device and the current state of understanding of ePMRs (Sections 2.3 to 2.5).

2.1 The case for using electricity as a reagent in chemical synthesis

Electrons have been used as a reagent in chemical synthesis since at least the late 1880s with the high temperature electrolysis of aluminum ores.^{8,51} Reactions such as the chloralkali process and Kolbe electrolysis⁵² have been used at large scale since the 20th century. Readily-available fossil energy stagnated the development of large-scale electrosynthesis methods for nearly 100 years, but environmental concerns have reignited interest in electrosynthesis since the 2000s.⁵³ In addition to the opportunity to reduce CO₂ emissions, there are also a number of other benefits to using electricity to drive a chemical reaction. Safety is increased by avoiding stoichiometric reducing and oxidizing agents, and waste generated during the reaction can be decreased by electrochemically generating the reactant in situ.⁴

A primary challenge of using electricity to manufacture chemicals lies in developing electrosynthesis technologies that are cost competitive with thermochemical methods.^{3,6,8} This challenge is complicated by two major factors: i) the low price of hydrocarbon-derived thermal energy (\$0.011/kWh)⁵⁴ in comparison to electricity (\$0.067/kWh)⁵⁵ and; ii) the high operational costs of existing organic electrosynthesis platforms, stemming from high cell voltages, low cell currents, and costly separation of product from an electrolyte.^{56,57} The cost of renewable electricity

has dropped precipitously — \$0.068/kWh in the U.S. in 2019 compared to \$0.380/kWh in the U.S. in 2010,⁵⁸ and solar energy prices have recently been reported as low as \$0.013/kWh.⁵⁹ However, reduced operational costs must be realized for organic electrosynthesis to gain industrial relevance and supplant large-scale thermochemical processes.

The electrification of hydrogenation reactions present an attractive opportunity to decrease CO₂ emissions because this reaction is used across diverse industries at large scale.^{8,60–63} The use of renewable hydrogen in chemical manufacturing has the potential to reduce carbon emissions from this industry by 1.4 Gt.¹ Electrosynthetic hydrogenation provides a pathway to realize these carbon emissions by eliminating two significant sources of CO₂ in this process: i) thermally derived heat, and ii) fossil-derived H₂ gas. More than 96% of all heat generated for manufacturing (6879 TBtu out of a total of 7204 TBtu),⁶⁴ and 95% of H₂ produced worldwide is produced from non-renewable sources.¹³ It is against this backdrop that I investigated the use of the ePMR for efficient, electrically-driven hydrogenation reactions.

2.2 Hydrogenation in chemical manufacturing

Hydrogenation changes the reactivity, viscosity and energy density of the chemical feedstock. This reaction is deployed at large scale in three industries; i) food production, ii) (bio)fuel refining, and iii) specialty chemical synthesis and plays a unique role in each case.⁶⁵ Vegetable and animal fats are hydrogenated to increase the viscosity of the oil to produce a solid fats for use primarily in packaged foods.⁶⁶ These products are made by hydrogenating the *cis*-alkenes of a triglyceride. (Bio)fuel production accounts for the largest use of hydrogen gas worldwide,⁶⁵ and requires hydrogenation steps or analogues including hydrodesulfurization and hydrodeoxygenation to remove impurities from fossil- and biomass- derived feedstocks, respectively.⁶⁷ Specialty chemicals used in the production of pharmaceuticals, agrichemicals, dyes

and additives are a diverse set of comparatively high value, low volume products. Hydrogenation steps are used in the production of 10-20% of these chemicals and span diverse functionalities (olefins, carbonyls, aromatics, and a host of N-containing unsaturations) requiring high site selectivities and high functional group tolerance.⁹ The functional groups most relevant to each industry are summarized below (Figure 2.1)

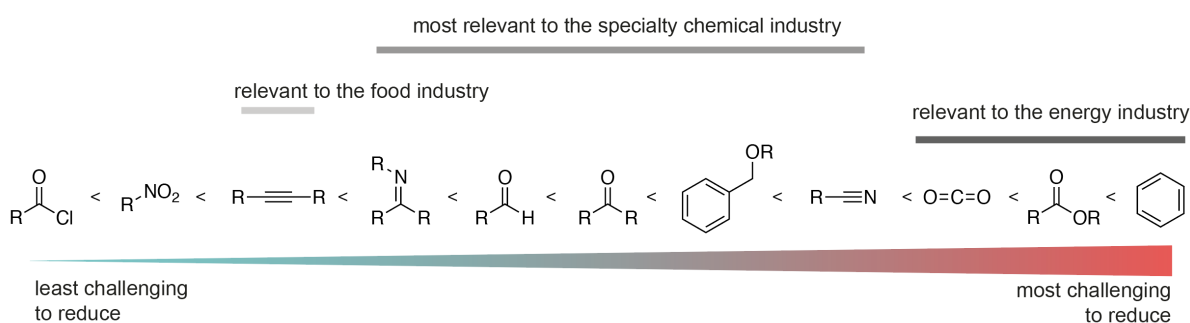


Figure 2.1 Substrates are ranked from least to most challenging to reduce on a Pd catalyst surface. The substrate structure, solvent and use of co-catalysts affect the sequence of hydrogenation difficulty. This figure is a qualitative guide based on published reduction tables.⁶⁸

2.2.1 Thermochemical hydrogenation

Thermochemical hydrogenation (TCH) is used for the majority of all industrial hydrogenation processes.⁶⁰ For TCH, reactive hydrogen sourced from pressurized H₂ gas and the reactant are delivered to a metal catalyst. The H₂ is homolytically cleaved at the catalyst surface to form adsorbed H atoms, which react with the gaseous, liquid, or dissolved substrate (Figure 2.2a).⁶⁹ The advantages of TCH are a low cost of fossil fuel combustion for the input energy, the amenability to high throughput reactors, and the established methods of product purification. Heterogeneous hydrogenation can be carried out in batch-type or flow-type reactors, with the latter dominating large-scale industrial processes.⁷⁰ Control over the hydrogenation reaction is enabled

by modifying the catalyst, pressure and temperature of the reaction.⁷¹ The primary motivation for replacing TCH arises because this method relies on fossil fuel combustion to heat the reactor and feedstock (up to 350 °C),⁷¹ and natural gas reforming for H₂ production.¹³ This method also requires capital intensive infrastructure for safely managing high temperature and pressure H₂ gas.⁷²

2.2.2 Chemical reduction

Transfer hydrogenation and reducing agents are alternatives to TCH that use stoichiometric reagents to reduce the unsaturated substrate (Figure 2.2b).^{14,68} An advantage these chemical reduction (CR) methods is that these reactions proceed at substantially lower temperatures than TCH, and can therefore be used with temperature-sensitive reagents, or catalysts. Transfer hydrogenation sources hydrogen from alcohols (e.g., isopropanol) to produce the corresponding aldehyde or ketone as a reaction byproduct.¹⁴ This method can be paired with a homogeneous catalyst to mediate asymmetric hydrogenation, a type of transformation particularly important in the pharmaceutical industry.^{62,73} Metal hydrides share the advantage of low temperature reaction conditions with transfer hydrogenation, but generally do not enable enantioselective transformations.⁶³ These reagents are mainly used to reduce heteroatom-containing unsaturations (e.g., C=O, and C≡N bonds).⁶⁸ Metal hydrides are not used at large scale due to high costs.⁶³ The cost per mole of H derived from: NaBH₄ is 11.9 USD/mol H; LiAlH₄ is 37.7 USD/mol H while the cost of H₂ is only 0.01 USD/mol H, representing a >100-fold cost decrease by using H₂(g) rather than these common reducing agents.

2.2.3 Electrochemical hydrogenation

Electrochemical hydrogenation (ECH) is an alternative approach to TCH and CR that uses electricity, instead of heat or stoichiometric reagents, to drive hydrogenation. In ECH, electrolysis and hydrogenation are coupled to circumvent the use of H₂ gas (Figure 2.2c). An oxidation reaction at the anode produces H⁺ equivalents that are subsequently reduced at the cathode to produce reactive H atoms. Harsh reaction conditions, and flammable reagents are not required for ECH, eliminating the need for much of the safety infrastructure used in TCH or CR setups. The reactive hydride is produced continuously *in situ* and benign oxygen gas, or an oxidized organic substrate is the only waste product of the reaction.

In ECH, reactive hydrogen formation and hydrogenation of the organic substrate occur at the same catalyst surface. This scenario presents two major challenges: i) the solvent is responsible for dissolution of both an electrolyte and the organic substrate. Typically, a highly-polar aqueous medium favors electrolyte dissolution and comparatively non-polar organic solvents favoring the dissolution of the organic substrate.⁶ Mixtures of water and organic solvent are commonly used to address this challenge, but are highly resistive and reduce the energy efficiency of the reaction;¹⁹ ii) high concentrations of the electrolyte necessary to achieve low overpotentials and high applied current densities for industrially-relevant ECH. Organic-compatible electrolytes are expensive, and the shared solvent for electrolyte and organic substrate creates the need to separate the product from the mother liquor so both the solvent and electrolyte can be recycled. This separation is often cited as the most critical issue facing industrial application of electrosynthesis technologies^{6,53} To address both challenges, an ECH reactor must be capable of performing both electrolysis and hydrogenation in favorable conditions, using an inexpensive electrolyte that is readily separated from the reaction product.

2.2.4 Electrocatalytic palladium membrane reactors

The electrocatalytic palladium membrane reactor (ePMR) is an electrosynthesis platform that circumvents many of the issues with conventional ECH setups. An ePMR uses a hydrogen-permeable Pd membrane to physically separate the electrochemistry from a hydrogenation reaction (Figure 2.2d), enabling the electrolysis to proceed in aqueous electrolyte and the hydrogenation to proceed in organic solvent. Hydrogen is supplied to the reaction from water electrolysis in an electrochemical compartment. By isolating the electrochemistry from the hydrogenation reaction, neither solubilizing agents nor an organic electrolyte are needed,¹⁹ which minimizes side reactions, simplifies operation, increases energy efficiency and enables indefinite electrolyte reuse (which is relevant if using expensive deuterated electrolytes²¹).⁵ At the opposite face of the membrane, the hydrogenation reaction proceeds in an additive-free organic solvent that can be readily removed from the hydrogenated product by evaporation, circumventing costly purification steps.²¹ Each of the processes occurring at the membrane surface, and the advantages of this architecture and described in detail in section 2.3.

These reactors are relatively understudied in the academic literature, with only ~30 reports of these devices (or analogues) published. Most of these studies have been reported since 1996, and only three groups that have reported on this device since 2016. These reports to date are sufficient to highlight the advantages of separating the electrochemistry from hydrogenation, but significant development is required to apply the ePMR to industrial synthesis.

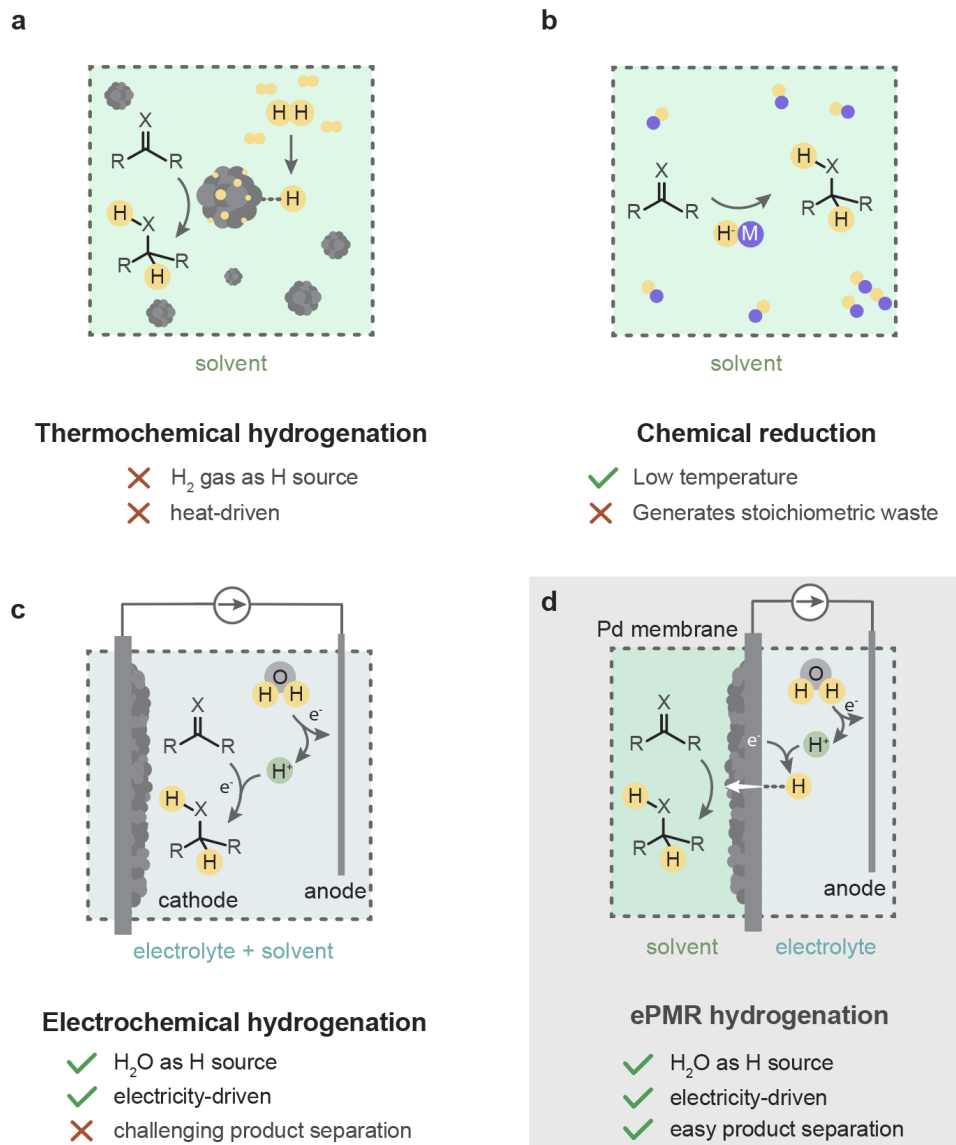


Figure 2.2 Comparison of the ePMR to TCH and ECH. a) Thermochemical hydrogenation requires fossil-derived H₂ and heat to drive hydrogenation of an organic feedstock at a nanoparticle catalyst. b) Chemical reduction (i.e., transfer hydrogenation or reduction with metal hydrides) uses stoichiometric reagents to reduce the feedstock, at low temperature, but generates undesired chemical waste. c) Electrochemical hydrogenation sources H atoms from water, then uses them to hydrogenate the feedstock dissolved in the electrolyte at an electrode. d) The electrochemical palladium membrane reactor (ePMR) separates reactive H formation from the hydrogenation process using a palladium membrane. This architecture solves the key challenges with both TCH and ECH setups.

2.3 Operation principles of electrocatalytic palladium membrane reactors

In this section I will review the key processes that occur during hydrogenation in an ePMR – hydrogen production, transport, and hydrogenation – and highlight the advantages of using a membrane for catalysis.

2.3.1 Hydrogen evolution and evolution at a palladium surface

The hydrogen evolution reaction (HER) is the cathodic half reaction occurring at the palladium surface during water electrolysis. This process of forming $\text{H}_2(\text{g})$ from two protons and two electrons proceeds through two steps (Figure 2.3).^{74,75} For the first step (i.e., the Volmer step; Figure 2.3a), a proton diffuses to the catalyst surface and is reduced by one electron to produce a surface adsorbed H atom. The second step forms $\text{H}_2(\text{g})$ and can proceed either by a faradaic, or non-faradaic pathway. Two adsorbed H atoms can recombine in a non-faradic reaction (the Tafel step; Figure 2.3b), or a second proton can be reduced at the surface in close proximity to the first adsorbed H atom to form $\text{H}_2(\text{g})$ through the Heyrovsky step (Figure 2.3c).

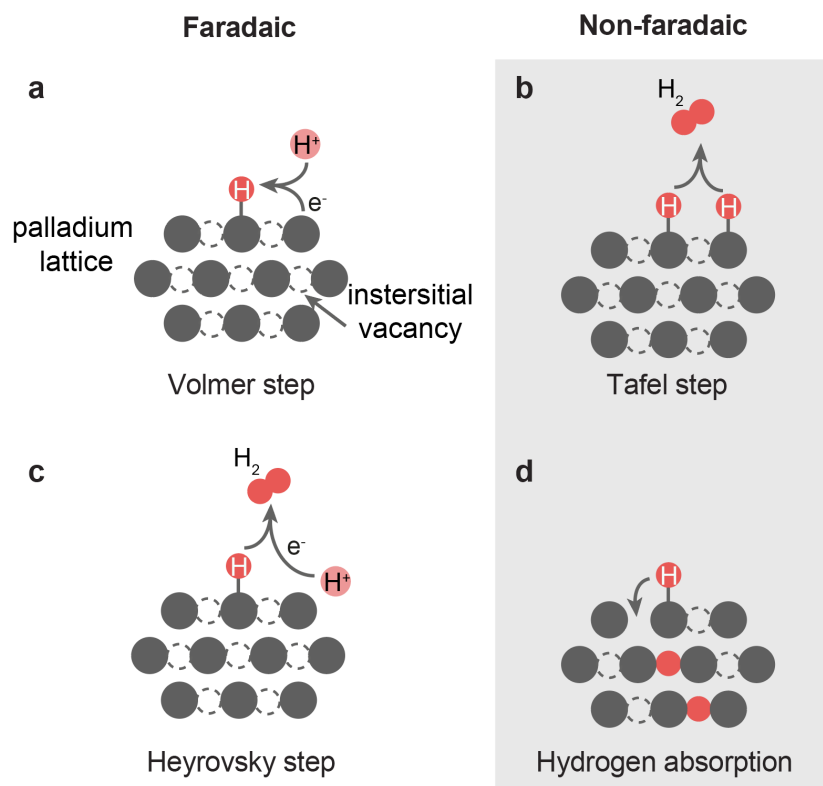


Figure 2.3 Illustrations of the four processes that proceed during water electrolysis at a cathodic palladium surface: a) the Volmer step, b) the Tafel step, c) the Heyrovsky step, and d) hydrogen absorption.

A unique feature of the palladium electrode (compared to other single metal HER catalysts) is that adsorbed H atoms can also absorb into the palladium lattice (Figure 2.3d). Hydrogen absorption induces a phase transition in the *fcc* metal to form β -PdH_x (with $x \sim 0.6$ – 0.9), causing the lattice to expand 3.4%.⁷⁶ This absorption process is exothermic⁷⁷ and proceeds through α -PdH_x (with $x < 0.01$) and, a mixed α/β phase (with $0.01 < x < 0.6$), before the transition to β -PdH_x (with $x > 0.6$) is complete.⁷⁸ For a palladium thin film (< 100 nm-thick) this absorption process completes within ~ 1 minute of the start of electrolysis,⁷⁹ thereafter β -PdH is the active surface for HER, a nuance that is often neglected in the electrocatalysis literature.^{80,81} The concentration of H atoms

hosted within the Pd lattice in the β -PdH_x can be manipulated with applied potential, temperature, or pressure, with $x \geq 0.875$ possible with low-temperature electrolysis setups.^{82,83}

Palladium is an excellent HER catalyst⁷⁵, and it might seem counterintuitive that hydrogen permeates through a palladium membrane rather than just evolving on the electrochemical surface. In reality, HER and absorption are competitive processes and H₂(g) is evolved on both faces of the membrane.^{84,85} The kinetic barrier to absorption is higher than recombination, however absorption is more thermodynamically favourable.²⁴ Reaction conditions (e.g., current density, solvent, or electrolyte) can be manipulated to enable the majority of the hydrogen produced to permeate through the membrane.^{17,24} H₂(g) evolved at each face of the membrane can be measured using gas chromatography (GC or atmospheric mass spectrometry; atm-MS). HER outcompetes H absorption and permeation at moderate currents, with an aqueous solvent in the hydrogenation chamber of the ePMR (Figure 2.4a), while ~90% of the hydrogen permeates through the membrane with a non-polar non-coordinating solvent (Figure 2.4b).¹⁷ The conditions at either side of the membrane can therefore be manipulated to enable nearly all the hydrogen formed to be delivered to the hydrogenation site at the opposite side of the membrane.

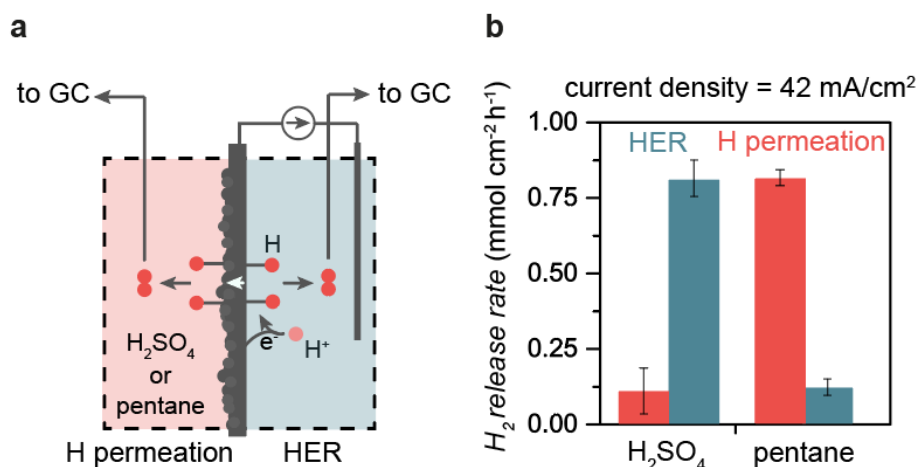


Figure 2.4 a) Illustration depicting hydrogen permeation and evolution measurements performed on both sides of the membrane using a gas chromatograph (GC). b) Hydrogen evolution and permeation rates using H_2SO_4 and pentane on the permeation side of the membrane, with hydrogen permeation dominating when a non-polar, non-coordinating solvent is used. Data presented in panel b is adapted from ref. ¹⁷.

2.3.2 Hydrogenation at a palladium surface

The last step required for hydrogenation to occur in an ePMR is hydrogen addition to the organic substrate. For olefin hydrogenation in a thermochemical reactor, the reaction proceeds through the stepwise addition of H atoms to the unsaturated substrate.^{86,87} Reactive hydrogen atoms are first formed through the dissociative adsorption of $\text{H}_2(\text{g})$ onto the palladium catalyst surface. The olefin adsorbs parallel to the catalyst surface through either two σ -bonds or one π -bond, with the former exhibiting a higher bond strength.^{88,89} An adsorbed hydrogen atom is transferred from the metal surface to the organic substrate to form an sp^3 C-H bond. The partially-hydrogenated intermediate then undergoes a second H addition at the other C atom before desorbing as the fully-hydrogenated adduct. For alkynes, both hydrogenations proceed through the same stepwise process, though the alkene intermediate can either desorb as the reaction product,

or proceed directly to the alkane.⁹⁰ Both alkyne and alkene hydrogenation step are exothermic, with the first hydrogenation step releasing 172 kJ/mol, and the alkene hydrogenation releasing a more modest 136 kJ/mol.⁹¹

While the mechanism of alkyne hydrogenation at a palladium surface is well understood,⁸⁸ the role of subsurface hydrogen has been the subject of more recent debate.⁹² Ultrahigh vacuum studies have shown that concentration of hydrogen dissolved in the catalyst influences selectivity of alkyne hydrogenation for the alkene or alkane products.^{93–96} Teschner *et al.* showed that the formation of carbonaceous deposits (alkylidenes/ynes⁸⁹) on the surface of the palladium catalyst decreases the amount of H in the lattice and in turn drives selectivity toward the alkene rather than the alkane.⁹⁷ There are two hypotheses offered to rationalize these effects: i) hydrogen located in the palladium subsurface influences the adsorption state of the alkyne on the surface, with the β -PdH_x surface more efficiently activating the adsorbed species,^{98,99} or; ii) subsurface hydrogen has a higher chemical potential and can react with more energy than surface-adsorbed hydrogen through either a direct,^{100,101} or indirect mechanism.⁹² Regardless of the mechanism, the amount of hydrogen absorbed into the palladium catalyst plays a critical role in determining hydrogenation activity.

2.3.3 Advantages of using palladium as a membrane for catalysis

There are a number of advantages to using a palladium membrane for catalysis (Figure 2.5). As a membrane material, palladium is inert to most organic solvents, and electrolytes, and is highly selective to H-atom permeation, enabling >99% H₂(g) purities after passing through the lattice.¹⁰² Palladium is mechanically stable after both absorption and desorption, though it should be noted that hydrogen embrittlement occurs after repeated loading-deload cycles.¹⁰³ By comparison, other transition metals that also absorb large amounts of hydrogen (e.g., V, Nb, Ti,

Ta, and Y)¹⁰⁴⁻¹⁰⁶ undergo more drastic structural changes at high hydrogen absorption stoichiometries and lose mechanical stability, making these materials less suitable for use as a membrane.¹⁰⁷

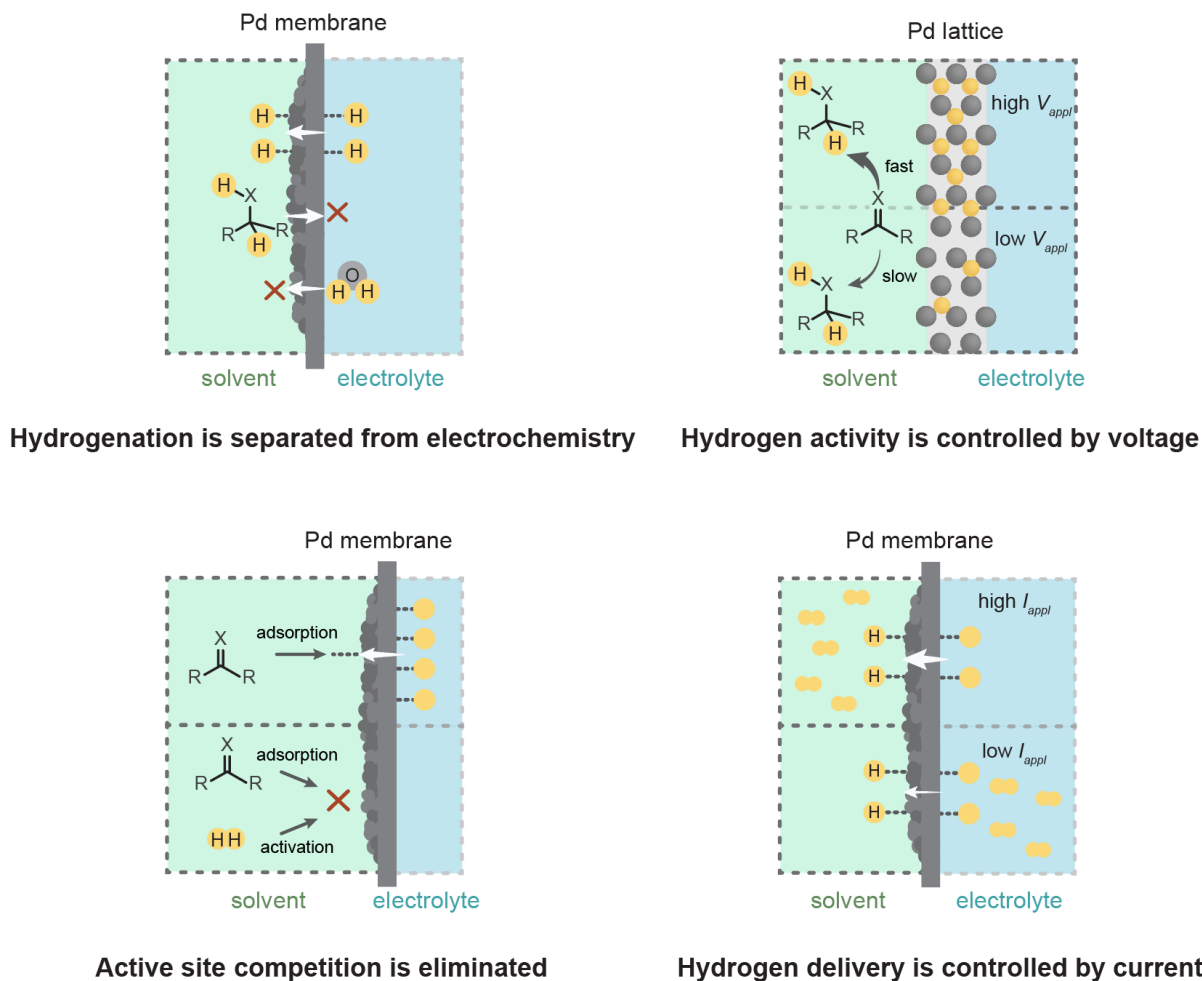


Figure 2.5 Illustrations summarizing the attributes of using electrolytic hydrogen driven through a membrane for hydrogenation. “C=X” refers a generic unsaturation with X referring to either a C, N, or O atom. R groups are not shown for simplicity.

There are also reactivity advantages to delivering hydrogen to the reaction site through a membrane rather than directly to the catalyst surface. Studies of thermochemical palladium

membrane reactors have found that hydrogenation reaction rates are faster when the hydrogen is supplied through a Pd membrane than those where the hydrogen and reactant are mixed at the same Pd surface.^{108–110} There are two possible explanations for this effect: 1) the substrate and hydrogen do not need to compete for surface binding sites during activation/reaction¹¹⁰ and; 2) hydrogen permeating through the membrane may react primarily from the subsurface rather than the surface (as discussed in section 2.3.2).¹⁰⁸ This debate in the literature is, at present, unsettled. Notwithstanding, it has been demonstrated that reaction rates are >10-fold higher when hydrogen is supplied through the membrane, rather than bubbled at the catalyst surface in an ePMR.¹¹¹

The use of electrolytic hydrogen has marked advantages over using hydrogen gas as an H-source. The activity of electrolytic hydrogen delivered to the reaction site is controlled with an applied voltage,^{26,27} rather than by pressure. This setup enables small changes in the applied voltage (100s of mVs) to mediate large increases (100's of atmospheres) in hydrogen fugacity.¹¹² High effective pressures can therefore be achieved without introducing the safety concerns that accompany high pressure reactions.¹¹² This advantage is most notable with liquid-phase hydrogenation reactants, which proceed at much slower reaction rates when H₂(g) is supplied to a palladium membrane rather than electrolytic hydrogen.^{113–116} The H₂(g) pressure can be increased in gas-fed systems to drive higher reaction rates but also introduces the complication of engineering the membrane to withstand the increased pressure,¹¹⁷ whereas hydrogen flux can be increased in an electrolytic system by operating at a higher current density.^{17,22} An electrocatalytic setup also enables the reaction to proceed at lower temperatures than thermochemical analogues. Low temperature operation suppresses the formation of carbonaceous deposits that deactivate the catalyst over time.⁸⁹ This characteristic potentially enables a higher durability of the hydrogenation

catalyst in an ePMR than a heat-driven hydrogenation reactor. There remains an opportunity to experimentally demonstrate this advantage of ePMRs over thermochemical setups.

2.4 Hydrogenation in an ePMR

The previous section has described the advantages of using an electrochemical driving force to drive hydrogen through a palladium membrane enable efficient hydrogenation without the use of $\text{H}_2(\text{g})$. This section describes how reaction outcomes (i.e., rate, selectivity and efficiency) are controlled in an ePMR and provides examples of how this reactor can be used to produce useful chemicals.

2.4.1 Variables that control reaction outcomes in an ePMR

Hydrogenation in an ePMR is simple to set up and most studies to date have been conducted in divided electrochemical cells (H-cells) common to research laboratories (Figure 2.6a). The H-cell has two separate chambers separated by a palladium foil: an electrochemical chamber with an aqueous electrolyte and reference and counter electrodes; and a chemical chamber with the reactant dissolved in an organic solvent. Hydrogen atoms produced in the electrochemical chamber either absorb into the palladium membrane (the desired process), or recombine at the metal surface and evolve as $\text{H}_2(\text{g})$ (an undesired byproduct). For alkyne hydrogenation the alkyne is hydrogenated initially to produce the alkene. When most of the alkyne starting material is consumed, the alkane adduct begins to form from the alkene intermediate (Figure 2.6b).

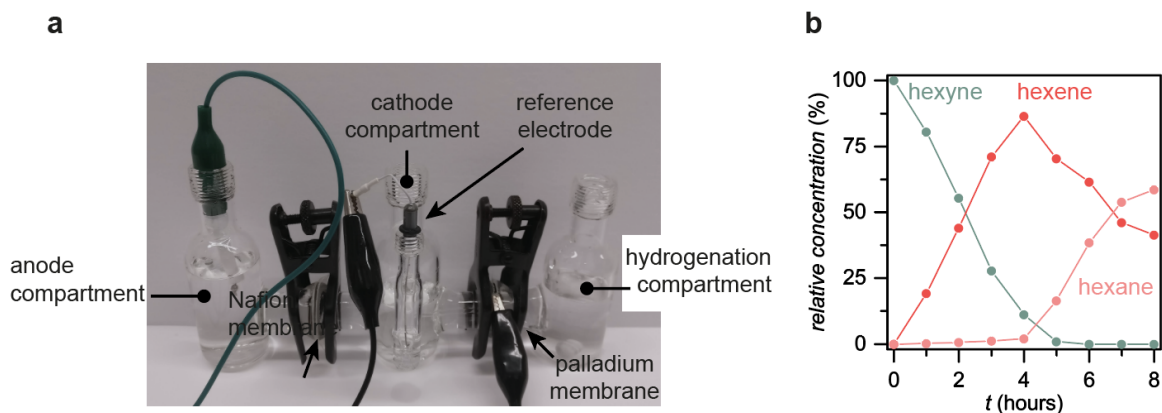


Figure 2.6 a) Labeled image of an ePMR H-cell setup used for hydrogenation of alkynes. b) Plot of alkyne, alkene, and alkane relative concentration as a function of time during sustained electrolysis in an ePMR adapted from ref. ¹⁷.

The most commonly-measured responding variables for electrocatalytic hydrogenation are the reaction rate (quantified here as the % conversion of the starting material to product), selectivity (e.g., the % formation of the alkene intermediate when hydrogenating an alkyne substrate to an alkane), and current efficiency (the percentage of electrons directed toward hydrogenation rather than HER). There has been very little study of the factors that influence these reaction outcomes, with electrochemical conditions (e.g., current density and electrolyte composition) receiving the most attention.¹⁷ Limited examples of chemical variables (e.g., catalyst, or solvent effects) have also been reported and are reviewed here.^{31,44,45}

Current density is the most commonly reported variable used to control reaction rate (Figure 2.7a), selectivity and efficiency in an ePMR. For C-C unsaturations, higher current densities drive faster alkyne hydrogenation rates at the cost of both the selectivity for the alkene intermediate and the current efficiency¹⁷ — increasing current from 25 to 75 mA/cm² (measured as the geometric area of the electrode) increases the conversion rate of 1-hexyne from 0.3 to 1 mmol/h, though decreases the selectivity for the partially-hydrogenated alkene from 87% to 63%.¹⁷

These effects on reaction outcomes can be directly traced to the palladium membrane. Higher current density (or overpotential) increases the hydrogen loading in the palladium membrane.⁷⁹ A higher concentration of hydrogen in the palladium catalyst in turn drives a higher selectivity for the fully-hydrogenated product (as described in detail in section 2.2).^{96,97} A cost of using higher current density to drive faster hydrogenation rates is that current efficiency decreases with higher electrolysis currents. Hydrogen atoms that are not added to the organic feedstock are evolved as H₂(g), an undesired byproduct. Current efficiency of hydrogenation reactions for reactants such as alkynes are ~60-75% at 42 mA/cm²,¹⁷ though can be improved markedly by carrying out the reaction in a flow cell (which I discuss in Chapter 4).

Electrolysis current also provides control over the driving force for the reaction. Alkynes can be hydrogenated at very low current densities (10 mA/cm²)²², while stronger heteroatom-containing bonds (C=O, and C=N)¹¹⁸ generally require current densities in excess of 100 mA/cm² for the reaction to proceed.²¹ Current density can therefore be manipulated to target specific functionalities. However, this approach comes with the tradeoff that unsaturations with large kinetic barriers will inevitably result in low current efficiencies. The use of low current densities (<100 mA/cm²) to avoid overhydrogenation of alkynes results in low rates of product formation. This dichotomy highlights the importance of discovering new strategies to control reaction performance in an ePMR, to drive hydrogenations at high conversion rates, and high current efficiencies simultaneously.

Electrolyte composition also affects reaction outcomes in an ePMR. A near-neutral bicarbonate electrolyte facilitates ~25% more alkene formation compared to an acidic 1 M H₂SO₄ electrolyte (Fig. 2d).¹⁷ This effect is linked to the hydrogen permeation through the membrane, with the acidic electrolyte corresponding to a higher hydrogen flux through the membrane.^{17,22} The

result is that a higher concentration of the desirable alkene is formed at the same current density (87% vs. 53%).¹⁷ Iwakura *et al.* hydrogenated CO₂ using highly-concentrated basic electrolyte (6 M KOH) in the electrochemical compartment. This is an unusual electrolyte choice given the highly caustic nature of such a concentrated solution, However, no explanation for selecting these conditions was provided, potentially alluding to an ionic strength, or pH effect on the activity of H atoms delivered to the hydrogenation site that warrants further study.

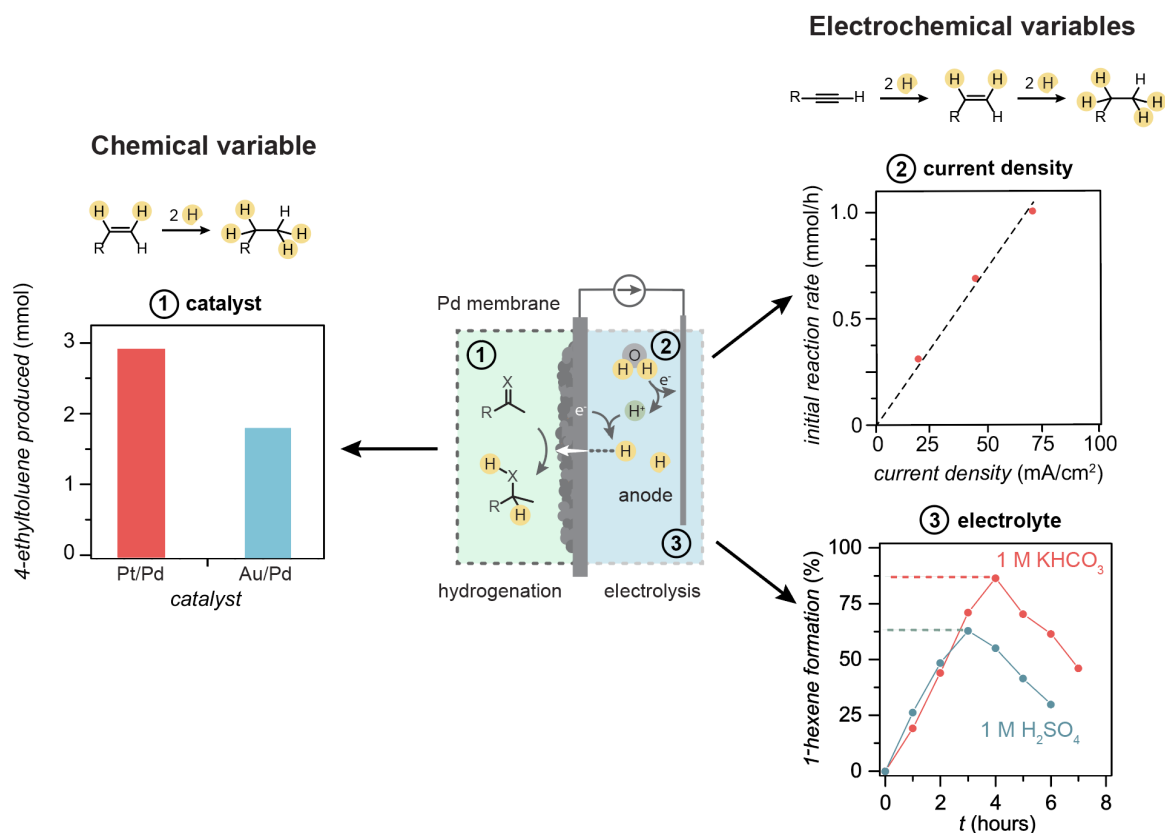


Figure 2.7 Reaction outcomes can be manipulated in an ePMR using current density, and electrolyte or catalyst composition. Catalyst data (leftmost plot) was reproduced from ref.³¹ Current density and electrolyte data (rightmost plots) were adapted from ref.¹⁷.

Catalyst morphology or composition can also be manipulated to engender new reactivities in an ePMR. A high surface area palladium catalyst is typically deposited onto the hydrogenation surface of the membrane by electrodeposition¹⁷ or electroless plating.²⁹ This high surface catalyst layer increase reaction rates $>10\times$ compared to a flat foil.¹⁷ Nanoparticle catalysts can also be pressed onto the Pd membrane surface to increase reactivity for aromatic functionalities. Two studies show that commercial Pt/Al₂O₃ catalysts in contact with the Pd membrane can hydrogenate the aromatic C=C unsaturations in toluene(g) at only moderately elevated temperatures (80 °C).^{44,45} A final example of catalyst design for the ePMR shows that secondary metals (Au, Pt, Cu and Zn) can be reduced from their cation onto the membrane surface using the H atoms permeating through the palladium foil.³¹ This strategy enables Au and Pt to be deposited in appreciable amounts, though the activity of H atoms was insufficient to reduce Cu and Zn ions. Platinum and gold catalyst-coated membranes mediated hydrogenation of the benzylic C=C bond of methylstyrene. However, the authors did not compare these results to a bare Pd membrane, so it is unclear if the activity exceeded the bare Pd-black deposit. Notwithstanding, a key insight from these studies on catalyst-coated palladium membranes is that secondary metals can be incorporated on the membrane surface without impeding hydrogen permeation, provided they are sufficiently thin (I estimate up to ~420 nm for Au and ~460 nm for Pt based on gravimetric mass loading reported by the authors, and assume a dense metal layer).³¹ These studies provided a precedent for the catalytic thin films Dr. Kurimoto and I developed in Chapter 5.

2.4.2 Applications of the ePMR

A variety of substrates can be hydrogenated in an ePMR including alkynes and alkenes,^{17,19,26,27,32} heteroatom-containing unsaturations including carbonyls,^{39,49} quinones,⁴³

immines,²¹ nitrous oxide³³ and a number of complex small molecules (dyes and antioxidants).^{34,43} These broad capabilities position this ePMR as a versatile reactor for hydrogenation, that could be used for applications in chemical synthesis. Studies to date have been largely centered around model reactants. This section highlights industrially-relevant substrates that can be hydrogenated based on current capabilities of the ePMR.

Alkyne and alkene hydrogenation have been the most extensively studied reactions in the ePMR.^{17,19,26,27,32} The disproportionate focus on these substrates likely arise because C=C bonds are easier to hydrogenate than carbonyl groups (polar C=O bonds are stronger than non-polar C=C bonds; 93 kcal/mol vs. 63 kcal/mol)¹¹⁸ and that there are fewer possible side reactions compared to carbonyl groups (e.g., hydrodeoxygenation), making this a convenient model system.¹¹³ These reactions have been successful under a variety of conditions — at current densities between 10 and 400 mA/cm², using either acidic¹⁹ or basic aqueous electrolyte,³⁰ or an organic hydrogen source.¹⁷ While to date there have been very few examples of application-oriented hydrogenations in the ePMR, olefin hydrogenation is one of the most industrially important transformations. The capabilities of the ePMR for efficient C=C hydrogenation may be applied to produce molecules including: hydrogenated vegetable oils; vitamin precursors (e.g., pseudoionone, biotin) and a host of other chemicals (e.g., ethylene; succinic acid; cis-butenediol; and dihydronaphthalene, among many others).^{11,119,120}

Hydrogenation of oxygen- and nitrogen- containing functionalities, including aldehydes,³⁹ ketones, imines,²¹ quinones,⁴³ in an ePMR have received significantly less attention than olefin hydrogenations. The limited examples reported have used highly-caustic electrolytes, and operating at high current densities >100 mA/cm². These functionalities are of particular relevance in pharmaceutical⁶³ and fragrance⁶¹ production. Sodium borohydride is generally used as a

reducing agent for these reactions,⁶³ except in cases where asymmetric hydrogenation steps are required.⁷³ Continued development of the relevant reaction chemistries to perform these reductions (both to the partially reduced alcohol/amine, or fully-reduced alkane) in an ePMR would provide the opportunity to eliminate the requirement for stoichiometric reducing agents often used in these applications (as discussed in detail in section 2.2.2).⁶³

One final case study describing how the ePMR can be used in the synthesis of useful materials is the production of deuterated materials. Deuterium can be incorporated into organic molecules to increase the half-life of pharmaceuticals¹²¹ and higher efficiency organic electronic devices.^{122–124} D-containing materials are attractive for pharmaceutical applications because the C–D bond is less prone to metabolic cleavage, thereby enabling a lower drug dosing. Within the electronics community deuterated molecules enable more efficient charge transfer by strengthening covalent interactions between polymer chains.^{124,125} An ePMR holds a particular advantage for deuteration because deuterium atoms derived from D₂O are 20-fold less expensive than D₂(g). The Berlinguette group demonstrated this capability by using the ePMR to deuterate a precursor of a common drug, Cinacalcet.²¹ Deuteration of pharmaceutical precursors proceeded in the ePMR with excellent site-selectivity, high deuterium incorporation and high purity.²¹ This same concept could be similarly applied for the synthesis of other deuterated compounds by deuteration of unsaturated C=C, C=O and C=N bonds.

2.5 Membrane and reactor design for ePMRs

Two key hardware components of the ePMR define the reaction rate, selectivity and efficiency of this device: the membrane and reactor design (as discussed in sections 2.3 and 2.4). In this section I review membrane and reactor designs reported for ePMRs to date, and relevant analogues in the electrosynthesis literature.

2.5.1 Palladium membrane designs

The vast majority of ePMRs studies have used a dense palladium foil as the catalytic membrane. This membrane design is readily accessible (through purchase, or rolling of a palladium coin), and meets many of the requirements for efficient operation in this application — the membrane must be an efficient HER catalyst, permeate large amounts of H atoms formed at the cathodic surface of the foil, and mediate hydrogenation at the opposite surface of the membrane. However, the high mass of palladium ($\sim 30 \text{ mg/cm}^2$ for a 25 μm -thick Pd foil) leads to high membrane costs ($\sim 20 \text{ USD/cm}^2$, >100 -fold higher than ion exchange membranes). These costs are not readily decreased for foil membranes because thin foils $<12 \mu\text{m}$ -thick are prohibitively fragile.



Figure 2.8 Membrane designs for ePMRs reported to date. The vast majority of studies use dense Pd foils as the electrocatalyst, membrane and hydrogenation catalyst. Pd membranes are prone to mechanical degradation due to lattice expansion and contraction during hydrogen absorption-desorption cycling which causes the foil to crinkle, embrittle and eventually crack. Delima *et al.* report a supported Pd membrane architecture (image reprinted from ref. ²⁰) and Iwakura *et al.* provide proof of concept for using Pd-free hydrogen storage alloy membranes in this application.

There are two strategies reported for decreasing the Pd loading of the membrane. The first is to design supported membranes, and the second is the development of palladium-free

membranes. Supported membranes use an inert substrate to reinforce a thin palladium layer (expanded-PTFE; e-PTFE,²⁰ or porous polycarbonate are good candidates⁴⁶). Delima *et al.* developed Pd-coated e-PTFE membranes for the ePMR that enable diffusion of organic solvents and have high Pd surface area for reaction due to the textured e-PTFE.²⁰ These membranes reduced Pd content to 5% of a foil membrane, but were only compatible with non-polar solvents due to poor wettability. An alternative supported membrane design positions a thin Pd film in contact with a polymer exchange membrane (PEM).⁴¹ A PEM is more mechanically robust than e-PTFE, however, the dense polymer support leaves no pathway for incidental H₂(g) evolved at the Pd|electrolyte interface to be removed. Resultantly, these membranes can only be operated at very low current densities (~10 mA/cm²) to avoid damaging the Pd layer from gas evolution.⁴¹

Alloy membranes do not require mechanical supports and therefore do not suffer from the same challenges as Pd thin film membranes. A single study reports the use of non-Pd hydrogen storage alloys for use in an ePMR. The LaNi₅ and Ni_{3.6}Mn_{0.4}Al_{0.3}Co_{0.7} catalytic membranes hydrogenated styrene at low current density (3-15 mA/cm²).²⁸ However, the membranes showed signs of cracking after only 20 hours of electrolysis, but serve to demonstrate proof-of-concept for the use of palladium-free membranes in this application. There is yet to be reported a single membrane design that is inexpensive, durable, and amenable to high current density operation, representing a significant opportunity for innovation in this field (as discussed in Chapter 6).

2.5.2 Flow chemistry for organic transformations

There are two common reactor architectures used in the development of electrochemical cells: H-cells and flow cells. H-cells are named for their physical shape — two discrete chambers are separated by a membrane, or frit in the middle of the cell (Figure 2.8a).^{126,127} H-cells are typically used in the early development stages of an electrochemical technology because of their

simplicity (in both setup and operation), commonality to the research laboratory, and versatility. Baran and coworkers have made efforts to standardize this architecture to improve experimental reproducibility,¹²⁸ with the goal of making organic electrosynthesis commonplace within the research laboratory. However, even with standardized cell designs, there are fundamental challenges with developing new chemistries within the H-cell. These simple batch reactors are hindered by low reaction rates (due to poor mass transport¹²⁷), low energy efficiencies, and are limited to mg-scale reactions.⁵⁷

Flow cells enable faster, scalable and more energy-efficient electrosynthesis than H-cells (Figure 2.8b).^{57,126,127} The distinguishing feature of a flow cell is that reactants are delivered to the electrodes through forced-convection, rather than passive diffusion. These improved mass transport kinetics are enabled by pumping the reactant along the surface of the electrode, enabling up to 1000-fold improvements in the transport rate (k_m) to the catalytic surface (Figure 2.8c).¹²⁷ Flow cells are particularly useful for electrochemical reactions because at high overpotentials, an electrochemical reaction rate can exceed the rate of diffusion.¹²⁹ By alleviating the mass transport limitations, faster reaction rates can be achieved without increasing the surface area of the electrode or the catalyst loading. Flow cells can also be designed with smaller (<1 mm) interelectrode distances than H-cells (>1 cm).¹³⁰ This smaller gap between the anode and cathode results in lower ohmic losses from ion diffusion through the electrolyte, decreasing the cell voltage required to drive the reaction and increasing the energy efficiency of the process.⁵⁷

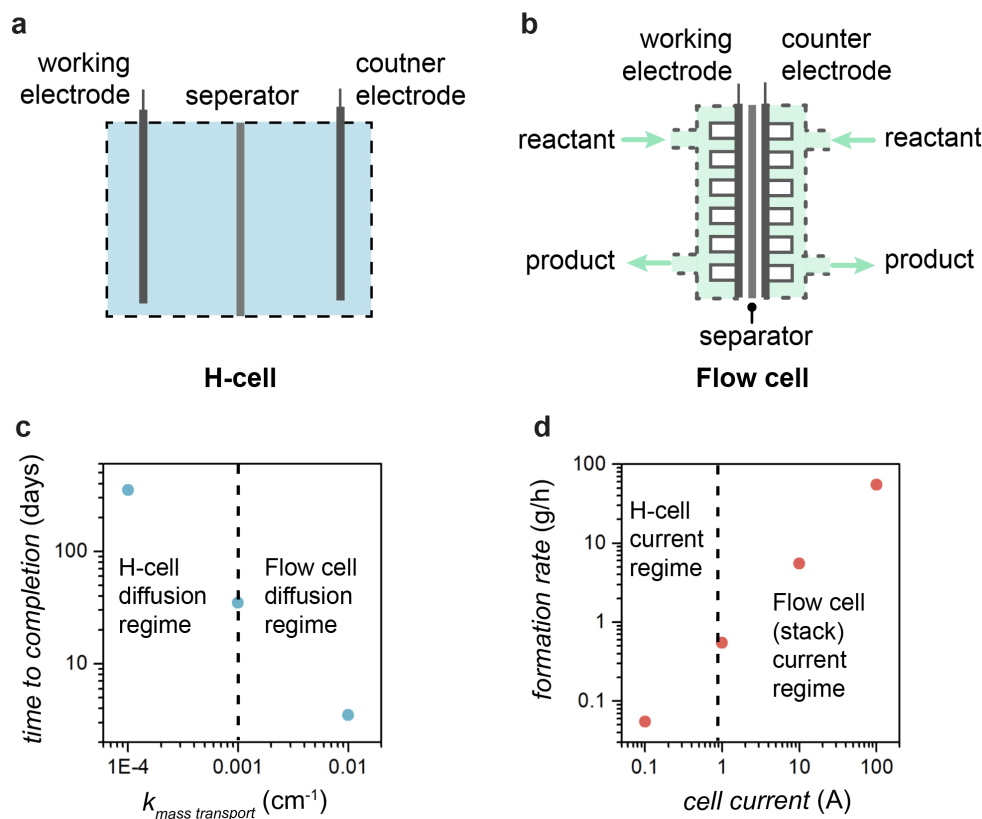


Figure 2.9 Illustrations of a) H-cell and b) flow cell reactors used in organic electrosynthesis. Flow cells enable faster conversion by increasing c) mass transport kinetics and d) current density. Data presented in panels c and d adapted from ref. ¹²⁷.

Within the context of chemical manufacturing, flow cells enable additional advantages beyond enhancements in reaction rate and efficiency. Flow chemistry is more time efficient than batch reactions because there are fewer repetitive, non-productive steps (e.g., adding reagent, cleaning, pressurizing, heating and cooling the reactor).⁷⁰ Flow processes can also enable the product to be produced at the rate it is consumed, so the product does not need to be stored for long periods of time.⁷⁰

A common flow cell architecture used at both lab and industrial scales is the parallel plate flow reactor (Figure 2.8b).¹³¹ These cells couple flow field plates to porous electrodes. The flow

field plate provides a discrete path for the reactant along the catalyst surface and a turbulence layer is used to disrupt laminar flow and increase mixing at the catalyst surface.¹³² A separator (e.g., a PEM or frit) serves as both an electrical insulator to prevent shorting across the electrodes, and a means of transporting reactants from one electrode to the other. This architecture is straightforward to scale by stacking numerous cells, which increases the surface area of the reactive interface (Figure 2.8d).^{133,134} Parallel plate flow reactor designs reported in the CO₂ electrolysis,¹³⁰ water electrolysis,¹³⁵ and hydrogen fuel cell¹³⁶ literature provided the inspiration for the ePMR flow cell I report in Chapter 4.

Chapter 3: Strain Influences the Hydrogen Evolution Activity and Absorption Capacity of Palladium

3.1 Introduction

Efficient operation of an ePMR requires efficient HER, hydrogen absorption into a palladium electrode and hydrogenation at the opposite surface. In this work, I investigated how two of these properties – HER and hydrogen absorption – can be manipulated by applying an external force to a flexible palladium electrode. This chapter provides a background of strain engineering approaches in electrocatalysis, and presents mechanical strain as an enabling method for studying the influence of strain on palladium-hydrogen interactions.

3.1.1 Strain engineering in electrocatalysis

Heterogeneous electrocatalytic activity is dictated by the adsorption energies of reactants and intermediates to the catalyst surface.^{81,137} Catalytic activity is highest when the binding strength of the intermediate is sufficiently strong that the substrate is activated at the catalyst surface, but not so high that the product does not desorb from the active site. This qualitative relationship between activity and intermediate binding strength is called the Sabatier principle.¹³⁷ A key outcome of this principle is that for every catalytic reaction at a heterogeneous surface there is an optimal binding energy that enables the highest activity.¹³⁷

One method for optimizing the binding energy of adsorbates to a metallic catalyst surface is to manipulate the lattice spacing of the metal.^{138–141} Norskov's "*d*-band model" provides a theoretical basis for how expanding or contracting (i.e., straining) a lattice influences the binding strength of intermediates to a catalyst surface.¹³⁸ Tensile strain (i.e., lattice expansion) reduces *d*-

orbital overlap in transition metals, narrowing and shifting the *d*-band to higher energy.¹³⁸ These higher energy *d*-states promote stronger interaction with adsorbates. Conversely, compressive strain (i.e., lattice contraction) widens the *d*-band, and induces a shift to a lower energy level resulting in weaker surface-adsorbate binding affinities.¹³⁸ The activity of a catalyst can therefore be manipulated by adjusting the spacing between the atoms at the metal surface.^{138,140,142}

Strain engineered catalysts have been studied for noble metal electrocatalysts for a range of reactions related to sustainable energy production and storage, including the hydrogen evolution reaction (HER),^{141,143} oxygen reduction reaction (ORR),¹⁴⁴ and the CO₂ reduction reaction (CO₂RR).^{142,145} Studies of ORR catalysis show that imparting strain through lattice mismatch, alloying or synthesis of nanomaterials leads to notable increases in ORR activities.^{140,144,146} Compressive, biaxial strain applied to a Pt thin film by a NiTi shape memory alloy substrate yields a 52% enhancement in the kinetic rate constant of ORR, while strain in Pd@Pt core-shell icosahedral nanomaterials is responsible for a striking 29-fold increase in activity.^{147,146} Chorkendorff and coworkers provided one of the most defining studies on how strain affects electrocatalysis by systematically imposing compressive strain through on platinum through alloying with a series of lanthanides.¹⁴⁴ Not only did this approach yield catalysts with up to six-fold enhancements in activity over pure platinum, but the experimental data yielded a high-resolution volcano plot of platinum activity as a function of lattice spacing.¹⁴⁴ This study is, however, an anomaly in the literature and no other study of epitaxially-strained catalysts is as comprehensive. These methods are challenged by arduous catalyst fabrication – a unique sample must also be designed for each data point, and the strain effect can be easily masked by surfactants used in the synthesis,^{140,148} or if the epitaxial layer is more than a few monolayers thick.¹⁴⁹

An alternative approach to accessing strained catalysts is to mechanically stretch or

compress a flexible electrode while monitoring changes in electrocatalytic activity.^{150–154} Peterson, Kumar and coworkers describe a method where flexible, thin film electrodes are inserted into an electrochemical cell that is fitted to a tensile testing apparatus capable of quantitatively applying and measuring mechanical strain. Palladium and platinum thin films evaporated onto polymer-supported metallic glass substrates were shown to withstand mechanical strain from -2% to $+2\%$ using this method. Electrochemical measurements were performed while strain was adjusted *in situ* and the authors were able to demonstrate a strain-activity relationship for ORR.¹⁵⁴ The mechanical application of strain offers many advantages over conventional epitaxial methods, including the ability to test a larger scope of samples by virtue of vastly easier sample preparation than epitaxial methods, accessibility to intermediate strain values, and *in situ* characterization.

A key challenge with studying catalysis at mechanically-strained electrodes is that the amount of applied strain that translates to lattice strain at the metal surface is unknown. Surface roughness of both the polycrystalline catalyst and the substrate cause inhomogeneities in the strain distribution across the surface. Notwithstanding, proponents of this method argue that, in spite of these strain relief mechanisms, mechanically-applied strain influences catalytic activity similarly to strain induced through lattice-mismatch epitaxy. This argument has been supported by comparing the change in activity induced by mechanical strain to epitaxial strain. Kumar *et al.* and Chorkendorf each show that the ORR activity at a Pt catalyst increases under compressive strain.^{144,152} Mechanically-induced changes in activity are also supported by computational approaches. DFT calculations show that the catalytic activity of a mechanically-strained polycrystalline film changes similarly to a modelled single crystal. There are currently no studies that have empirically characterized strain at a mechanically-strained catalyst surface. This gap in the literature motivated my use of XRD to measure strain at the catalyst surface.

3.1.2 Strain engineering palladium electrodes

The effect of tensile strain at palladium electrodes has been mapped for ORR¹⁵⁵ and CO₂RR,¹⁴⁵ but the study of HER at a palladium electrocatalyst is made complicated by the concurrent absorption of hydrogen into the palladium lattice (denoted herein as the hydrogen absorption reaction, “HAR”).⁷⁴ To address this gap in the literature, I designed experiments that isolate how lattice strain affects HER and HAR for thin palladium electrocatalytic films. The results presented herein aim to inform the design of palladium materials for HER catalysis,⁷⁵ and hydrogen^{156,157} and energy storage¹⁵⁸ schemes.

When a negative potential (versus the reversible hydrogen electrode; RHE) is applied to a palladium electrode immersed in protic electrolyte, protons are electrochemically reduced at the metal surface to produce adsorbed hydrogen atoms which can either absorb into the palladium bulk (i.e., HAR) or recombine to evolve as H₂(g) (i.e., HER).⁷⁹ During sustained electrolysis, HAR induces a phase change in the palladium lattice to form β -PdH_x (where x is ~0.7 in ambient conditions)⁷⁸ and the active surface for HER becomes the hydrided phase.⁷⁵ Common methods used to measure the activity of electrocatalysts (e.g., cyclic voltammetry or linear sweep voltammetry)^{79,159} can therefore overestimate the HER activity for palladium electrodes because the measured current includes contributions from both HAR and HER. This situation necessitated the development of methods to characterize how strain affects HAR and HER in isolation.

To correlate the influence of strain to changes in HAR (a bulk process) and HER (a surface process) I needed a technique capable of producing strain throughout the entire thickness of the palladium electrode. This criterion disqualified lattice mismatch epitaxy or modulation of nanoparticle shapes and sizes, each of which confine strain to a few monolayers of the electrocatalyst surface.^{140,145} I instead used mechanical force to stretch polymer-supported

palladium thin films to induce strain throughout the bulk of the electrode. External force was delivered to the 50 nm-thick palladium film using a flexible polymer support that was mechanically stretched. This method of stretching a flexible substrate with a 10-50 nm layer of metal electrocatalyst on the surface has been used to correlate activity to strain for various electrochemical reactions (e.g., HER,^{150,151,153,160,161} OER,¹⁵⁹ ORR^{147,152,154,162} and others.¹⁶³⁻¹⁶⁶), but not for HER at a palladium electrode.

I designed a tensile testing electrochemical device (“TED”) to strain flexible palladium electrodes while HAR and HER activity were monitored (Figure 3.1a, b). This device is capable of applying a broader range of tensile strain to electrocatalytic films than those previously reported,^{151,154,159} and is hermetically sealed to enable electrolyte to be flowed across the surface of the electrode during electrochemical measurements.⁷⁹ These design features provided me with the ability to independently measure the amount of hydrogen that absorbed into the palladium and HER activity while mechanically subjecting palladium electrodes to controlled amounts of tensile strain. I validated that the TED provided access to lattice strain in palladium by conducting a series of X-ray diffraction experiments wherein I used a custom sample stage to stretch the flexible palladium samples while monitoring the change in reflection peak position, which is proportional to lattice strain.¹⁶⁷ The results of these studies show that mechanically-induced tensile strain increases HER activity at a β -PdH_x surface and decreases the amount of hydrogen that absorbs into the bulk. This work highlights how mechanically applied strain can be used to map strain-property relationships for electrocatalytic materials.

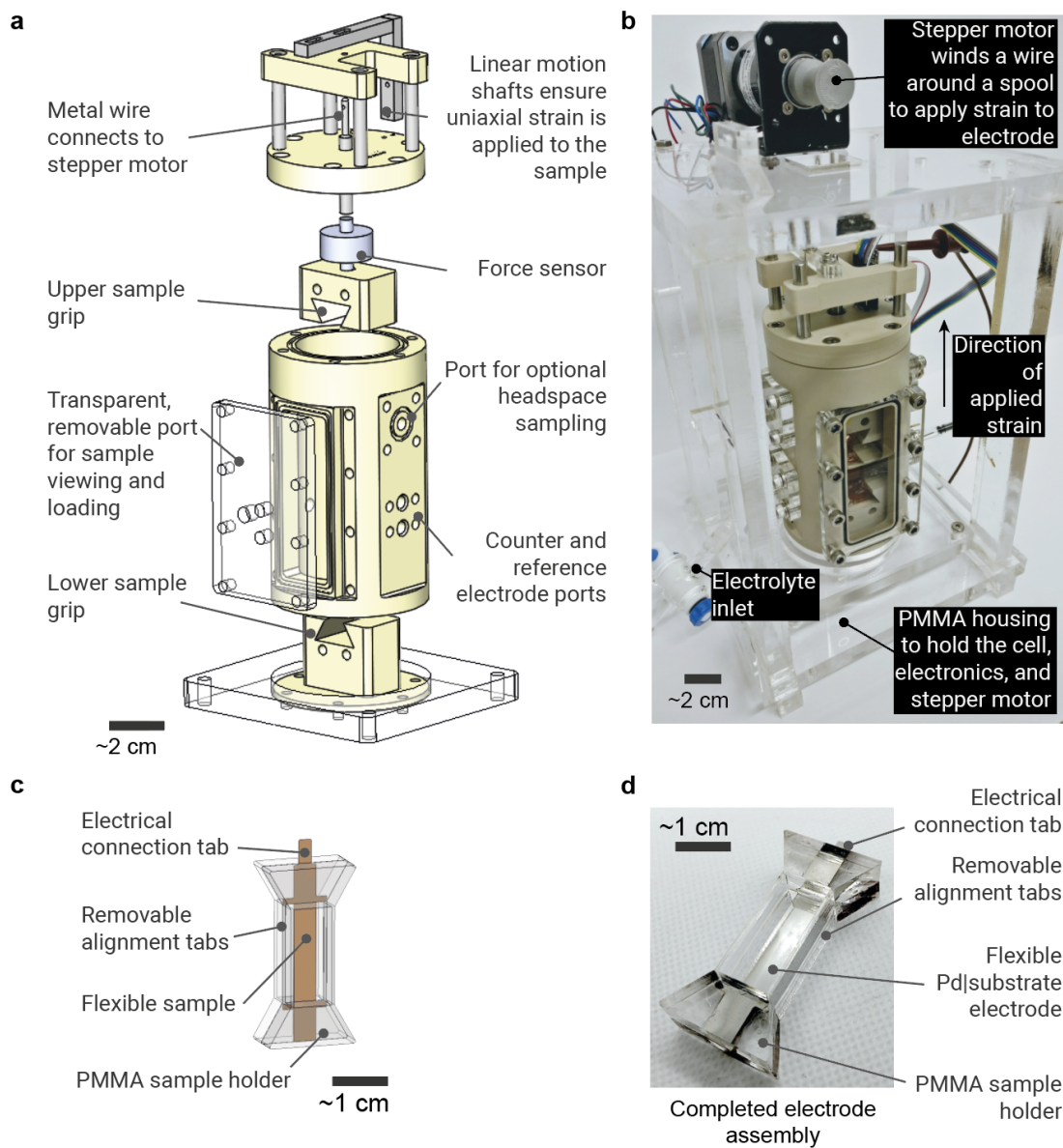


Figure 3.1 a) Schematic of the tensile-testing electrochemical device (TED) designed for this study. b) Photograph of the TED in a support housing, which holds the data acquisition equipment (not shown for simplicity) and a stepper motor. c) Schematic of the completed sample assembly consisting of a flexible sample sandwiched between two polymethylmethacrylate (PMMA) sample holders. d) Photograph of a completed sample assembly with a flexible Pd|substrate electrode installed between the sample holders.

3.2 Results

3.2.1 Design of a tensile testing electrochemical device (“TED”)

For the first stage of this study, I designed and constructed a TED to measure the electrocatalytic properties of palladium electrodes subjected to mechanically-applied tensile strain ($\epsilon_{\text{applied}}$). The apparatus consists of a hermetically-sealed chamber that houses a three-electrode electrochemical testing setup, and position and force sensors to measure strain and stress, respectively. For mechanical testing this chamber was mounted in a rigid housing that includes a linear actuator (i.e., a stepper motor that actuate the upper sample grip; Figure 3.1b), and data acquisition electronics. The TED was built to the design specifications outlined in Table A1.1. These criteria were devised based on a goal of creating a generalized platform for mechanical testing of electrochemical materials exposed to aqueous and organic electrolytes, and non-ambient gas atmospheres. This study thereby serves to validate our design in addition to providing unique insights about the palladium-hydrogen system.

I assessed the accuracy of the tensile-testing capabilities of the TED by recording tensile curve for Kapton polyimide films (300HN, 75 μm -thick) cut into rectangular strips according to guidelines by the American Society of Testing and Materials (ASTM D882-12). The Kapton samples were sandwiched between two disposable sample holders laser-cut from cast PMMA sheets and fixed in place with epoxy (Figure 3.1c, d). The sample holder included thin, removable alignment tabs to facilitate sample assembly, and dovetail-shaped ends that matched the sample grips of the TED. Five tensile tests collected at fresh Kapton samples in the TED agreed with data recorded with a commercial mechanical testing instrument (Figure A1.5).

I next fabricated flexible electrodes by depositing 50 nm of palladium on a Kapton 300HN polyimide substrate with a 10 nm chromium adhesion layer and 20 nm gold conductive layer (denoted herein as “Pd|substrate”).⁷⁹ With this sample architecture, stretching the Kapton substrate mechanically strains the palladium film adhered to its surface.¹⁶⁸ While the Kapton substrate allows for mechanical strains as high as 150% to be achieved (Figure A1.4), I did not exceed ~10.5% for samples in this study because at large strains the metal film fractures (*vide infra*). The Pd|substrate sample design enabled reproducible fabrication of electrodes for tensile testing experiments. The challenge of handling thin metal foils that are easily damaged during electrode fabrication was also circumvented by using this sample architecture. A weakness of this sample design was that compressive strain regimes could not be tested because of the thin, flexible Kapton support.

I next conducted electrochemical experiments in the TED by installing a Pd|substrate working electrode, Pt wire mesh counter electrode and Ag/AgCl reference electrode. This assembly was hermetically sealed in the electrochemical cell by installing the transparent PMMA cover. Electrolyte (1 M H₂SO₄) was injected through an inlet valve (Figure 3.1b) and the three electrodes were connected to a potentiostat to complete the setup. This general setup procedure was used for all electrochemical experiments.

I measured the amount of hydrogen that absorbed into the Pd|substrate electrodes in the TED by adapting a coulometry method developed by Sherbo *et al.*⁷⁹ The implementation of this procedure required that fluid inlets be installed on the transparent front cover so electrolyte could be continuously flowed toward the surface of the electrode to remove hydrogen bubbles from the catalyst during electrolysis (setup shown in Figure A1.6). This technique enabled the quantity of hydrogen absorbed into the palladium electrode to be measured in the following three steps: i) -

0.35 V (vs. Ag/AgCl) was applied to the electrode for 120 s to facilitate HER and hydrogen absorption into the palladium lattice (Figure 3.2a); ii) Next, 0.30 V (vs. Ag/AgCl) was applied, which oxidized hydrogen absorbed in the lattice back into protons (Figure 3.2a); and iii) the total current passed during this oxidation step was integrated to calculate the H:Pd ratio (Figure 3.2b). An average hydrogen absorption ratio (i.e., H:Pd ratio) of 0.675 ± 0.039 was measured for five Pd|substrate electrodes, which is consistent with prior literature.⁷⁹

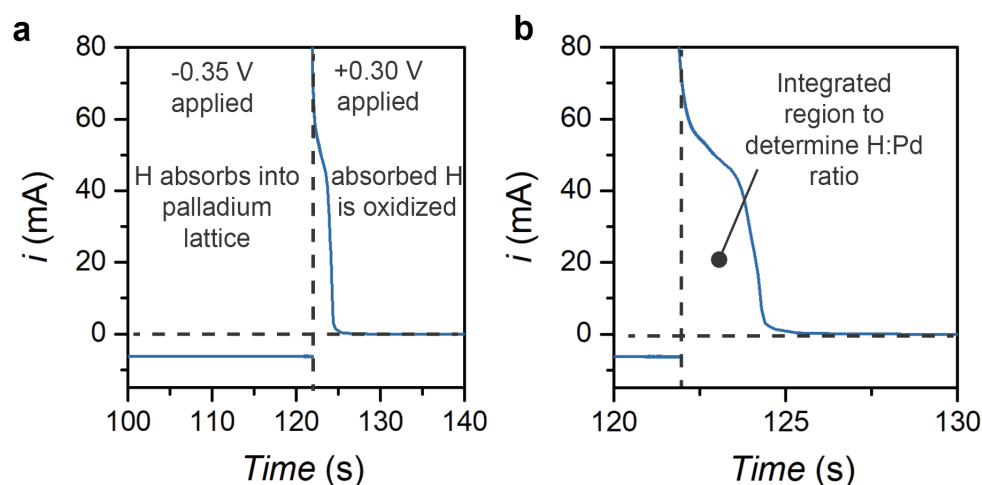


Figure 3.2 a) A prototypical chronoamperometric plot illustrating the two stages of a hydrogen absorption measurement using coulometry.⁷⁹ Hydrogen is absorbed into the palladium lattice during electrolysis at -0.35 V vs Ag/AgCl. Hydrogen is then desorbed from the lattice by applying an oxidative potential of 0.30 V vs. Ag/AgCl to the electrode. b) Chronoamperometric curve highlighting the integrated region of the oxidative step used to calculate the amount of hydrogen absorbed into the palladium lattice (i.e., H:Pd ratio).

Electrochemical HER activities of the Pd|substrate electrodes were measured chronoamperometrically to avoid interference from HAR currents. For these experiments, the working electrode was subjected to a constant potential (-0.35 V vs. Ag/AgCl) while current was recorded. During sustained electrolysis hydrogen absorbed into the Pd|substrate electrode to form

β -PdH_x (denoted herein as “ β -PdH_x|substrate”) with a constant H:Pd ratio (Figure 3.3a).⁷⁹ After ~60 s of electrolysis the measured H:Pd ratio and electrochemical current reached a steady state, signaling that hydrogen absorption was complete and I attributed the current measured at the β -PdH_x surface after 60 s exclusively to HER (Figure 3.3b). This assumption was validated experimentally using in-line gas chromatography to verify that H₂(g) was the only cathode product (see appendix 1 for details). I carried out all HER activity measurements in static electrolyte because the chronoamperometric curves resolved with a higher signal to noise ratio than in flowing conditions (Figure A1.10). A consequence of collecting these measurements in static electrolyte was that hydrogen bubbles accumulated on the surface of the electrode and caused activity to slowly decrease throughout the duration of the measurement (Figure 3.3b).

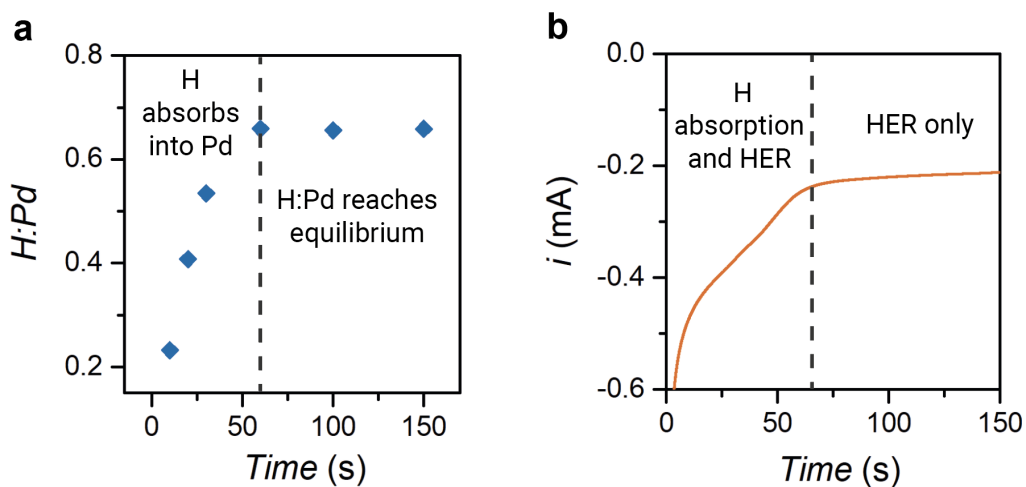


Figure 3.3 a) Plot of the H:Pd ratio as a function of electrolysis time (at -0.35 V vs Ag/AgCl in 1 M H₂SO₄) for a Pd|substrate electrode. H:Pd increases abruptly during the first 60 s of electrolysis, forming the β -hydride phase,⁷⁸ then remains constant as the H:Pd ratio reaches equilibrium **b)** Chronoamperometric trace for a Pd|substrate electrode under sustained electrolysis (at -0.35 V vs Ag/AgCl in 1 M H₂SO₄). The initial decrease in current as a function of time is inferred to represent the completion of hydrogen absorption, that occurs concomitantly with HER.

3.2.2 Measuring the effect of mechanical strain on HER and H:Pd at a palladium electrode

With our instrument design and electrochemical protocols validated, I measured the influence of $\epsilon_{\text{applied}}$ on the H:Pd ratio and HER activity of the Pd|substrate and $\beta\text{-PdH}_x$ |substrate electrodes, respectively. Strain mediated a decrease in H:Pd ratio of $1.1\% \pm 0.4\%$ at $\epsilon_{\text{applied}} = 2\%$ (Figure 3.4a). I replicated this result at four, fresh Pd|substrate samples, and the H:Pd ratio decreased as $\epsilon_{\text{applied}}$ was increased in every instance with a linear regression fit of $R^2 > 0.95$ (Table A1.1). For each sample, the H:Pd ratio was determined at increasing values of $\epsilon_{\text{applied}}$ by repeating the following two-step workflow: i) the amount of hydrogen that absorbed into the lattice was measured coulometrically using the protocol described above (Figure 3.2),⁷⁹ then; ii) $\epsilon_{\text{applied}}$ was incrementally increased. The H:Pd ratio was measured at unique x-values for each sample as a consequence of the indirect strain control by the stepper motor used to actuate the electrodes. $\epsilon_{\text{applied}}$ was adjusted by winding the stepper motor 20 steps, which increased $\epsilon_{\text{applied}}$ between 0.3% and 1.1%. I performed a control experiment to verify that multiple coulometric measurements on a single electrode had ostensibly no influence on the amount of hydrogen that absorbed into the palladium thin film. The standard deviation for 10 consecutive measurements of the H:Pd ratio at a single, unstrained electrode was 0.001 (Figure A1.8). I also observed that the effect of mechanical strain on the H:Pd ratio was reversible by incrementally straining an electrode to 1.2%, then relieving the strain back to 0%. The initial and final H:Pd ratios were within 0.2% (Figure A1.9).

The HER activity of the $\beta\text{-PdH}_x$ |substrate electrode was found to increase to $5.7\% \pm 1.7\%$ at an $\epsilon_{\text{applied}}$ of 4.5% (Figure 3.4b). The influence of strain on HER activity was determined by conducting electrolysis at a constant potential (-0.35 V vs. Ag/AgCl) until the electrochemical current reached a steady-state, then $\epsilon_{\text{applied}}$ was incrementally increased while changes in the HER

current were measured. I observed a slow decrease in HER current throughout the duration of the experiment as a result of $\text{H}_2(\text{g})$ bubble accumulation on the surface of the electrode (Figure A1.11). I therefore report the cumulative % change in HER activity as a function of applied strain in Figure 3.4b (see Figure A1.12 and Eq. A1.3 for details). I replicated this experiment at four fresh $\beta\text{-PdH}_x|\text{substrate}$ samples and found that the dataset from every electrode fit to a second-order polynomial function (i.e., $R^2 > 0.99$ for each sample; Table A1.2). The reversibility of the strain effect on HER activity was verified at a separate $\beta\text{-PdH}_x|\text{substrate}$ electrode by incrementally increasing $\epsilon_{\text{applied}}$ to 1.0%, then relieving the strain back to 0%. The HER activity was observed to increase as tension was applied, and decrease when strain was relaxed (Figure A1.13). When strain exceeded $\sim 6\%$ fractures in the catalyst film (discussed below) caused a sharp decrease in the catalytic activity.

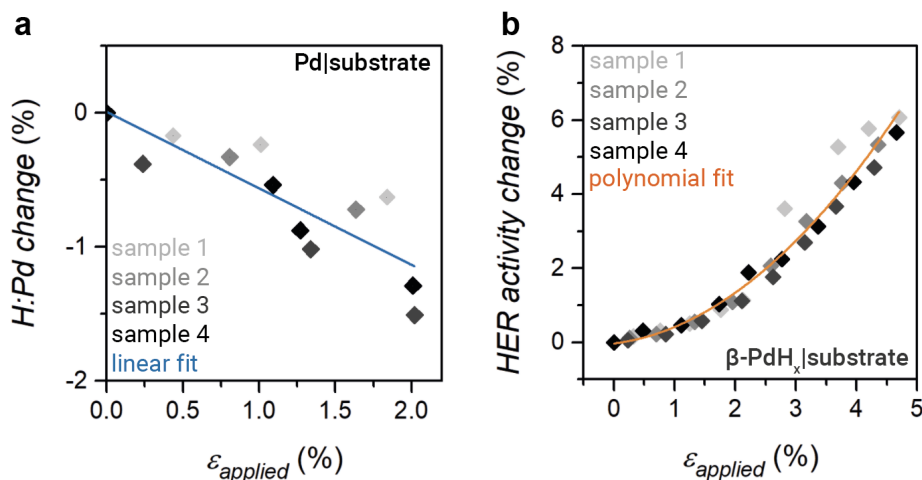


Figure 3.4 a) Plot of the % change in the H:Pd ratio at a Pd|substrate electrode as a function of applied tensile strain ($\epsilon_{\text{applied}}$). This result was replicated four separate times, each at a fresh Pd|substrate sample. Data collected for every sample is overlaid and the entire dataset fit with a linear regression, shown in blue. **b)** Plot of the % change in HER activity as a function of $\epsilon_{\text{applied}}$ collected at four fresh $\beta\text{-PdH}_x|\text{substrate}$ electrodes. The orange line is a second-order polynomial fit of the compiled data from all samples.

3.2.3 Correlation of applied mechanical strain to palladium lattice strain

I next conducted experiments to correlate mechanically applied strain to changes in the palladium lattice using a custom-built XRD sample stage interfaced with a powder X-ray diffractometer. Lattice macrostrain was measured ($\epsilon_{\text{macrostrain}}$; i.e., the average strain across many crystallites) as a function of $\epsilon_{\text{applied}}$ (Figure 3.5a) for a Pd|substrate sample using this setup.^{167–170} The amount of mechanical strain applied to the sample was controlled by adjusting the distance between the sample clamps by incrementally turning a lead screw. A prototypical diffractogram of a Pd|substrate sample is shown in Figure A1.14. I used the Pd(311) reflection as a diagnostic signature for tracking changes in the palladium lattice using the established $\ln(d)$ versus $\sin^2\psi$ relationship (Figure 3.5b).^{168–171} This method correlates lattice strain to changes in the diffraction peak position, measured at increasing goniometer angles relative to the sample normal (ψ).¹⁶⁸ I observed an approximately linear increase in $\epsilon_{\text{macrostrain}}$ as $\epsilon_{\text{applied}}$ was increased to 2.1% (Eq. 1, $R^2 = 0.97$), and that the value of $\epsilon_{\text{macrostrain}}$ did not change for $\epsilon_{\text{applied}} > 2.1\%$ (Figure 3.5c). Control experiments revealed that $\epsilon_{\text{macrostrain}}$ in the palladium film did not relax throughout the 24 hours required for XRD data acquisition (see methods section below). Note that I was not able to measure how $\epsilon_{\text{applied}}$ affected the lattice constant of $\beta\text{-PdH}_x$ because our experimental setup could not accommodate a hydrogen atmosphere.

$$\epsilon_{\text{macrostrain}} = 0.11 \times \epsilon_{\text{applied}} + 0.06 \quad (\text{Eq. 1})$$

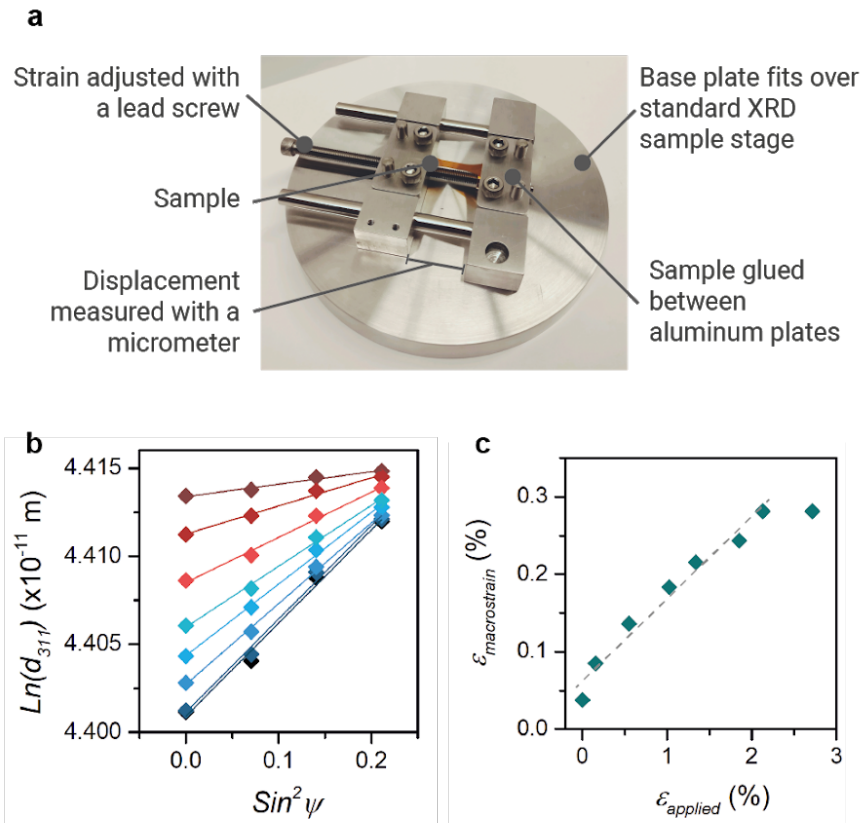


Figure 3.5 a) Photograph of the custom x-ray diffraction strain stage fabricated to measure the effect of mechanical strain on the metal lattice using the $\ln(d)$ vs. $\sin^2\psi$ relationship. **b)** $\epsilon_{\text{macrostrain}}$ is proportional to the slope of $\ln(d)$ vs. $\sin^2\psi$ with each linear fit representing one $\epsilon_{\text{macrostrain}}$ data point **c)** $\epsilon_{\text{macrostrain}}$ in the 50-nm thick palladium film increases linearly up to $\epsilon_{\text{applied}} = 2.1\%$. The dotted line represents a linear fit ($R^2 = 0.97$) of the data over a $\epsilon_{\text{applied}}$ range of 0 to 2.1%.

For our final set of experiments I used scanning electron microscopy (SEM) to image the surface of Pd|substrate electrodes exposed to increasing mechanical strain. These samples were loaded into the TED and immersed in 1 M H_2SO_4 electrolyte. The immersed samples were strained to 2.0%, 4.3% or 10.3% for 60 s and then released. The SEM images in Figure 3.6 show that the surface morphology of the Pd|substrate samples did not change at $\epsilon_{\text{applied}} = 2.0\%$ whereas fractures

propagated perpendicular to the axis of $\epsilon_{\text{applied}}$ for samples subjected to 4.7% and 10.3% mechanical strain. This result shows that the decrease in H:Pd ratio measured at strained Pd|substrate samples was not due to fracturing of the electrode surface.

A second set of samples was prepared to evaluate changes in surface morphology as $\epsilon_{\text{applied}}$ was increased for $\beta\text{-PdH}_x$ |substrate electrodes. These samples were prepared electrochemically in the following sequence: i) a reducing potential (-0.35 V vs. Ag/AgCl) was applied to a Pd|substrate electrode for 100 s to promote hydrogen absorption and form the hydride; ii) a mechanical strain of 4.7%, 5.4% or 7.8% was applied in a single step and held for 60 s, then; iii) mechanical strain was released, and; iv) an oxidative potential (+0.30 V vs. Ag/AgCl) was applied for 45 s to desorb hydrogen from the lattice. Only the sample subjected to the greatest strain, $\epsilon_{\text{applied}} = 7.8\%$, exhibited any evidence of fracturing in the SEM images shown in Figure 3.6.

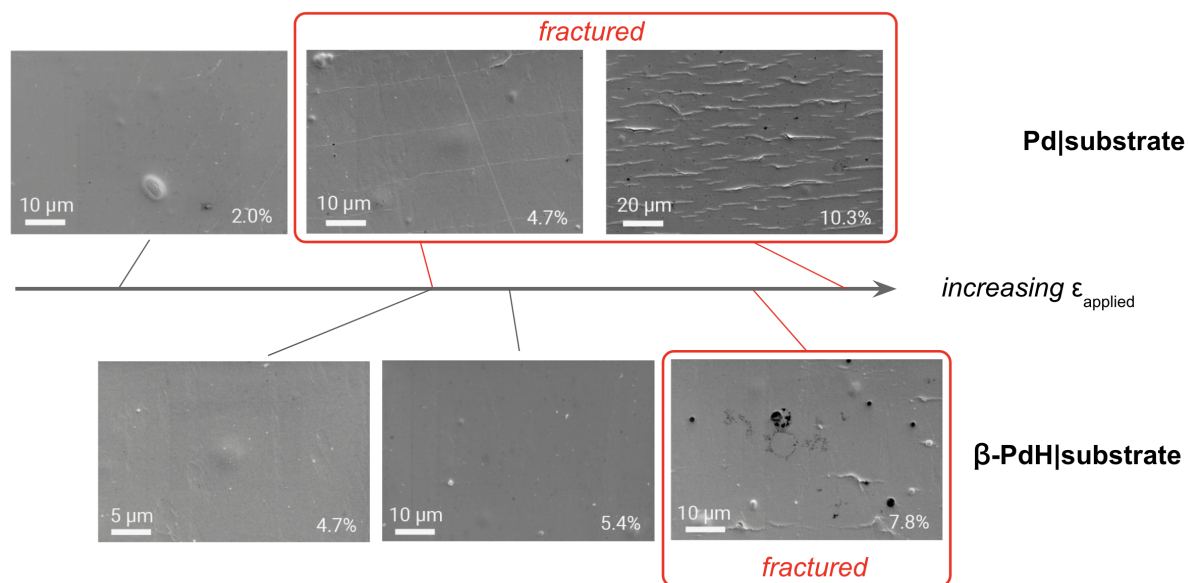


Figure 3.6 Scanning electron microscope (SEM) images of (top) Pd|substrate samples mechanically strained to 2.0%, 4.7% and 10.3%, and (bottom) hydrided $\beta\text{-PdH}_x$ |substrate electrodes strained to 4.7%, 5.4% and 7.8%. Fractures perpendicular to the direction of applied mechanical strain were observed for electrodes strained to levels greater than 2.0% and 5.4% for Pd|substrate and $\beta\text{-PdH}_x$ |substrate, respectively.

3.3 Discussion

This study outlines a method to resolve the influence of tensile strain on hydrogen absorption and HER activity at a palladium electrode. Isolating these effects is challenging because hydrogen absorption, HER, and lattice expansion are inextricably linked. I addressed this challenge by developing an electrochemical cell capable of mechanically applying tensile strain to palladium electrodes while conducting coulometry or chronoamperometry measurements. This experimental design was based on the insight that stretching a flexible substrate induces tensile strain in a thin metal film deposited on the substrate surface. I validated that mechanically-applied strain, a method used previously by the electrocatalysis community,^{151–154} correlates to lattice strain by using a custom-built XRD stage to measure lattice macrostrain of palladium as a function of $\epsilon_{\text{applied}}$.^{167–169,171}

Our XRD experiments show that applying a 2.1% mechanical strain to Pd|substrate imparts a lattice macrostrain of 0.3% (Figure 3.5c). This measurement provides direct evidence that mechanical strain modulates the lattice strain of the electrocatalyst, whereas previous studies have relied on indirect comparisons to intrinsically-strained electrocatalysts¹⁵⁴ or electron binding energies determined by X-ray photoelectron spectroscopy.¹⁵² Mechanical strain is inefficiently transmitted to the palladium lattice (i.e., $\epsilon_{\text{macrostrain}} \propto 0.11 \times \epsilon_{\text{applied}}$), which may explain the relatively modest changes in electrochemical properties of the metal films as a function of $\epsilon_{\text{applied}}$. While these XRD measurements were made on Pd|substrate samples only, I infer that mechanically applied strain also increases the $\epsilon_{\text{macrostrain}}$ within the lattice of the hydrided $\beta\text{-PdH}_x$ |substrate samples based on the similar elastic behavior of Pd and $\beta\text{-PdH}_x$.¹⁷²

When up to 2% mechanical strain was applied to Pd|substrate, coulometry measurements resolved a decrease in the H:Pd ratio of $1.1\% \pm 0.4\%$ (Figure 3.4a). The linear response of both

$\epsilon_{\text{macrostrain}}$ and the H:Pd ratio between 0% and 2% $\epsilon_{\text{applied}}$ lead me to infer that the change in H:Pd ratio is the result of mechanically-induced strain in the palladium lattice. I hypothesize that this decrease in H:Pd ratio is mediated by an increasing rate of hydrogen recombination at the palladium surface. This hypothesis is in line with prior literature – Johnson *et al.* linked the amount of hydrogen that absorbs into palladium nanoparticles to hydrogen recombination kinetics, with fast hydrogen recombination correlating to decreased hydrogen absorption.^{75,172} I conjecture that tensile strain may therefore increase the rate of hydrogen recombination at palladium hydride surface, thereby decreasing the quantity of hydrogen that absorbs into the lattice.

When tensile mechanical strain was applied to the $\beta\text{-PdH}_x$ |substrate electrode, I observed an exponential increase in HER activity (Figure 3.4b). The rate-limiting step for HER (at modest overpotentials) is the recombination of adsorbed hydrogen atoms at the surface of the electrocatalyst (i.e., the Tafel step).^{75,173} Our observation that tensile strain increases hydrogen increases HER activity supports our assertion that strain increases hydrogen recombination rates at the catalyst surface. This result also enables us to report on the binding energy of H to a $\beta\text{-PdH}_x$ surface. The highest activity for HER occurs at surfaces where the H binding energy is ~ 0 eV. According to the d-band theory, tensile strain increases the strength of metal-adsorbate interactions. Therefore our data suggest that the free energy of adsorption of H onto a polycrystalline $\beta\text{-PdH}_x$ surface is > 0 eV. However, none of the well-established volcano plots for HER include $\beta\text{-PdH}_x$,⁷⁶ representing a significant gap in the literature. We welcome additional computational studies to corroborate our findings.

To provide additional evidence that changes to the H:Pd ratio and HER activity (Figure 3.4) are a result of lattice strain rather than morphological changes to the electrode surface, I collected SEM images of Pd|substrate and $\beta\text{-PdH}_x$ |substrate at progressively higher tensile strain

values (Figure 3.6). I observed that Pd|substrate fractured when $\epsilon_{\text{applied}}$ exceeded 2.0%, and that β -PdH_x|substrate fractured at $\epsilon_{\text{applied}}$ values greater than 5.4%. I therefore do not report changes in the H:Pd and HER activity for samples exceeding 2% and 5% strain, respectively, to ensure that fracturing was not responsible for any changes in electrochemical response. The different $\epsilon_{\text{applied}}$ values required to induce fracturing for Pd and β -PdH_x is expected given that the latter is characterized by a larger lattice (i.e., the absorption of hydrogen into Pd to form β -PdH_x expands the lattice by 3.4%¹⁷³). The Kapton substrate is unaffected by hydrogen absorption and thus β -PdH_x may initially be under compressive strain prior to the Kapton film being mechanically stretched. This proposition is consistent with β -PdH_x fracturing at higher $\epsilon_{\text{applied}}$ values of 5.4%.¹⁷² The proportionality between lattice strain and mechanical strain indicated by XRD measurements (Figure 3.5c) suggests that designing electrode materials that can be deformed to large strains without fracturing may enable access to even larger lattice strains, and thereby larger changes in electrochemical response of the metal, than the relatively modest changes that were observed using the nanocrystalline materials in this study.

3.4 Conclusion

Conventional strain engineering methods (e.g., shape-strained nanoparticles and lattice mismatched epitaxial adlayers) can induce more drastic changes in electrocatalytic activity than mechanical-induced methods.^{140,175,176} However, testing the effects of strain through materials synthesis is challenging. Not only is the fabrication of appropriate samples difficult and slow, but it is non-trivial to deconvolute strain effects from synthetic artifacts.¹³⁰ In contrast, the application of lattice strain by mechanically deforming an electrode enables in situ access to strained materials. This attribute positions mechanical-modulation of strain as an effective analytical method for

determining strain-property relationships in thin electrocatalytic films.¹⁷⁶ In this study I used mechanically-applied strain to investigate how tensile strain influences the electrochemical and physical properties of a palladium electrocatalyst. This experimental effort utilized a custom tensile testing electrochemical device, “TED”, to impart mechanical strain to 50 nm palladium thin films deposited on a flexible Kapton substrate while the change in the quantity of hydrogen absorbed into the palladium and the HER activity at the metal surface was measured. Our results highlight the opportunity to strain engineer palladium to enable higher HER activity and decreased hydrogen absorption capacity.

3.5 Experimental Methods

3.5.1 Materials

Cast PEEK sheet and rod stock, cast PMMA sheets, stainless steel dowel pins, wire rope, brass rods, stainless steel fasteners, and Viton® o-rings for the fabrication of the electrochemical cell and X-ray strain stage were purchased from McMaster-Carr. Aluminum (6061 alloy) sheet for the XRD strain stage sample clamps was purchased from Metal Supermarkets. Hatchbox ABS filament was used for 3D printed components and was purchased from Amazon. The load cell (LC201-100) was purchased from Omega Engineering. The linear encoder (ID1102L) and control circuit board (EPT002) were purchased from Prologue technology. Arduino (Uno, R3) microcontrollers and a stepper motor (NEMA 17, 12V, 667 oz-in) were purchased from RobotShop. A load cell amplifier (1568-1436-ND), copper wire and connectors were purchased from Digi-Key Electronics.

Kapton (300HN) film was purchased from American Durafilm. Acetone, IPA and sulfuric acid (95-98%, ACS reagent grade) were purchased from Sigma Aldrich. Cr, Au, Pt, and Pd pellets

for evaporation were purchased from Kurt J. Lesker. Nitric acid (70%) was purchased from Fisher Scientific. Pt wire counter electrodes were purchased from CH Instruments, Ag/AgCl reference electrodes (RE-5B) were purchased from Bioanalytical Systems Inc. All reagents and materials were used as received unless stated otherwise.

3.5.2 Thin film deposition

Substrates were prepared by sonicating a 5.5" diameter circular Kapton 300HN film with a thickness of 0.003" for 1 minute each in DI water, IPA, acetone, IPA and DI water. The substrate was subsequently blown dry with N₂ gas. This initial cleaning was followed by 1 minute of O₂ plasma stripping at 100 W under 50 mbar of O₂. Thermal and electron beam evaporation in a Kurt J. Lesker PVD75 system was used to deposit thin films of Cr, Pt and Pd at room temperature. Cr was deposited by thermal evaporation while Pt and Pd were deposited by electron beam evaporation. For all films, deposition was started when the base pressure was 2×10^{-6} torr or less. For Cr, Au and Pt trilayer films the deposition rates were 0.8 \AA s^{-1} , 1.4 \AA s^{-1} and $0.7\text{--}1.3 \text{ \AA s}^{-1}$, and film thicknesses were 10 nm, 20 nm and 50 nm as measured by the integrated quartz crystal microbalance (QCM) thickness monitor, respectively. For Cr, Au and Pd trilayer films, the deposition rates were 0.4 \AA s^{-1} , 1.5 \AA s^{-1} 0.7 \AA s^{-1} , and film thicknesses measured by the QCM monitor were 10 nm, 20 nm and 50 nm respectively.

3.5.3 X-ray diffraction experiments

Powder x-ray diffraction experiments were performed using a Rigaku Smartlab diffractometer using Bragg-Brentano focusing optics and Cu K α radiation. Data was collected between 2θ angles of 5° and 90° with a step size of 0.04° and incidence angle of 0.35° . The scan

rate was 4° min^{-1} . Residual strain analyses were performed in a parallel beam optics configuration using Cu $K\alpha$ radiation. Data was collected between 2θ angles of 81° and 84° with a step size of 0.025° and a scan rate of $0.12^\circ \text{ min}^{-1}$. The ψ angle was adjusted four times between 0° and -27° in increments linear in $\sin^2\psi$.

A palladium electrode was glued onto the aluminum clamp on the custom tensile testing XRD stage. This device interfaced with the standard sample stage of a Rigaku Smartlab diffractometer and was designed with thin ($1/16''$) sample clamps to prevent blocking of the incident x-rays at low angles ($< 9^\circ$ in 2θ). To verify that the electrode was mounted into the strain stage at 0% mechanical strain, lattice macrostrain was measured before and after the sample was loaded. The difference in lattice macrostrain before and after mounting to the strain stage was 0.04%, which we take to be a negligibly small difference. To ensure that $\epsilon_{\text{macrostrain}}$ was not relieved throughout the 24-hour acquisition of the data presented in figure 3.6c, a Pd|substrate sample was strained to $\epsilon_{\text{applied}} = 2\%$, then $\epsilon_{\text{macrostrain}}$ was measured immediately, and again after 72 hours. $\epsilon_{\text{macrostrain}}$ was found to decrease by only 0.03% (i.e., from 0.28% to 0.25%) indicating that the microstructure of the palladium film remained effectively unchanged over the course of the $\epsilon_{\text{macrostrain}}$ measurements.

3.5.4 Fabrication of electrode assemblies

Dovetail-shaped sample holders were designed in Solidworks and cut from a 0.25''-thick PMMA sheet using a Trotec Speedy 400 laser cutter with a CO_2 laser. Sample holders were fabricated from PMMA because of its high Young's modulus relative to other chemically compatible plastics (e.g., PTFE or PEEK). The electrode holders were designed to enable fabrication by laser cutting; which is an inexpensive and fast machining method but can only

engrave features in 2D. Laser machining the electrodes enabled batch fabrication of up to 100 sample holders and circumvented more complicated machining methods like milling. The electrode shape was rendered in Solidworks to match the guidelines outlined in ASTM D882-12 and scaled down to the size of the PMMA holder. The electrodes were cut from a sheet of 50 nm Pd, 20 nm Au and 10 nm of Cr, supported on Kapton 300HN using a Cricut Explore Air 2 plotter cutter. Each electrode was cut to achieve an active area of 1.27 cm^2 (25.4 mm long and 5 mm wide). The cut electrode was affixed to a PMMA sample holder using Devcon 2-ton epoxy, dried for >1 hour in ambient conditions, then a subsequent layer of epoxy was applied to the electrode-sample holder assembly and a second sample holder was placed on top to complete the assembly. Gentle pressure was applied to the complete electrode-sample holder assembly to ensure sufficient adhesion between the electrode and sample holders. The completed assembly was dried overnight before use.

3.5.5 Tensile test experiments

Tensile tests were performed according to guidelines outlined in ASTM protocol D882-12. The tensile testing apparatus was controlled with a custom Labview program. Signals from the load cell and linear encoder were recorded and output as text files. The software also controlled the stepper motor, which actuated the electrode. The load cell was calibrated between 0 and 100 N by hanging 5 test masses (10 N, 32 N, 61 N, 92 N) from the upper sample holder and measuring the response in mV. A calibration factor was then applied to convert the electrical signal (in mV) to a force measurement in N.

Before all experiments, the upper and lower sample clamps were aligned using a precisely-machined PMMA alignment block. The alignment block was inserted into the clamps prior to the

final tightening of the lid fasteners, which enabled the upper and lower dovetail clamps to be reproducibly aligned before each experiment. The strain rate was subsequently calibrated by adjusting the delay between motor steps to attain a consistent strain rate of 2.5 mm min^{-1} . For validation experiments, Kapton 300HN sample assemblies were loaded into the electrochemical cell through the front port, the sensor acquisition was started, and the samples were strained at a constant rate of 2.5 mm min^{-1} until $>10\%$ strain was achieved. For electrochemical experiments, the samples were loaded into the TED, the front hatch was installed, and stepwise strain was applied at a rate of 2.5 mm min^{-1} between electrochemical measurements.

Tensile testing data were analyzed using Matlab. Force measured by the load cell was converted to stress by dividing by the cross-sectional area of the sample. Displacement measured by the linear encoder was converted to strain by first performing a toe correction, a procedure detailed in the ASTM D882-12 guidelines. The toe correction was performed by first fitting the linear region of a plot of stress vs. displacement with a linear regression then extrapolating the best-fit line to the x-axis intercept. The displacement at the x-intercept was taken as the displacement at 0 strain, and the x-axis was rescaled accordingly. Strain was calculated based on this 0-displacement point, according to Equation A1.2 A plot of strain vs. time was used to determine the incremental strain applied after completing the electrochemical measurements.

3.5.6 Electrochemical measurements

The electrochemical cell was disassembled and cleaned by soaking all parts exposed to electrolyte for > 1 hour in a 1:1 v/v solution of 1 M H_2SO_4 and 1 M HNO_3 . After soaking, the cell was rinsed with MilliQ water and dried in air. Electrode assemblies were cleaned by sonication in EtOH then MilliQ water for 1 minute each then dried in air. Following cleaning, a 2" length of Cu

tape (3M) was attached to the electrode connection tab, masked with Kapton tape to prevent electrolyte contacting the Cu tape during the experiment, and the alignment tabs were removed by hand. The complete assembly was loaded into the cell by inserting the dovetail-shaped ends of the sample holders into the matching clamps in the TED cell. The front hatch was fastened onto the cell, and the Pt wire counter electrode and Ag/AgCl reference electrodes were installed through their respective ports. The sealed TED cell was filled with electrolyte by injecting 90 mL of 1 M H₂SO₄ through a peripheral port with a 100 mL syringe.

All electrochemical experiments were performed using a Metrohm Autolab PGSTAT302N potentiostat. Pt wire was used as a counter electrode and Ag/AgCl (3 M) as a reference. Uncompensated resistance was measured before every experiment using the i-interrupt method and was approximately ~7 Ohms. No potential correction was performed due to the low uncompensated resistance. Following the measurement of the uncompensated resistance, the magnetic drive centrifugal pump was started and run for ~2 minutes to enable equilibration of the flow rate and removal of air bubbles from the flow system.

3.5.7 Hydrogen absorption quantification

All H:Pd absorption values were determined by converting the oxidative (desorption) charge to moles using Faraday's constant. The moles of palladium in the sample divided the absorbed moles of hydrogen. The moles of palladium were calculated from the mass of palladium deposited during electron beam deposition as determined by in situ QCM. We assume that the Pd thickness was uniform across the entirety of the 5.5" diameter substrate.

To validate the flow cell conversion of the TED for these measurements we collected cyclic voltammograms at a platinum|substrate electrode (as a proxy for palladium that does not absorb

hydrogen into its lattice). We did not observe any oxidative current on the anodic scan of the CV, indicating H₂ gas was successfully removed from the electrode surface (Figures A1.7).

3.5.8 Calculation of uncertainty for electrochemical measurements

Measurement uncertainty for the % change in H:Pd ratio and HER activity were calculated by fitting the dataset from each sample to linear, and second-order polynomial regressions, respectively. The average and standard deviation for each constant in the fit equations was calculated (see Tables A1.1 and A1.2). Uncertainty in the % change of the H:Pd ratio and HER activity was propagated by substituting in the standard deviation of each constant into the equation of the fit, then solving for y taking $x = 2.0\%$, and $x = 4.5\%$, respectively.

3.5.9 Scanning electron microscopy

Scanning electron microscopy (SEM) was performed on palladium thin films using an FEI Helios NanoLab 650 dual-beam scanning electron microscope. Imaging data was acquired with an electron beam accelerating voltage of 1 kV and a beam current of 50 pA.

Chapter 4: Electrocatalytic Hydrogenation Using a Palladium Membrane

Flow Cell

4.1 Introduction

In this chapter I demonstrate that reaction rate, efficiency, and selectivity of hydrogenation in an ePMR are increased through improved reactor design. All ePMR studies prior to this work had been carried out in H-cells (Figure 4.1a), a divided electrochemical cell common to research laboratories. H-cells (reviewed in section 2.5.2) are simple to operate and convenient for proof-of-concept demonstration,¹⁷⁷ but are not scalable for commercial application. In this chapter I show how a flow architecture enables efficient electrically-driven hydrogenation and provides pathway for scaling ePMRs for chemical synthesis.

Parallel plate flow architectures place a flow field plate the anode and cathode, and use porous electrodes to provide a path for the flowing reagent to reach the catalyst surface. Ions produced and consumed in the reaction to diffuse to the reaction surface from the opposite face of the catalyst. An ion exchange membrane placed between the electrodes separates the reactant and product streams at the anode and cathode. This architecture has been used successfully in electrochemical flow-cell systems such as hydrogen fuel cells¹⁷ and CO₂ electrolyzers (reviewed in section 2.5.2).⁴⁹ The requirements for an ePMR flow cell are, however, unique compared to these previously-reported reactors because the hydrogenation process in an ePMR occurs at three catalytic interfaces (water oxidation, proton reduction and hydrogenation each proceed at distinct surfaces), rather than two. The ePMR flow cell therefore required a custom design.

The first step in the flow cell design was to identify the rate limiting step in a hydrogenation process in an ePMR. There are five major steps that must proceed for hydrogenation to occur in

these devices: i) water oxidation at an anode; ii) proton reduction at the cathode surface; iii) hydrogen permeation through the palladium membrane; iv) diffusion of an organic substrate to the surface of the membrane; and v) hydrogen addition across the unsaturations of the organic substrate. Previous studies provided evidence that the hydrogenation step is rate limiting in an ePMR. Sherbo *et al.* demonstrated that at modest current densities (25 mA/cm²) more hydrogen is delivered to the reaction site than is consumed in the reaction, suggesting that hydrogen production and delivery (steps i-iii) were not limiting the hydrogenation rate.^{17,20} Iwakura *et al.* showed that depositing a rough, high surface area Pd-black catalyst on the surface of the membrane substantially increases reaction rate, suggesting that hydrogen addition (step iv) was rate limiting in an H-cell.^{17,19} Current density is known to increase reaction rates in an ePMR.⁸⁶ I therefore hypothesized that at very high current densities, the reaction would become rate limited by the transport of the organic species to the catalyst surface, and accordingly designed the ePMR flow cell to include a flow field to deliver the reactant to the hydrogenation surface of the membrane.

I found that the ePMR flow cell enables faster, more selective and higher efficiency hydrogenation. I validated this approach by studying the hydrogenation of phenylacetylene as a model reaction in this custom-designed flow cell, and tracked the factors that determine reaction rate, selectivity and efficiency. Through reactor design alone (i.e., flowing the organic reactant to the catalyst surface and decreasing the solution resistance in the electrolysis chamber), I was able to achieve 15-fold higher hydrogenation rates than can be accessed in an H-cell at a similar applied voltage.

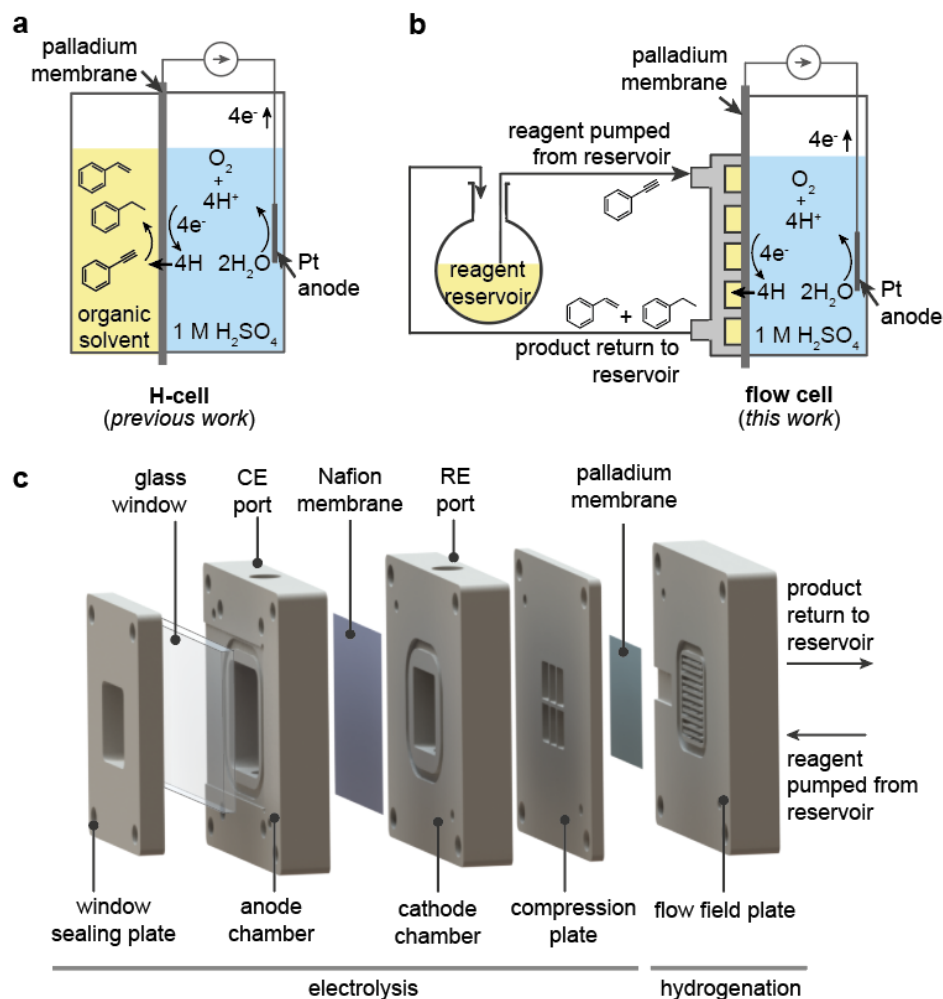


Figure 4.1 Illustrations of a) the two-compartment H-cell reactor architecture used to date for electrocatalytic palladium membrane hydrogenation reactions,⁹⁰ and b) the ePMR flow cell architecture reported here, wherein the organic reagent is delivered to the catalyst surface through a flow field plate. c) Rendering of the ePMR flow cell, which includes electrolysis and hydrogenation compartments partitioned by a palladium membrane. The electrolysis compartment houses a 3-electrode electrochemical setup, and the hydrogenation compartment includes a flow field plate with a triple serpentine flow pattern for efficient reagent delivery (see Figure A2.1 for an image of the complete setup).

The ePMR flow cell also enabled us to reveal insights into the factors that determine reaction performance in an ePMR. Hydrogenation proceeded following the well-established sequential hydrogenation mechanism,¹⁷ and also through a direct hydrogenation pathway wherein the alkyne is directly converted to the alkane adduct in a single step.^{17,19,20} Hydrogen content in the membrane was found to be deterministic of hydrogenation rate, where more absorbed hydrogen leads to faster, albeit less selective, conversion. These findings highlight that both reactor design and palladium membrane properties play a role in hydrogenation performance, and provide design principles for future studies of the ePMR.

4.2 Results and Discussion

4.2.1 Design of an electrochemical palladium membrane flow cell

For the first stage of this study I designed a 3-chamber ePMR flow cell (Figure 4.1c). This device includes: i) separate electrochemical compartments to contain the platinum anode, and the reference electrode and palladium membrane; and ii) a hydrogenation flow field plate with a (2 cm × 2 cm) triple serpentine flow pattern and 1 mm × 1 mm flow channels. The anode and cathode chambers were separated by a Nafion membrane to isolate oxidative electrochemistry from proton reduction at the palladium cathode (3 cm × 3 cm),^{17,19,26} which was held securely against the flow field by a compression plate. O-rings (Viton, square cross section) were used to seal the intercompartmental interfaces. This sealing strategy enabled more efficient use of the palladium foil, with a 3.7-fold increase in the active area of palladium (from 1.2 cm² to 4 cm²) compared to gaskets used for our previously-reported H-cell configuration, despite using only a 1.4× larger Pd foil.

To conduct hydrogenation experiments in the flow cell, the cathode and anode compartments were both first filled with 8 mL of 1 M H₂SO₄ electrolyte, then a Ag/AgCl reference electrode (RE) and platinum mesh counter electrode (CE) were inserted through the dedicated ports in each half of the electrolysis compartment. For each hydrogenation reaction, a fresh solution of phenylacetylene (PA) [25 mL, 0.1 M in dichloromethane (DCM)] contained in a 50 mL reservoir, was continuously recirculated through the hydrogenation flow field at a rate of 20 mL/min using a peristaltic pump. Water electrolysis was driven galvanostatically at a current of 10, 50, 100, 250, or 400 mA/cm², and reaction progress was monitored by quantifying the amounts of phenylacetylene (PA), styrene (ST) and ethylbenzene (EB) in 20- μ L aliquots taken from the reagent reservoir using gas chromatography–mass spectrometry (GC–MS). These data were used to generate concentration versus time plots (Figure 4.2a; Figures A2.9 and A2.16a) which were subsequently analyzed to determine reaction rate, selectivity and current efficiency.

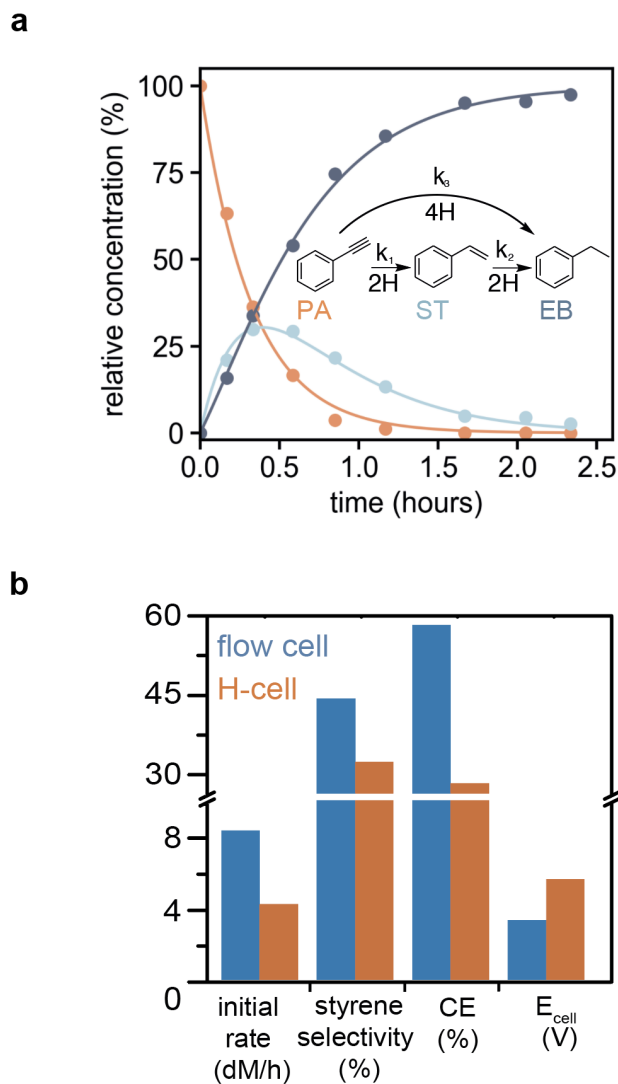


Figure 4.2 a) Concentration profile of a hydrogenation reaction carried out at 250 mA/cm² in the ePMR flow cell. The inset scheme shows that hydrogenation of phenylacetylene (PA) may proceed via a styrene intermediate or directly to ethylbenzene (EB) in a single step. Kinetic fits (indicated by solid lines) are described by Equations A2.4 to A2.6. **b)** Bar chart comparing reaction performance in an H-cell and a flow cell (with an identical Pd surface area) using four reaction performance metrics: initial reaction rate; maximum styrene concentration; current efficiency (CE); and cell voltage (E_{cell}) at 100 mA/cm². This flow architecture enables higher performance in every metric than the H-cell.

4.2.2 Benchmarking hydrogenation reaction performance in the flow cell

I conducted a series of experiments to compare hydrogenation performance (i.e., reaction rate, selectivity and current efficiency) in the flow cell to an H-cell setup. A hydrogenation reaction was carried out in each cell architecture at a fixed current density of 100 mA/cm² using 25 mL of 0.1 M phenylacetylene in DCM as the reactant and 1 M H₂SO₄ as the electrolyte. The H-cell was assembled according to our previously-reported procedures,¹⁹ using a (2.5 cm × 2.5 cm) palladium foil to separate the stirred hydrogenation and electrolysis chambers. To enable a direct comparison of reaction performance metrics between each cell architecture, I used Kapton film to mask the surface of the palladium foil used in the flow cell so that the active area of the catalyst was equal in both setups (i.e., 1.2 cm²).

This benchmarking experiment revealed that the flow cell outperforms the H-cell on every performance metric measured (i.e., reaction rate, selectivity, current efficiency and cell voltage; Figure 4.2b). The initial reaction rate increased 2-fold when the reaction was run in flow compared to the static H-cell. Selectivity for styrene production was also found to be slightly higher in the flow cell (43% maximum styrene concentration c.f. 32% in the H-cell), and current efficiency was found to be 28% higher in the flow cell than in the H-cell. Flow rate also adjusted reaction rate and selectivity, with higher flow rates driving faster hydrogenation (i.e., 0.18 M/s at a flow rate of 10 mL/min, and 0.26 M/s at 40 mL/min; Figure A2.8). The cell design modifications also facilitated a substantial decrease in cell voltage (from 5.6 V to 3.3 V) required to drive a 100 mA/cm² electrolysis current (Figure A2.7). These results show how this reactor design alone enabled significant increase in performance without requiring catalyst or materials design modifications.

Our benchmarking experiments also aimed to show that electrolysis current density controls reaction rate, selectivity, and current efficiency. I hydrogenated PA in the flow cell using the entire 4 cm² surface area of the foil at 10, 50, 100, 250, and 400 mA/cm². Higher current densities corresponded to faster reaction rates (Figure 4.3a) and higher selectivity for the fully-hydrogenated ethylbenzene adduct (Figure 4.3b), albeit at the cost of lower current efficiencies (Figure 4.3c). These experiments show that electrochemical control of the reaction rate, selectivity, and efficiency^{86,177} were not sacrificed by modifying the reactor architecture. Our results also highlight the marked effect that current density has on reaction performance, with the ability to modulate reaction rate 19-fold, selectivity 5-fold, and current efficiency 3-fold by adjusting electrolysis current between 10 and 400 mA/cm².

As a final validation experiment, I demonstrated that the reaction scale can be adjusted by changing the size of the chemical reservoir. I hydrogenated a 200 mL, 0.2 M (40 mmol, 3.8 g, in DCM) solution of phenylacetylene at 100 mA/cm², which required 24 h of continuous electrolysis to consume the starting material (see Figure A2.10). Selectivity for the styrene intermediate was roughly 2-fold higher than the reaction conducted using a 0.1 M PA solution. This experiment also demonstrates that the palladium membrane is sufficiently durable for at least day-long operation.

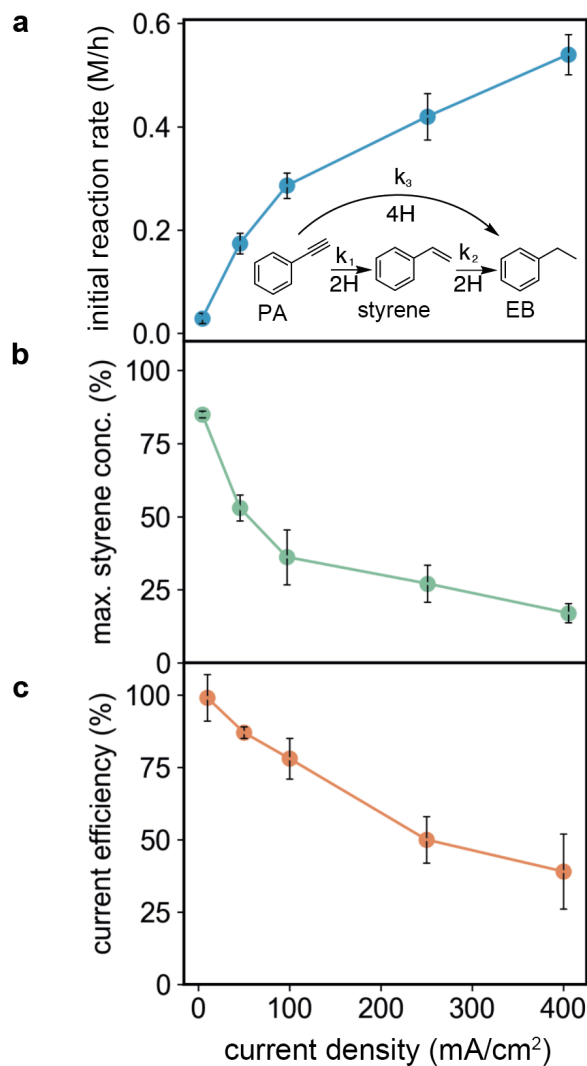


Figure 4.3 Plots showing the effect of current density on; a) the initial rate of phenylacetylene (PA) hydrogenation to styrene and ethylbenzene (EB) (reaction scheme inset), b) maximum styrene concentration, and c) current efficiency, as a function of current density in an ePMR flow cell. Current density increases the hydrogenation reaction rate while concurrently decreasing selectivity and current efficiency. Each data point represents the average value from at least three reactions with error bars representing ± 1 standard deviation of the mean value.

4.2.3 Palladium membrane properties determine hydrogenation reaction performance

I constructed a kinetic model to understand the processes that govern hydrogenation rate, selectivity and current efficiency in an ePMR. This kinetic model (described in detail in Appendix 2) used a custom Python script to extract effective rate constants (i.e., the rate constant multiplied by $[H]$; denoted as k_x')^{86,178} for each step of the hydrogenation reaction by fitting a system of differential equations to reaction concentration profiles. The reaction was found to be first order in phenylacetylene and styrene for current densities >10 mA/cm² and 0-order in the organic reactants for the lowest current density tested (Table A2.1; Figures A2.11 to A2.15). This finding indicates that the reaction is rate-limited by hydrogen delivery at 10 mA/cm² and hindered by either hydrogen addition or substrate diffusion at higher current densities (≥ 50 mA/cm²). This assertion is supported by current efficiency data (Figure 4.3c), showing that at 10 mA/cm² nearly all hydrogen produced is consumed by the hydrogenation reaction and at currents ≥ 50 mA/cm², excess hydrogen is produced and evolved as H₂(g) byproduct.

Horiuti and Polanyi^{90,179} proposed a sequential hydrogenation mechanism that proceeds through a partially-hydrogenated alkene (i.e., styrene) intermediate, which can either desorb from the metal surface or react further to form the alkane (i.e., ethylbenzene) adduct.^{97,179} I found that also accounting for a direct hydrogenation pathway,^{90,180} wherein phenylacetylene is converted to ethylbenzene in a single step (Figure 4.2a inset scheme), provides a higher goodness-of-fit at every current density tested (Table A2.2; Figures A2.17 to A2.20). A key outcome of this model is that current density appears to gate the preference for the sequential or direct hydrogenation pathways. The effective rate constant for the direct hydrogenation pathway (k_3') is nearly 100-fold larger relative to the sequential pathway (k_1', k_2') at 400 mA/cm² than at 10 mA/cm² (see Table A2.3). High current densities (≥ 100 mA/cm²) therefore result in low selectivity for the styrene

intermediate because styrene is simply hydrogenated to the fully-saturated adduct before desorption can occur.

Next I turned my attention to the palladium membrane to understand the influence that electrochemical current exerts over the hydrogenation reaction performance. I measured how reaction performance correlates to: i) the hydrogen content of the palladium membrane; and ii) the amount of hydrogen that evolves from each side of the membrane using a four-step workflow. A coulometry method previously developed by our group^{181,182} was first used to conduct *ex situ* measurements of the hydrogen content in the Pd membrane (expressed as the H:Pd ratio) at a range of cathode potentials between 0 and -1.0 V vs RHE (Figure 4.4a). The average voltage at each current density (10, 50, 100, 250, and 400 mA/cm²) was then used to estimate the palladium membrane hydrogen content during hydrogenation (Figure 4.4b; see Equation A2.20; Figure A2.23). I next related the initial reaction rate, and reaction selectivity to the estimated hydrogen content in the membrane (Figures 4.4c and d, respectively).

These experiments show that hydrogen content in the membrane affects reaction rate and selectivity: a lower concentration of hydrogen in the membrane leads to slower, but more selective, hydrogenation (Figure 4.4c and d, respectively). This finding is qualitatively consistent with studies of thermochemical hydrogenation systems. Teschner *et al.* showed that catalytic promoters dissolved in the palladium catalyst (e.g., carbon,^{97,181} silver^{182,183}) decrease hydrogen loading, and resultantly increase the selectivity for the alkene intermediate (but at the cost of a decreased reaction rate).¹⁸²⁻¹⁸⁴ The ePMR enables reaction rate and selectivity to be modulated by adjusting the current density, rather than through manipulating catalyst composition.^{185,186} The electrochemical control of the hydrogen content in the membrane enabled us to use this device to study the

influence of absorbed hydrogen on reaction performance, where previous studies of hydrogenation catalysts have required high-vacuum setups.^{181,186,187}

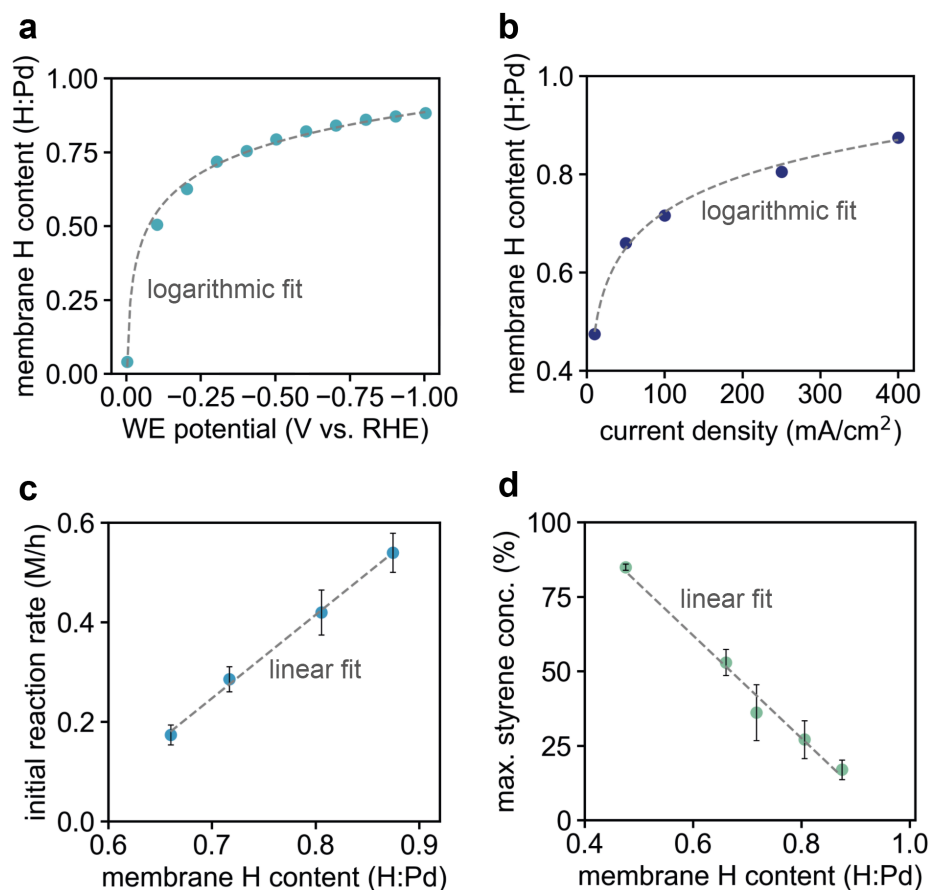


Figure 4.4 Plots illustrating the effect of a) applied voltage and b) current density on the amount of hydrogen that absorbs into the palladium membrane, showing direct electrochemical control over the palladium membrane hydrogen content (expressed as the H:Pd ratio). Plots showing that higher membrane hydrogen content c) increases the initial reaction rate and d) decreases selectivity for the styrene intermediate. Error bars represent ± 1 standard deviation of the mean value for at least 3 reactions.

A final experiment was conducted to measure how current density influenced current efficiency. *In situ* mass spectrometry to measure the amount of hydrogen evolved from each side of the palladium membrane during electrolysis. An atmospheric-mass spectrometer (atm-MS) was connected to the organic reagent reservoir filled with only 25 mL of DCM (Figure 4.5a).

Electrolysis was conducted for >1000 s at a current density of 10, 50, 100, 250, then 400 mA/cm² while DCM was continuously recirculated through the hydrogenation flow field. The amount of hydrogen that permeated through the membrane was measured by monitoring the mass to charge ratio for hydrogen (m/z = 2) with the atm-MS. Hydrogen permeation rate (which is proportional to the ion current) measured at each side of the membrane increased with current density (see Figure 4.5b for the reagent reservoir measurement; see Figure A2.24 for the hydrogen measured in the electrolysis chamber). Current efficiency tracks linearly with permeated hydrogen (Figure 4.5c), leading us to conjecture that H₂ gas evolved from the hydrogenation face of the palladium membrane is not involved in the hydrogenation reaction. This observation also highlights that a potential avenue for increasing current efficiency may be to incorporate catalysts that decrease hydrogen recombination rates to avoid H₂ formation.

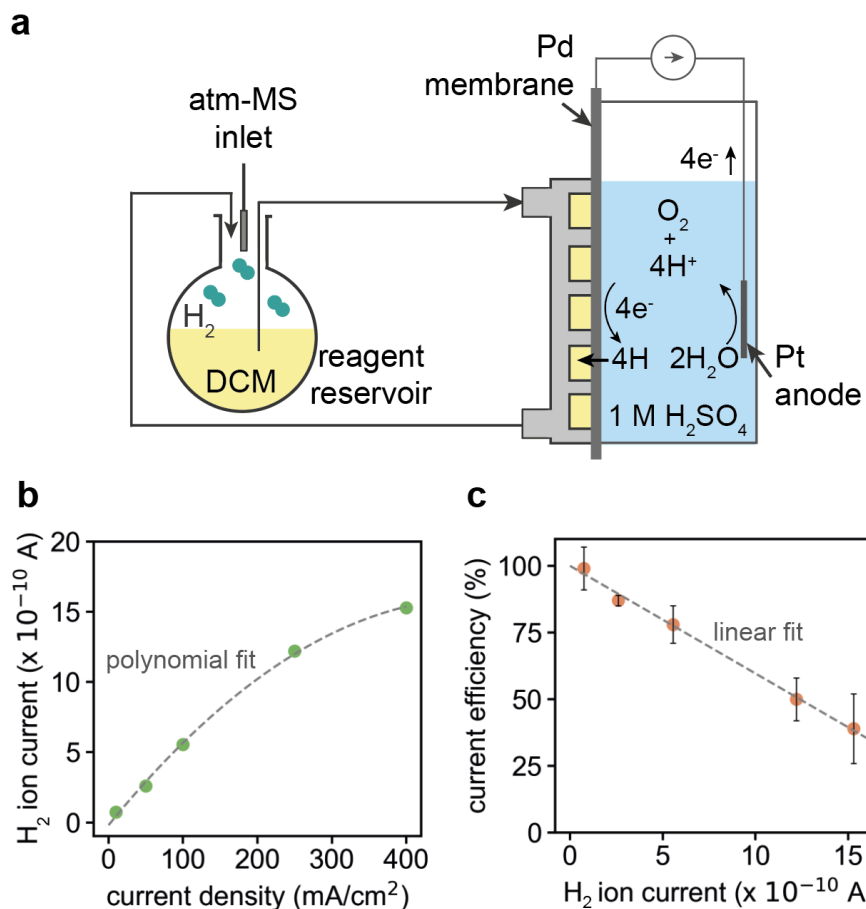


Figure 4.5 a) Illustration of the experiment setup used to measure the amount of hydrogen that permeates through the palladium membrane by tracking the $m/z = 2$ ion current using in situ atmospheric–mass spectrometry b) The amount of the hydrogen that permeates through the membrane increases with current density and is described by a polynomial fit. c) Plot showing that current efficiency decreases linearly with increasing hydrogen evolved at the side of the membrane where hydrogenation occurs. Error bars represent ± 1 standard deviation of the mean value for at least 3 reactions.

4.3 Conclusions

Electrocatalytic palladium membrane reactors can hydrogenate organic molecules dissolved in any organic solvent without requiring an H₂ gas feedstock. This attribute positions this technology as a sustainable alternative to conventional high temperature and pressure

hydrogenation methods for fine chemical and industrial-scale applications. This work provides a design for a flow-reactor architecture and illuminates factors that mediate hydrogenation performance in these devices. Cell design considerations alone (i.e., improving mass transport of the organic feedstock to the palladium surface, and increasing the maximum electrolysis current density) enable a 15-fold hydrogenation rate-enhancement compared to the previously-reported H-cell. Applied voltage was also found to control the hydrogen content in the palladium membrane, which in turn defines reaction rate and selectivity with higher rates, but lower selectivity corresponding to a high Pd H-content.

4.4 Experimental Methods

4.4.1 Materials

Pd (99.95%) was purchased as a 1 oz wafer bar from Silver Gold Bull. Phenylacetylene (98%) was purchased from Acros organics. Dichloromethane (DCM; obtained from a solvent purification system), H₂O₂ solution (30 wt. % in H₂O) were purchased from Sigma Aldrich. Pt gauze (52 mesh, 99.9%) and Pt wire (0.5 mm, 99.95%) were purchased from Alfa Aesar. Nitric acid (68-70%) was purchased from VWR. Nafion 117 membranes were purchased from Fuel Cell Store. Ag/AgCl reference electrodes (RE5B) were purchased from BASi. Cast PEEK sheets, borosilicate sheets, stainless steel dowel pins, stainless steel fasteners, and Viton o-rings and tubing and PVDF Luer lock quick connect tubing couplings for the fabrication of the flow cell were purchased from McMaster-Carr. The reaction mixture was pumped with a Low-Flow Chemical Metering Pump (part no. 4049K55, McMaster-Carr).

4.4.2 Pd foil preparation

Pd foils were rolled from a 1 oz Pd wafer bar. The bar was rolled to 25 μm thick foils as determined by a Mitutoyo digital micrometer and annealed at 850 $^{\circ}\text{C}$ for 1.5 hours in an Ar atmosphere. The Pd foils were cleaned using 1:1:1 conc. $\text{HNO}_3:\text{H}_2\text{O}:\text{H}_2\text{O}_2$ v/v ratio solution until vigorous bubbling subsided (~ 20 min). Electrodeposition was performed immediately following this cleaning step (see catalyst preparation below).

4.4.3 Electrochemistry

A Metrohm Autolab PGSTAT302N potentiostat was used to control the electrochemical experiments. A palladium foil was fitted between the hydrogenation flow field and the electrolysis compartment. A Nafion 117 membrane (50- μm thick) was installed between the anode and cathode compartments. Viton o-rings were used to seal both the palladium foil and the Nafion membrane in place and ensure a reliable seal. Each electrolysis compartment was filled with 8 mL of 1 M H_2SO_4 , and an Ag/AgCl electrode (3.0 M NaCl) was used as a reference electrode and a Pt mesh was used as an anode/counter electrode. Electrolysis was driven galvanostatically, where a reductive current was applied by the potentiostat to the Pd foil working electrode (cathode) and the potential was measured between the Pd and the reference electrode. No iR correction was performed because the high salt concentration of the electrolyte and close proximity of the reference electrode to the palladium cathode (~ 3 mm) resulted in negligibly small uncompensated resistances of $<0.1 \Omega$. Cell potential (E_{cell}) was measured between the anode and cathode and is reported in this work as the absolute value for ease of comparison. The thickness of the foil was 25 μm and the geometric surface area of the foil was $\sim 9 \text{ cm}^2$.

4.4.4 Catalyst preparation

A high surface area palladium catalyst was electrodeposited onto the foil to increase the hydrogenation reaction rate. The cell was assembled without the cathode pressure plate installed, and with the side of the foil to which the organic substrate would be exposed during the reaction was instead exposed to the electrochemical compartment. The electrochemical chamber of the cell was filled with 15 mL of 15.9 mM PdCl₂ in 1 M HCl and a Ag/AgCl reference electrode and Pt mesh counter electrode were fitted to the cell. -0.3 V vs. Ag/AgCl was applied to the working electrode foil until 36 C of charge (9 C/cm²) had been passed (~20 mg of Pd). The deposition current was approximately 20–30 mA. The resulting black-coloured palladium catalyst was used for a maximum of 4 reactions before being removed from the foil using concentrated nitric acid and gentle mechanical abrasion. The foil was then cleaned and replated with the catalyst for continued use. The palladium foils were used in this manner until pin holes formed in the foil as a result of: i) hydrogen embrittlement from repeated hydrogen absorption and desorption; ii) etching of the foil during cleaning; and iii) repeated clamping of the foil in the flow cell. The palladium membranes were reused for >10 reactions before pin-holes formed occurred.

4.4.5 Hydrogenation experiments in a flow cell

To perform a hydrogenation reaction in the ePMR flow cell the device was assembled by first placing a palladium foil with the catalyst facing the hydrogenation flow field. The compression plate, cathode chamber, Nafion membrane, and anode chamber were positioned over the foil. Four fasteners situated at the corners of the cell were tightened sequentially to compress the Viton O-rings and create a hermetic seal between the component and component-membrane interfaces. Viton tubing (1/8" ID, 1/4" OD) was connected to the inlet and outlet of the hydrogenation

flow plate via PVDF Luer lock couplings, and connected the 50 mL organic reactant reservoir, peristaltic pump, and palladium membrane reactor. Phenylacetylene (0.26 g, 2.5 mmol) and DCM (25 mL) were added to the organic reagent reservoir and stirred at a consistent rate. Reaction aliquots were sampled every 1–30 minutes, depending on the current density and the duration of the reaction (e.g., 400 mA/cm² reactions were sampled approximately every 1 minute for the first 5 samples, then every 10 minutes for the remaining samples, and 10 mA/cm² reactions were sampled approximately every 30 minutes from start to finish), such that 10–15 samples were collected for each reaction. Reactions were monitored by gas chromatography–mass spectrometry (GC–MS) by diluting 20 µL of the reaction mixture in 1 mL of DCM.

4.4.6 Hydrogenation experiments in an H-cell

Hydrogenation in H-cell was performed in air at room temperature. The oven-dried hydrogenation compartment with a magnetic stir bar was filled with substrate (2.5 mmol of phenylacetylene) and solvent (DCM, 25 mL). Electrolyte (1 M H₂SO₄, 35 mL) was added to each electrochemical compartment separated by a Nafion membrane. A constant current density of 100 mA/cm² was applied (vs. Ag/AgCl₂) for 8 h. Both the reaction mixture and electrolyte solution were stirred at a constant rate throughout the experiment. Reaction aliquots were sampled every 1 h to monitor the reaction progress by GC-MS.

4.4.6 Gas chromatography–mass spectrometry

GC–MS experiments were conducted on an Agilent GC–MS using an HP-5ms column and electron ionization. The samples were run using an auto-sampler with a 1 µL injection volume and a split ratio of 20:1. The oven temperature was static at 50°C for 1 min, ramped to 65°C at 3 °C

min⁻¹, then to 200°C at 100°C. A solvent delay of 4.6 min was employed. Peaks for phenylacetylene (PA), styrene (ST), and ethylbenzene (EB) were identified by searching the NIST database for matching mass spectra and eluted at 5.4, 5.8, and 5.1 minutes respectively. Relative concentration was determined using peak integration of the three fully-separated peaks. Calibration curves were collected for PA, ST, and EB, and the instrument response for each species was found to be identical within acceptable error ($\pm 1 \sigma$) of three repeats of each calibration curve. Therefore, no calibration factor was applied.

4.4.7 Atmospheric–mass spectrometry

The cell was set up identically as for membrane reactor hydrogenation experiments with a few minor modifications to enable monitoring of hydrogen evolution at both sides of the membrane: i) no phenylacetylene was added to the reagent reservoir; ii) the reference electrode was removed and replaced with an inlet connector for the atmospheric–mass spectrometer; and iii) the electrolysis was performed using a two-electrode setup (i.e., no reference electrode was used) given that the reference electrode port was used instead for gas sampling. Electrolyte (8 mL of 1 M H₂SO₄) was added to both electrochemical compartments with a Nafion membrane in between. Hydrogen evolution at the side of the membrane exposed to the organic solvent was monitored through a MS inlet tube connected to the reagent reservoir. The 2 m/z ion current was monitored using an ESS CatalySys atmospheric–mass spectrometer with a flow rate into the instrument of 10 mL min⁻¹. The reagent reservoir was stirred and DCM was pumped through the hydrogenation compartment of the cell throughout the experiment. Monitoring between the reagent reservoir and electrochemical compartment was switched every 5 s with a 3 s purge to measure H₂ evolving at

both sides of the membrane simultaneously in a single experiment. Once H₂ evolution had equilibrated.

4.4.8 Flow coulometry experiments

For the H:Pd measurements, a 3-step workflow was employed to collect each data point, using an electrochemical cell and protocol published previously.¹⁸⁶ First, a reductive potential between 0 and -1 V vs. RHE was applied to the electrode for 2000 s to drive hydrogen absorption into the palladium lattice. Next, 0.30 V (vs. Ag/AgCl) was applied for 1200 s, which oxidized hydrogen absorbed in the lattice back into protons, while the amount of charge passed during this step was measured. Lastly, the total current passed during this oxidation step was integrated to yield the total charge associated with the oxidation of adsorbed hydrogen.¹⁸⁷ All H:Pd absorption values were determined by converting the oxidative (desorption) charge to moles using Faraday's constant. The moles of palladium in the sample divided the absorbed moles of hydrogen. The moles of palladium were calculated from the dry mass of the palladium sample.

4.4.9 Kinetic modelling

To determine the reaction order in phenylacetylene and styrene, I fit the relative concentration versus time profiles with a system of ordinary differential equations for zero, first and second order reactions using a custom Python script (see Equations A2.1 to A2.9 below; Figures A2.10 to A2.14). The concentration profiles were fit following a time delay (denoted herein as 'permeation time'; Figure A2.21) from the start of electrolysis to when hydrogenation commences (Figure A2.22). The model output effective rate constants^{17,19-21,26,27,188} (k') which were used in turn to calculate the concentration of each species in solution. The comparison of the

conventional Horiuti-Polanyi mechanism and direct hydrogenation mechanism (proposed here) was carried out by comparing the quality of the fits for a system of equations that included the direct pathway (Equations A2.13 to A2.15), to a system of equations that omitted the direct pathway (i.e., Horiuti-Polanyi mechanism; Equations A2.10 to A2.12).

Chapter 5: Physical Separation of H₂ Activation from Hydrogenation

Chemistry Reveals the Specific Role of Secondary Metal Catalysts

5.1 Introduction

A primary challenge of performing electrolytic hydrogenation efficiently is designing a catalyst that effectively mediates two distinctive reaction steps: (i) proton reduction to form reactive hydrogen atoms and; (ii) substrate hydrogenation.¹⁸⁸ Electrocatalytic palladium membrane reactors (ePMRs) provide an opportunity to address this challenge. The ePMR uses a solid, hydrogen-permeable membrane to physically separate the hydrogenation reaction from proton reduction (Figure 5.1a).^{17,19–21,26,27,189} The use of a dense palladium membrane enables hydrogenation chemistry to be performed at one interface using H atoms sourced from water electrolysis at the opposite side of the foil. This separation enables the reaction occurring at each face of the palladium membrane to be independently optimized.

Studies to date have optimized the hydrogenation and electrolysis reactions by conducting each reaction in a different solvent.³¹ An organic solvent used in the hydrogenation compartment, and an aqueous electrolyte in the electrolysis chamber, enables higher energy efficiencies than could otherwise be achieved in a conventional ECH system (Sherbo et al. show up to a 1 V reduction in cathode voltage³¹). Another opportunity to leverage this unique membrane reactor architecture is to use a different catalyst at each face of the membrane – the proton reduction can therefore proceed at an efficient HER catalyst, and the hydrogenation catalyst can be tailored to the substrate. Iwakura *et al.* were the first to demonstrate this concept.^{21,39} These authors chemically reduced a secondary metal catalyst (Pt, Au, Cu or Zn) on the hydrogenation face of the palladium membrane and analyzed the reactivity for C=C bonds.^{9,73} The activity of the catalysts

affected C=C hydrogenation conversion rates, with Pt demonstrating the highest reactivity (0.88 mmol h⁻¹, vs. 0.6 mmol h⁻¹ for Au), while Cu and Zn exhibited almost no catalytic activity.^{12,188} The reactivity of these catalyst-coated membranes was never compared to an unmodified palladium membrane of similar surface area, so it is unclear if the secondary metals improved or hindered reactivity relative to an untreated surface. Notwithstanding, this study shows that thin metal coatings can have a significant influence on reactivity. Dr. Kurimoto and I investigated whether catalyst coated membranes could be designed for the hydrogenation of carbonyl groups.^{12,189} Carbonyl groups are relevant for a wide variety of pharmaceutical,¹⁸⁹⁻¹⁹¹ and renewable chemical^{12,190} transformations and are challenging to hydrogenate at palladium surfaces in an ePMR.

A catalyst-coated membrane is differentiated from a conventional hydrogenation catalyst because hydrogen is activated at a distinct site from where the hydrogenation takes place. In this architecture reactive hydrogen atoms are formed in the electrochemical compartment, and then delivered to the hydrogenation site by permeating through the palladium lattice.¹⁹⁰⁻¹⁹² A second aspect of this study was to investigate if catalysts that are traditionally considered poor hydrogenation catalysts because they exhibit very weak M-H interactions (e.g., Au),¹⁹¹⁻¹⁹³ could exhibit high hydrogenation activities in an ePMR because reactive hydrogen does not need to be formed on the secondary catalyst surface for the reaction to proceed.

In this work work, Dr. Aiko Kurimoto and I measure how secondary metal catalysts coated on the palladium membrane affect the rates of hydrogenation of C=O and C=C bonds. I deposited a thin layer of a secondary metal catalyst (Pt, Au, or Ir) on the hydrogenation surface of the membrane (Figure 5.1b) and Dr. Kurimoto conducted hydrogenation experiments to analyze how acetophenone and styrene hydrogenation rates were influenced. Our results show that that the

secondary catalyst dictates the reactivity towards C=O and C=C bonds and that hydrogenation occurs at the secondary metal catalyst and not the underlying palladium foil. The separation of substrate hydrogenation from proton reduction additionally enabled us to determine that Au is an active C=O bond hydrogenation catalyst, a finding that opposes the established understanding that bulk Au is a poor hydrogenation catalyst.^{191–193} We also show that the thin secondary catalyst film increases the transport of H atoms through the membrane to the reaction site. This study serves to demonstrate that reactivity for specific functional groups can be tailored by changing the composition of the catalyst exposed to the organic substrate.

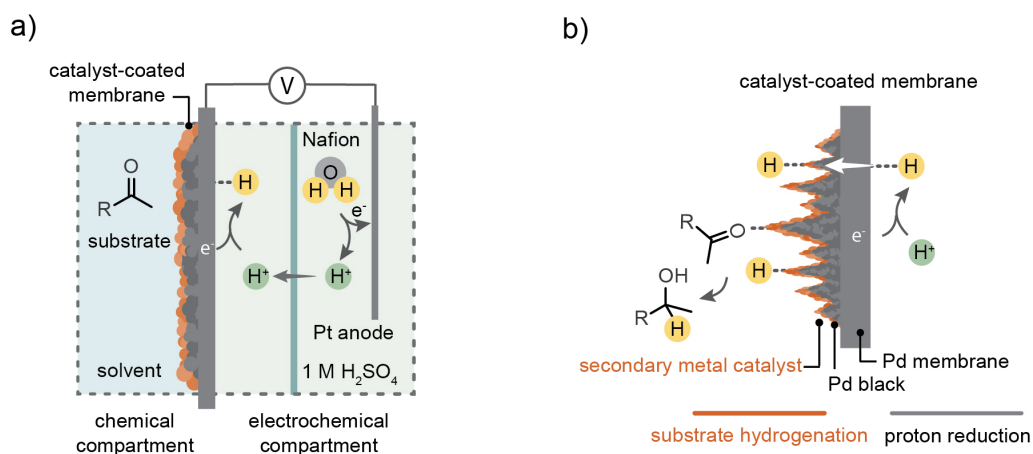


Figure 5.1 (a) Schematic diagram of the electrocatalytic palladium membrane reactor (ePMR) with a secondary metal catalyst (Pt, Au, Ir) deposited on the side of the palladium membrane exposed to the chemical compartment. (b) Illustration of the relevant processes occurring at the catalyst-coated membrane during hydrogenation: i) Proton reduction occurs on the Pd membrane to form H atoms; ii) H atoms diffuse through the Pd membrane to the secondary metal catalyst; iii) The substrate is hydrogenated on the secondary metal catalyst. The catalyst-coated membrane was prepared by depositing a 10 nm layer of the secondary metal catalyst layer (orange) over Pd black (grey), which was electrodeposited to increase the reaction surface area.

5.2 Results

The catalyst-coated membranes in this study consisted of a 25- μm thick palladium foil with a high surface area electrodeposited palladium catalyst (Pd black) and a 10-nm secondary metal catalyst deposited on the surface exposed to the hydrogenation compartment (Figure A3.1a). The Pd black layer was prepared (before being inserted into the ePMR) by electrodeposition from a PdCl_2 solution in 1 M HCl to increase the active surface area of the catalysts (membrane geometric surface area = 1.22 cm^2 , Figure A3.1b).^{194–196} Each catalyst layer was then deposited on the Pd black by sputter deposition, where the layer thickness (~ 10 nm) was confirmed by in situ quartz crystal microbalance. Scanning electron microscopy (SEM) images of the catalyst surface before and after secondary metal deposition showed that the high-surface morphologies of the electrodeposited Pd black layers were retained during sputter deposition (Figure A3.1c–e). High-resolution SEM images — on a Au-coated membrane — and transmission electron microscopy (TEM) images — on a Au-coated TEM grid — were taken to further examine the morphology of the secondary catalysts. These images show a uniformly deposited nanocrystalline Au film with a grain size of ~ 100 nm (Figure A3.2). Cross-sectional SEM images of the Au-coated membrane with an energy-dispersive X-ray spectroscopy (EDX) spot analysis suggested the bulk of the Au atoms were deposited on the top surface of the Pd black layer (Figure A3.3). Electrochemical surface area (ECSA) measurements were also performed before and after all secondary metal depositions and showed minimal change in the surface area ($\Delta\text{ECSA} \sim 5\%$) after deposition (Figure A3.4).

We tested the reactivity of each secondary metal catalysts (Pt, Ir, Au) and the palladium membrane with no additional catalyst (Pd) in the 3-compartment cell consisting of: (i) an electrochemical compartment containing a platinum mesh anode (where water oxidation occurs);

(ii) an electrochemical compartment containing both a Ag/AgCl reference electrode and a palladium cathode (where proton reduction and hydrogen absorption occurs); (iii) a chemical compartment (where the hydrogen that diffuses through the membrane reacts with an organic substrate) (Figure 5.2). The anode and cathode were separated by a Nafion membrane and each electrochemical compartment was filled with 35 mL of 1 M H₂SO₄ electrolyte. The palladium membrane used to separate the electrochemical and chemical compartments was positioned with the secondary metal facing the chemical compartment (Figure 5.2). For each hydrogenation reaction, 30 mL of 0.1 M reactant solution in either ethanol or toluene was added to the chemical compartment and a constant current of 200 mA was applied to drive water electrolysis and the subsequent hydrogenation reaction.

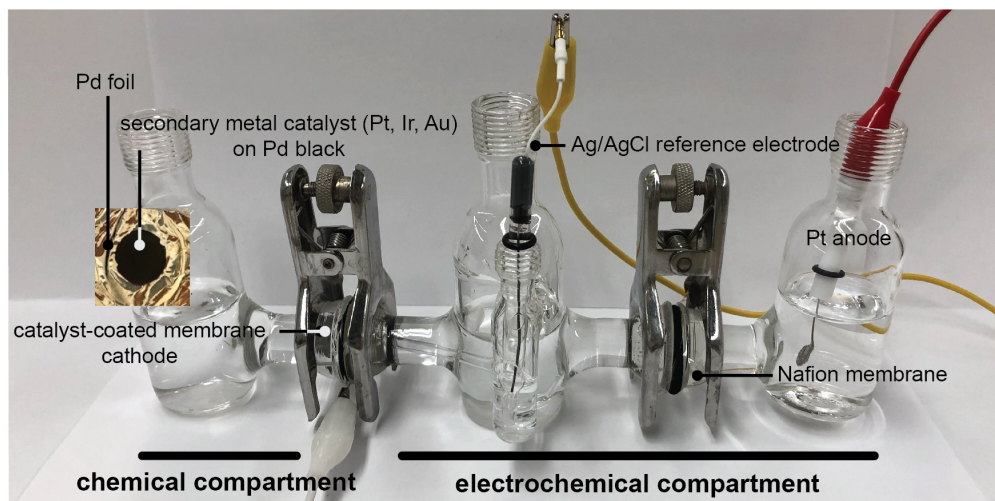


Figure 5.2 Photograph of the electrocatalytic Pd membrane reactor (ePMR) with a catalyst-coated membrane serving as proton reduction cathode, hydrogen-permeable membrane, and hydrogenation catalyst. The 3-compartment cell contains a divided electrochemical compartment filled with 1 M H₂SO₄ and one chemical compartment filled with organic solvent. The terminal electrochemical compartment contains a platinum mesh anode (where water oxidation occurs) and the middle electrochemical compartment contains a Ag/AgCl reference electrode, and the palladium cathode where protons are reduced then absorbed. The anode and

cathode are separated by a Nafion membrane. Secondary metal catalysts are coated on the face of the membrane exposed to the chemical compartment.

The first set of hydrogenation experiments reacted acetophenone with H permeating through the catalyst-coated palladium membrane. These experiments were designed to measure the reactivity of each secondary metal catalyst (Pt, Ir Au) and Pd towards C=O. For each experiment, a 0.1 M solution of acetophenone was dissolved in toluene. The reactor was run at a current density of 200 mA and the initial rate of acetophenone conversion for each metal catalyst was measured. The data in Figure 5.3a shows that secondary metal catalysts facilitate 10–20× faster initial acetophenone hydrogenation rates than the Pd foil (see also Table A3.1). The Pt catalyst exhibited the fastest hydrogenation rate (0.17 mmol h⁻¹) followed by Au (0.13 mmol h⁻¹), Ir (0.04 mmol h⁻¹), and Pd (0.005 mmol h⁻¹). The rate trend for the fastest and slowest acetophenone hydrogenation catalysts — Pt and Pd, respectively — are consistent with previously reported rates on supported metal catalysts.^{194,195} However, we observed an unexpectedly high rate of hydrogenation when using the Au catalyst (discussed below). We were unable to find comparable acetophenone hydrogenation rates for Ir in the literature.

The effect of solvent on hydrogenation activity was also tested by conducting acetophenone hydrogenation experiments in ethanol instead of toluene (Figure A3.5). The initial reaction rates in ethanol were 10-fold faster than those in toluene (Table A3.1). This trend is in agreement with previous studies of acetophenone hydrogenation on supported metal catalysts demonstrating up to a 10-fold increase in initial reaction rates in ethanol relative to cyclohexane.^{195–197} We note that the reactivity trend (Pt > Au > Ir > Pd) was not influenced by solvent choice.

We then compared the reactivity of each secondary metal catalyst (Pt, Ir, Au) and Pd towards C=C bonds by hydrogenating styrene (Figure 5.3b). Styrene was selected for comparison because the structure is similar to acetophenone, with each molecule consisting of an unsaturated functional group conjugated to an aromatic ring. The hydrogenation experiments conducted on 0.1 M styrene in toluene showed that Pd yielded 5–20% higher initial hydrogenation rates than any of the secondary metal catalysts (Table A3.1). The C=C hydrogenation reactivity followed a trend of Pd > Ir > Pt > Au, which tracks the general reactivity of supported metal catalysts (Pd > Ir \cong Pt > Au) toward styrene.^{198,199} These results highlight that reactivities of C=C and C=O bonds can be tailored by changing the secondary metal catalyst deposited on the membrane surface.

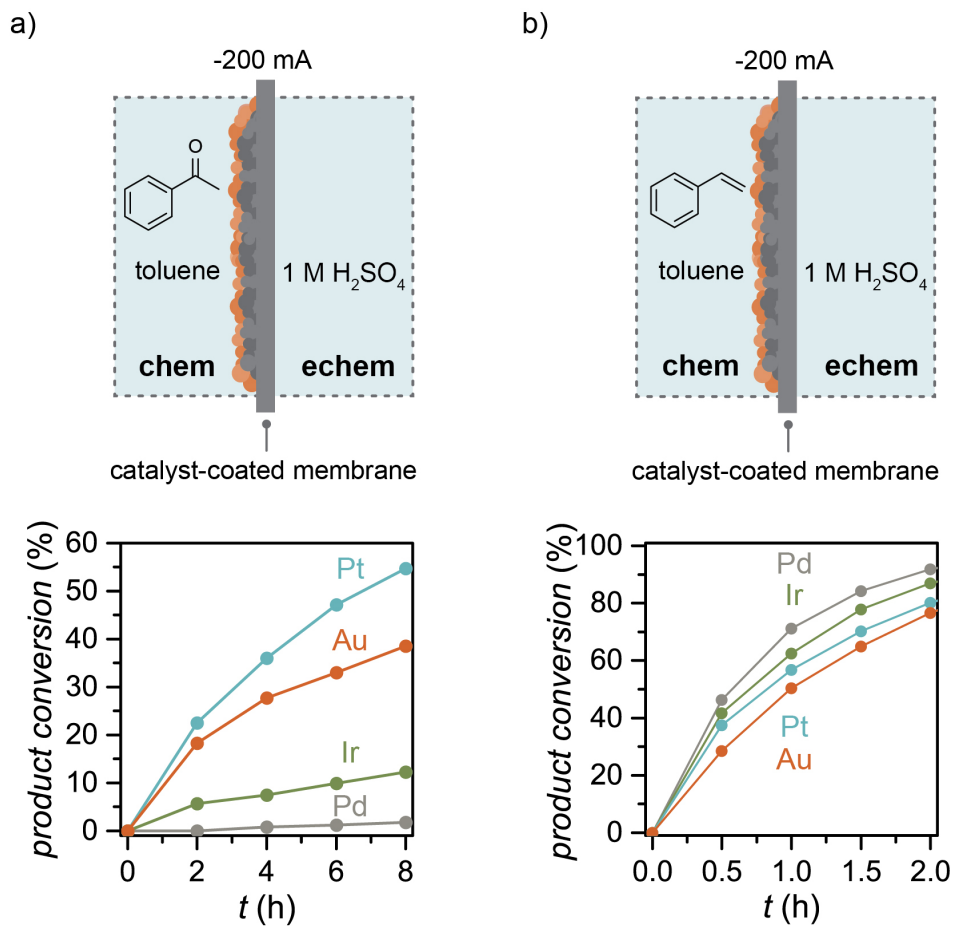


Figure 5.3 Hydrogenation performance of catalyst-coated membranes. Cell setup and product conversion for hydrogenation of (a) C=O bonds (acetophenone) and (b) C=C bonds (styrene) on catalyst-coated membrane (Pt, Ir, Au) and Pd catalysts at an applied current of 200 mA.

We next measured how the secondary metal catalyst influences the amount of hydrogen that permeates through the membrane (i.e., hydrogen flux) by using operando atmospheric mass spectrometry (atm-MS). The hydrogenation compartment was filled with toluene and the electrochemical compartment was filled with 1 M H₂SO₄ (Figure 5.4b). The hydrogen flux followed the trend of Au > Ir > Pt > Pd (Figure 5.4a). Similar experiments with ethanol in the

hydrogenation compartment did not significantly influence the amount of hydrogen that permeated through the membrane (Figure 5.4a). We therefore conclude that polarity of organic solvent has a negligible effect on hydrogen delivery to the hydrogenation compartment.

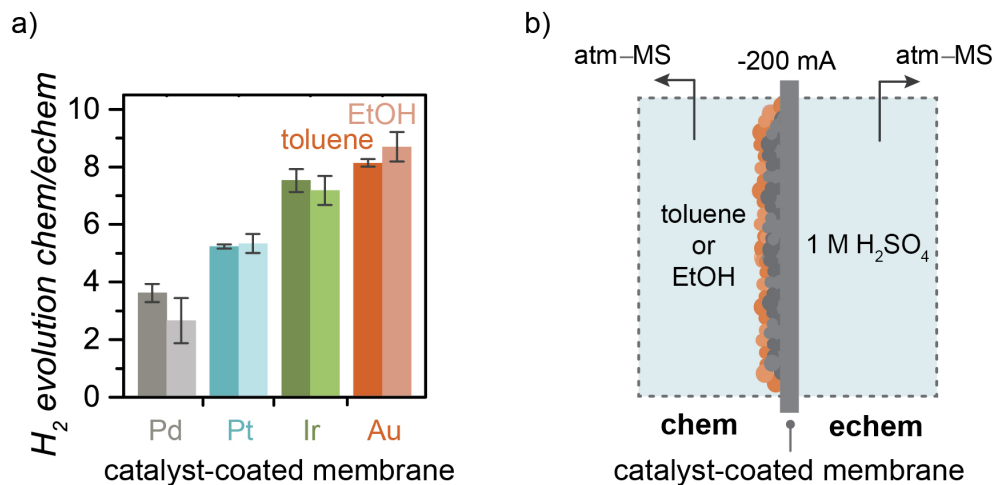


Figure 5.4 (a) Ratio of H₂ gas evolved on the chemical/electrochemical side of the Pd membrane with different secondary metal catalysts in toluene (dark color) and ethanol (light color). (b) Cell setup used to determine hydrogen flux through catalyst-coated membranes.

Hydrogen desorption kinetics were measured using an ex-situ temperature-programmed desorption (TPD) instrument developed by our group²⁰⁰ to investigate the relationship between metal-hydrogen binding energy and hydrogen flux. TPD samples were prepared by electrochemically loading hydrogen into the catalyst-coated membrane in 0.1 M HCl at a potential of -0.4 V (vs. Ag/AgCl) until a total charge of 10 C was passed. HCl was chosen over H₂SO₄ because SO₄²⁻ has been demonstrated to strongly adsorb on palladium and slow H desorption kinetics.²⁰⁰ This electrochemical protocol was designed to saturate the sample with absorbed hydrogen (H_{abs}). The samples were immediately quenched in liquid nitrogen for 30 s after loading

to suppress immediate desorption of H_{abs} before transfer into the TPD chamber. Hydrogen desorption was then monitored by the atm-MS while the temperature was increased at a rate of 10 K min^{-1} (Figure 5.5). The hydrogen desorption temperature (T_{desorb}), defined as the temperature of the desorption peak maximum (Figure 5.5). The observed trend ($\text{Pd} > \text{Pt} > \text{Ir} > \text{Au}$), tracks the metal-hydrogen binding energy^{202,203} as discussed in depth below.

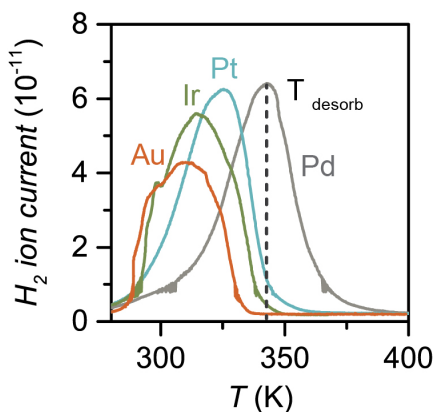


Figure 5.5 Temperature programmed desorption spectra of H_2 ($m/z = 2$) from catalyst-coated membranes. Each sample was loaded with hydrogen in 0.1 M HCl at a reductive potential of -0.4 V (vs. Ag/AgCl) until a total charge of 10 C was passed.

5.3 Discussion

In this study, we used the ePMR to resolve how three different secondary metal catalysts (Pt, Ir, and Au) affect hydrogenation chemistry when the need to generate H atoms is imparted on a different surface. We found that the secondary metal catalysts influenced the reactivity towards the C=O and C=C bonds of acetophenone and styrene, respectively. The hydrogenation of C=O followed the trend $\text{Pt} > \text{Au} > \text{Ir} > \text{Pd}$, whereas reactivity for C=C bonds followed a pattern of $\text{Pd} > \text{Ir} > \text{Pt} > \text{Au}$ (Figure 5.3). These reactivity trends are consistent with established volcano plots relating hydrogenation reactivity to metal-substrate adsorption energies, which predict that Pt and

Pd are most reactive towards C=O and C=C bonds, respectively.^{201,202} This correlation to established reactivity trends supports our assertion that hydrogenation is occurring at the secondary metal surface and not the underlying palladium.

One unexpected result was the high rate of C=O hydrogenation mediated by the Au catalyst. While Au is effective at absorbing carbonyls,^{203,204} bulk Au is considered to be a poor hydrogenation catalyst because Au is a poor H₂ activation and HER catalyst.^{191–193} In the ePMR, Au is effective at mediating hydrogenation in the chemical compartment because proton reduction occurs in the electrochemical compartment and not at the Au surface. Our results highlight that Au is an effective hydrogenation catalyst when it is tasked to mediate the hydrogenation step only.

The rate at which C=O bonds were hydrogenated in ethanol — a polar, protic solvent — were faster than those performed in non-polar toluene (Figure A3.6). It is reasonable to assume that protic polar solvents increase the hydrogenation rates of polar bonds ($\delta^+C=O\delta^-$) through hydrogen bonding between the substrate and solvent.^{196,205} Polarity of organic solvent in the chemical compartment did not affect hydrogen flux: a similar amount of reactive hydrogen was delivered to the reaction surface regardless of the organic media used (Figure 5.3a). The fact that solvent does not affect H atom delivery stands in stark contrast to H₂ gas-fed hydrogenation, where the solvent governs H₂ solubility²⁰⁶ and, in turn, the amount of hydrogen that can be delivered to the reaction surface (e.g., H₂ is generally more soluble in non-polar solvents than protic polar solvents).^{206,207} The ePMR architecture enables protic polar solvent to be used as a hydrogenation medium without adversely affecting generation and delivery of H atoms.

The rate at which hydrogen permeates through the membrane was higher when a secondary metal catalyst was deposited on the Pd membrane. This observation was confirmed by hydrogen desorption temperature (T_{desorp}) measurements recorded ex situ by TPD. The desorption

temperature trend of Pd > Pt > Ir > Au (Figure 5.5) tracks the hydrogen adsorption energy (ΔG_{H^*}) for the pure metal surface²⁰⁷ (i.e., M–H binding energy; Figure A3.7a). The metals characterized by weaker binding energies lead to faster desorption rates. In situ measurements of hydrogen flux through the membrane (Figure 5.6a) mirror these findings: a weak M–H binding energy (where M = secondary metal catalyst) leads to a higher hydrogen flux into the chemical compartment of the ePMR (Figure 5.6b). The striking influence of secondary metal catalysts on hydrogen flux supports our assertion that the hydrogen desorbs from the secondary metal surface and not the underlying palladium. We note that there is a possibility that hydrogen is desorbing from the interface of the Pd|secondary metal. However, we contend that this possibility is unlikely given the clear relationship between the hydrogen desorption temperature and the metal-hydrogen binding energy of the secondary metals.

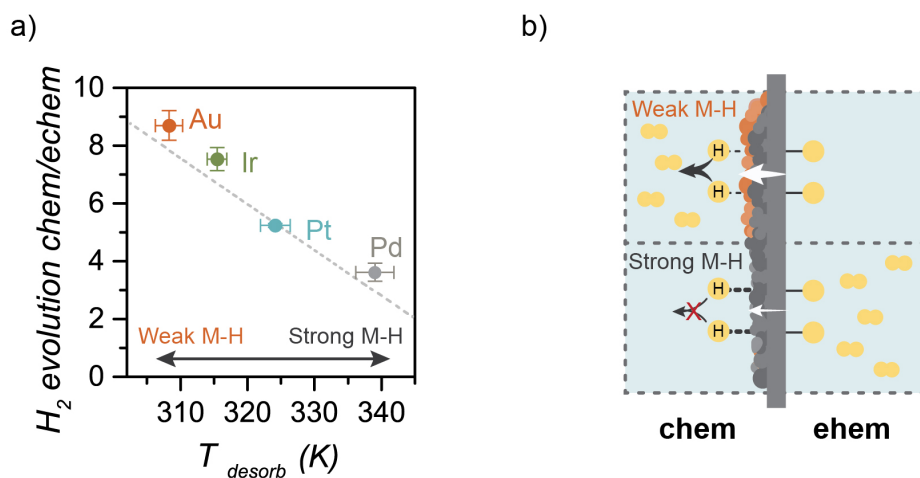


Figure 5.6 (a) Ratio of H₂ gas evolved on the chemical/electrochemical side of the catalyst-coated membrane as a function of their hydrogen desorption temperature determined by TPD. **(b)** Schematic representation illustrating the influence of M–H binding strength on hydrogen flux. Weak M–H binding strength leads to higher hydrogen flux, whereas strong M–H binding strength results in lower hydrogen flux.

These hydrogen flux measurements also point to the secondary catalysts changing the rate-limiting step of hydrogen permeation. In the absence of the secondary catalyst, the rate-limiting step for a 25 μm -thick Pd membrane is expected to be the desorption of adsorbed H atoms from the membrane surface.²⁰⁸ We observed that catalysts with weaker M–H binding yielded a higher hydrogen flux through the membrane, which is consistent with the desorption step being accelerated by the catalyst (Figure 5.7a, b). We conducted experiments to confirm that hydrogen flux increases with decreasing M–H binding energy. The changes in hydrogen flux were not as significant for metals with weak M–H binding energies (e.g., Ir and Au), which signals that the rate of permeation is less dependent on M–H binding energy. We therefore conjecture that the secondary metal catalyst can decrease the activation barrier for desorption ($E_{a\text{desorption}}$) to sufficiently large extent that hydrogen permeation becomes diffusion limiting (Figure 5.7c).

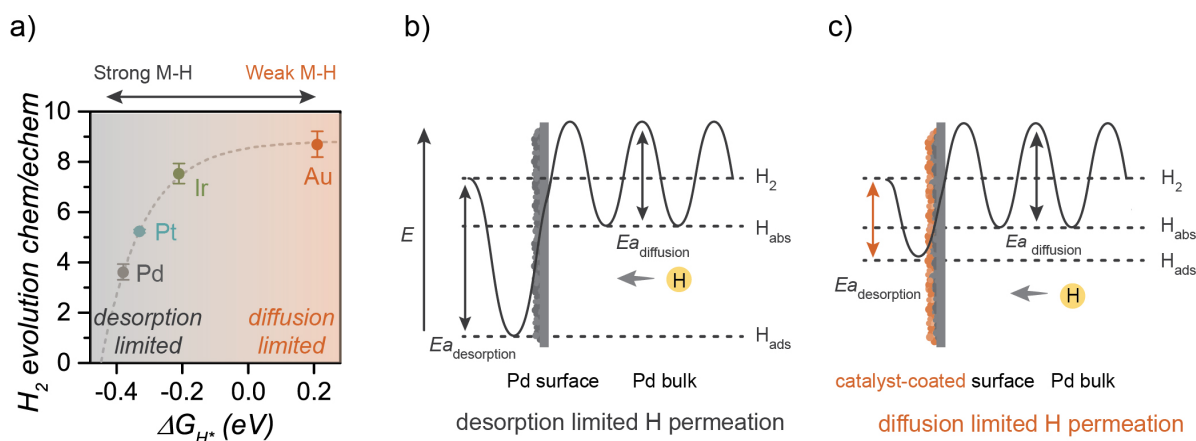


Figure 5.7 (a) Ratio of H_2 gas evolved on the chemical/electrochemical side of the catalyst-coated membrane as a function of hydrogen adsorption energy for the pure metal surface (ΔG_{H^*})²⁰⁹. Potential energy diagram for hydrogen permeation (diffusion then desorption) of absorbed hydrogen in the catalyst-coated membrane when the process is (b) desorption limited and (c) diffusion limited.

5.4 Conclusion

The physical separation of hydrogenation from proton reduction in an ePMR enables the independent manipulation of hydrogenation reactivity C=O and C=C bonds without adversely affecting the production and delivery of H atoms to the hydrogenation site. By coating a palladium membrane with a series of secondary metal hydrogenation catalysts, we were able to resolve the hydrogenation activities of each catalyst towards acetophenone and styrene model reactants. The acceleration of the hydrogenation reaction by these secondary catalysts also increased the amount of hydrogen permeating through the membrane from the electrochemical compartment. These permeation rates were found to correlate with the M–H binding energy of the coated catalysts.

While Au is not an effective hydrogenation catalyst in conventional thermochemical or electrochemical hydrogenation reactors, Au was found to be effective at hydrogenation in an ePMR where it does not also have to perform H₂ activation or proton reduction. Another distinguishing feature of the ePMR is that reaction rates of C=O bonds were higher in polar protic solvents but hydrogen flux was unaffected. In thermochemical hydrogenation reactor, which uses H_{2(g)}, the reaction chemistry is influenced by H₂ solubility. These observations highlight the opportunity to access unique reaction chemistries enabled by the ePMR that physically separates proton reduction and substrate hydrogenation.

5.5 Experimental methods

5.5.1 Materials and instrumentation

Pd (99.95%) was obtained from Silver Gold Bull as a 1 oz wafer bar. Potassium hexafluorophosphate ($\geq 99\%$, recrystallized), potassium chloride, dichloromethane-*d*₂ (99.5 atom %D), acetophenone (99%), styrene ($\geq 99\%$), toluene, ethanol, sulfuric acid (95.0-98.0%), H₂O₂

solution (30 wt. % in H₂O) and dimethylsulfone (quantitative NMR standard, TraceCERT) were purchased from Sigma Aldrich and used as received. Nitric acid (68-70%) was purchased from VWR. Pt gauze (52 mesh, 99.9%) and Pt wire (0.5 mm, 99.95%) were obtained from Alfa Aesar. Ag/AgCl reference electrodes (RE5B) were purchased from BASi. Nafion 117 membranes were purchased from Fuel Cell Store. Viton foam gasket material (1/8" thick) was purchased from McMaster Carr.

5.5.2 Pd foil and Pd-black catalyst preparation

Pd foils were rolled from a 1 oz palladium wafer bar to a thickness of 25 μm . The thickness of the foil was measured by a Mitutoyo digital micrometer to an accuracy of $\pm 1 \mu\text{m}$. The freshly-rolled foil was annealed in Ar at 850 °C for 1.5 hours and stored in air. Prior to a hydrogenation experiment, the annealed foils were cleaned by soaking the foil in a 0.5:0.5:1 (by volume) conc. HNO₃:H₂O:30% H₂O₂ for ~20 minutes. The foil was removed from the cleaning solution, rinsed with ultrapure water then the Pd-black catalyst was immediately electrodeposited onto the surface. The cell was assembled as described above, however, the cathode compartment was filled with an electrodeposition solution (15.9 mM PdCl₂ in 1 M HCl) in lieu of the 1 M HCl electrolyte. A voltage of -0.3 V vs. Ag/AgCl was applied to the Pd foil working electrode to reduce the Pd ions in solution. The electrodeposition was stopped when 9 C of charge (7.38 C/cm²) had been passed, which corresponds to a catalyst loading of ~5 mg. This additional catalyst layer increases the surface area of the chemical side of the palladium foil up to 250-fold that increases the hydrogenation rate.¹ The same Pd-black catalysts were used up to 2 hydrogenation cycles. Immediately following electrodeposition, the foils were thoroughly rinsed with MilliQ water, covered in a 4" diameter petri dish to maintain cleanliness, and stored in ambient conditions.

5.5.3 Catalyst-coated membrane preparation

The catalyst-coated membranes were prepared by sputter deposition. The electrodeposited palladium foils were secured against the deposition plate of a Leica EM MED020 coating system using Kapton tape, the chamber was sealed, and a vacuum applied to achieve a base pressure of 2×10^{-5} mbar (which required ~ 20 minutes). After the base pressure was reached, argon was continuously flowed into the chamber to maintain a pressure of 1×10^{-2} mbar, the plasma was ignited, and voltage was adjusted to maintain a constant sputter current of 70 mA for iridium, and 30 mA for gold and platinum. Following a 30 s presputter, the target shutter was opened and 10 nm of a secondary metal catalyst (Au, Ir or Pt) was sputtered onto the electrodeposited palladium catalyst. The sputtering rate for every metal was 0.2 nm/s, as determined by in situ quartz crystal microbalance. Following deposition, the shutter was closed, chamber vented, and foil removed from the deposition plate. The foils were used for hydrogenation experiments without any further processing. The catalyst-coated membranes were used for up to 2 hydrogenation reactions. The secondary catalysts were removed with concentrated nitric acid then the foil was cleaned (described above), replated, and reused. Each palladium foil was used for ~ 5 cleaning cycles. The complete catalyst fabrication scheme is shown in appendix 3 (Figure A3.1a)

5.5.4 Electrochemistry

A Metrohm Autolab PGSTAT302N/PGSTAT204M potentiostat was used for electrochemical experiments. To set up the electrocatalytic palladium membrane reactor, a palladium foil was fitted between the chemical and cathode electrochemical compartment of the cell. A Nafion membrane was positioned between the two electrochemical compartments. Viton foam gaskets were used to seal both the palladium foil and the Nafion membrane in place and prevent leaking. The chemical compartment was filled with 30 mL of reactant solution (e.g., 0.1

M acetophenone or styrene in toluene or ethanol for hydrogenation experiments and permeation experiments.) The two electrochemical compartments were filled with 35 mL of 1 M H₂SO₄. A Ag/AgCl reference electrode (3.0 M NaCl) and a Pt mesh counter electrode were inserted into the cathode and anode electrochemical compartments, respectively. Electrolysis was conducted galvanostatically at -200 mA ($V_{\text{avg}} = -1.1$ V vs. Ag/AgCl). The uncompensated resistance was 3-5 Ω for all experiments, and no IR correction was used. The thickness of the foil was 25 μm and the geometric surface area of the foil was 1.22 cm².

5.5.5 Hydrogenation of acetophenone and styrene in a palladium membrane reactor

Acetophenone hydrogenation was performed using either toluene or ethanol as the solvent. Styrene hydrogenation was performed using toluene. All reactions were carried out in air at room temperature. An oven-dried chemical compartment with a magnetic stir bar was filled with a substrate (3 mmol of acetophenone or styrene) and solvent (toluene or ethanol, 30 mL). 1 M H₂SO₄ electrolyte solution (35 mL) was added to each electrochemical compartment and a constant current of 200 mA was applied for 8 h. Both the reaction mixture and electrolyte solution were stirred at a constant rate (400 rpm) throughout the experiment. Reaction aliquots were sampled every 2 h to monitor the reaction progression of acetophenone hydrogenation by ¹H NMR spectroscopy or every 0.5 h to monitor the hydrogenation of styrene by GC-MS. The initial rate of acetophenone conversion for each metal catalyst was determined by the slope of the first 2 h of acetophenone consumption (mmol h⁻¹) and the first 0.5 h of styrene consumption (mmol h⁻¹).

5.5.6 Product quantification

Proton nuclear magnetic resonance (¹H NMR) was used for product quantification for acetophenone hydrogenation. 500 μL of the reaction mixture (0.1 M) and 250 μL 0.2 M dimethylsulfone internal standard in CD₂Cl₂ were added to an NMR tube. ¹H NMR spectra were

acquired on a Bruker Avance 400dir, 400inv, or 400sp spectrometer at 298 K. Relative concentrations were determined by comparing an aromatic peak corresponding to 2 protons for acetophenone, an CH_3 peak corresponding to 3 protons for 1-phenylethanol. In each case the internal standard was integrated to 6. Gas chromatography–mass spectrometry (GC–MS) were used for product quantification for styrene hydrogenation. GC–MS experiments were conducted on an Agilent GC–MS using an HP-5ms column and electron ionization. The samples were run using an auto-sampler with a 1 μL injection volume and a split ratio of 20:1. The oven temperature was static at 50°C for 1 min, ramped to 65°C at 3 °C min⁻¹ then to 200°C at 100°C. A solvent delay of 4.6 min was employed. Peaks for styrene and ethylbenzene were identified by searching the NIST database for matching mass spectra. Relative concentration was determined using peak integration of the two peaks. Calibration curves were collected for styrene and ethylbenzene, and the instrument response for each species was found to be identical within acceptable error (+1 σ) of three repeats of each calibration curve. Therefore, no calibration factor was applied.

5.5.7 Hydrogen permeation

Hydrogen permeation experiments were conducted with 1 M sulfuric acid (H_2SO_4) in each electrochemical compartment and toluene or ethanol (EtOH) in the chemical compartment. The palladium foil was placed between the electrochemical and chemical compartments with the secondary metal catalyst surface facing into the chemical compartment (as per the usual setup for hydrogenation experiments). The production of gaseous H_2 (2 m/z) in the chemical and electrochemical compartment with constant stirring was monitored by atmospheric mass spectrometry (atm MS) with a flow rate of 10 mL/min into the instrument. Detection was switched between the chemical and electrochemical compartment every 5 s with a 3 s purge. Permeation experiments were repeated at least 3 times using a different foil for each experiment. The ion

current value was taken once the signal had equilibrated and was used to determine the ratio of chemical/electrochemical H₂ evolution. The average value for at least 3 experiments is reported, with error bars representing one standard deviation of the mean.

5.5.8 Temperature Programmed Desorption (TPD)

The atm MS used for hydrogen permeation experiments was also used as the detector for TPD measurements. The inlet to the mass spectrometer was connected through a leak valve to the TPD sample chamber designed by our group (M. Moreno, manuscript in preparation) and the TPD profile was measured while passing a constant Ar flow (15 mL min⁻¹) through the sample chamber. The experiment was carried out at atmospheric pressure and the sample was heated at a rate of 10 K min⁻¹. Mass analysis was performed every 50 ms for the following mass/charge fragments: 2 (H₂), 32 (O₂), 18 (H₂O), Ar (40) and 44 (CO₂). Prior to the TPD measurements, the palladium samples were loaded with hydrogen electrochemically in a standard H-cell, 3-electrode setup by applying -0.4 V (vs Ag/AgCl) to the Pd foil immersed in 0.1 M HCl until a total charge of 10 C was passed. The samples were dried in air and immediately transferred to the liquid N₂ for 30 seconds before being transferred to the TPD chamber, then the linear temperature ramp was started. The TPD chamber was stored in dry ice before the sample was transferred.

5.5.9 Hydrogenation of acetophenone with 1 atm H₂ gas

Gas-phase acetophenone hydrogenation was performed using toluene with 1 atm H₂. An oven-dried chemical compartment with a magnetic stir bar was filled with toluene (30 mL) and the electrochemical compartment was kept empty. The chemical compartment was sealed with a rubber septum and the toluene was purged with H₂ gas for 30 min. Acetophenone (3 mmol) was then added using a syringe. A constant flow of H₂ gas was kept for 2h then the venting needle was replaced with a 1 L H₂ balloon.

The H₂ gas-fed hydrogenation control experiment was performed to show that delivering electrochemically-produced hydrogen through a catalyst-coated membrane results in faster hydrogenation than that can be achieved by directly delivering H₂ gas to the hydrogenation surface of the catalyst. The chemical compartment containing 0.1 M acetophenone in toluene was placed under 1 atm of H₂ gas without applying any electrochemical bias (Figure A3.8a). The acetophenone conversion was found to be negligible (<2% for all catalysts) after 8 h of reaction (Figure A3.8b). This control experiment highlights that ePMRs enable substantially higher reactivity than can otherwise be achieved at ambient pressure.

5.5.10 Scanning electron microscope (SEM and transmission electron microscopy (TEM))

Scanning Electron Microscope (SEM) and energy-dispersive X-ray spectroscopy (EDX) experiments were performed using a Helios NanoLab 650 Focused Ion Beam SEM. Cross-sections were milled using a focused ion beam with a gallium ion source and imaged at an angle of 52 degrees. EDX data was acquired from 1 μm^2 regions over 50 s on cross-sections at 10 kV accelerating voltage and 1.6 nA. Transmission electron microscope (TEM) images were obtained using a Hitachi H7600 TEM operating at 80 kV. Samples were prepared by sputtering 10 nm Au on a 400 mesh formvar carbon-film-coated Cu grid (Ted Pella, Inc) using the same deposition process as the membranes. The TEM image of the Au deposited on the TEM grid suggests that the 10 nm thick secondary metal forms a continuous nanocrystalline film. However, we note that the deposition on a TEM grid is not necessarily identical to deposition directly on the Pd black layer.

5.5.11 Electrochemical surface area (ECSA) determination

ECSA measurements were performed in CH₃CN with 0.15 M KPF₆ following a methodology reported by Surendranath.²⁰⁹ A value of $11 \pm 5 \text{ uF cm}^{-2}$ was assumed as the areal capacitance (C_s) for all membranes under study. A series of small (50 mV) window cyclic

voltammograms were recorded, with the start and end of each sweep centered on the open-circuit potential (OCP). The difference in the anodic and cathodic current ($i_a - i_c$) at the OCP was plotted as a function of the scan rate (sr), and the slope of the linear fit of $i_a - i_c$ vs. sr is equal to twice the double-layer capacitance (C_{dl}). C_{dl} was subsequently divided by C_s to obtain the ECSA. All ECSA measurements were performed using a leak-free Ag/AgCl reference electrode using a leakless junction (eDAQ ET072). The electrode was rinsed with Milli-Q water prior to use and referenced vs. a 4.0 M KCl glass-body Ag/AgCl master reference electrode (Fisher Scientific 13-620-53) by measuring the open-circuit potential between both electrodes in a saturated KCl solution. The master electrode was stored in a saturated KCl solution when not in use.

Chapter 6: Conclusions and Future Work

6.1 Conclusions

The ePMR can reduce carbon emissions from industrial hydrogenation reactions. This electrochemical reactor eliminates the requirements for fossil-derived heat and H₂ formed from natural gas, two prominent sources of CO₂ from hydrogenation. In the ePMR, hydrogen is produced from water electrolysis in aqueous electrolyte and hydrogenation proceeds in a completely separate chamber, in organic solvent. This architecture circumvents the need to separate the organic product from the electrolyte by leveraging the unusual hydrogen-selective permeation properties of Pd.²¹⁰ This membrane reactor architecture solves problems that have plagued conventional electrosynthesis setups, specifically the isolation of product from electrolyte, high cell voltages and low current densities.

The present capabilities of the ePMR enable a host of C≡C, C=C and some C=O and C=N unsaturations to be hydrogenated (or deuterated), in ambient conditions using only electrons and (heavy) water as reagents. However, to compete with mature thermochemical methods, ePMRs must: i) enable high rates of product formation; ii) operate at excellent energy efficiencies, and; iii) produce a broad scope of products. This thesis presents advances towards these goals by improving understanding of the palladium-hydrogen system during reductive electrolysis (Chapter 3), and providing reactor (Chapter 4) and catalyst design strategies (Chapter 5) to increase reaction rates, efficiencies, and expand the diversity of functional groups that can be hydrogenated in this reactor.

Chapter 3 showcased how mechanically-applied strain can be used to access strained states that would otherwise be challenging to access through materials fabrication alone. This study provided the first empirical measurements of tensile strain effects on hydrogen evolution

reactivity, and the amount of hydrogen that absorbs into a palladium electrode. I used X-ray diffraction to measure the changes in lattice macrostrain as a function applied strain to show that mechanically stretching an electrode increases the average spacing between the palladium atoms. This increase in lattice spacing in turn increased hydrogen evolution reaction rates, and decreased the amount of hydrogen that absorbed into the palladium lattice.

Chapter 4 focused on efficient electrochemical hydrogenation in an ePMR, enabled by improvements to reactor design. I built the first ePMR flow cell, an approach that was inspired by commercialized electrochemical cells, including hydrogen fuel cells and water electrolyzers. The ePMR flow reactor drives electrolysis up to 15-fold faster by using a flow field plate to deliver the alkyne feedstock to the palladium surface. This reactor also served as a platform to measure how the hydrogen content in the palladium membrane influences the rate, selectivity and efficiency of the reaction.

Chapter 5 provided a strategy for enabling new chemistries in an ePMR through catalyst design. In this work, Dr. Kurimoto and I incorporated secondary catalysts at the hydrogenation surface of the membrane and measured how hydrogenation reactivity for carbonyl bonds was affected. The catalysts increased reactivity for C=O bonds, but did not impede hydrogen delivery through the membrane. The solvent used at the hydrogenation surface of the membrane was also found to impact hydrogenation rates, with a polar protic solvent increasing carbonyl hydrogenation rates through hydrogen-bonding stabilization of the transition state. This work sets a precedent for using non-palladium materials as the hydrogenation catalyst in an ePMR.

6.2 Future work: Advancing the ePMR towards applications in chemical synthesis

Historically, electrochemical cells are deployed in industry when they are more cost effective to operate or enable new chemistries that are otherwise impossible using conventional

methods.^{210,211} With modest advances, an ePMR can meet these criteria. Attributes such as ease of product separation, low temperature operation, and hydride-free hydrogenation provide opportunities for ePMRs to compete with established hydrogenation methods. In this section I highlight a few of these potential applications.

Chemical waste can be converted into useful products through hydrogenation. This application is an appealing, but underexplored, use of the ePMR. Gaseous CO₂ can be hydrogenated in this reactor to formic acid, a commodity chemical and prospective fuel,²¹¹ under ambient conditions with up to 85% current efficiency (at 10 mA/cm²).^{12,189,213} The separation of electrochemistry from hydrogenation is particularly advantageous for this process because no electrolyte is required to mediate the reaction. This attribute dramatically simplifies the reaction interface, which typically requires careful consideration of water and ion management. The highly selective palladium membrane additionally prevents crossover of the CO₂ reactant and liquids, circumventing these known issues with ion membranes typically used in CO₂ electrolyzers.^{212,213}

Another opportunity for the ePMR is converting oxygen-containing biomass to hydrocarbon fuels and chemicals through hydrodeoxygenation (HDO). Our group has shown that HDO of benzaldehyde (a lignocellulosic biomass model compound) can proceed with up to 90% selectivity in ambient conditions in an ePMR. This transformation was mediated by a palladium nanocube catalyst immobilized on the palladium membrane. This concept could conceivably be used to transform waste products (e.g., furfural, lignin, or vegetable fats) into renewable plastic precursors, solvents, fuels and specialty chemicals.^{12,190,214} The key advantage of separating the electrolysis from hydrogenation here is that the organic feedstocks can be solubilized in any organic solvent, or potentially reacted neat. Typical ECH systems are only capable of reacting dilute solutions of reactants dissolved in polar electrolyte.

The ePMR may also displace stoichiometric reducing agents in chemical synthesis. Low temperature hydrogenation methods, including transfer hydrogenation or chemical reduction with metal hydrides, are used for reducing C=O and C=N bonds.^{17,19,21} These reagents are often used when working with a feedstock that is sensitive to the high temperatures required for thermochemical hydrogenation. However, both transfer hydrogenation and hydride reagents generate stoichiometric amounts of chemical waste as reaction byproducts. The ePMR can perform the same site-selective C-O and C-N hydrogenation (or deuteration) at ambient temperature,^{21,39} but without the associated chemical waste. In the context of hydrogenation, the reduction of these bonds without hydride reagents translates to improved safety by avoiding air-sensitive chemistries. These benefits are maintained for deuterating unsaturated bonds as well, but also correspond to a >20-fold per-atom D cost decrease.¹¹² These cost savings arise because the ePMR can derive D atoms from D₂O, rather than D₂ gas, or deuteride transfer reagents.

6.3 Research and development roadmap for the ePMR

To use the ePMR for diverse applications in chemical synthesis (including those described above), future development of the ePMR must focus on increasing the diversity of hydrogenatable substrates, decreasing catalytic membrane costs, and increasing energy efficiency (Figure 6.1). This section suggests strategies for moving this technology toward these goals.

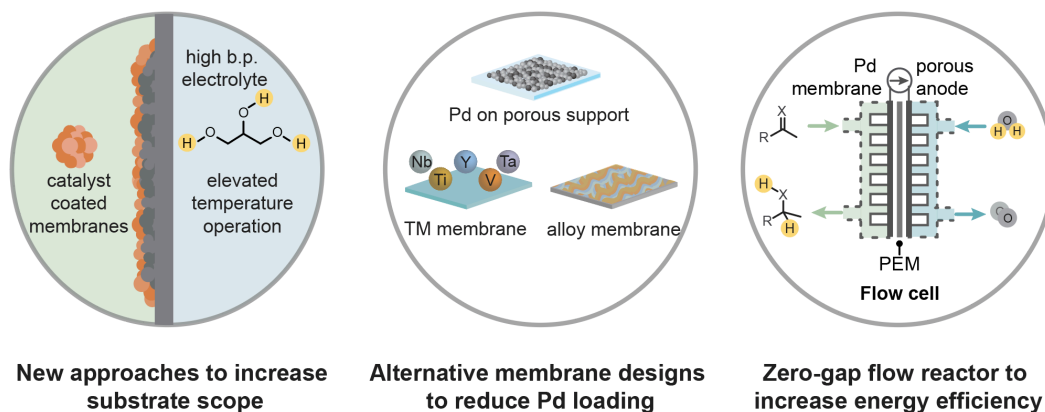


Figure 6.1 Summary of suggested future research directions for the ePMR.

6.3.1 Research direction 1: Increased substrate scope

New strategies to expand the scope of hydrogenatable substrates are required to enable a broad scope of applications for the ePMR. Studies to date show that many alkynes and alkenes can be readily hydrogenated (or deuterated) with excellent site selectivity.²² However, fewer examples of oxygen- and nitrogen- containing unsaturations are reported.²¹³ High current densities (>100 mA/cm²) are typically used to increase carbonyl hydrogenation rates.²¹⁴ But applying currents in excess of 250 mA/cm² increases undesired H₂(g) production dramatically.^{31,44} An alternative strategy is increasing the reaction temperature. The use of a high boiling hydrogen source (e.g., glycerol²¹⁵) and operating the reactor at elevated temperatures may enable hydrogenation of substrates with higher activation energy barriers. Elevated temperature operation has been successful for hydrogenating aromatic groups in the gas phase,²¹⁵ though this approach has yet to be demonstrated for any liquid-phase reagent.

A second approach to increasing substrate scope is incorporating secondary catalysts on the palladium membrane. Work by Yoshida *et al.* and Sato *et al.* with catalyst-coated membranes set a precedent for using non-palladium materials as the hydrogenation catalyst in an ePMR.²¹⁶

Our work (described in Chapter 5) demonstrates how sputtered catalysts can enable new reactivities in the ePMR. Future approaches could include commercial hydro(deoxy)genation catalysts (e.g., Pd/C, Pt/C, Ru/Al₂O₃ among others) onto the palladium membrane using spray coating, a catalyst layer fabrication method well established in CO₂ electrolysis literature.²¹⁶ A catalyst ink formulated by mixing the catalyst powder with a solvent and polymer binder, could be deposited onto the hydrogenation surface of the palladium membrane. This basic approach could be used to immobilize any catalyst powder on the membrane surface, though is just one of many commonly used catalyst deposition techniques (e.g., physical and chemical vapor deposition, or decal transfer) that could be applied in this application.

6.3.2 Research direction 2: Palladium-free membranes

An ideal membrane for use in the ePMR must drive efficient HER, absorb and permeate large amounts of monoatomic H, and efficiently mediate a hydrogenation reaction. Other criteria include high durability so that gas evolution does not damage the layer, sufficient rigidity to enable multiple reuses, and low cost. There is yet to be reported a single membrane that satisfies all of these criteria. One path forward is to develop supported Pd-membranes, or developing Pd-free membranes based on hydrogen permeable alloys (as discussed in Chapter 2; section 2.5.1). In addition to these to designs of supported membrane architectures, other materials that permeate hydrogen may be applied in this application.

Metal oxide membranes (WO_x) have been used to conduct protons and electrons to transport hydrogen into an electrochemical cell (i.e., the opposite direction that hydrogen is transported in an PMR). In this study by Yan *et al.*, H₂(g) was first activated on small Pt nanoparticles on one side of the WO_x membrane, then transferred into the WO_x membrane through a process called hydrogen spillover.²¹⁷ Hydrogen oxidation subsequently occurred on the opposite

electrochemical side of the membrane.²¹⁷ These same membranes could be conceivably used in hydrogenation reactions by driving hydrogen through the membrane opposite way (i.e., out of the electrochemical compartment, and into a hydrogenation compartment). The bulk of the membrane could be comprised of WO_x , with a Pd or Pt thin films on either side to mediate the hydrogen evolution, and hydrogenation reactions, respectively. Recently, TiN_x semiconductors have also demonstrated gas-phase hydrogen absorption.^{107,218} A supported architecture with thin (electro)catalysts deposited on each side of the TiN_x membrane could potentially be used as a catalytic membrane in an ePMR similarly to the WO_x membranes described above.

6.3.3 Research direction 3: Zero-gap reactor design

Electrode assemblies used commonly in water and CO_2 electrolyzers may be adapted to increase the energy efficiency, and current density of ePMRs. These electrolyzers use a “zero-gap” membrane electrode assemblies (MEA), which place a high-surface area anode and cathode in contact with opposite sides of a thin (<125 μm -thick) polymer electrolyte.^{41,48} This design enables high rates of product formation at low cell voltages (e.g., water electrolyzers can operate at currents $\geq 1 \text{ A/cm}^2$ at $\leq 2 \text{ V}$).²¹⁹ Two studies reported specially-designed MEAs for use in an ePMR H-cell.²¹⁸ Palladium, platinum or gold catalysts chemically deposited on either side of a Nafion proton exchange membrane enabled styrene hydrogenation in an organic solvent.²¹⁹ However, the cell operated at high voltages (4-8 V) and low current densities (1-10 mA/cm^2). Operating these MEAs in a flow cell, and increasing the surface area of the metal|polymer interface may be routes to mitigating these issues.

6.4 Outlook: How ePMRs can contribute to a future of carbon-neutral chemical manufacturing

Global carbon emissions can be reduced by at least 5% by using renewable electricity to power chemical manufacturing.²¹⁹ The impact of offsetting these emissions is significant – equivalent to eliminating all CO₂ emitted by Germany and Japan combined.²²⁰ However, there are a number of challenges to realizing a future of carbon-neutral chemical manufacturing. The first challenge is that the infrastructure to efficiently process, separate, and transport chemicals manufactured at large, centralized facilities has been well established for nearly a century. A second challenge is that the thermally-derived heat used to drive these processes is ~10-fold cheaper less costly than renewable electricity.¹⁶⁸ Industry-specific low carbon legislation (e.g., the Canadian clean fuel standard²²¹ for the energy industry) and carbon taxes will facilitate the transition to sustainable alternatives. However, widespread adoption of low carbon innovations requires that these alternatives be cost-competitive with incumbents, and also address fundamental pains of using thermochemistry. A compelling alternative technology must offer lower operational costs and also add value through time savings, fewer pre- and post- processing steps, or increased safety.

The ePMR is a platform technology that can meet the above criteria for hydrogenation reactions. The use of this reactor for chemical reduction is a promising target in the short term, given that the cost of electrolytic hydrogen is 100-fold less than reducing agents (i.e., ~0.1 USD/mol H versus ~10-20 USD/mol H). Though major carbon savings will only be accessed by displacing large-scale processes that use H₂ gas. This goal is significantly more difficult because fossil-derived H₂ is roughly half the cost of electrolytic hydrogen. Cost competitiveness may be enabled by other attributes of this reactor: safety (by avoiding the use of H₂ at high temperatures);

constant flow operation; and decreased instance of side reactions, for example. Detailed technoeconomic analysis is required to understand these opportunities. I hope that the research directions proposed above, and the opportunity to realize a future of carbon-neutral chemical manufacturing inspires continued development of these reactors.

References

- (1) IEA. *Technology Roadmap Energy and GHG Reductions in the Chemical Industry via Catalytic Processes*; 2013.
- (2) Schiffer, Z. J.; Manthiram, K. Electrification and Decarbonization of the Chemical Industry. *Joule* **2017**, *1* (1), 10–14.
- (3) De Luna, P.; Hahn, C.; Higgins, D.; Jaffer, S. A.; Jaramillo, T. F.; Sargent, E. H. What Would It Take for Renewably Powered Electrosynthesis to Displace Petrochemical Processes? *Science* **2019**, *364* (6438), 1–9.
- (4) Frontana-Uribe, B. A.; Daniel Little, R.; Ibanez, J. G.; Palma, A.; Vasquez-Medrano, R. Organic Electrosynthesis: A Promising Green Methodology in Organic Chemistry. *Green Chem.* **2010**, *12* (12), 2099–2119.
- (5) Blanco, D. E.; Modestino, M. A. Organic Electrosynthesis for Sustainable Chemical Manufacturing. *Trends in Chemistry* **2019**, *1* (1), 8–10.
- (6) Pletcher, D. Organic Electrosynthesis – A Road to Greater Application. A Mini Review. *Electrochem. commun.* **2018**, *88*, 1–4.
- (7) Minter, S. D.; Baran, P. Electrifying Synthesis: Recent Advances in the Methods, Materials, and Techniques for Organic Electrosynthesis. *Acc. Chem. Res.* **2020**, *53* (3), 545–546.
- (8) Orella, M. J.; Román-Leshkov, Y.; Brushett, F. R. Emerging Opportunities for Electrochemical Processing to Enable Sustainable Chemical Manufacturing. *Curr. Opin. Chem. Eng.* **2018**, *20*, 159–167.
- (9) Roessler, F. Catalysis in the Industrial Production of Pharmaceuticals and Fine Chemicals. *CHIMIA* **1996**, *50* (3), 106–109.
- (10) Werner Bonrath, Jonathan Medlock, Jan Schütz, Bettina Wüstenberg, Thomas Netscher. Hydrogenation in the Vitamins and Fine Chemicals Industry – An Overview. In *Hydrogenation*; Karamé, I., Ed.; intechopen, 2012.
- (11) Jang, E. S.; Jung, M. Y.; Min, D. B. Hydrogenation for Low Trans and High Conjugated Fatty Acids. *Compr. Rev. Food Sci. Food Saf.* **2005**, *4* (1), 22–30.
- (12) Ameen, M.; Azizan, M. T.; Yusup, S.; Ramli, A.; Yasir, M. Catalytic Hydrodeoxygenation of Triglycerides: An Approach to Clean Diesel Fuel Production. *Renew. Sustain. Energy Rev.* **2017**, *80*, 1072–1088.
- (13) Hydrogen Production: Natural Gas Reforming <https://www.energy.gov/eere/fuelcells/hydrogen-production-natural-gas-reforming> (accessed Feb 21, 2020).
- (14) Wang, D.; Astruc, D. The Golden Age of Transfer Hydrogenation. *Chem. Rev.* **2015**, *115* (13), 6621–6686.
- (15) Nystrom, R. F.; Brown, W. G. Reduction of Organic Compounds by Lithium Aluminum Hydride. II. Carboxylic Acids. *J. Am. Chem. Soc.* **1947**, *69* (10), 2548–2549.
- (16) Málek, J.; Černý, M. Reduction of Organic Compounds by Alkoxyaluminumhydrides. *Synthesis* **2002**, *1972* (05), 217–234.
- (17) Sherbo, R. S.; Delima, R. S.; Chiykowski, V. A.; MacLeod, B. P.; Berlinguette, C. P. Complete Electron Economy by Pairing Electrolysis with Hydrogenation. *Nat. Catal.* **2018**, *1* (7), 501–507.

- (18) Iwakura, C.; Abe, T.; Inoue, H. A New Successive System for Hydrogenation of Styrene Using a Two-Compartment Cell Separated by a Pd Sheet Electrode. *J. Electrochem. Soc.* **1996**, *143* (4), L71.
- (19) Sherbo, R. S.; Kurimoto, A.; Brown, C. M.; Berlinguette, C. P. Efficient Electrocatalytic Hydrogenation with a Palladium Membrane Reactor. *J. Am. Chem. Soc.* **2019**, *141* (19), 7815–7821.
- (20) Delima, R. S.; Sherbo, R. S.; Dvorak, D. J.; Kurimoto, A.; Berlinguette, C. P. Supported Palladium Membrane Reactor Architecture for Electrocatalytic Hydrogenation. *J. Mater. Chem. A Mater. Energy Sustain.* **2019**, *7* (46), 26586–26595.
- (21) Kurimoto, A.; Sherbo, R. S.; Cao, Y.; Loo, N. W. X.; Berlinguette, C. P. Electrolytic Deuteration of Unsaturated Bonds without Using D₂. *Nat. Catal.* **2020**, *3* (9), 719–726.
- (22) Jansonius, R. P.; Kurimoto, A.; Marelli, A. M.; Huang, A.; Sherbo, R. S.; Berlinguette, C. P. Hydrogenation without H₂ Using a Palladium Membrane Flow Cell. *Cell Rep. Phys. Sci.* **2020**, *1* (7), 100105.
- (23) McLennan, K. G.; Gray, E. M.; Dobson, J. F. Deuterium Occupation of Tetrahedral Sites in Palladium. *Phys. Rev. B Condens. Matter* **2008**, *78* (1), 014104.
- (24) Ward, T. L.; Dao, T. Model of Hydrogen Permeation Behavior in Palladium Membranes. *Journal of Membrane Science* **1999**, *153* (2), 211–231.
- (25) Berlinguette, C. P.; Chiang, Y.-M.; Munday, J. N.; Schenkel, T.; Fork, D. K.; Koningstein, R.; Trevithick, M. D. Revisiting the Cold Case of Cold Fusion. *Nature* **2019**, *570* (7759), 45–51.
- (26) Inoue, H.; Abe, T.; Iwakura, C. Successive Hydrogenation of Styrene at a Palladium Sheet Electrode Combined with Electrochemical Supply of Hydrogen. *Chem. Commun.* **1996**, No. 1, 55–56.
- (27) Iwakura, C.; Yoshida, Y.; Inoue, H. A New Hydrogenation System of 4-Methylstyrene Using a Palladinized Palladium Sheet Electrode. *J. Electroanal. Chem.* **1997**, *431* (1), 43–45.
- (28) Iwakura, C.; Abe, T.; Inoue, H. Successive Hydrogenation of Styrene Using a Two-Compartment Cell Separated by Hydrogen Storage Alloy Sheet Electrodes. 電気化学および工業物理化学 **1997**, *65* (12), 1120–1121.
- (29) Inoue, H.; Ueda, K.; Yoshida, Y.; Ogata, S.; Iwakura, C. Chemical Deposition of Palladium Black and Its Catalytic Effect on Hydrogenation of 2-Octene. 電気化学および工業物理化学 **1997**, *65* (12), 1061–1065.
- (30) Inoue, H.; Yoshida, Y.; Ogata, S.; Shimamune, T.; Iwakura, C. Effect of Pd Black Deposits on Successive Hydrogenation of 4-Methylstyrene with Active Hydrogen Passing Through a Pd Sheet Electrode. *J. Electrochem. Soc.* **1998**, *145* (1), 138.
- (31) Yoshida, Y.; Ogata, S.; Nakamatsu, S.; Shimamune, T.; Inoue, H.; Iwakura, C. Chemical Deposition of Foreign Metals on a Pd Sheet and Its Application to Continuous Hydrogenation of 4-Methylstyrene. *J. Electroanal. Chem.* **1998**, *444* (2), 203–207.
- (32) Iwakura, C.; Yoshida, Y.; Ogata, S.; Inoue, H. New Hydrogenation Systems of Unsaturated Organic Compounds Using Noble Metal-Deposited Palladium Sheet Electrodes with Three-Dimensional Structures. *J. Mater. Res.* **1998**, *13* (4), 821–824.
- (33) Yoshida, Y.; Ogata, S.; Nakamatsu, S.; Inoue, H.; Iwakura, C. Catalytic Reduction of Nitrous Oxide with Atomic Hydrogen Permeating through Palladized Pd Sheet Electrodes. *Electrochim. Acta* **1999**, *44* (20), 3585–3587.

- (34) Enayatzamir, K.; Alikhani, H. A.; Yakhchali, B.; Tabandeh, F.; Rodríguez-Couto, S. Decolouration of Azo Dyes by Phanerochaete Chrysosporium Immobilised into Alginate Beads. *Environ. Sci. Pollut. Res. Int.* **2010**, *17* (1), 145–153.
- (35) Inoue, H.; Ito, T.; Iwakura, C. Dehydrogenation System of Formic Acid Combined with Electrochemical Oxidation of Atomic Hydrogen Permeating Through a Palladinized Pd Sheet Electrode. *Electrochem. Solid-State Lett.* **1998**, *2* (2), 75.
- (36) Inoue, H.; Abe, T.; Ito, T.; Iwakura, C. Selectivity Control of Products in Consecutive Hydrogenation of Diphenylacetylene with Chemisorbed Hydrogen. *Electrochem. Solid-State Lett.* **1999**, *2* (11), 572.
- (37) Iwakura, C.; Ito, T.; Inoue, H. Construction of a New Dehydrogenation System Using a Two-Compartment Cell Separated by a Palladized Pd Sheet Electrode. *J. Electroanal. Chem.* **1999**, *463* (1), 116–118.
- (38) Maki, S.; Harada, Y.; Hirano, T.; Niwa, H.; Yoshida, Y.; Ogata, S.; Nakamatsu, S.; Inoue, H.; Iwakura, C. Selective Alkene Hydrogenation with Atomic Hydrogen Permeating Through a Pd Sheet Electrode. *Synth. Commun.* **2000**, *30* (19), 3575–3583.
- (39) Inoue, H.; Ito, T.; Iwakura, C. Control of Product Distribution in the Hydrogenation of Crotonaldehyde, Butyraldehyde and Crotyl Alcohol Using the Successive Hydrogenation System. *Electrochemistry* **2001**, *69* (9), 699–701.
- (40) Maki, S.; Harada, Y.; Matsui, R.; Okawa, M.; Hirano, T.; Niwa, H.; Koizumi, M.; Nishiki, Y.; Furuta, T.; Inoue, H.; Iwakura, C. Effect of Solvent and Hydrogen during Selective Hydrogenation. *Tetrahedron Lett.* **2001**, *42* (47), 8323–8327.
- (41) Iwakura, C.; Tsuchiyama, Y.; Higashiyama, K.; Higuchi, E.; Inoue, H. Successive Hydrogenation and Dechlorination Systems Using Palladized Ion Exchange Membranes. *J. Electrochem. Soc.* **2003**, *151* (1), D1.
- (42) Gutierrez, M.; Nazareno, M. A.; Sosa, V.; López de Mishima, B. A.; Mishima, H. T. Hydrogenation of Chalcones Using Hydrogen Permeating through a Pd and Palladized Pd Electrodes. *Electrochim. Acta* **2010**, *55* (20), 5831–5839.
- (43) Itoh, N.; Aketa, M.; Sato, T.; Kamimura, H.; Takagi, F. Regeneration of Anti-Oxidant in Lubrication Oil on Bifunctional Palladium Membrane Electrode. *J. Jpn. Pet. Inst.* **2012**, *55* (3), 215–218.
- (44) Sato, T.; Sato, S.; Itoh, N. Using a Hydrogen-Permeable Palladium Membrane Electrode to Produce Hydrogen from Water and Hydrogenate Toluene. *Int. J. Hydrogen Energy* **2016**, *41* (12), 5419–5427.
- (45) Sato, T.; Takada, A.; Itoh, N. Low-Temperature Hydrogenation of Toluene by Electrolysis of Water with Hydrogen Permeable Palladium Membrane Electrode. *Chem. Lett.* **2017**, *46* (4), 477–480.
- (46) Yan, B.; Bisbey, R. P.; Alabugin, A.; Surendranath, Y. Mixed Electron-Proton Conductors Enable Spatial Separation of Bond Activation and Charge Transfer in Electrocatalysis. *J. Am. Chem. Soc.* **2019**, *141* (28), 11115–11122.
- (47) Kanyanee, T.; Fletcher, P. J.; Madrid, E.; Marken, F. Indirect (Hydrogen-Driven) Electrodeposition of Porous Silver onto a Palladium Membrane. *J. Solid State Electrochem.* **2020**, *24* (11), 2789–2796.
- (48) Ogumi, Z.; Nishio, K.; Yoshizawa, S. Application of the Spe Method to Organic Electrochemistry—II. Electrochemical Hydrogenation of Olefinic Double Bonds. *Electrochim. Acta* **1981**, *26* (12), 1779–1782.

- (49) Iwakura, C.; Takezawa, S.; Inoue, H. Catalytic Reduction of Carbon Dioxide with Atomic Hydrogen Permeating through Palladized Pd Sheet Electrodes. *J. Electroanal. Chem.* **1998**, *459* (1), 167–169.
- (50) Jansonius, R. P.; Schauer, P. A.; Dvorak, D. J.; MacLeod, B. P.; Fork, D. K.; Berlinguette, C. P. Strain Influences the Hydrogen Evolution Activity and Absorption Capacity of Palladium. *Angew. Chem. Int. Ed.* **2020**, *59* (29), 12192–12198.
- (51) Prasad, S. Studies on the Hall-Heroult Aluminum Electrowinning Process. *J. Braz. Chem. Soc.* **2000**, *11* (3), 245–251.
- (52) Kolbe, H. Untersuchungen Über Die Elektrolyse Organischer Verbindungen. *Ann. Chem. Pharm.* **1849**, *69* (3), 257–294.
- (53) Yan, M.; Kawamata, Y.; Baran, P. S. Synthetic Organic Electrochemical Methods Since 2000: On the Verge of a Renaissance. *Chem. Rev.* **2017**, *117* (21), 13230–13319.
- (54) U.S. Energy Information Administration (EIA). Electric Power Monthly. *Electric Power Monthly*, 2021.
- (55) Total Energy Monthly Data - U.S. Energy Information Administration (EIA) <https://www.eia.gov/totalenergy/data/monthly/> (accessed Dec 17, 2020).
- (56) Yuan, Y.; Lei, A. Is Electrosynthesis Always Green and Advantageous Compared to Traditional Methods? *Nat. Commun.* **2020**, *11* (1), 802.
- (57) Pletcher, D. Electrolysis Cells for Laboratory Organic Synthesis. *Current Opinion in Electrochemistry* **2020**, *24*, 1–5.
- (58) Michael Taylor, Pablo Ralon, Harold Anuta, Sonia Al-Zoghoul. *Renewable Power Generation Costs in 2019*; ISBN 978-92-9260-244-4; International Renewable Energy Agency, 2020.
- (59) *Central Solar Com o Mais Baixo Preço Do Mundo Será Instalada Entre Albufeira e Vilamoura*; Prado, M., Ed.; Expresso, 2020.
- (60) Stoffels, M. A.; Klauk, F. J. R.; Hamadi, T.; Glorius, F.; Leker, J. Technology Trends of Catalysts in Hydrogenation Reactions: A Patent Landscape Analysis. *Adv. Synth. Catal.* **2020**, *362* (6), 1258–1274.
- (61) Saudan, L. A. Hydrogenation Processes in the Synthesis of Perfumery Ingredients. *Acc. Chem. Res.* **2007**, *40* (12), 1309–1319.
- (62) Shultz, C. S.; Krska, S. W. Unlocking the Potential of Asymmetric Hydrogenation at Merck. *Acc. Chem. Res.* **2007**, *40* (12), 1320–1326.
- (63) Magano, J.; Dunetz, J. R. Large-Scale Carbonyl Reductions in the Pharmaceutical Industry. *Org. Process Res. Dev.* **2012**, *16* (6), 1156–1184.
- (64) Static Sankey Diagram of Process Energy in U.S. Manufacturing Sector (2010 MECS) <https://www.energy.gov/eere/amo/static-sankey-diagram-process-energy-us-manufacturing-sector-2010-mecs> (accessed Feb 12, 2021).
- (65) Mc Williams, A. *Merchant Hydrogen: Industrial Gas and Energy Markets*; CHM042D; BCC Research, 2018.
- (66) Jackson, L. S.; Al-Taher, F. Chapter 23 - Processing Issues: Acrylamide, Furan and Trans Fatty Acids. In *Ensuring Global Food Safety*; Boisrobert, C. E., Stjepanovic, A., Oh, S., Lielieveld, H. L. M., Eds.; Academic Press: San Diego, 2010; pp 383–410.
- (67) Biswas, R. *Green Diesel: Further Developments in the Alternative Fuel Space*; EGY169A; BCC Research, 2019; Vol. 110, p P20. <https://doi.org/10.1002/aorn.12817>.
- (68) Hudlicky, M. Reduction and Oxidation Tables. *J. Chem. Educ.* **1977**, *54* (2), 100.

- (69) Rylander, P. Chapter 3 - Hydrogenation of Olefins. In *The Catalytic Hydrogenation in Organic Syntheses*; Rylander, P., Ed.; Academic Press, 1979; pp 31–63.
- (70) Chapter Four - Industrial and Laboratory Reactors. In *Modeling of Chemical Kinetics and Reactor Design*; Coker, A. K., Kayode, C. A., Eds.; Gulf Professional Publishing: Woburn, 2001; pp 218–259.
- (71) Pettinari, C.; Marchetti, F.; Martini, D. Metal Complexes as Hydrogenation Catalysts. In *Comprehensive Coordination Chemistry II*; McCleverty, J. A., Meyer, T. J., Eds.; Pergamon: Oxford, 2003; pp 75–139.
- (72) Hosseini, N.; Givehchi, S.; Maknoon, R. Cost-Based Fire Risk Assessment in Natural Gas Industry by Means of Fuzzy FTA and ETA. *J. Loss Prev. Process Indust.* **2020**, *63*, 104025.
- (73) Johnson, N. B.; Lennon, I. C.; Moran, P. H.; Ramsden, J. A. Industrial-Scale Synthesis and Applications of Asymmetric Hydrogenation Catalysts. *Acc. Chem. Res.* **2007**, *40* (12), 1291–1299.
- (74) Kibler, L. A. Hydrogen Electrocatalysis. *Chemphyschem* **2006**, *7* (5), 985–991.
- (75) Sarkar, S.; Peter, S. C. An Overview on Pd-Based Electrocatalysts for the Hydrogen Evolution Reaction. *Inorg. Chem. Front.* **2018**, *5* (9), 2060–2080.
- (76) Baranowski, B.; Majchrzak, S.; Flanagan, T. B. The Volume Increase of Fcc Metals and Alloys Due to Interstitial Hydrogen over a Wide Range of Hydrogen Contents. *J. Phys. F: Met. Phys.* **1971**, *1* (3), 258.
- (77) Lewis, F. A. The Hydrides of Palladium and Palladium Alloys. *Platin. Met. Rev.* **1960**, *4* (4), 132–137.
- (78) Wicke, E.; Brodowsky, H.; Züchner, H. Hydrogen in Palladium and Palladium Alloys. In *Hydrogen in Metals II: Application-Oriented Properties*; Alefeld, G., Völkl, J., Eds.; Springer Berlin Heidelberg: Berlin, Heidelberg, 1978; pp 73–155.
- (79) Sherbo, R. S.; Moreno-Gonzalez, M.; Johnson, N. J. J.; Dvorak, D. J.; Fork, D. K.; Berlinguette, C. P. Accurate Coulometric Quantification of Hydrogen Absorption in Palladium Nanoparticles and Thin Films. *Chem. Mater.* **2018**, *30* (12), 3963–3970.
- (80) Adit Maark, T.; Peterson, A. A. Understanding Strain and Ligand Effects in Hydrogen Evolution over Pd(111) Surfaces. *J. Phys. Chem. C* **2014**, *118* (8), 4275–4281.
- (81) Nørskov, J. K.; Bligaard, T.; Logadottir, A.; Kitchin, J. R.; Chen, J. G.; Pandelov, S.; Stimming, U. Trends in the Exchange Current for Hydrogen Evolution. *J. Electrochem. Soc.* **2005**, *152* (3), J23–J26.
- (82) Skoskiewicz, T. Superconductivity in the Palladium-Hydrogen and Palladium-Nickel-Hydrogen Systems. *Phys. Stat. Sol* **1972**, *11* (2), 123–126.
- (83) Harper, J. M. E. Effect of Hydrogen Concentration on Superconductivity and Clustering in Palladium Hydride. *Phys. Lett* **1974**, *47A* (1), 69–70.
- (84) Manolatos, P.; Duret-Thual, C.; Le Coze, J.; Jerome, M. The Electrochemical Permeation of Hydrogen in Palladium: Boundary Conditions during a Galvanostatic Charging under Low Charging Current Densities. *Corros. Sci.* **1995**, *37* (11), 1797–1807.
- (85) Devanathan, M. A. V.; Stachurski, Z.; Tompkins, F. C. The Adsorption and Diffusion of Electrolytic Hydrogen in Palladium. *Proc. R. Soc. Lond. A Math. Phys. Sci.* **1962**, *270* (1340), 90–102.
- (86) Horiuti, I.; Polanyi, M. Exchange Reactions of Hydrogen on Metallic Catalysts. *Trans. Faraday Soc.* **1934**, *30* (0), 1164–1172.

- (87) Yan, H.; Lv, H.; Yi, H.; Liu, W.; Xia, Y.; Huang, X.; Huang, W.; Wei, S.; Wu, X.; Lu, J. Understanding the Underlying Mechanism of Improved Selectivity in Pd1 Single-Atom Catalyzed Hydrogenation Reaction. *J. Catal.* **2018**, *366*, 70–79.
- (88) He, H.; Dasgupta, A.; Rioux, R. M.; Meyer, R. J.; Janik, M. J. Competitive Hydrogenation between Linear Alkenes and Aromatics on Close-Packed Late Transition Metal Surfaces. *J. Phys. Chem. C* **2019**, *123* (13), 8370–8378.
- (89) Zaera, F. Key Unanswered Questions about the Mechanism of Olefin Hydrogenation Catalysis by Transition-Metal Surfaces: A Surface-Science Perspective. *Phys. Chem. Chem. Phys.* **2013**, *15* (29), 11988–12003.
- (90) Wilhite, B. A.; McCready, M. J.; Varma, A. Kinetics of Phenylacetylene Hydrogenation over Pt/ γ -Al₂O₃ Catalyst. *Ind. Eng. Chem. Res.* **2002**, *41* (14), 3345–3350.
- (91) Takht Ravanchi, M.; Sahebdehfar, S.; Komeili, S. Acetylene Selective Hydrogenation: A Technical Review on Catalytic Aspects. *Rev. Chem. Eng.* **2018**, *34* (2), 215–237.
- (92) Ohno, S.; Wilde, M.; Mukai, K.; Yoshinobu, J.; Fukutani, K. Mechanism of Olefin Hydrogenation Catalysis Driven by Palladium-Dissolved Hydrogen. *J. Phys. Chem. C* **2016**, *120* (21), 11481–11489.
- (93) Rennard, R. J.; Kokes, R. J. Hydrogenation of Ethylene and Propylene over Palladium Hydride. *J. Phys. Chem.* **1966**, *70* (8), 2543–2549.
- (94) Johnson, A. D.; Daley, S. P.; Utz, A. L.; Ceyer, S. T. The Chemistry of Bulk Hydrogen: Reaction of Hydrogen Embedded in Nickel with Adsorbed CH₃. *Science* **1992**, *257* (5067), 223–225.
- (95) Ceyer, S. T. The Unique Chemistry of Hydrogen beneath the Surface: Catalytic Hydrogenation of Hydrocarbons. *Acc. Chem. Res.* **2001**, *34* (9), 737–744.
- (96) Révay, Z.; Belgya, T.; Szentmiklósi, L.; Kis, Z.; Wootsch, A.; Teschner, D.; Swoboda, M.; Schlögl, R.; Borsodi, J.; Zepernick, R. In Situ Determination of Hydrogen Inside a Catalytic Reactor Using Prompt γ Activation Analysis. *Anal. Chem.* **2008**, *80* (15), 6066–6071.
- (97) Teschner, D.; Borsodi, J.; Wootsch, A.; Révay, Z.; Hävecker, M.; Knop-Gericke, A.; Jackson, S. D.; Schlögl, R. The Roles of Subsurface Carbon and Hydrogen in Palladium-Catalyzed Alkyne Hydrogenation. *Science* **2008**, *320* (5872), 86–89.
- (98) Stacchiola, D.; Burkholder, L.; Tysoe, W. T. Ethylene Adsorption on Pd(111) Studied Using Infrared Reflection–Absorption Spectroscopy. *Surf. Sci.* **2002**, *511* (1), 215–228.
- (99) Stacchiola, D.; Tysoe, W. T. The Effect of Subsurface Hydrogen on the Adsorption of Ethylene on Pd(111). *Surf. Sci.* **2003**, *540* (2–3), L600–L604.
- (100) Michaelides, A.; Hu, P.; Alavi, A. Physical Origin of the High Reactivity of Subsurface Hydrogen in Catalytic Hydrogenation. *J. Chem. Phys.* **1999**, *111* (4), 1343–1345.
- (101) Ledentu, V.; Dong, W.; Sautet, P. Heterogeneous Catalysis through Subsurface Sites. *J. Am. Chem. Soc.* **2000**, *122* (8), 1796–1801.
- (102) Rahimpour, M. R.; Samimi, F.; Babapoor, A.; Tohidian, T.; Mohebi, S. Palladium Membranes Applications in Reaction Systems for Hydrogen Separation and Purification: A Review. *Chem. Eng. Process. Process Intensif.* **2017**, *121*, 24–49.
- (103) Jimenez, G.; Dillon, E.; Dahlmeyer, J.; Garrison, T.; Garrison, T.; Darkey, S.; Wald, K.; Kubik, J.; Paciulli, D.; Talukder, M.; Nott, J.; Ferrer, M.; Prinke, J.; Villaneuva, P.; Massicotte, F.; Rebeiz, K.; Nesbit, S.; Craft, A. A Comparative Assessment of Hydrogen Embrittlement: Palladium and Palladium-Silver (25 Weight% Silver) Subjected to Hydrogen Absorption/Desorption Cycling. *Adv. Chem. Eng. Sci.* **2016**, *06* (03), 246–261.

- (104) Schober, T.; Wenzl, H. The Systems NbH(D), TaH(D), VH(D) : Structures, Phase Diagrams, Morphologies, Methods of Preparation. In *Hydrogen in Metals II: Application-Oriented Properties*; Alefeld, G., Völkl, J., Eds.; Springer Berlin Heidelberg: Berlin, Heidelberg, 1978; pp 11–71.
- (105) *Electronic Structure and Properties of Hydrogen in Metals*; Jena, P., Satterthwaite, C. B., Eds.; Springer, Boston, MA, 1983.
- (106) Gibb, T. R. P.; Kruschwitz, H. W. The Titanium—Hydrogen System and Titanium Hydride. I. Low-Pressure Studies. *J. Am. Chem. Soc.* **1950**, *72* (12), 5365–5369.
- (107) Pal, N.; Agarwal, M.; Maheshwari, K.; Solanki, Y. S. A Review on Types, Fabrication and Support Material of Hydrogen Separation Membrane. *Mater. Today-Proc* **2020**, *28*, 1386–1391.
- (108) Shirai, M.; Arai, M. Hydrogenation of Furan with Hydrogen Atoms Permeating through a Palladium Membrane. *Langmuir* **1999**, *15* (4), 1577–1578.
- (109) Nagamoto, H.; Inoue, H. The Hydrogenation of 1,3-Butadiene over a Palladium Membrane. *Bull. Chem. Soc. Jpn.* **1986**, *59* (12), 3935–3939.
- (110) Itoh, N.; Xu, W. C.; Sathe, A. M. Capability of Permeate Hydrogen through Palladium-Based Membranes for Acetylene Hydrogenation. *Ind. Eng. Chem. Res.* **1993**, *32* (11), 2614–2619.
- (111) Kurimoto, A.; Jansonius, R. P.; Huang, A.; Marelli, A. M.; Dvorak, D. J.; Hunt, C.; Berlinguette, C. P. Physical Separation of H₂ Activation from Hydrogenation Chemistry Reveals the Specific Role of Secondary Metal Catalysts. *Angew. Chem. Int. Ed.* **2021**, *60* (21), 11937–11942.
- (112) Maoka, T.; Enyo, M. Hydrogen Absorption by Palladium Electrode Polarized in Sulfuric Acid Solution Containing Surface Active Substances—I. The Cathodic Region. *Electrochim. Acta* **1981**, *26* (5), 607–614.
- (113) Dittmeyer, R.; Höllein, V.; Daub, K. Membrane Reactors for Hydrogenation and Dehydrogenation Processes Based on Supported Palladium. *J. Mol. Catal. A Chem.* **2001**, *173* (1), 135–184.
- (114) Dittmeyer, R.; Svajda, K.; Reif, M. A Review of Catalytic Membrane Layers for Gas/Liquid Reactions. *Top. Catal.* **2004**, *29* (1–2), 3–27.
- (115) Shu, J.; Grandjean, B. P. A.; Van Neste, A.; Kaliaguine, S. Catalytic Palladium-Based Membrane Reactors: A Review. *The Canadian Journal of Chemical Engineering* **1991**, *69* (5), 1036–1060.
- (116) Gryaznov, V. M.; Karavanov, A. N.; Belosljudova, T. M.; Ermolaev, A. V.; Maganjuk, A. P.; Sarycheva, I. K. Process for Producing C₄–C₁₀ Ethylene Alcohols. 4388479, June 14, 1983.
- (117) Augustine, A. S.; Ma, Y. H.; Kazantzis, N. K. High Pressure Palladium Membrane Reactor for the High Temperature Water–Gas Shift Reaction. *Int. J. Hydrogen Energy* **2011**, *36* (9), 5350–5360.
- (118) Fox, M. A.; Whitesell, J. K. *Organic Chemistry*; Jones & Bartlett Learning, 2004.
- (119) Botte, G. G. Electrochemical Manufacturing in the Chemical Industry. *Electrochem. Soc. Interface* **2014**, *23* (3), 49.
- (120) Bonrath, W.; Medlock, J.; Schutz, J.; Wustenberg, B.; Netscher, T. Hydrogenation in the Vitamins and Fine Chemicals Industry – An Overview. *Hydrogenation*. 2012. <https://doi.org/10.5772/48751>.

- (121) Pirali, T.; Serafini, M.; Cargnin, S.; Genazzani, A. A. Applications of Deuterium in Medicinal Chemistry. *J. Med. Chem.* **2019**, *62* (11), 5276–5297.
- (122) LeCloux, Daniel, David Fennimore, Adam Gao, Weiyang Radu, Nora, Sabina Wu, Weishi Rostovstev, Vsevolod Howard Jr., Michael, Henry Meng, Hong Shen, Yulong. Deuterated Compounds for Electronic Applications. 2015/0021586 A1, 2015.
- (123) Tong, C. C.; Hwang, K. C. Enhancement of OLED Efficiencies and High-Voltage Stabilities of Light-Emitting Materials by Deuteration. *J. Phys. Chem. C* **2007**, *111* (8), 3490–3494.
- (124) Nguyen, T. D.; Hukic-Markosian, G.; Wang, F.; Wojcik, L.; Li, X.-G.; Ehrenfreund, E.; Vardeny, Z. V. Isotope Effect in Spin Response of Pi-Conjugated Polymer Films and Devices. *Nat. Mater.* **2010**, *9* (4), 345–352.
- (125) Shao, M.; Keum, J.; Chen, J.; He, Y.; Chen, W.; Browning, J. F.; Jakowski, J.; Sumpter, B. G.; Ivanov, I. N.; Ma, Y.-Z.; Rouleau, C. M.; Smith, S. C.; Geohegan, D. B.; Hong, K.; Xiao, K. The Isotopic Effects of Deuteration on Optoelectronic Properties of Conducting Polymers. *Nat. Commun.* **2014**, *5*, 3180.
- (126) Plutschack, M. B.; Pieber, B.; Gilmore, K.; Seeberger, P. H. The Hitchhiker’s Guide to Flow Chemistry. *Chem. Rev.* **2017**, *117* (18), 11796–11893.
- (127) Pletcher, D.; Green, R. A.; Brown, R. C. D. Flow Electrolysis Cells for the Synthetic Organic Chemistry Laboratory. *Chem. Rev.* **2018**, *118* (9), 4573–4591.
- (128) Yan, M.; Kawamata, Y.; Baran, P. S. Synthetic Organic Electrochemistry: Calling All Engineers. *Angew. Chem. Int. Ed.* **2018**, *57* (16), 4149–4155.
- (129) Bard, A. J.; Faulkner, L. R.; Others. Fundamentals and Applications. *Electrochemical Methods* **2001**, *2* (482), 580–632.
- (130) Weekes, D. M.; Salvatore, D. A.; Reyes, A.; Huang, A.; Berlinguette, C. P. Electrolytic CO₂ Reduction in a Flow Cell. *Acc. Chem. Res.* **2018**, *51* (4), 910–918.
- (131) Walsh, F. C.; Ponce de León, C. Progress in Electrochemical Flow Reactors for Laboratory and Pilot Scale Processing. *Electrochim. Acta* **2018**, *280*, 121–148.
- (132) Ralph, T. R.; Hitchman, M. L.; Millington, J. P.; Walsh, F. C. Mass Transport in an Electrochemical Laboratory Filterpress Reactor and Its Enhancement by Turbulence Promoters. *Electrochim. Acta* **1996**, *41* (4), 591–603.
- (133) Goodridge, F.; Scott, K. Electrolytic Reactor Design, Selection, and Scale-Up. In *Electrochemical Process Engineering: A Guide to the Design of Electrolytic Plant*; Goodridge, F., Scott, K., Eds.; Springer US: Boston, MA, 1995; pp 177–244.
- (134) Noël, T.; Cao, Y.; Laudadio, G. The Fundamentals Behind the Use of Flow Reactors in Electrochemistry. *Acc. Chem. Res.* **2019**, *52* (10), 2858–2869.
- (135) Pletcher, D.; Li, X. Prospects for Alkaline Zero Gap Water Electrolysers for Hydrogen Production. *Int. J. Hydrog. Energy* **2011**, *36* (23), 15089–15104.
- (136) Zhang, J.; Zhang, H.; Wu, J.; Zhang, J. Chapter 2 - Design and Fabrication of PEM Fuel Cell MEA, Single Cell, and Stack. In *Pem Fuel Cell Testing and Diagnosis*; Zhang, J., Zhang, H., Wu, J., Zhang, J., Eds.; Elsevier: Amsterdam, 2013; pp 43–80.
- (137) Medford, A. J.; Vojvodic, A.; Hummelshøj, J. S.; Voss, J.; Abild-Pedersen, F.; Studt, F.; Bligaard, T.; Nilsson, A.; Nørskov, J. K. From the Sabatier Principle to a Predictive Theory of Transition-Metal Heterogeneous Catalysis. *J. Catal.* **2015**, *328*, 36–42.
- (138) Mavrikakis, M.; Hammer, B.; Nørskov, J. K. Effect of Strain on the Reactivity of Metal Surfaces. *Phys. Rev. Lett.* **1998**, *81* (13), 2819–2822.

- (139) Khorshidi, A.; Violet, J.; Hashemi, J.; Peterson, A. A. How Strain Can Break the Scaling Relations of Catalysis. *Nat. Catal.* **2018**, *1* (4), 263–268.
- (140) Luo, M.; Guo, S. Strain-Controlled Electrocatalysis on Multimetallic Nanomaterials. *Nat. Rev. Mater.* **2017**, *2*, 17059.
- (141) You, B.; Tang, M. T.; Tsai, C.; Abild-Pedersen, F.; Zheng, X.; Li, H. Enhancing Electrocatalytic Water Splitting by Strain Engineering. *Adv. Mater.* **2019**, *31* (17), e1807001.
- (142) Jansson, R. P.; Reid, L. M.; Virca, C. N.; Berlinguette, C. P. Strain Engineering Electrocatalysts for Selective CO₂ Reduction. *ACS Energy Lett.* **2019**, *4* (4), 980–986.
- (143) Zheng, J.; Zhou, S.; Gu, S.; Xu, B.; Yan, Y. Size-Dependent Hydrogen Oxidation and Evolution Activities on Supported Palladium Nanoparticles in Acid and Base. *J. Electrochem. Soc.* **2016**, *163* (6), F499–F506.
- (144) Escudero-Escribano, M.; Malacrida, P.; Hansen, M. H.; Vej-Hansen, U. G.; Velázquez-Palenzuela, A.; Tripkovic, V.; Schiøtz, J.; Rossmeisl, J.; Stephens, I. E. L.; Chorkendorff, I. Tuning the Activity of Pt Alloy Electrocatalysts by Means of the Lanthanide Contraction. *Science* **2016**, *352* (6281), 73–76.
- (145) Huang, H.; Jia, H.; Liu, Z.; Gao, P.; Zhao, J.; Luo, Z.; Yang, J.; Zeng, J. Understanding of Strain Effects in the Electrochemical Reduction of CO₂: Using Pd Nanostructures as an Ideal Platform. *Angew. Chem. Int. Ed.* **2017**, *56* (13), 3594–3598.
- (146) Xiong, Y.; Shan, H.; Zhou, Z.; Yan, Y.; Chen, W.; Yang, Y.; Liu, Y.; Tian, H.; Wu, J.; Zhang, H.; Yang, D. Tuning Surface Structure and Strain in Pd-Pt Core-Shell Nanocrystals for Enhanced Electrocatalytic Oxygen Reduction. *Small* **2017**, *13* (7). <https://doi.org/10.1002/sml.201603423>.
- (147) Du, M.; Cui, L.; Cao, Y.; Bard, A. J. Mechanochemical Catalysis of the Effect of Elastic Strain on a Platinum Nanofilm for the ORR Exerted by a Shape Memory Alloy Substrate. *J. Am. Chem. Soc.* **2015**, *137* (23), 7397–7403.
- (148) Cao, Z.; Zacate, S. B.; Sun, X.; Liu, J.; Hale, E. M.; Carson, W. P.; Tyndall, S. B.; Xu, J.; Liu, X.; Liu, X.; Song, C.; Luo, J.-H.; Cheng, M.-J.; Wen, X.; Liu, W. Tuning Gold Nanoparticles with Chelating Ligands for Highly Efficient Electrocatalytic CO₂ Reduction. *Angew. Chem. Int. Ed.* **2018**, *130* (39), 12857–12861.
- (149) Hwang, D.-M. D. Strain Relaxation in Lattice-Mismatched Epitaxy. *Mater. Chem. Phys.* **1995**, *40* (4), 291–297.
- (150) Yan, K.; Maark, T. A.; Khorshidi, A.; Sethuraman, V. A.; Peterson, A. A.; Guduru, P. R. The Influence of Elastic Strain on Catalytic Activity in the Hydrogen Evolution Reaction. *Angew. Chem. Int. Ed.* **2016**, *128* (21), 6283–6289.
- (151) Yan, K.; Kim, S. K.; Khorshidi, A.; Guduru, P. R.; Peterson, A. A. High Elastic Strain Directly Tunes the Hydrogen Evolution Reaction on Tungsten Carbide. *J. Phys. Chem. C* **2017**, *121* (11), 6177–6183.
- (152) Yang, Y.; Maark, T. A.; Peterson, A.; Kumar, S. Elastic Strain Effects on Catalysis of a PdCuSi Metallic Glass Thin Film. *Phys. Chem. Chem. Phys.* **2015**, *17* (3), 1746–1754.
- (153) Deng, Q.; Smetanin, M.; Weissmüller, J. Mechanical Modulation of Reaction Rates in Electrocatalysis. *J. Catal.* **2014**, *309*, 351–361.
- (154) Yang, Y.; Kumar, S. Elastic Strain Effects on the Catalytic Response of Pt and Pd Thin Films Deposited on Pd–Zr Metallic Glass. *J. Mater. Res.* **2017**, *32* (14), 2690–2699.

- (155) Shao, M.; Liu, P.; Zhang, J.; Adzic, R. Origin of Enhanced Activity in Palladium Alloy Electrocatalysts for Oxygen Reduction Reaction. *J. Phys. Chem. B* **2007**, *111* (24), 6772–6775.
- (156) Johnson, N. J. J.; Lam, B.; MacLeod, B. P.; Sherbo, R. S.; Moreno-Gonzalez, M.; Fork, D. K.; Berlinguette, C. P. Facets and Vertices Regulate Hydrogen Uptake and Release in Palladium Nanocrystals. *Nat. Mater.* **2019**, *18* (5), 454–458.
- (157) Adams, B. D.; Chen, A. The Role of Palladium in a Hydrogen Economy. *Mater. Today* **2011**, *14* (6), 282–289.
- (158) Mohtadi, R.; Orimo, S. I. The Renaissance of Hydrides as Energy Materials. *Nat. Rev. Mater.* **2016**, *2* (3), 1–15.
- (159) Wang, A.; Zhao, Z.; Hu, D.; Niu, J.; Zhang, M.; Yan, K.; Lu, G. Tuning the Oxygen Evolution Reaction on a Nickel-Iron Alloy via Active Straining. *Nanoscale* **2018**, No. 11, 426–430.
- (160) Lee, J. H.; Jang, W. S.; Han, S. W.; Baik, H. K. Efficient Hydrogen Evolution by Mechanically Strained MoS₂ Nanosheets. *Langmuir* **2014**, *30* (32), 9866–9873.
- (161) Benson, E. E.; Ha, M.-A.; Gregg, B. A.; van de Lagemaat, J.; Neale, N. R.; Svedruzic, D. Dynamic Tuning of a Thin Film Electrocatalyst by Tensile Strain. *Sci. Rep.* **2019**, *9* (1), 15906.
- (162) Wang, H.; Xu, S.; Tsai, C.; Li, Y.; Liu, C.; Zhao, J.; Liu, Y.; Yuan, H.; Abild-Pedersen, F.; Prinz, F. B.; Nørskov, J. K.; Cui, Y. Direct and Continuous Strain Control of Catalysts with Tunable Battery Electrode Materials. *Science* **2016**, *354* (6315), 1031–1036.
- (163) Deng, Q.; Gossler, D.-H.; Smetanin, M.; Weissmüller, J. Electrocapillary Coupling at Rough Surfaces. *Phys. Chem. Chem. Phys.* **2015**, *17* (17), 11725–11731.
- (164) Matta, M.; Pereira, M. J.; Gali, S. M.; Thuau, D.; Olivier, Y.; Briseno, A.; Dufour, I.; Ayela, C.; Wantz, G.; Muccioli, L. Unusual Electromechanical Response in Rubrene Single Crystals. *Mater. Horiz.* **2018**, *5* (1), 41–50.
- (165) Smetanin, M.; Kramer, D.; Mohanan, S.; Herr, U.; Weissmüller, J. Response of the Potential of a Gold Electrode to Elastic Strain. *Phys. Chem. Chem. Phys.* **2009**, *11* (40), 9008–9012.
- (166) Zhang, H.; An, C.; Yuan, A.; Deng, Q.; Ning, J. A Non-Conventional Way to Modulate the Capacitive Process on Carbon Cloth by Mechanical Stretching. *Electrochem. Commun.* **2018/4**, *89*, 43–47.
- (167) Noyan, I. C.; Huang, T. C.; York, B. R. Residual Stress/Strain Analysis in Thin Films by X-Ray Diffraction. *Crit. Rev. Solid State Mater. Sci.* **1995**, *20* (2), 125–177.
- (168) Renault, P. O.; Villain, P.; Coupeau, C.; Goudeau, P.; Badawi, K. F. Damage Mode Tensile Testing of Thin Gold Films on Polyimide Substrates by X-Ray Diffraction and Atomic Force Microscopy. *Thin Solid Films* **2003**, *424* (2), 267–273.
- (169) Renault, P. O.; Badawi, K. F.; Bimbault, L.; Goudeau, P.; Elkaim, E.; Lauriat, J. P. Poisson's Ratio Measurement in Tungsten Thin Films Combining an x-Ray Diffractometer with in Situ Tensile Tester. *Appl. Phys. Lett.* **1998**, *73* (14), 1952–1954.
- (170) Badawi, K. F.; Villain, P.; Goudeau, P.; Renault, P.-O. Measuring Thin Film and Multilayer Elastic Constants by Coupling in Situ Tensile Testing with X-Ray Diffraction. *Appl. Phys. Lett.* **2002**, *80* (25), 4705–4707.

- (171) Welzel, U.; Ligot, J.; Lamparter, P.; Vermeulen, A. C.; Mittemeijer, E. J. Stress Analysis of Polycrystalline Thin Films and Surface Regions by X-Ray Diffraction. *J. Appl. Crystallogr.* **2005**, *38* (1), 1–29.
- (172) Goods, S. H.; Guthrie, S. E. Mechanical Properties of Palladium and Palladium Hydride. *Scripta Metall. Mater.* **1992**, *26* (4), 561–565.
- (173) Conway, B. E.; Tilak, B. V. Interfacial Processes Involving Electrocatalytic Evolution and Oxidation of H₂, and the Role of Chemisorbed H. *Electrochim. Acta* **2002**, *47* (22), 3571–3594.
- (174) Bu, L.; Zhang, N.; Guo, S.; Zhang, X.; Li, J.; Yao, J.; Wu, T.; Lu, G.; Ma, J.-Y.; Su, D.; Huang, X. Biaxially Strained PtPb/Pt Core/Shell Nanoplate Boosts Oxygen Reduction Catalysis. *Science* **2016**, *354* (6318), 1410–1414.
- (175) Liu, F.; Wu, C.; Yang, S. Strain and Ligand Effects on CO₂ Reduction Reactions over Cu–Metal Heterostructure Catalysts. *J. Phys. Chem. C* **2017**, *121* (40), 22139–22146.
- (176) Adit Maark, T.; Nanda, B. R. K. Enhancing CO₂ Electroreduction by Tailoring Strain and Ligand Effects in Bimetallic Copper–Rhodium and Copper–Nickel Heterostructures. *J. Phys. Chem. C* **2017**, *121* (8), 4496–4504.
- (177) Wang, J.; Wang, H.; Fan, Y. Techno-Economic Challenges of Fuel Cell Commercialization. *Proc. Est. Acad. Sci. Eng.* **2018**, *4* (3), 352–360.
- (178) Mattson, B.; Foster, W.; Greimann, J.; Hoette, T.; Le, N.; Mirich, A.; Wankum, S.; Cabri, A.; Reichenbacher, C.; Schwanke, E. Heterogeneous Catalysis: The Horiuti–Polanyi Mechanism and Alkene Hydrogenation. *J. Chem. Educ.* **2013**, *90* (5), 613–619.
- (179) Studt, F.; Abild-Pedersen, F.; Bligaard, T.; Sørensen, R. Z.; Christensen, C. H.; Nørskov, J. K. Identification of Non-Precious Metal Alloy Catalysts for Selective Hydrogenation of Acetylene. *Science* **2008**, *320* (5881), 1320–1322.
- (180) Al-Ammar, A. S.; Webb, G. Hydrogenation of Acetylene over Supported Metal Catalysts. Part 1.—Adsorption of [¹⁴C] Acetylene and [¹⁴C] Ethylene on Silica Supported Rhodium, Iridium and Palladium and Alumina Supported Palladium. *J. Chem. Soc., Faraday Trans. 1 F* **1978**, *74*, 195–205.
- (181) Wilde, M.; Fukutani, K.; Ludwig, W.; Brandt, B.; Fischer, J.-H.; Schauer mann, S.; Freund, H.-J. Influence of Carbon Deposition on the Hydrogen Distribution in Pd Nanoparticles and Their Reactivity in Olefin Hydrogenation. *Angew. Chem. Int. Ed.* **2008**, *47* (48), 9289–9293.
- (182) Huang, D. C.; Chang, K. H.; Pong, W. F.; Tseng, P. K.; Hung, K. J.; Huang, W. F. Effect of Ag-Promotion on Pd Catalysts by XANES. *Catal. Letters* **1998**, *53*, 155–159.
- (183) Khan, N. A.; Shaikhutdinov, S.; Freund, H.-J. Acetylene and Ethylene Hydrogenation on Alumina Supported Pd-Ag Model Catalysts. *Catal. Letters* **2006**, *108* (3), 159–164.
- (184) Ludwig, W.; Savara, A.; Brandt, B.; Schauer mann, S. A Kinetic Study on the Conversion of Cis-2-Butene with Deuterium on a Pd/Fe₃O₄ Model Catalyst. *Phys. Chem. Chem. Phys.* **2011**, *13* (3), 966–977.
- (185) Ludwig, W.; Savara, A.; Dostert, K.-H.; Schauer mann, S. Olefin Hydrogenation on Pd Model Supported Catalysts: New Mechanistic Insights. *J. Catal.* **2011**, *284* (2), 148–156.
- (186) Doyle, A. M.; Shaikhutdinov, S. K.; Jackson, S. D.; Freund, H.-J. Hydrogenation on Metal Surfaces: Why Are Nanoparticles More Active than Single Crystals? *Angew. Chem. Int. Ed.* **2003**, *42* (42), 5240–5243.
- (187) Daley, S. P.; Utz, A. L.; Trautman, T. R.; Ceyer, S. T. Ethylene Hydrogenation on Ni(111) by Bulk Hydrogen. *J. Am. Chem. Soc.* **1994**, *116* (13), 6001–6002.

- (188) Lopez-Ruiz, J. A.; Andrews, E.; Akhade, S. A.; Lee, M.-S.; Koh, K.; Sanyal, U.; Yuk, S. F.; Karkamkar, A. J.; Derewinski, M. A.; Holladay, J.; Glezakou, V.-A.; Rousseau, R.; Gutiérrez, O. Y.; Holladay, J. D. Understanding the Role of Metal and Molecular Structure on the Electrocatalytic Hydrogenation of Oxygenated Organic Compounds. *ACS Catal.* **2019**, *9* (11), 9964–9972.
- (189) Jansonius, R. P.; Kurimoto, A.; Marelli, A. M.; Huang, A.; Sherbo, R. S.; Berlinguette, C. P. Hydrogenation without H₂ Using a Palladium Membrane Flow Cell. *Cell Rep. Phys. Sci.* **2020**, *1* (7), 100105.
- (190) Lange, J.-P.; van der Heide, E.; van Buijtenen, J.; Price, R. Furfural--a Promising Platform for Lignocellulosic Biofuels. *ChemSusChem* **2012**, *5* (1), 150–166.
- (191) Hammer, B.; Norskov, J. K. Why Gold Is the Noblest of All the Metals. *Nature* **1995**, *376* (6537), 238–240.
- (192) Thomas, J. M.; John Thomas, W. *Principles and Practice of Heterogeneous Catalysis*; John Wiley & Sons, 2014.
- (193) Pan, M.; Brush, A. J.; Pozun, Z. D.; Ham, H. C.; Yu, W.-Y.; Henkelman, G.; Hwang, G. S.; Mullins, C. B. Model Studies of Heterogeneous Catalytic Hydrogenation Reactions with Gold. *Chem. Soc. Rev.* **2013**, *42* (12), 5002–5013.
- (194) Liu, H.; Lu, G.; Guo, Y.; Wang, Y.; Guo, Y. Synthesis of Mesoporous Pt/Al₂O₃ Catalysts with High Catalytic Performance for Hydrogenation of Acetophenone. *Catal. Commun.* **2009**, *10* (9), 1324–1329.
- (195) Drelinkiewicz, A.; Waksmondzka, A.; Makowski, W.; Sobczak, J. W.; Król, A.; Zieba, A. Acetophenone Hydrogenation on Polymer–Palladium Catalysts. The Effect of Polymer Matrix. *Catal. Letters* **2004**, *94* (3–4), 143–156.
- (196) Wan, H.; Vitter, A.; Chaudhari, R. V.; Subramaniam, B. Kinetic Investigations of Unusual Solvent Effects during Ru/C Catalyzed Hydrogenation of Model Oxygenates. *J. Catal.* **2014**, *309*, 174–184.
- (197) Bertero, N. M.; Trasarti, A. F.; Apesteguía, C. R.; Marchi, A. J. Solvent Effect in the Liquid-Phase Hydrogenation of Acetophenone over Ni/SiO₂: A Comprehensive Study of the Phenomenon. *Appl. Catal. A* **2011**, *394* (1), 228–238.
- (198) Corvaisier, F.; Schuurman, Y.; Fecant, A.; Thomazeau, C.; Raybaud, P.; Toulhoat, H.; Farrusseng, D. Periodic Trends in the Selective Hydrogenation of Styrene over Silica Supported Metal Catalysts. *J. Catal.* **2013**, *307*, 352–361.
- (199) Luza, L.; Rambor, C. P.; Gual, A.; Alves Fernandes, J.; Eberhardt, D.; Dupont, J. Revealing Hydrogenation Reaction Pathways on Naked Gold Nanoparticles. *ACS Catal.* **2017**, *7* (4), 2791–2799.
- (200) Moreno-Gonzalez, M.; Huang, A.; Schauer, P. A.; Hu, K.; Lam, B.; Grayson, J. W.; Bottomley, A.; Dvorak, D. J.; Fork, D. K.; Berlinguette, C. P. Sulfuric Acid Electrolyte Impacts Palladium Chemistry at Reductive Potentials. *Chem. Mater.* **2020**, *32* (21), 9098–9106.
- (201) Li, X.; Lan, X.; Wang, T. Highly Selective Catalytic Conversion of Furfural to γ -Butyrolactone. *Green Chem.* **2016**, *18* (3), 638–642.
- (202) Hagen, J. *Industrial Catalysis: A Practical Approach*; John Wiley & Sons, 2015.
- (203) Zanella, R.; Louis, C.; Giorgio, S.; Touroude, R. Crotonaldehyde Hydrogenation by Gold Supported on TiO₂: Structure Sensitivity and Mechanism. *J. Catal.* **2004**, *223* (2), 328–339.

- (204) Claus, P. Heterogeneously Catalysed Hydrogenation Using Gold Catalysts. *Appl. Catal. A* **2005**, *291* (1), 222–229.
- (205) Ravi Kumar, V.; Verma, C.; Umopathy, S. Molecular Dynamics and Simulations Study on the Vibrational and Electronic Solvatochromism of Benzophenone. *J. Chem. Phys.* **2016**, *144* (6), 064302.
- (206) Rajadhyaksha, R. A.; Karwa, S. L. Solvent Effects in Catalytic Hydrogenation. *Chem. Eng. Sci.* **1986**, *41* (7), 1765–1770.
- (207) Purwanto; Deshpande, R. M.; Chaudhari, R. V.; Delmas, H. Solubility of Hydrogen, Carbon Monoxide, and 1-Octene in Various Solvents and Solvent Mixtures. *J. Chem. Eng. Data* **1996**, *41* (6), 1414–1417.
- (208) Delmelle, R.; Ngene, P.; Dam, B.; Bleiner, D.; Borgschulte, A. Promotion of Hydrogen Desorption from Palladium Surfaces by Fluoropolymer Coating. *ChemCatChem* **2016**, *8* (9), 1646–1650.
- (209) Yoon, Y.; Yan, B.; Surendranath, Y. Suppressing Ion Transfer Enables Versatile Measurements of Electrochemical Surface Area for Intrinsic Activity Comparisons. *J. Am. Chem. Soc.* **2018**, *140* (7), 2397–2400.
- (210) Paglieri, S. N.; Way, J. D. Innovations in Palladium Membrane Research. *Sep. Purif. Methods* **2002**, *31* (1), 1–169.
- (211) Eppinger, J.; Huang, K.-W. Formic Acid as a Hydrogen Energy Carrier. *ACS Energy Lett.* **2017**, *2* (1), 188–195.
- (212) Ma, M.; Clark, E. L.; Therkildsen, K. T.; Dalsgaard, S.; Chorkendorff, I.; Seger, B. Insights into the Carbon Balance for CO₂ Electroreduction on Cu Using Gas Diffusion Electrode Reactor Designs. *Energy Environ. Sci.* **2020**, *13* (3), 977–985.
- (213) Zhang, J.; Luo, W.; Züttel, A. Crossover of Liquid Products from Electrochemical CO₂ Reduction through Gas Diffusion Electrode and Anion Exchange Membrane. *J. Catal.* **2020**, *385*, 140–145.
- (214) Du, X.; Zhang, H.; Sullivan, K. P.; Gogoi, P.; Deng, Y. Electrochemical Lignin Conversion. *ChemSusChem* **2020**, *13* (17), 4318–4343.
- (215) Verma, S.; Lu, S.; Kenis, P. J. A. Co-Electrolysis of CO₂ and Glycerol as a Pathway to Carbon Chemicals with Improved Technoeconomics Due to Low Electricity Consumption. *Nat. Energy* **2019**, *4* (6), 466–474.
- (216) Lees, E. W.; Mowbray, B. A. W.; Salvatore, D. A.; Simpson, G. L.; Dvorak, D. J.; Ren, S.; Chau, J.; Milton, K. L.; Berlinguette, C. P. Linking Gas Diffusion Electrode Composition to CO₂ Reduction in a Flow Cell. *J. Mater. Chem. A Mater. Energy Sustain.* **2020**, *8* (37), 19493–19501.
- (217) Prins, R. Hydrogen Spillover. Facts and Fiction. *Chem. Rev.* **2012**, *112* (5), 2714–2738.
- (218) Kura, C.; Kunisada, Y.; Tsuji, E.; Zhu, C.; Habazaki, H.; Nagata, S.; Müller, M. P.; De Souza, R. A.; Aoki, Y. Hydrogen Separation by Nanocrystalline Titanium Nitride Membranes with High Hydride Ion Conductivity. *Nat. Energy* **2017**, *2* (10), 786–794.
- (219) Buttler, A.; Spliethoff, H. Current Status of Water Electrolysis for Energy Storage, Grid Balancing and Sector Coupling via Power-to-Gas and Power-to-Liquids: A Review. *Renew. Sustain. Energy Rev.* **2018**, *82*, 2440–2454.
- (220) Boden, T.A., G. Marland, and R.J. Andres. Global, Regional, and National Fossil-Fuel CO₂ Emissions, 2017. https://doi.org/doi.10.3334/CDIAC/00001_V2017.

- (221) Environment; Canada, C. C. Clean fuel standard <https://www.canada.ca/en/environment-climate-change/services/managing-pollution/energy-production/fuel-regulations/clean-fuel-standard.html> (accessed Feb 23, 2021).
- (222) Salvatore, D. A.; Weekes, D. M.; He, J.; Dettelbach, K. E.; Li, Y. C.; Mallouk, T. E.; Berlinguette, C. P. Electrolysis of Gaseous CO₂ to CO in a Flow Cell with a Bipolar Membrane. *ACS Energy Lett.* **2018**, 3 (1), 149–154.

Appendices

Appendix 1: Chapter 3

A1.1. Design and validation of a tensile testing electrochemical device (“TED”)

Table A1 Design specifications and approaches for the construction of the TED

Component	Design specification	Approach
Electrochemical cell housing	Chemically compatible with common electrolytes and solvents	Fabricated from PEEK
	Gas and liquid-tight	Viton O-rings used to seal all feedthroughs and interfaces
	Optical access to sample	Transparent sample loading port cover enables viewing of the electrode during experimentation
	Enables electrochemical testing	Included sealed feedthroughs for working, counter and reference electrodes
	Optional headspace sampling, or inert atmosphere (not used in this study)	Two sealable gas feedthroughs included in the cell headspace
Integrated tensile tester	Measures forces large enough to stretch a 75 μm Kapton electrode > 15% (~ 225 N)	Force sensor measures up to 440 N
	Enables application of > 10% strain to a 25.4 mm-long sample	37 mm actuator stroke length sufficient to apply 150 % strain to the sample
	Applies strain in increments of < 0.5% for a 25.4 mm-long sample	Position sensor resolves changes in strain of 0.05%. Stepper motor can apply strain in 0.3% increments
Sample holder	Chemically compatible with electrolyte, and does not deform under applied force	Fabricated from 0.25” PMMA, which is inert to most electrolytes is ~100stiffer than 75 μm Kapton
	Simple fabrication	Batch-fabricated by laser cutting from PMMA sheet
	Reliably grips flexible sample	Devcon® 2-ton epoxy was used to attach the sample to a disposable holder. Epoxy maintains grip on the sample when >60 N of force was applied
	Sample shape enables uniform strain application, and observable electrochemical current ($\geq 1 \mu\text{A}$)	Rectangular sample shape conforms to ASTM guidelines. 25 mm length and 5 mm width enables sufficient electrochemical response to resolve small changes in electrode properties

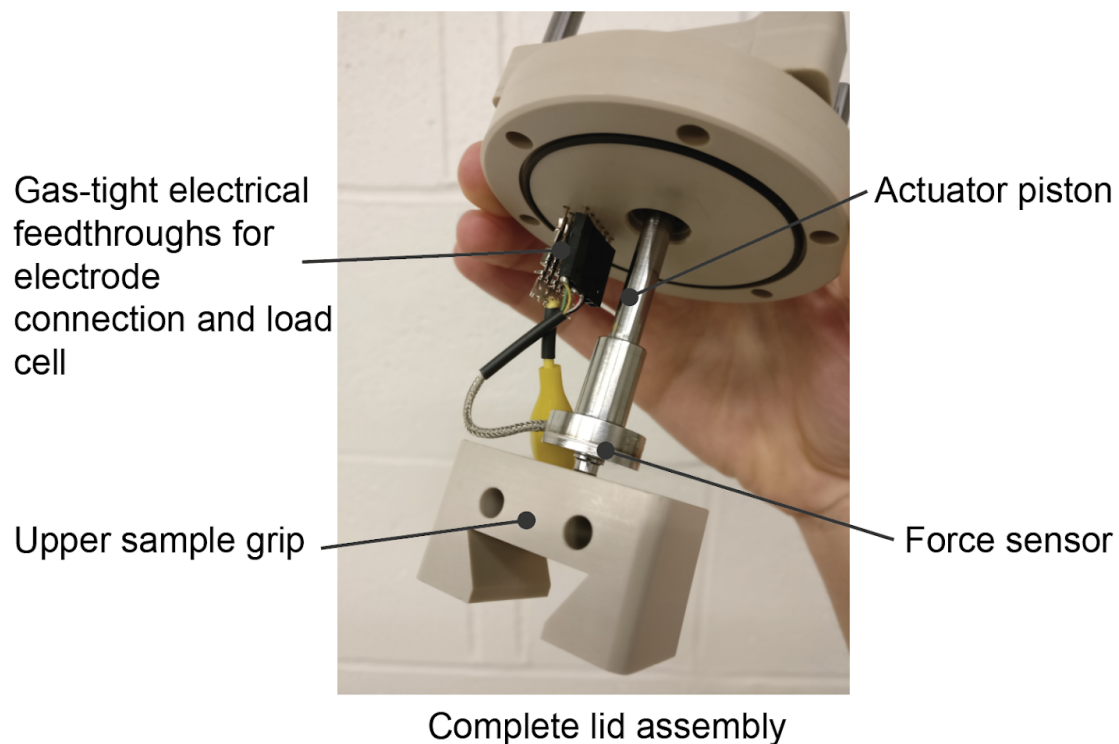


Figure A1.1 Image of the TED lid assembly, showing the hermetically-sealed feedthroughs for the force sensor and working electrode connection.

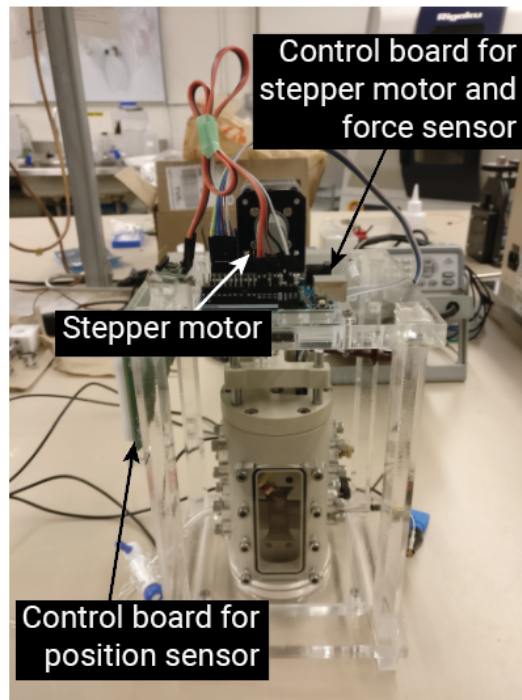


Figure A1.2 Image of the TED in the mechanical testing housing, showing the stepper motor and data acquisition electronics.

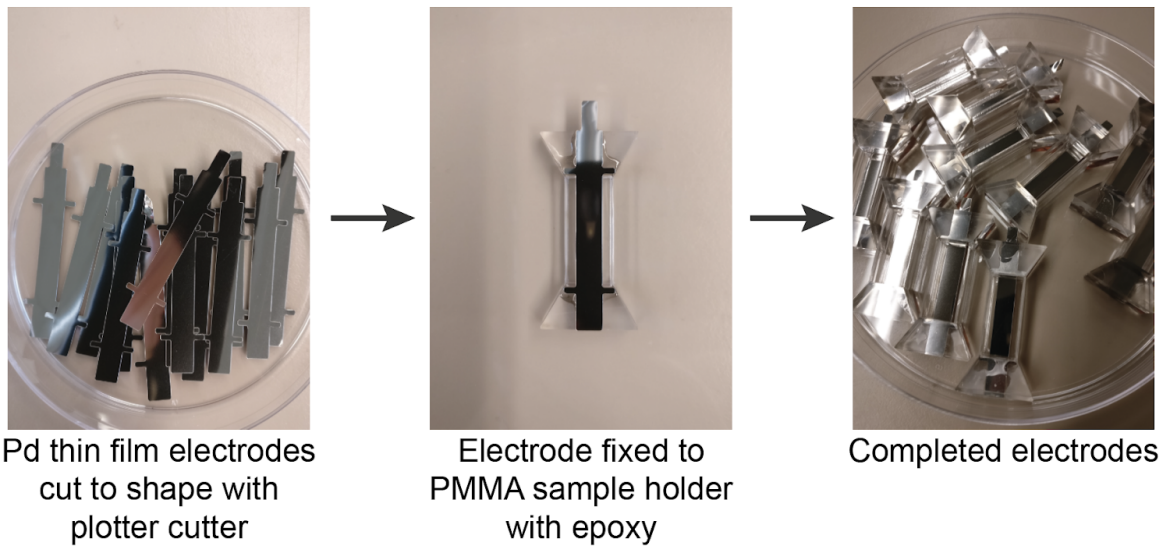


Figure A1.3 Images of each stage of the sample assembly workflow for Pd|substrate electrodes.

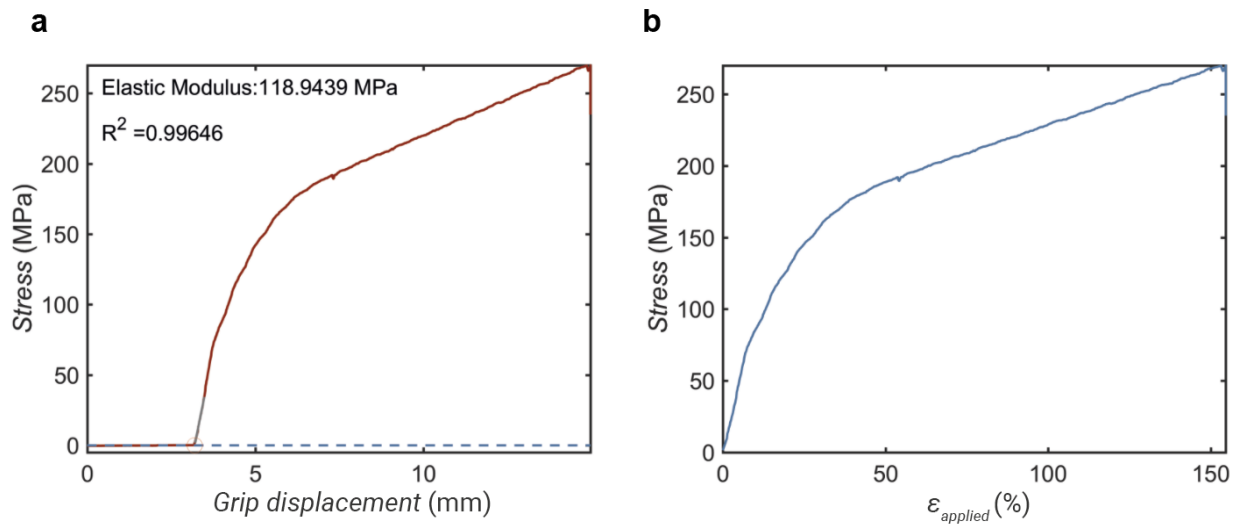


Figure A1.4 a) Plot of a prototypical tensile curve collected using the TED for Kapton 300HN samples. Stress was calculated from measured force using equation S1. The linear region (i.e., elastic region) was linearly fit and the slope of the resulting line of best fit represents the elastic

modulus (annotated on the graph with the R^2 value). The x-intercept of the linear fit was taken as the grip displacement at 0% strain, this calibration is called a “toe correction”. **b)** Plot of the stress vs. strain relationship for Kapton 300HN. The $\epsilon_{\text{applied}}$ axis was calculated from the measured displacement using equation S2.

$$\text{Stress} = \frac{F_{\text{measured}}}{A_{\text{crosssection}}} \quad (\text{Eq. A1.1})$$

$$\epsilon_{\text{applied}} = \frac{\Delta L_{\text{sample}}}{L_{\text{initial}}} \quad (\text{Eq. A1.2})$$

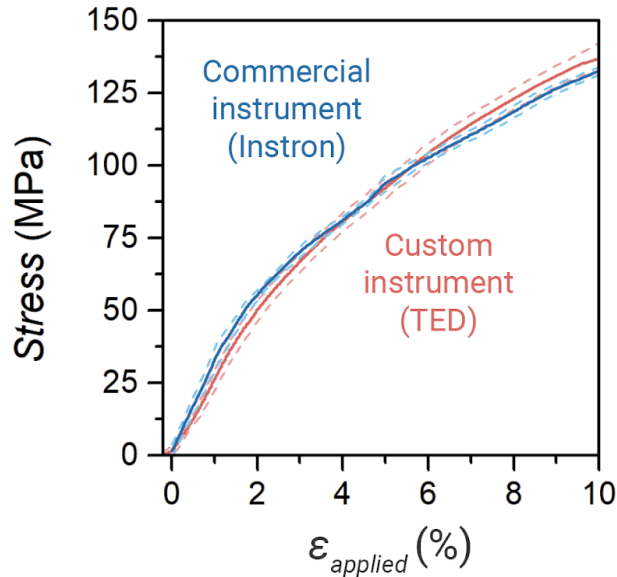


Figure A1.5 Tensile curves for Kapton 300HN collected using the TED (red) and commercial instrumentation (blue). Solid lines represent the average of five samples collected with each apparatus. Measurement uncertainty is shown with dotted lines and represents ± 1 standard deviation of the average stress at each strain.

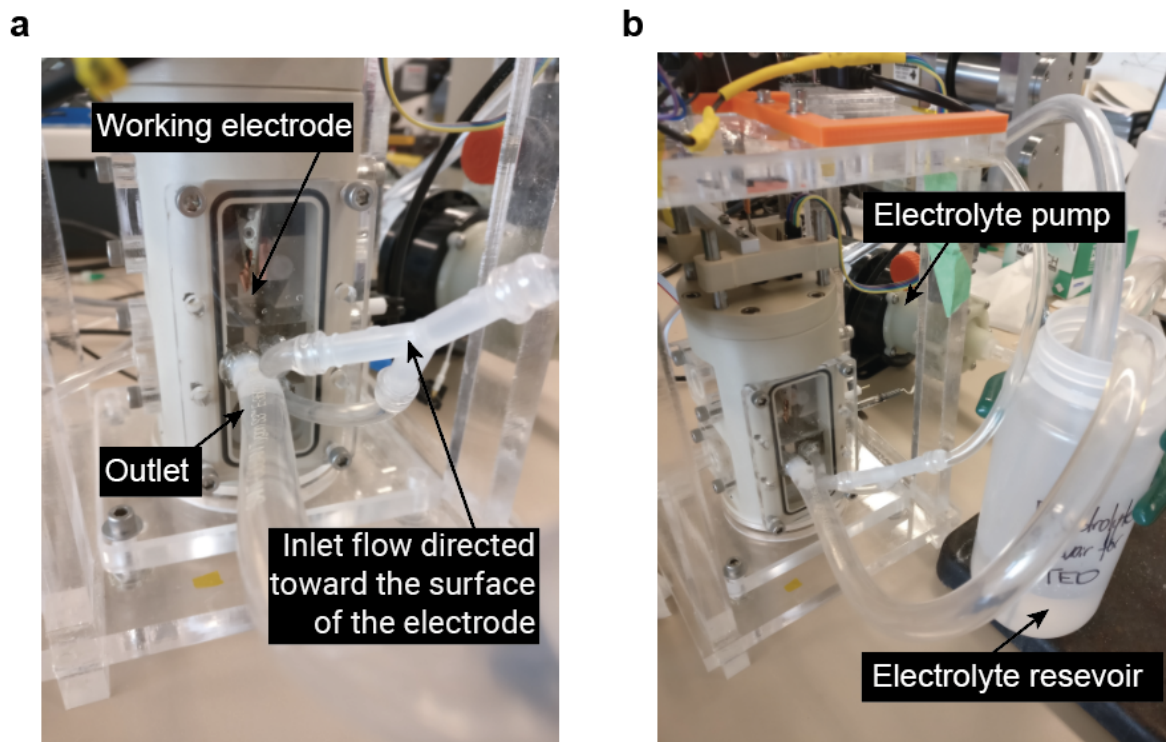


Figure A1.6 a) Image highlighting the modifications to the TED to enable flow coulometry to measure the H:Pd ratio of the palladium electrode. Three additional ports were laser cut into the transparent PMMA sample loading port and Tygon tubing was used to connect the dual inlet and single outlet ports to the pump and electrolyte reservoir. **b)** Image of the complete setup for coulometry measurements showing the electrolyte reservoir and centrifugal magnetic drive pump.

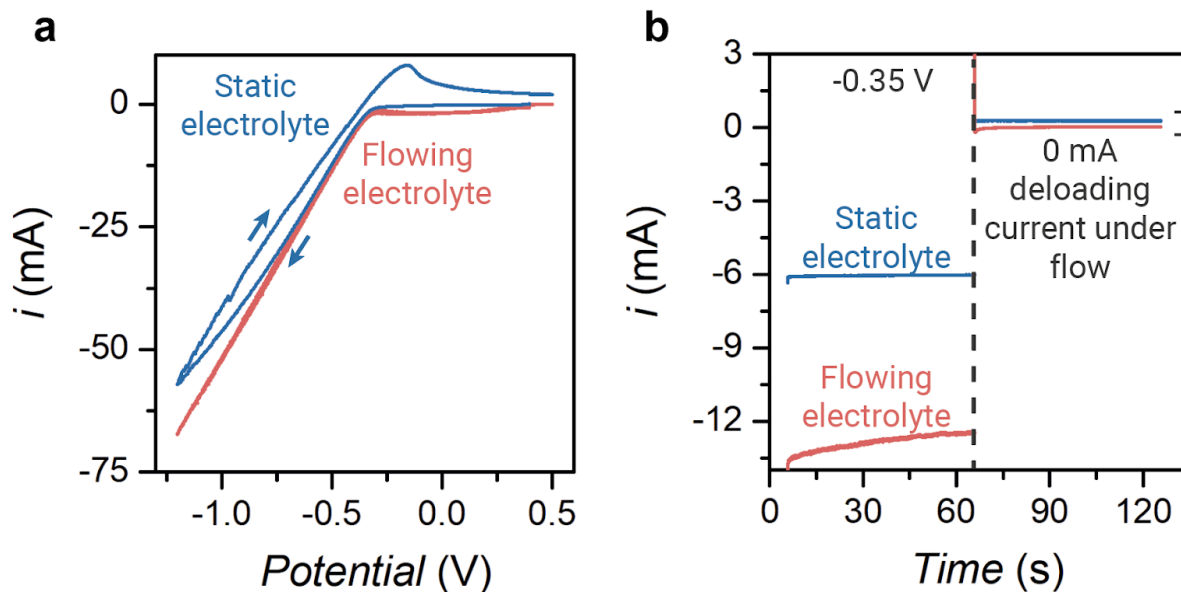


Figure A1.7 a) Cyclic voltammograms on a platinum|substrate electrode collected in flowing and static electrolyte. The oxidative current peak near -0.25 V vs. Ag/AgCl was not present for the measurement in flowing electrolyte, indicating successful removal of surface hydrogen bubbles. **b)** Plot of the coulometric stripping chronoamperograms for a platinum|substrate electrode.²²⁰ When an oxidative potential was applied, the platinum electrode exposed to flowed electrolyte equilibrates to 0 mA of current, indicating that the hydrogen gas was removed from the surface of the electrode and hydrogen oxidation reaction is successfully suppressed.

A1.2 Measuring the effect of mechanical strain on HER and H:Pd at a palladium electrode

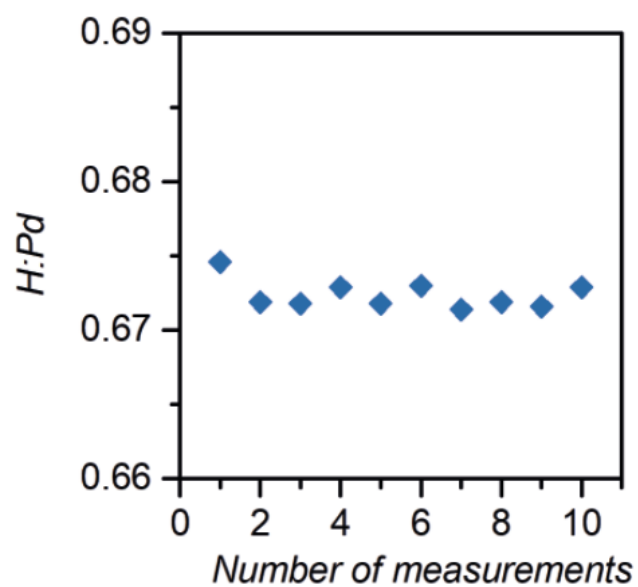


Figure A1.8 Plot of the H:Pd ratio vs. the number of repeated coulometry measurements for an unstrained Pd|substrate electrode.

Table A1.2 Linear fit parameters for each replicate measurement of the % change in H:Pd ratio as a function of applied tensile strain.

Sample	Slope	Intercept	R²
sample 1	-0.327	-0.009	0.95
sample 2	-0.428	-0.002	0.99
sample 3	-0.647	-0.031	0.97
sample 4	-0.698	-0.098	0.98
average	-0.525	-0.035	-
standard deviation	0.176	0.044	-

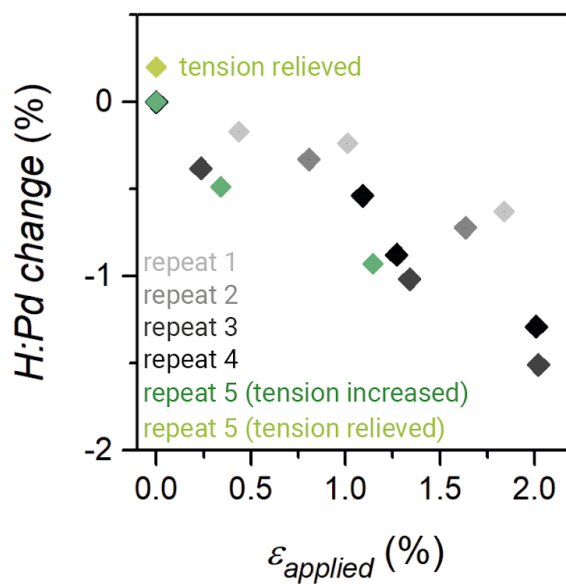


Figure A1.9 Plot of the % change in the H:Pd ratio for five distinct Pd|substrate electrodes strained incrementally. The H:Pd ratio decreased with increasing $\epsilon_{\text{applied}}$ for every electrode tested. Repeat 5 was strained to $\epsilon_{\text{applied}} = 1.2\%$ then strain was relieved and the change in H:Pd ratio consequently increased from -1.0% to 0.2% .

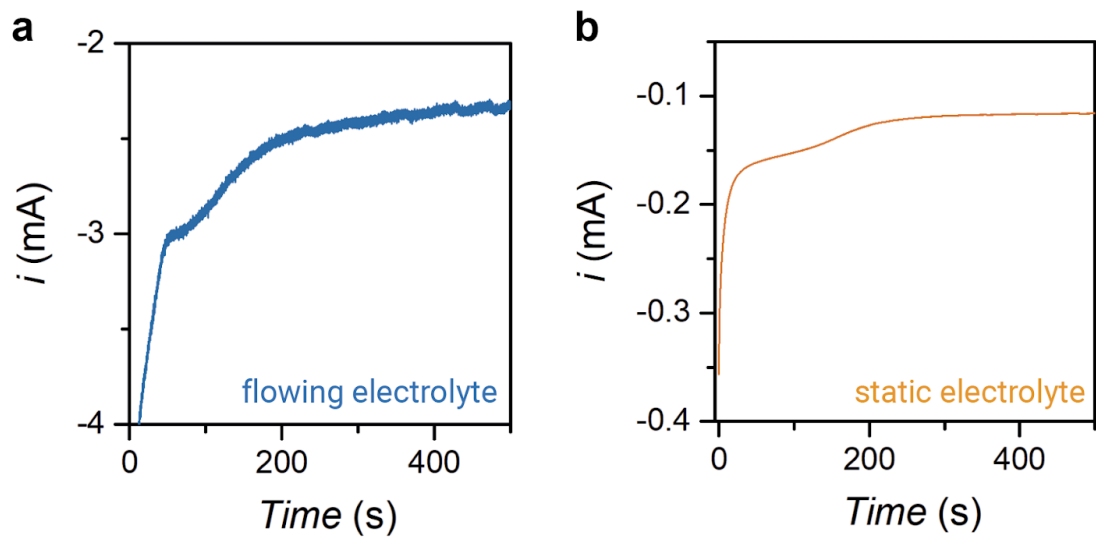


Figure A1.10 Comparison of chronoamperograms of a Pd|substrate electrode under **a)** flow and **b)** static electrolyte. A higher signal to noise ratio was observed for the measurement collected in static electrolyte.

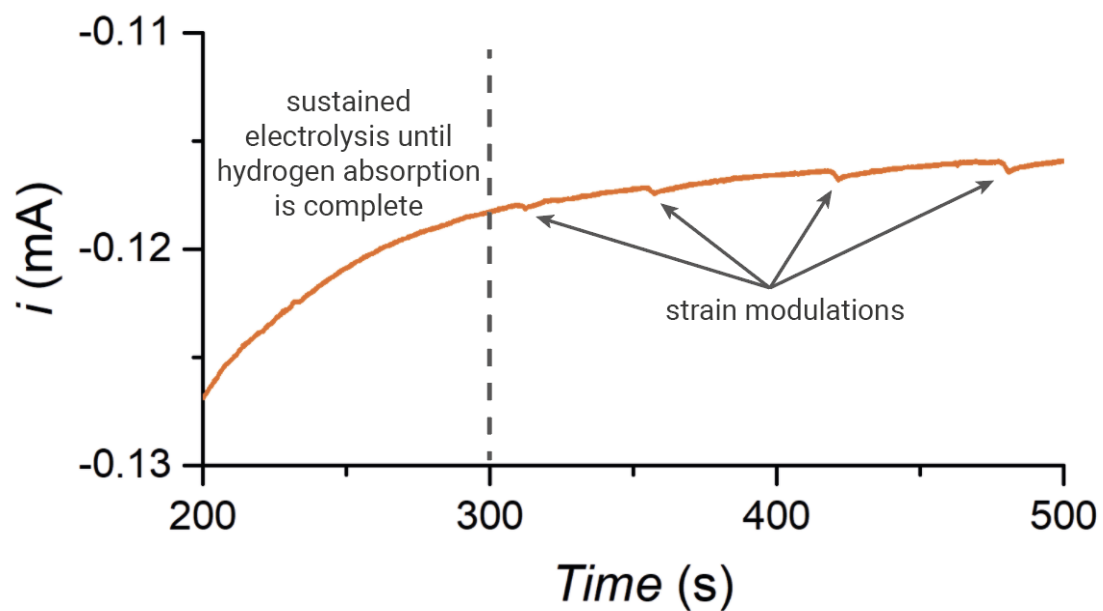


Figure A1.11 Prototypical chronoamperometric curve showing equilibration of current throughout the first ~ 300 s of the experiment. After current became approximately constant after 300 s of electrolysis, $\epsilon_{\text{applied}}$ was increased stepwise and an increase in current was observed.

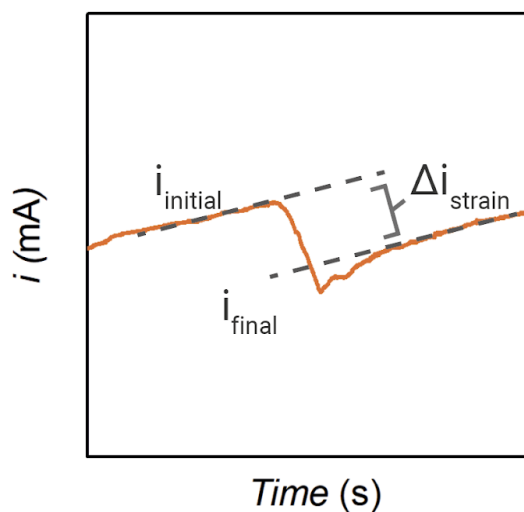


Figure A1.12 Throughout the duration of the experiment the HER current slowly decreases as hydrogen bubbles accumulate on the surface of the electrode. We performed a correction to isolate

the effect of $\varepsilon_{\text{applied}}$ on HER activity by adding the change in current (Δi) to initial current (i_{initial}) and report the total % change in current.

$$\% \text{ change} = \left(\frac{\Delta i}{i_{\text{initial}}} \right) \times 100\% \quad (\text{Eq. A1.3})$$

Table A1.3 Polynomial fit parameters for each replicate measurement of the % change in HER activity as a function of applied tensile strain. The equation of the polynomial fit takes the form shown in Equation S4.

Sample	a	b	c	R²
sample 1	0.200	0.538	-0.220	0.95
sample 2	0.258	0.143	-0.012	0.99
sample 3	0.224	0.190	0.068	0.99
sample 4	0.256	0.025	0.006	0.99
average	0.234	0.224	-0.039	-
standard deviation	0.027	0.220	0.125	-

$$y = ax^2 + bx + c \quad (\text{Eq. A1.4})$$

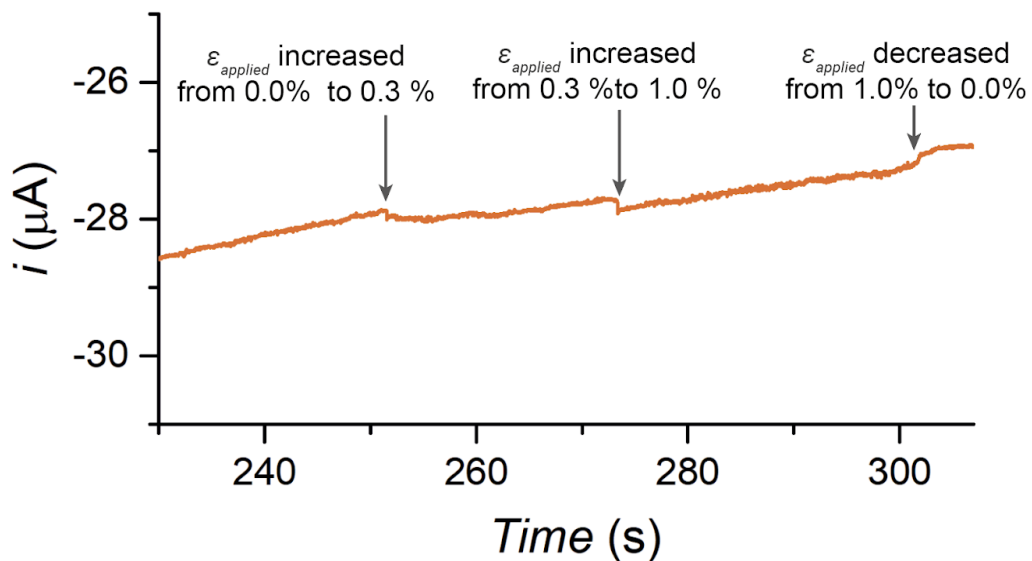


Figure A1.13 Chronoamperometric plot of HER activity vs. time. We tested the reversibility of the strain effect on HER by adjusting strain up to 1.0 % in two increments, then relieving strain back to 0.0 %. Increasing tensile strain increased HER activity, and relieving strain decreased HER activity.

A1.3. Correlating applied mechanical strain to palladium lattice strain using X-ray diffraction

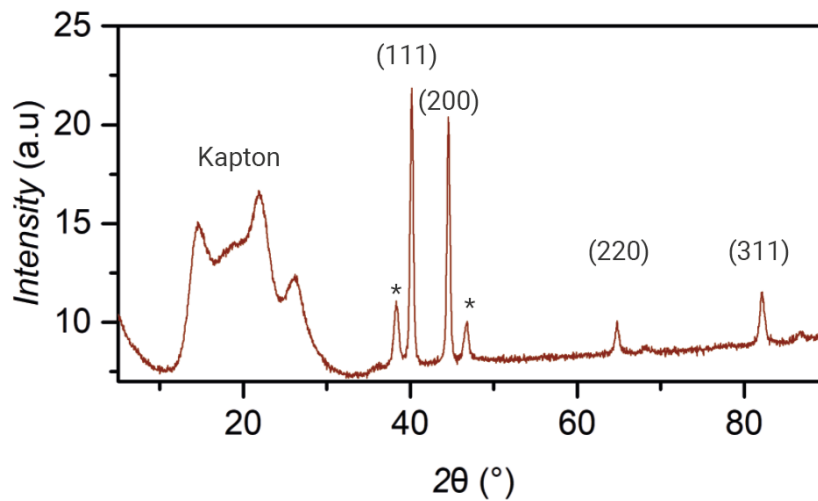


Figure A1.14 Prototypical XRD of a Pd|substrate sample with the Bragg reflections for each crystal facet annotated. (*) indicates diffraction originating from the 20 nm gold conducting layer.

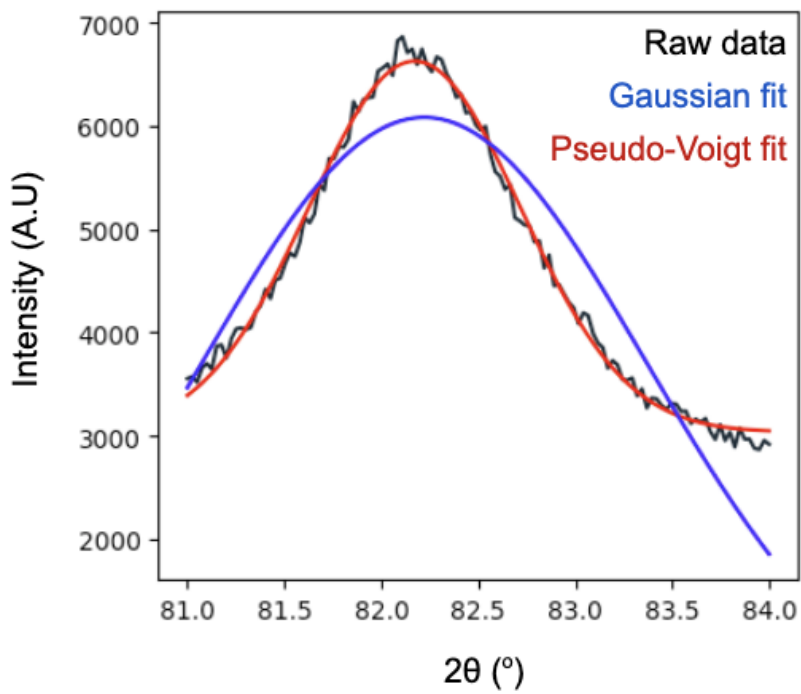


Figure A1.15 X-ray diffraction pattern for the Pd(311) reflection. The quality of fit for the Pd(311) peak was compared for Gaussian and Pseudo-Voigt functions using a Python script. The mean of the Pseudo-Voigt function was taken as the reflection peak position.

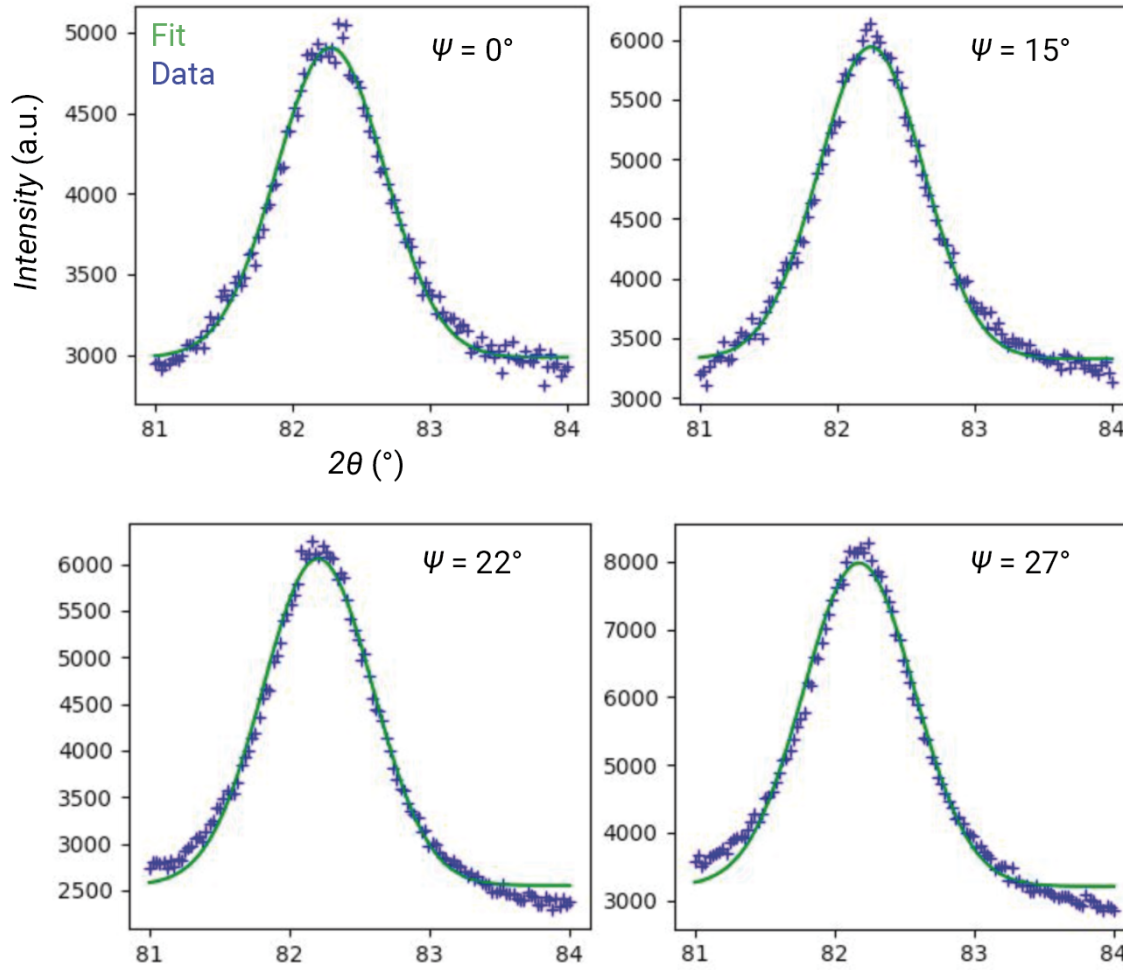


Figure A1.16 Prototypical dataset for a $\epsilon_{\text{macrostrain}}$ measurement. Peak position of the Pd(311) reflection was determined for each angle by fitting the raw data (blue) to a pseudo-Voigt function (green) using a Python script.

Table A1.3 Variables and values for measuring lattice macrostrain at a palladium electrode

Variable	Description	Value
d ₃₁₁	Interplanar spacing for the Pd(311) Bragg reflection	Calculated from (311) reflection using Bragg's law
	Euler angle measured between the sample normal and a diffraction plane ²²¹	Calculated from each angle
11A	Lattice macrostrain resulting from applied strain. Denoted in this work as macrostrain	Reported for each applied strain in Figure 6c
'	Poisson's ratio for palladium	0.35
s	Poisson's ratio for Kapton	0.35
33R	Residual strain in the metal film perpendicular to the direction of applied strain	0

Equation A1.4 Equation used to determine macrostrain by analyzing the Pd(311) diffraction peak position XRD. This analysis was adapted from similar measurements made on gold and tungsten thin films.⁸⁶

$$\ln(d_{311}) = \underbrace{\epsilon_{11}^A}_{y} \left(1 + \frac{\nu'(1-\nu_s)}{1-\nu'} \right) \underbrace{\sin^2 \psi}_{m} + \underbrace{\epsilon_{33}^R}_{x} - \frac{\nu'(1-\nu_s)}{1-\nu'} \underbrace{\epsilon_{11}^A}_{b} + \ln\left(\frac{1}{\sin \theta_0'}\right)$$

Equation A1.5 Equation of the linear fit of data in Figure 5c up to 2.1% applied strain.

$$\epsilon_{macrostrain} = 0.11 \times \epsilon_{applied} + 0.06$$

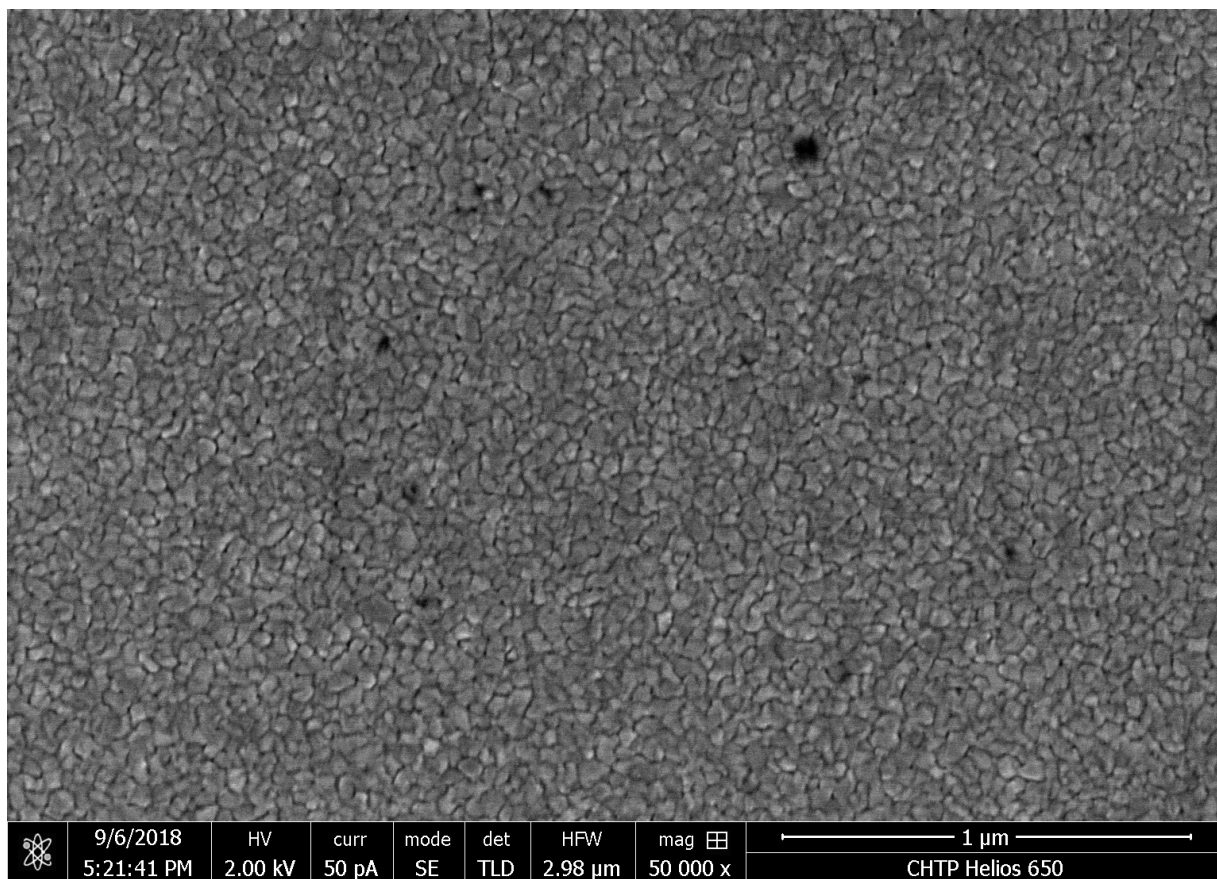


Figure A1.17 Scanning electron micrograph of the surface of a Pd|substrate sample prior to electrochemical experiments. The film is nanocrystalline with a grain size of approximately 50 nm.

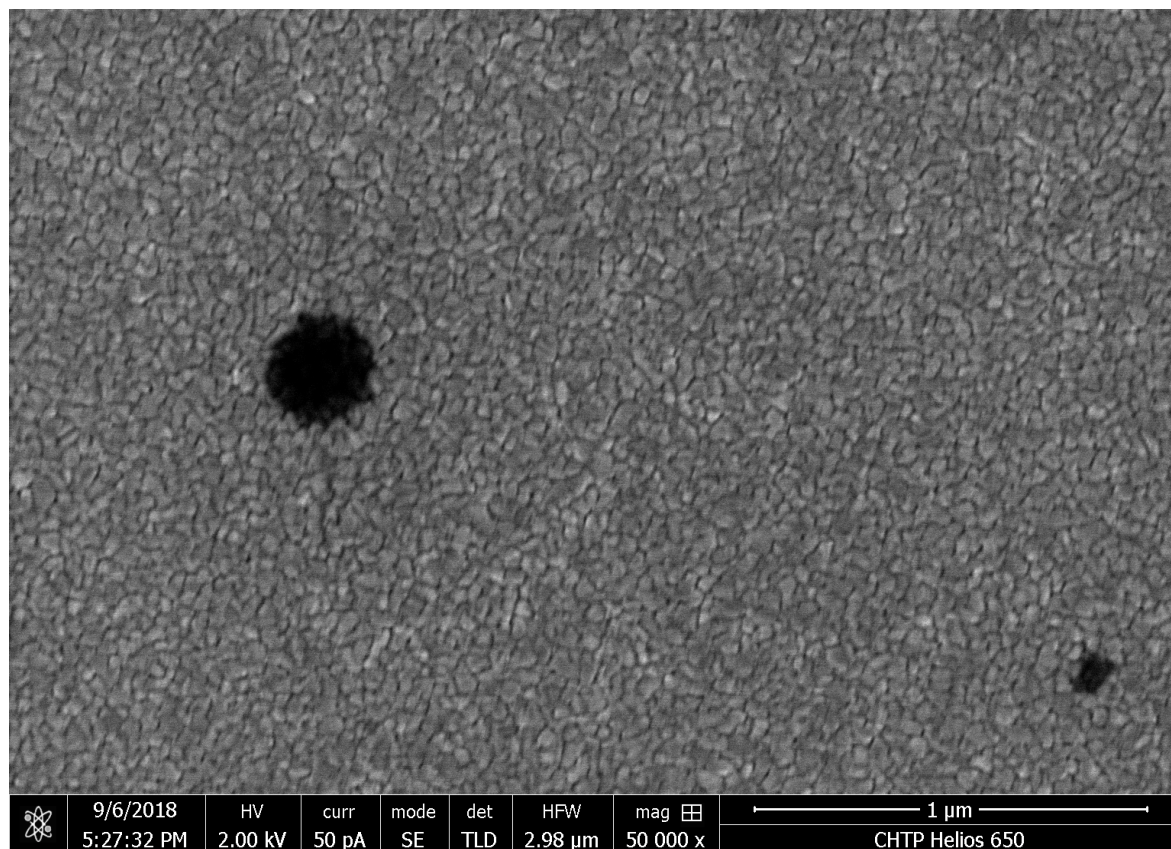


Figure A1.18 High-magnification scanning electron micrograph of the surface of a Pd|substrate sample exposed to 5.5% strain and a sustained electrolysis for 7500 s. No grain growth, boundary formation or any discernible change in surface morphology is observed by qualitative analysis. The dark spots on the film are carbon deposition from the decomposition of organic impurities by the electron beam.

A.1.3 Quantification of electrolysis products using gas chromatography

I experimentally verified that H₂ gas was the only product of the electrolysis reaction. For this control experiment we installed a Pd|substrate electrode into the TED, filled the instrument with 80 mL of H₂SO₄, fit a thin (0.5 mm ID, HPLC grade) tube through a port in the headspace of the cell, and bubbled compressed air into the electrolyte at a rate of 20 mL/min (see figure below

for the basic setup). I connected the TED to an in-line GC through the second headspace port to quantify the composition of gaseous effluent leaving the reactor.

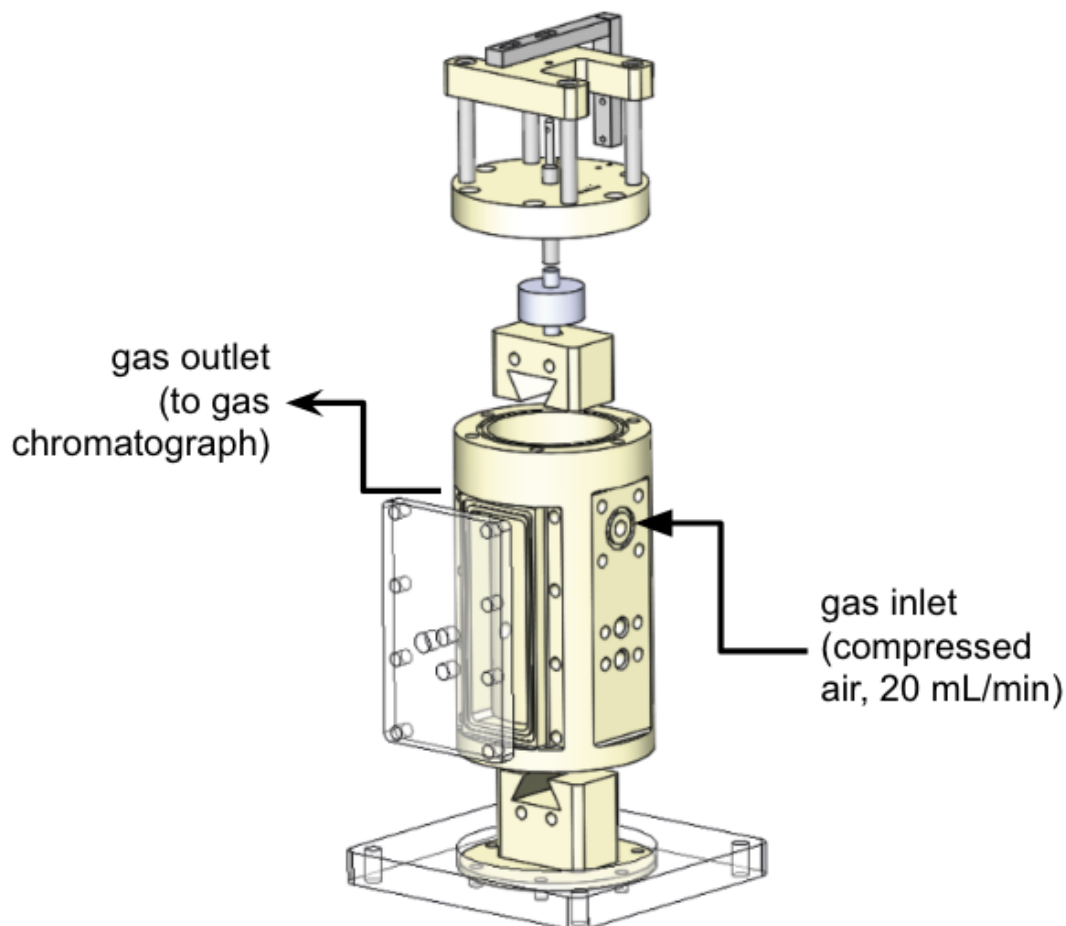


Figure A1.19 Simplified setup for conducting in-line gas chromatography experiments in the TED. The compressed air was bubbled into the electrolyte at a rate of 20 mL/min which continuously flowed the headspace gas into the gas chromatograph for quantification. This setup was inspired by setups used for CO₂ reduction experiments in our group.²²²

To produce sufficient H₂ gas to detect using the GC (SRI, multigas analyzer), I conducted electrolysis at a constant potential of -1.9 V vs. Ag/AgCl, which mediated a current between 107

and 126 mA. I collected chromatographs every 1500 s, for a total of 9000 s (6 samples total), and used the integrated peak area to determine the concentration of H₂ in the effluent gas stream using Equation S5 (the linear fit of a 3-point calibration curve). The Faradaic efficiency was calculated (using Equation S6) to be 100 ± 6 % based on this calibration. These data validate our assumption that H₂ gas is the exclusive product of the electrolysis reaction.

Table A1.4 Gas chromatographic analysis of electrolysis products

Area of H ₂ peak (a.u.)	Concentration of H ₂ in gas stream (ppm)	Partial current for H ₂ (mA)	Faradaic efficiency (%)
1394	16412	126	107
1674	19714	117	104
1824	21483	107	93
1432	16960	111	96
2178	25658	118	94
1319	15528	119	104

Equation A1.6 Equation of the linear fit for a 3 point calibration of the SRI GC used in this study to quantify effluent gas concentration.

$$y = 11.8x - 27$$

Equation A1.7 Equation used to calculate Faradaic efficiency

$$FE = \frac{n_k F x_k F_m}{I}$$

Where n_k is the number of electrons exchanged, F is Faraday's constant ($F = 96,485 \text{ C/mol}$), x_k is the mole fraction of the gas k in the gaseous mixture analyzed, F_m is the molar flow rate in mol/s, and I is the total current in A. The molar flow rate is derived from the volume flow rate F_v by the relation $F_m = pF_v/RT$, with p being the atmospheric pressure in Pa, R the ideal gas constant of 8.314 J/mol K and T the temperature in K.

Appendix 2: Chapter 4

A2.1 Palladium membrane flow cell and experimental setup

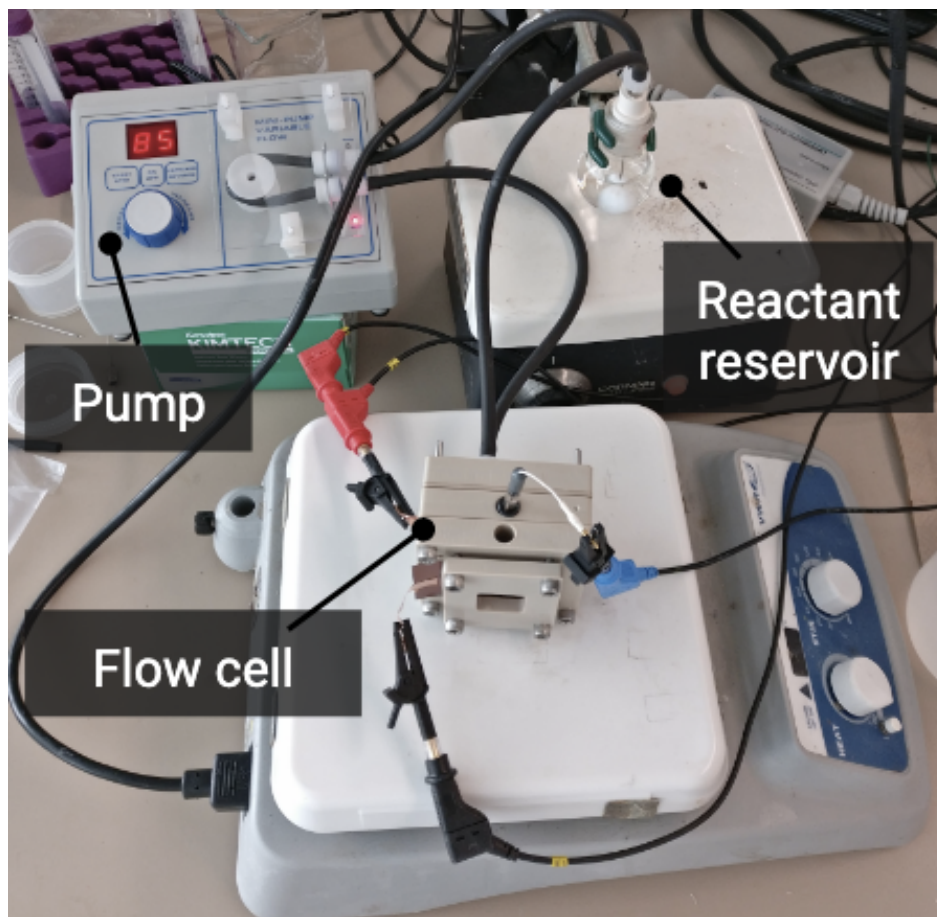


Figure A2.1 Labelled image of the functioning setup including the peristaltic pump, flow cell and reactant reservoir.

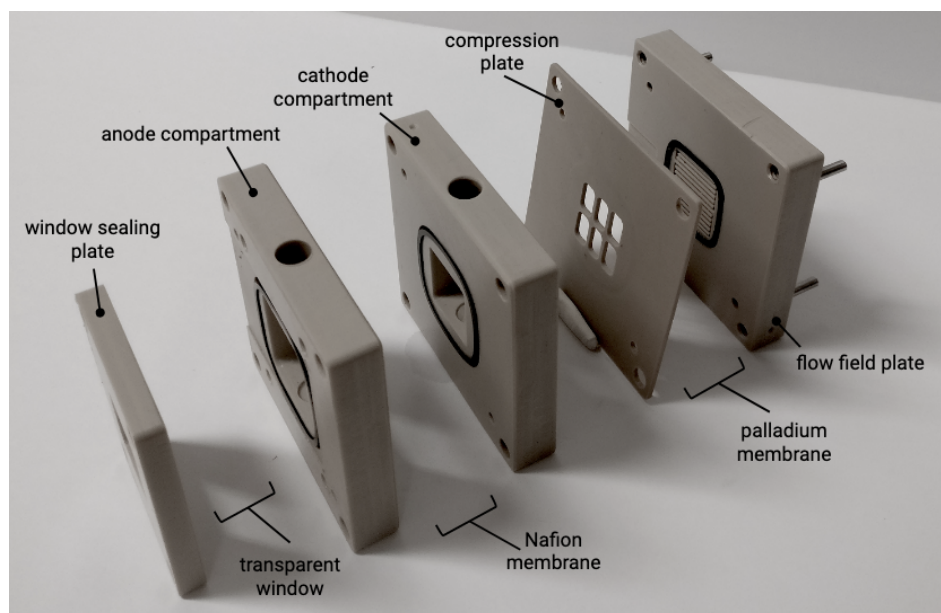


Figure A2.2 Labelled image of the electrocatalytic palladium membrane flow cell reported in this work

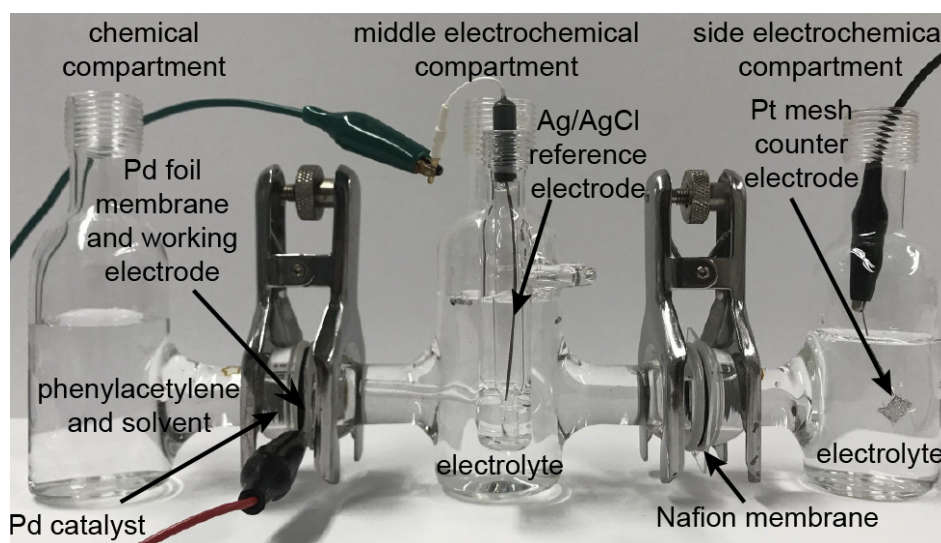


Figure A2.3 Labelled image of the electrocatalytic palladium membrane H-cell reported previously by our group.¹⁷⁸ Reprinted with permission from ref. 2. Copyright 2018 American Chemical Society.

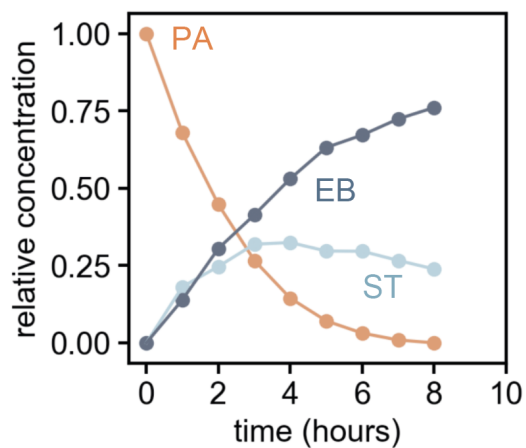


Figure A2.4 Concentration versus time plot for the hydrogenation of phenylacetylene in an ePMR H-cell. The phenylacetylene (PA) starting material was consumed after 8 hours of continuous electrolysis at 100 mA/cm², producing styrene (ST) and ethylbenzene (EB).

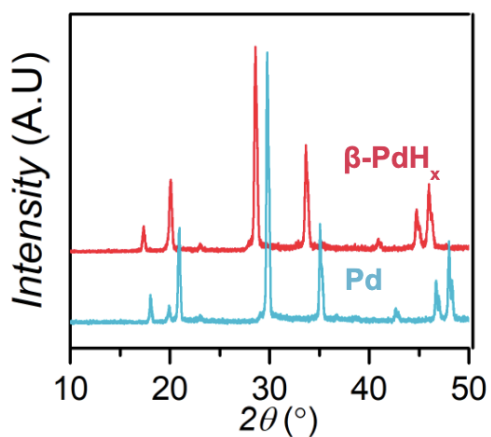


Figure A2.5. X-ray diffraction patterns of the as-prepared palladium membrane prior to electrolysis (Pd), and following electrolysis, during which the membrane absorbs hydrogen to form the hydride phase (β -PdH_x).

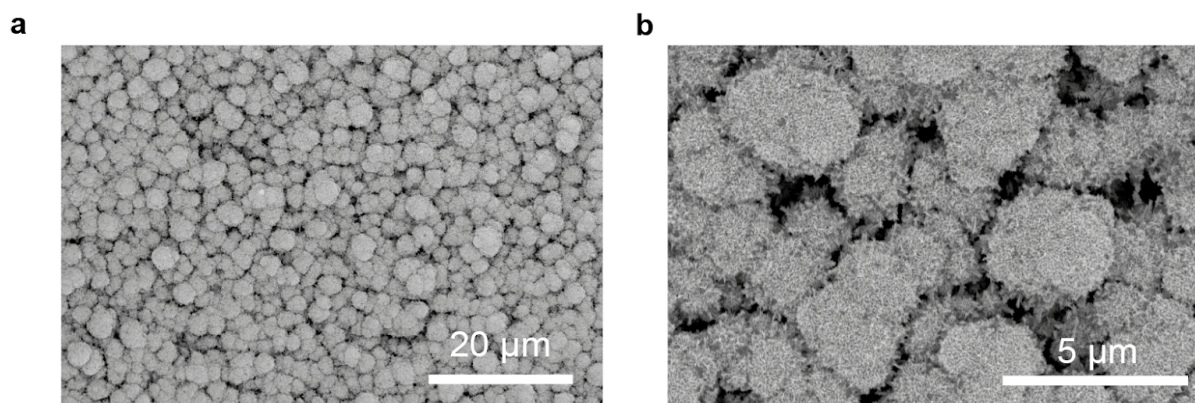


Figure A2.6 Scanning electron microscope images of the electrodeposited palladium electrocatalyst deposited on the hydrogenation surface of the palladium membrane at a magnification of; a) 2000, and b) 10000 times.

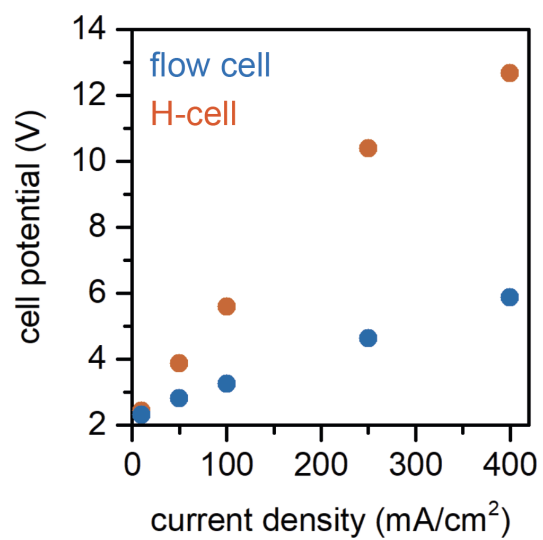


Figure A2.7 Plot of the cell voltage required to drive galvanostatic electrolysis at current densities between 10 and 400 mA/cm² in the previously reported H-cell and the novel flow cell presented in this work.

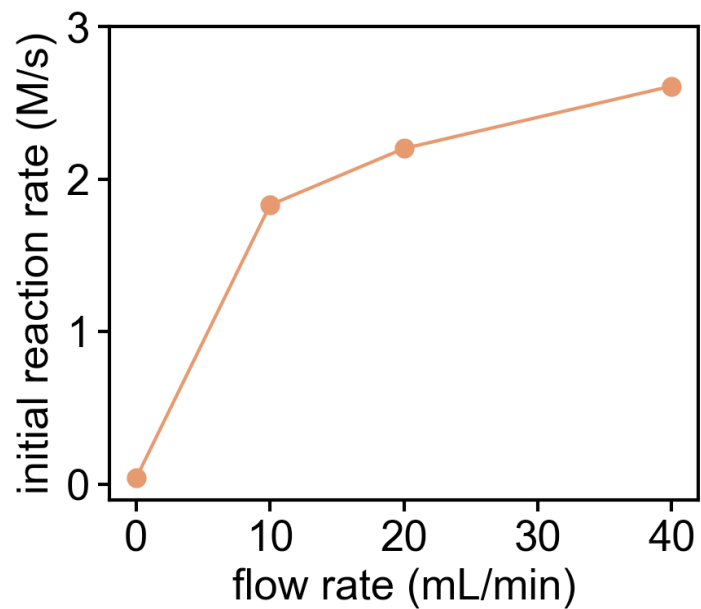


Figure A2.8 Plot showing the flow rate dependence of phenylacetylene hydrogenation rate in an ePMR at 100 mA/cm². The data point taken at 0 mL/min was collected in an H-cell. All other data points were collected using the ePMR flow cell presented in this work.

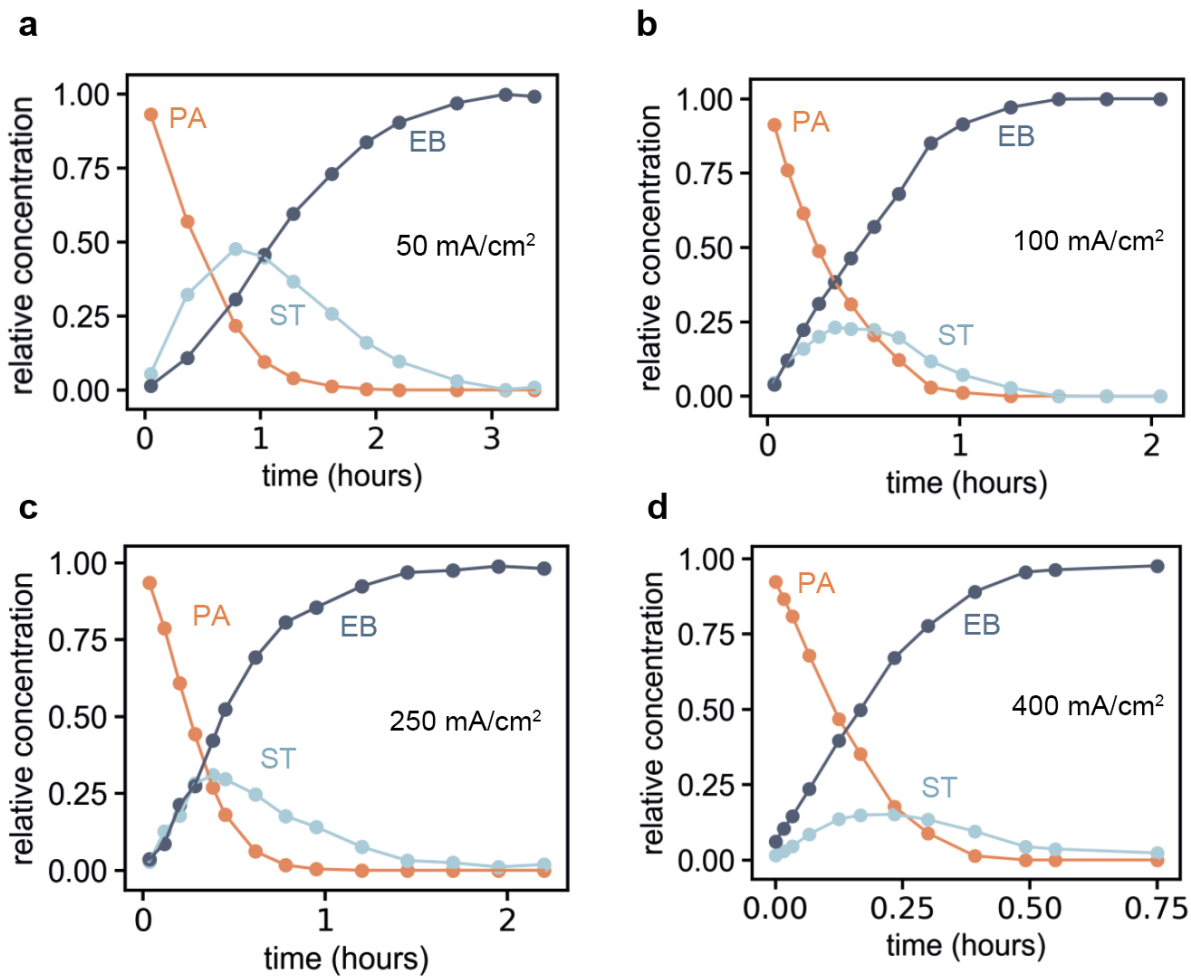


Figure A2.9 a) Plot of a reaction concentration profile for hydrogenation reactions carried out at a) 50 mA/cm² b) 100 mA/cm², c) 250 mA/cm² and d) 400 mA/cm². See Figure S16a for the 10 mA/cm² reaction profile.

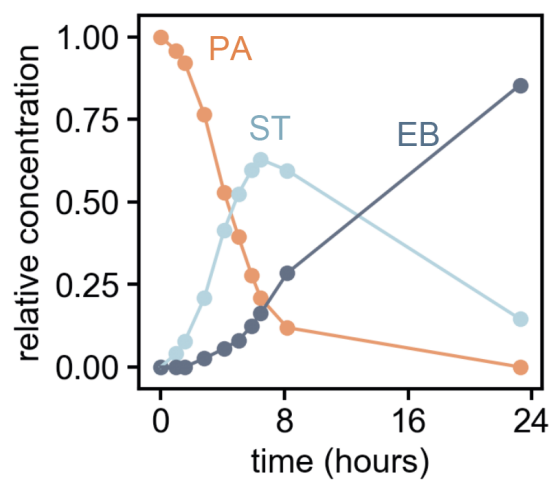
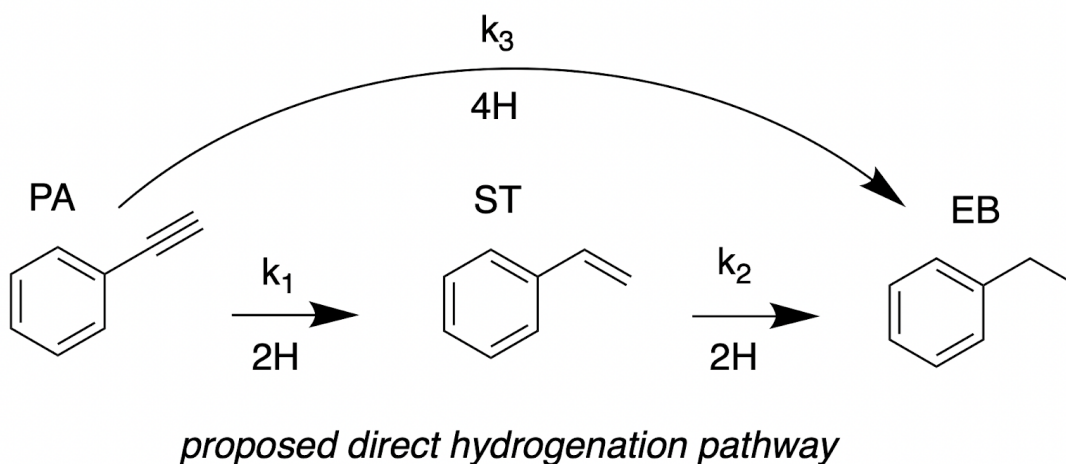


Figure A2.10 a) Plot of a reaction concentration profile for a 0.2 M, 200 mL solution of phenylacetylene, hydrogenated at 100 mA/cm².

A2.2 Kinetic modelling to determine phenylacetylene hydrogenation reaction order



Scheme A2.1. Hydrogenation scheme proposed here which includes a pathway for the direct hydrogenation of phenylacetylene to ethylbenzene. The conventional Horiuti-Polanyi mechanism omits the pathway for direct conversion of phenylacetylene to ethylbenzene (Scheme S2).¹⁷⁸

System of equations for fitting the hydrogenation concentration profiles to **zero-order** reaction kinetics:

$$\frac{dPA}{dt} = -k_1[H]^x - k_3[H]^x = -k'_1 - k'_3 \quad [\text{Eq. A2.1}]$$

$$\frac{dST}{dt} = k_1[H]^x - k_2[H]^x = k'_1 - k'_2 \quad [\text{Eq. A2.2}]$$

$$\frac{dEB}{dt} = k_2[H]^x + k_3[H]^x = k'_2 + k'_3 \quad [\text{Eq. A2.3}]$$

System of equations for fitting the hydrogenation concentration profiles to **first-order** reaction kinetics:

$$\frac{dPA}{dt} = -k'_1[PA] - k'_3[PA] \quad [\text{Eq. A2.4}]$$

$$\frac{dST}{dt} = k'_1[PA] - k'_2[ST] \quad [\text{Eq. A2.5}]$$

$$\frac{dEB}{dt} = k'_2[ST] + k'_3[PA] \quad [\text{Eq. A2.6}]$$

System of equations for fitting the hydrogenation concentration profiles to **second-order** reaction kinetics:

$$\frac{dPA}{dt} = -k'_1[PA]^2 - k'_3[PA]^2 \quad [\text{Eq. A2.7}]$$

$$\frac{dS}{dt} = k'_1[PA]^2 - k'_2[ST]^2 \quad [\text{Eq. A2.8}]$$

$$\frac{dEB}{dt} = k'_2[ST]^2 + k'_3[PA]^2 \quad [\text{Eq. A2.9}]$$

Table A2.1 Comparison of goodness of fit for zero, first and second order reaction models (with respect to the organic reagent) for hydrogenation of phenylacetylene. The highest R² for each current density is highlighted with bold-faced text

Reaction conditions	Order determination		
	R ² zero order	R ² first order	R ² second order
10 mA/cm ²	0.996	0.938	0.857
50 mA/cm ²	0.360	0.984	0.863
100 mA/cm ²	0.449	0.991	0.899
250 mA/cm ²	0.304	0.998	0.933
400 mA/cm ²	0.646	0.990	0.912

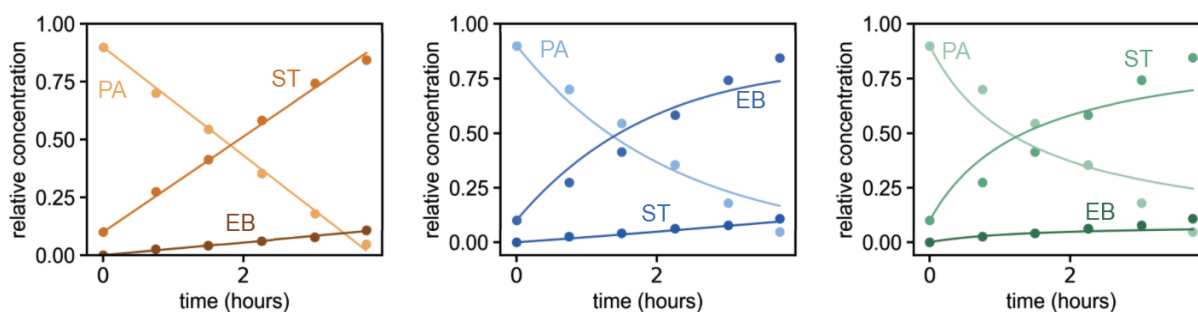


Figure A2.11 Comparison of fits for zero (orange), first (blue) and second (green) order reaction models to determine fit for hydrogenation when **10 mA/cm²** of electrolysis current was applied. Only the first 4 hours of the reaction were fit to each model to simplify the visual comparison. The 0-order equations (orange) provide the best fit.

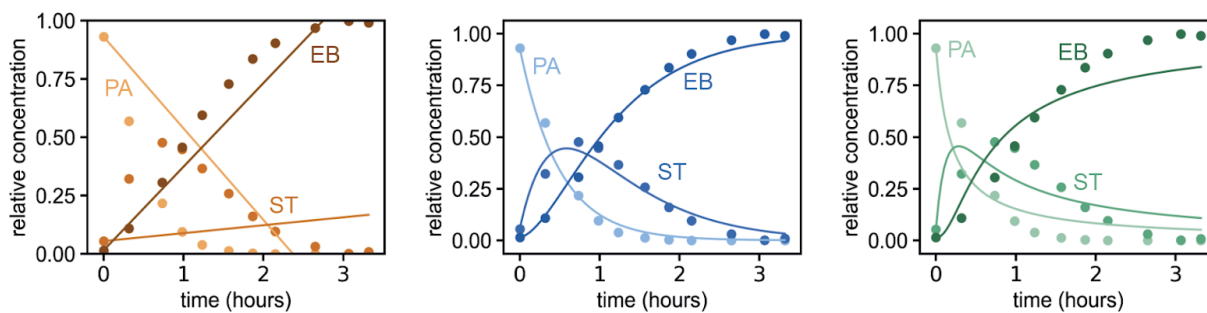


Figure A2.12 Comparison of fits for zero (orange), first (blue) and second (green) order reaction models to determine fit for hydrogenation when **50 mA/cm²** of electrolysis current was applied. The 1st-order equations provide the best fit.

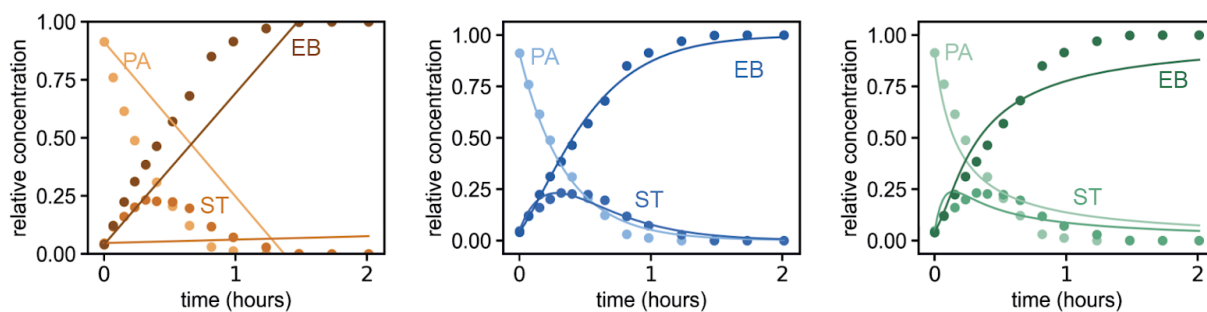


Figure A2.13 Comparison of fits for zero (orange), first (blue) and second (green) order reaction models to determine fit for hydrogenation when **100 mA/cm²** of electrolysis current was applied. The 1st-order equations provide the best fit.

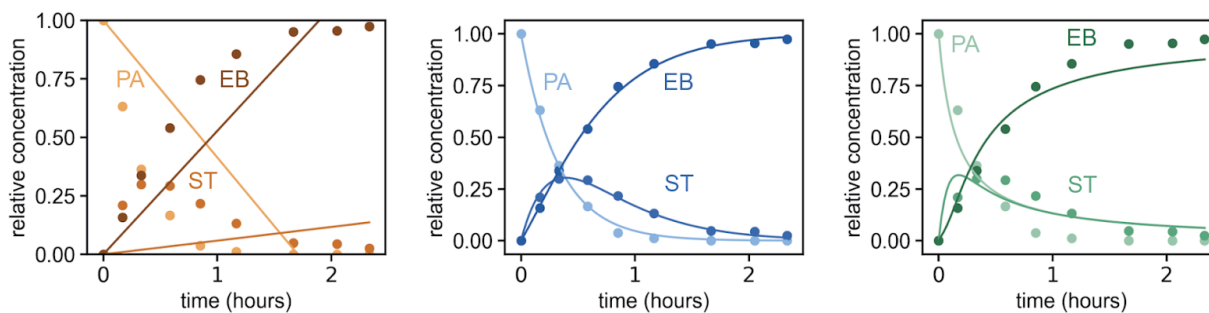


Figure A2.14 Comparison of fits for zero (orange), first (blue) and second (green) order reaction models to determine fit for hydrogenation when 250 mA/cm^2 of electrolysis current was applied. The 1st-order equations provide the best fit.

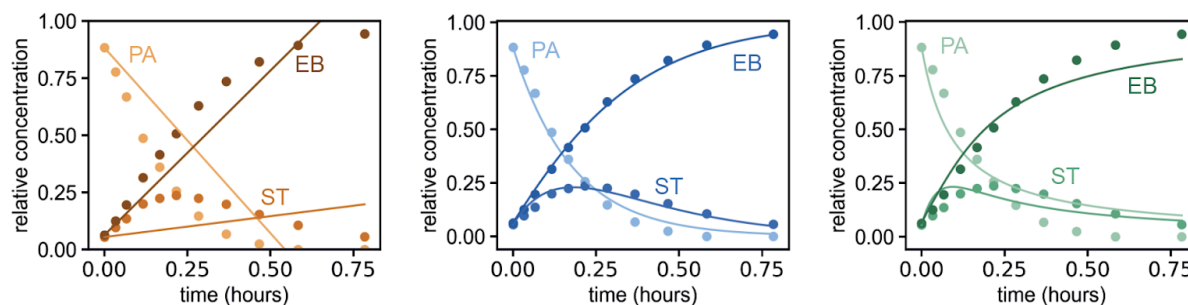
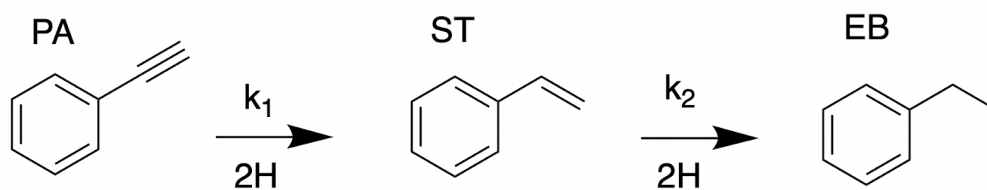


Figure A2.15 Comparison of fits for zero (orange), first (blue) and second (green) order reaction models to determine fit for hydrogenation when 400 mA/cm^2 of electrolysis current was applied. The 1st-order equations provide the best fit.

A2.3 Comparison of hydrogenation mechanisms

Scheme A2.2 Hydrogenation scheme consistent with the well-established Horiuti-Polanyi mechanism¹⁷⁸



Horiuti-Polanyi sequential hydrogenation pathway

System of equations for fits using a **sequential** hydrogenation mechanism, in line with the conventional Horiuti-Polanyi mechanism (Scheme S2):

$$\frac{dPA}{dt} = -k_1[H]^x[PA] = -k'_1[PA] \quad [\text{Eq. A2.10}]$$

$$\frac{dST}{dt} = k_1[H]^x[PA] - k_2[H]^x[ST] = k'_1[PA] - k'_2[ST] \quad [\text{Eq. A2.11}]$$

$$\frac{dEB}{dt} = k_2[H]^x[ST] = k'_2[ST] \quad [\text{Eq. A2.12}]$$

System of equations for fits which includes both the sequential, and also **direct** hydrogenation pathways (Scheme S1):

$$\frac{dPA}{dt} = -k'_1[PA] - k_3'[PA] \quad [\text{Eq. A2.13}]$$

$$\frac{dST}{dt} = k'_1[PA] - k'_2[ST] \quad [\text{Eq. A2.14}]$$

$$\frac{dEB}{dt} = k'_2[ST] + k_3'[PA] \quad [\text{Eq. A2.15}]$$

Table A2.2 Comparison of goodness of fit comparison for the direct and sequential reaction models for phenylacetylene hydrogenation

Reaction conditions	Order determination	
	R ² sequential model	R ² direct model
50 mA/cm ²	0.975	0.980
100 mA/cm ²	0.986	0.990
250 mA/cm ²	0.987	0.997
400 mA/cm ²	0.975	0.990

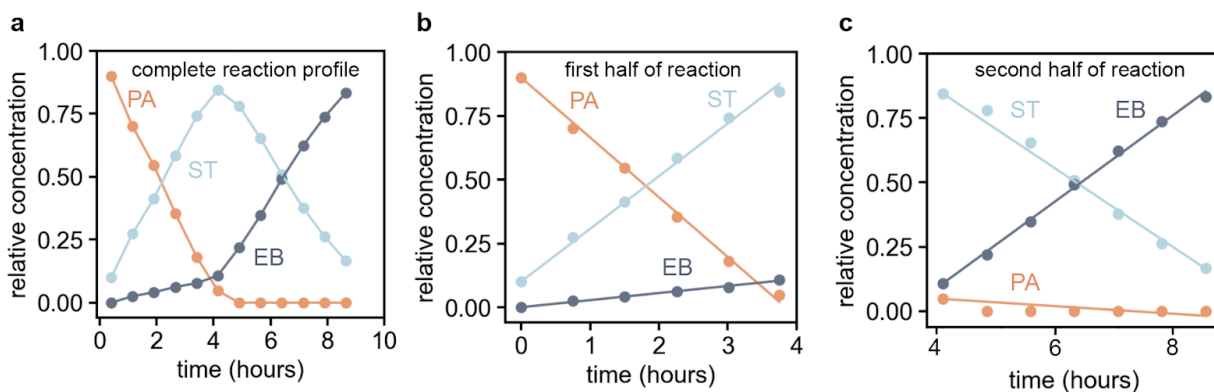


Figure A2.16 a) Plot of the complete reaction profile for phenylacetylene hydrogenation conducted at 10 mA/cm². The first and second 4-hour increments of the reaction were fit to the 0-order kinetic model separately (panels b and c, respectively) to identify the effective rate constants. b) We assume ethylbenzene formation during the first 4 hours of the reaction to correspond to the direct hydrogenation of phenylacetylene to ethylbenzene (see discussion section). The k_3' value was calculated based on this assumption. c) We take ethylbenzene formation during the final 4 hours of the reaction (when there is no phenylacetylene present) to correspond to hydrogenation of styrene to ethylbenzene and calculate k_2' based on this assumption.

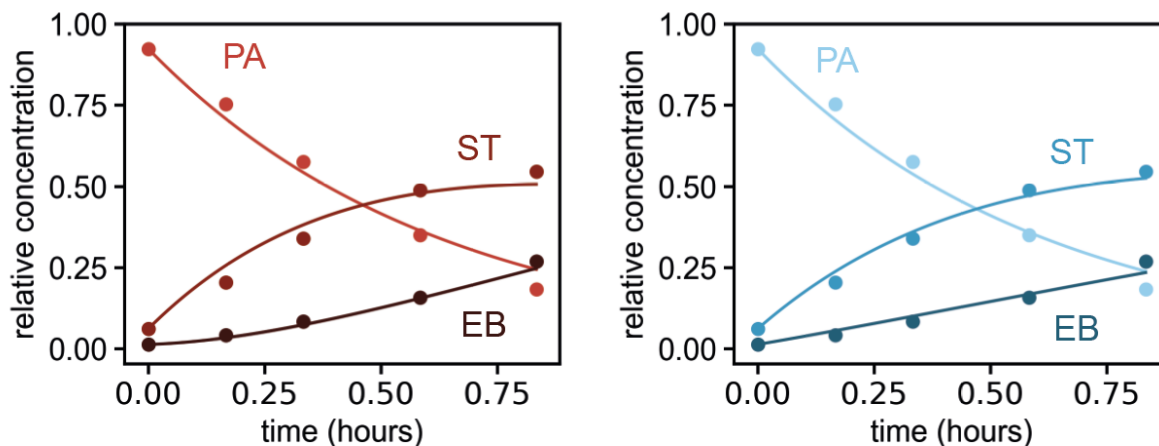


Figure A2.17 Comparison of the fits using the previously reported sequential hydrogenation pathway (red) and the proposed direct hydrogenation pathway (blue) for the hydrogenation of phenylacetylene under 50 mA/cm^2 electrolysis current. The best fit was provided by the system of equations that included a direct hydrogenation pathway.

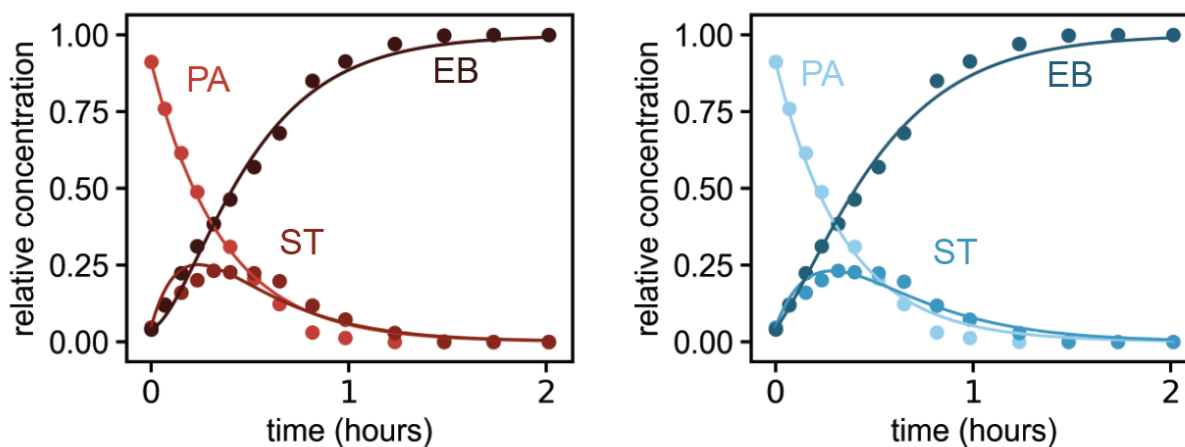


Figure A2.18 Comparison of the fits using the previously reported sequential hydrogenation pathway (red) and the proposed direct hydrogenation pathway (blue) for the hydrogenation of ethylbenzene under 50 mA/cm^2 electrolysis current. The best fit was provided by the system of equations that included a direct hydrogenation pathway.

phenylacetylene under 100 mA/cm^2 electrolysis current. The best fit was provided by the system of equations that included a direct hydrogenation pathway.

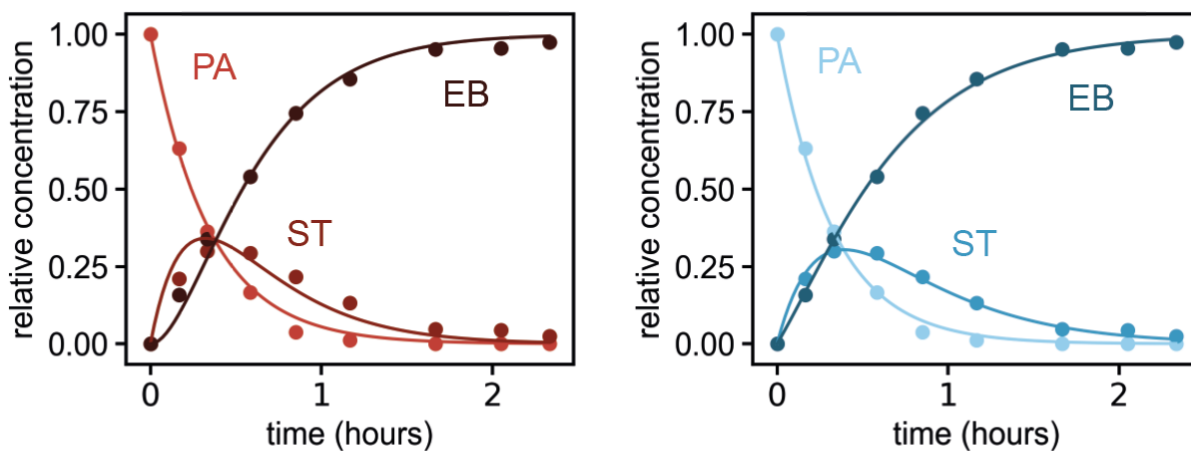


Figure A2.19 Comparison of the fits using the previously reported sequential hydrogenation pathway (red) and the proposed direct hydrogenation pathway (blue) for the hydrogenation of phenylacetylene under 250 mA/cm^2 electrolysis current. The best fit was provided by the system of equations that included a direct hydrogenation pathway.

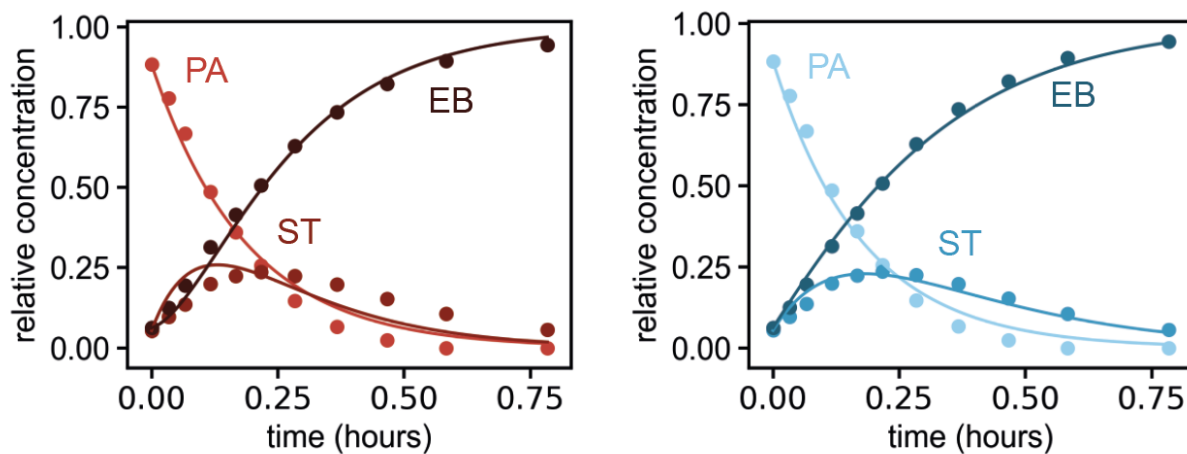


Figure A2.20 Comparison of the fits using the previously reported sequential hydrogenation pathway (red) and the proposed direct hydrogenation pathway (blue) for the hydrogenation of phenylacetylene under 400 mA/cm^2 electrolysis current. The best fit was provided by the system of equations that included a direct hydrogenation pathway.

A2.4 Analysis of hydrogenation reaction rate, selectivity and current efficiency

Table A2.3 Effective rate constants calculated using a kinetic model for the hydrogenation reaction (Scheme S1) carried out at each current densities between 10 and 400 mA/cm²

Reaction conditions	Effective rate constant (k') ^a		
	k ₁ '	k ₂ '	k ₃ '
Current density			
10 mA/cm ²	0.261 ± 0.025 ¹	0.003 ± 0.029	0.029 ± 0.011
50 mA/cm ²	1.500 ± 0.093	1.398 ± 0.240	0.145 ± 0.109
100 mA/cm ²	2.213 ± 0.239	2.378 ± 0.505	0.848 ± 0.009
250 mA/cm ²	2.253 ± 0.214	2.871 ± 1.278	1.182 ± 0.008
400 mA/cm ²	2.987 ± 0.446	5.856 ± 3.162	2.332 ± 0.496

^aNote that the units for the effective rate constants for the 10 mA/cm² reaction are M²/s, and the units for the reactions carried out at 50-400 mA/cm² are M/s.

Equation used to calculate the initial rate of phenylacetylene consumption using effective rate constants in Table S3.

$$\text{Rate}_{\text{initial}} = (k_1' + k_3') \times [\text{PA}]_{\text{initial}} \quad [\text{Eq. A2.16}]$$

Equations used to calculate the current efficiency (CE) of the hydrogenation reaction. Where: volume is the total volume of reactant solution used (25 mL in most cases); i_{total} is the current density multiplied by the geometric size of the Pd membrane; t is the time elapsed between data points, and ; F is Faraday's constant.

$$CE (\%) = (\text{moles of } H \text{ consumed} / \text{moles of } H \text{ produced}) \times 100\% \quad [\text{Eq. A2.17}]$$

$$\text{moles of } H \text{ consumed} = (2 \times \Delta[ST] + 4 \times \Delta[EB]) \times \text{volume} \quad [\text{Eq. A2.18}]$$

$$\text{moles of } H \text{ produced} = (i_{total} \times \Delta t) / F \quad [\text{Eq. A2.19}]$$

A2.5 Measurement of hydrogen absorption and permeation rate at the palladium membrane

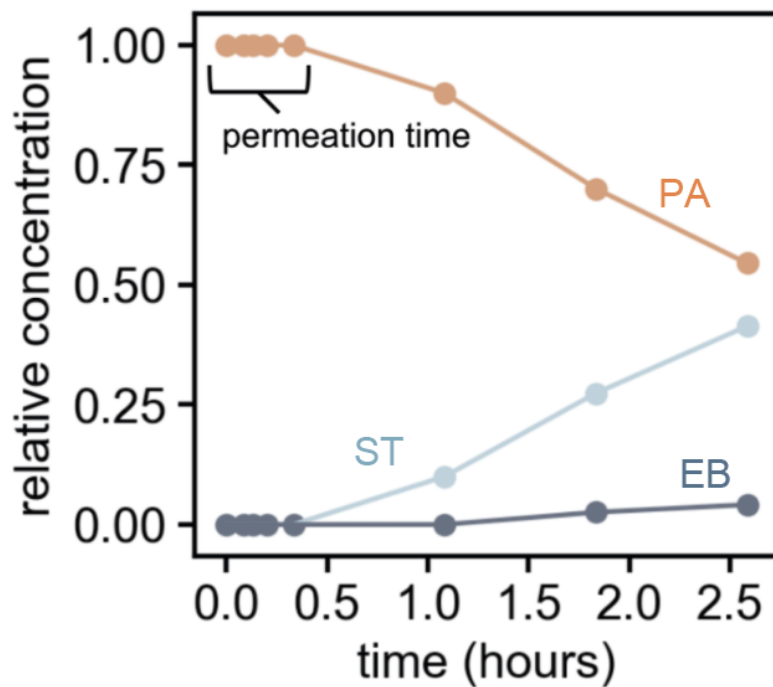


Figure A2.21 Tutorial plot showing a reaction concentration profile with the hydrogen permeation time annotated (which we define as the amount of time elapsed from the start of electrolysis to the first observation of hydrogenated products). See Figure S16a for the complete concentration profile for this reaction.

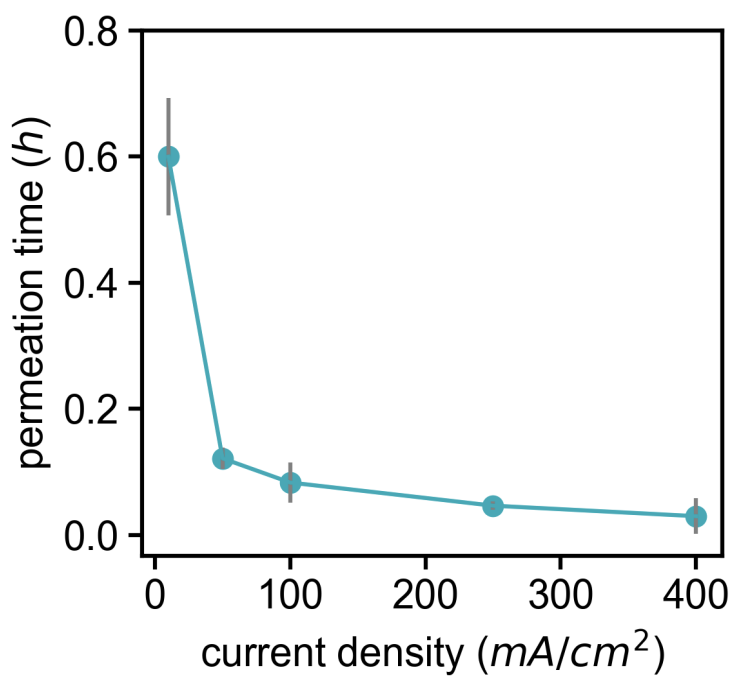


Figure A2.22 Plot showing that permeation time decreases exponentially with increasing current density. Error bars represent ± 1 standard deviation of the mean value for at least 3 reactions.

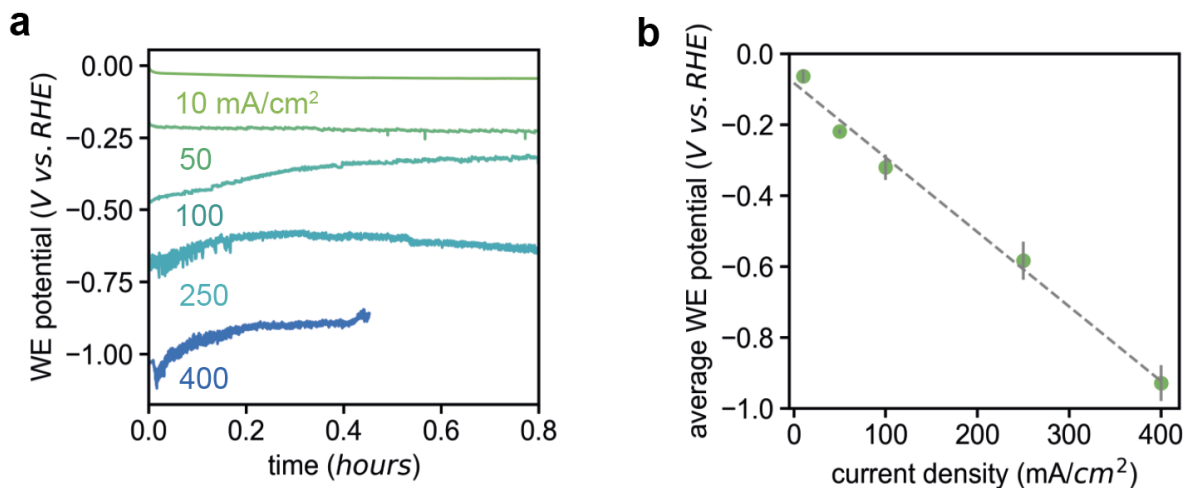


Figure A2.23 a) Overlay of chronopotentiometry traces for each electrolysis current density used in this study. The increase in the WE potential during electrolysis is likely due to hydrogen absorption into the palladium membrane to form β -PdH_x, which exhibits higher HER activity than Pd.⁷⁵ b) Plot of the average potential (vs. RHE) required to mediate electrolysis at each current density. Error bars represent ± 1 standard deviation of the average potential used to drive the galvanostatic electrolysis in panel (a).

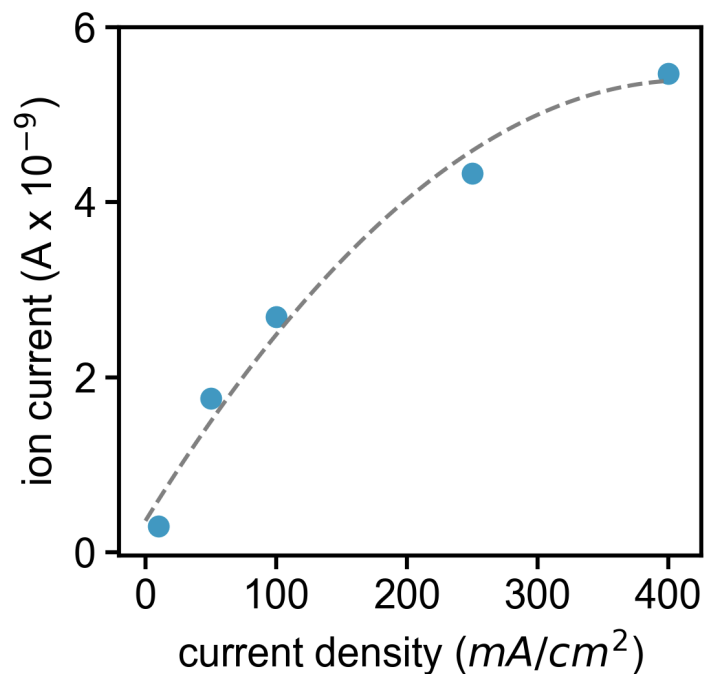


Figure A2.24 The amount of the hydrogen that evolves from the Pd membrane surface in the electrochemical chamber as current density increases is described by a 2nd order polynomial fit ($R^2 = 0.99$; dotted grey line).

Equation describing the relationship between the amount of hydrogen absorbed into the palladium membrane as a function of applied potential (vs. RHE).

$$y = 0.185 \ln|x| + 0.907$$

[A2.20]

Appendix 3: Chapter 5

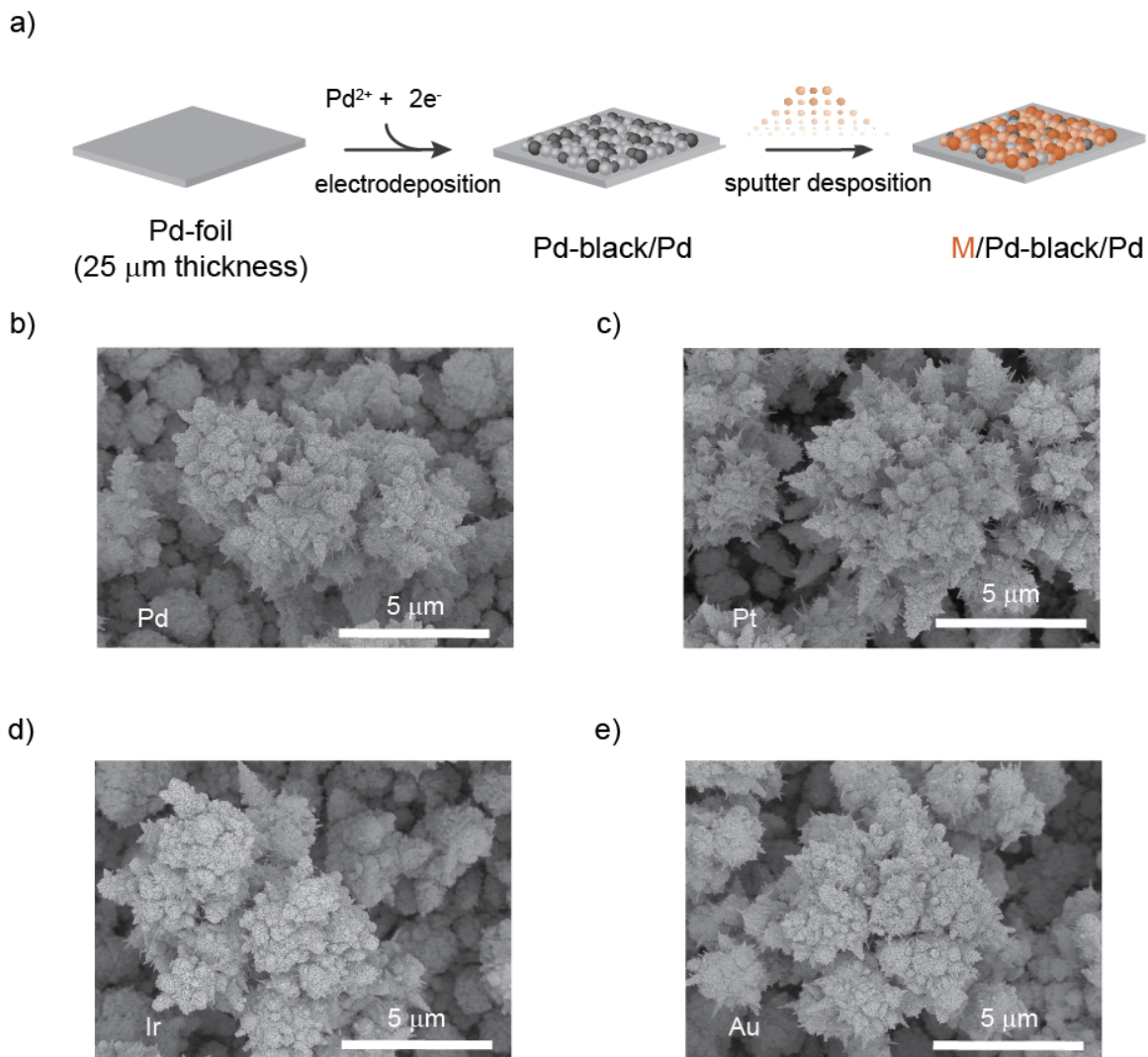


Figure A3.1 Catalyst-coated membrane preparation and the morphology of the catalysts.

a) Schematic representation of catalysts preparation. Scanning electron microscope images of b) electrodeposited palladium black, c) platinum, d) iridium, e) gold sputtered on the palladium black layer at a magnification of 10k.

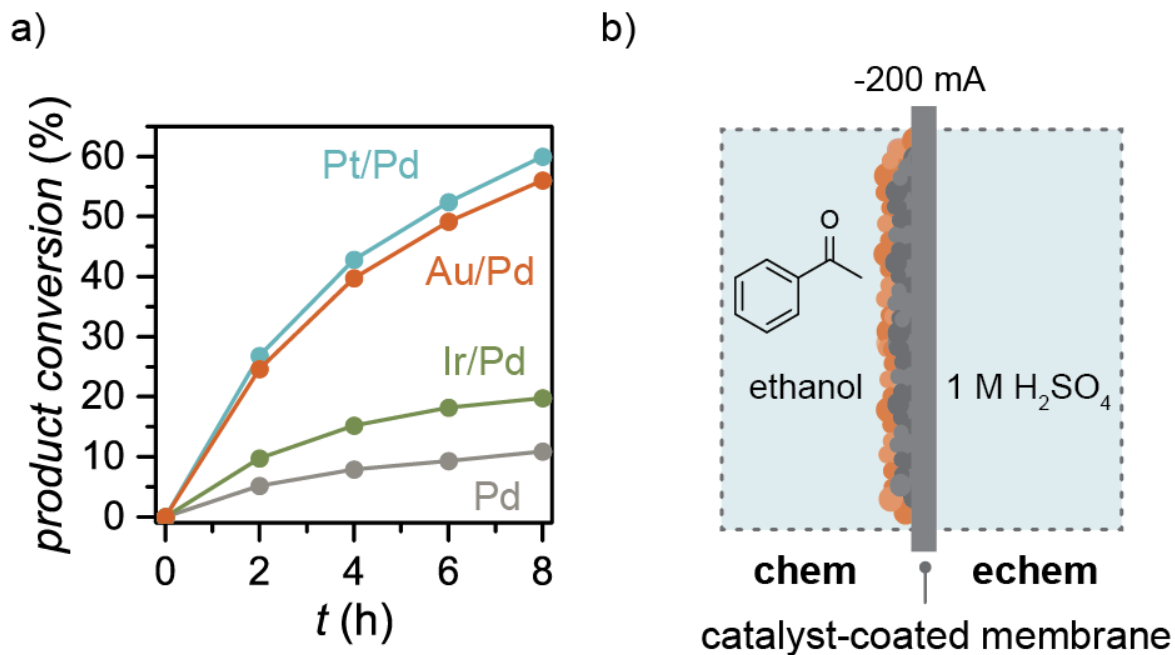


Figure A3.2 Hydrogenation of acetophenone in ethanol. a) product conversion and b) cell setup for hydrogenation of C=O bonds (acetophenone) on catalyst-coated membrane (M = Au, Ir, Pt) and Pd catalysts at 200 mA applied current.

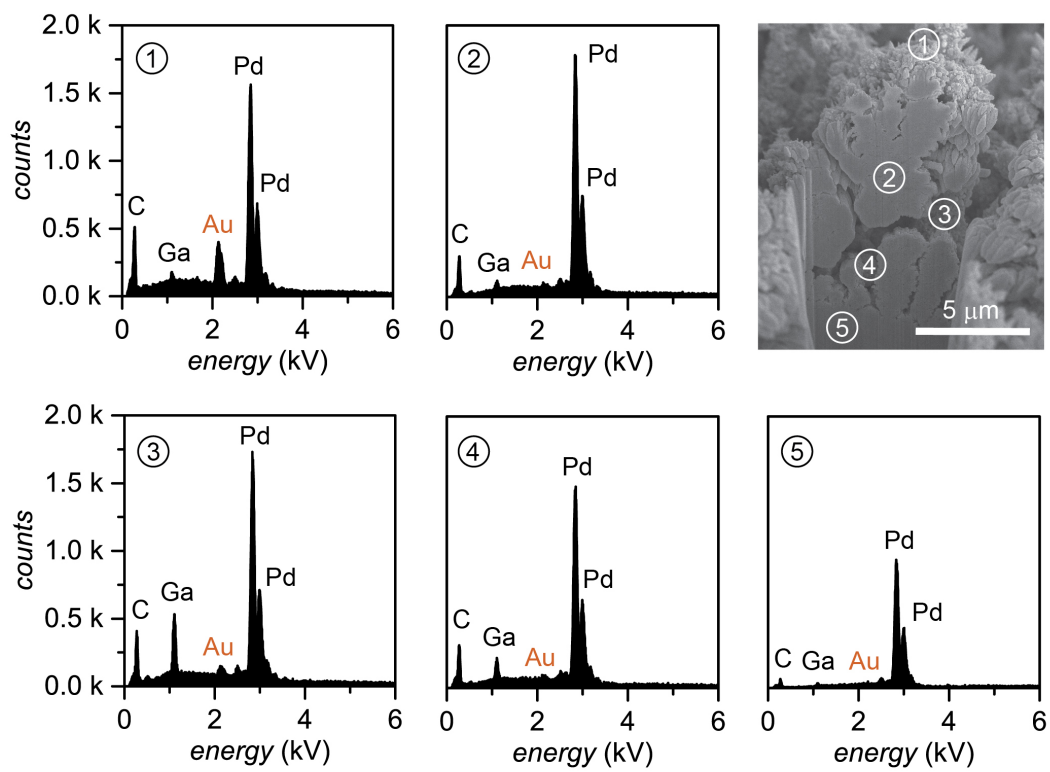


Figure A3.3. Cross-sectional SEM image and EDX elemental analyses of 10 nm thickness gold sputtered on palladium black at 5 different areas.

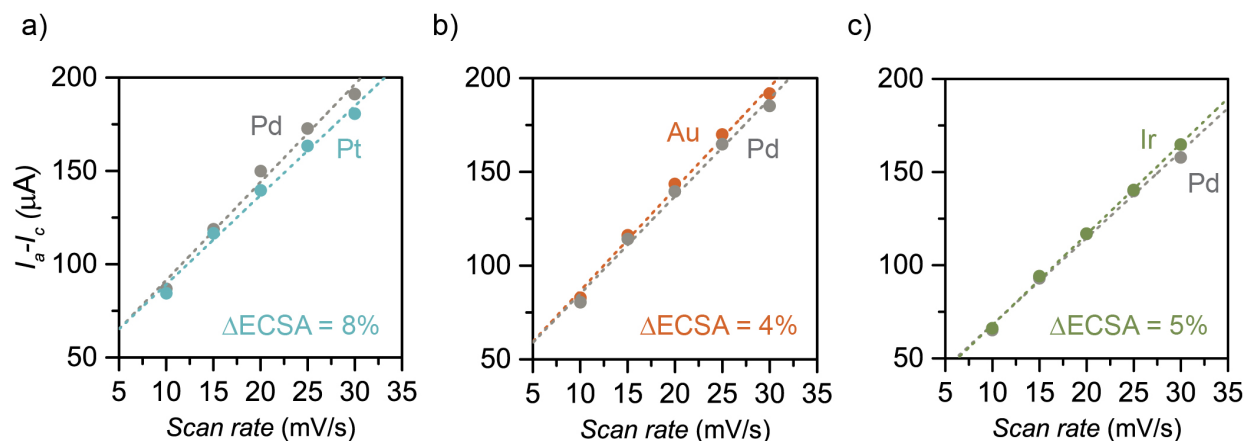


Figure A3.4. Electrochemical surface area (ECSA) measurements performed before and after deposition of a secondary metal. (a) Pt-coated. (b) Au-coated. (c) Ir-coated. All secondary metal layers are 10-nm thick and are located at the surface of the porous Pd-black catalyst. ΔECSA indicates the magnitude of change in the ECSA after deposition.

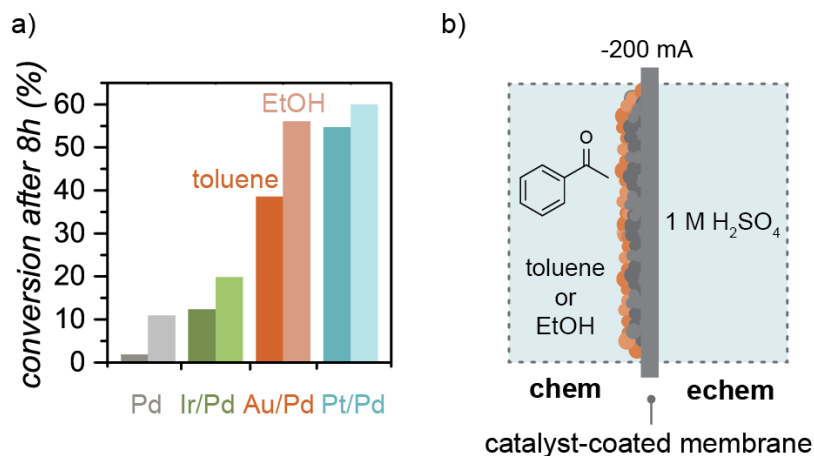


Figure A3.5 Solvent effect on reactivity for hydrogenation of acetophenone. a) Product conversion after 8h in toluene and EtOH with different secondary metal catalysts. b) Cell setup for hydrogenation of acetophenone in toluene and EtOH.

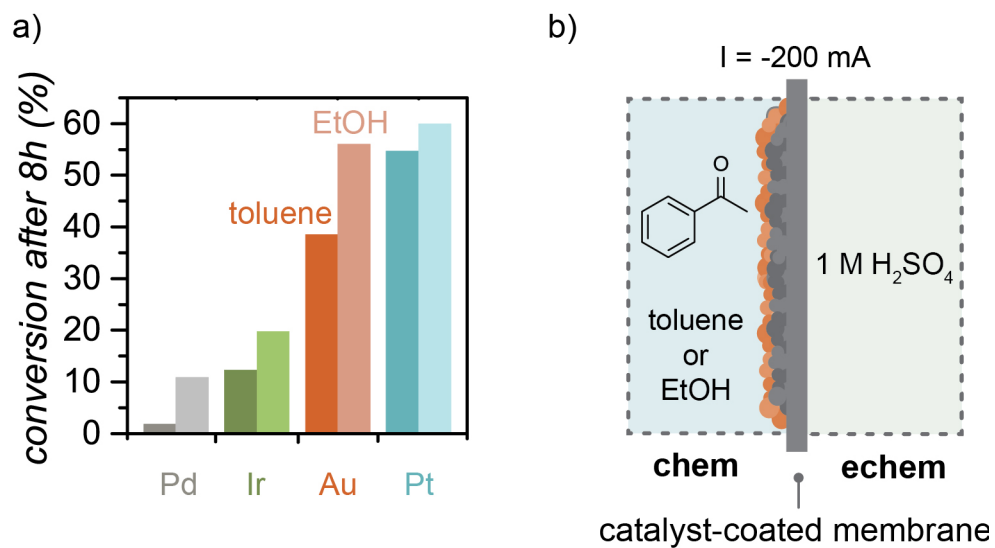


Figure A3.6. Solvent effect on reactivity for hydrogenation of acetophenone. (a) Product conversion after 8 h in toluene and EtOH with different secondary metal catalysts. (b) Cell setup for hydrogenation of acetophenone in toluene and EtOH.

Table A3.1 Initial hydrogenation rates (mmol h^{-1}) of acetophenone and styrene for different catalysts.^a

	Pt	Au	Ir	Pd
Acetophenone in toluene	0.16 ± 0.01	0.12 ± 0.02	0.036 ± 0.009	0.0058 ± 0.0008
Acetophenone in ethanol	0.21 ± 0.01	0.18 ± 0.01	0.077 ± 0.006	0.037 ± 0.002
Styrene in toluene	0.83 ± 0.03	0.74 ± 0.02	0.92 ± 0.03	1.08 ± 0.03

^a Initial rate of acetophenone conversion for each metal catalyst was determined by the slope of the first 2 h of acetophenone consumption (mmol h^{-1}) and the first 0.5 h of styrene consumption (mmol h^{-1}).

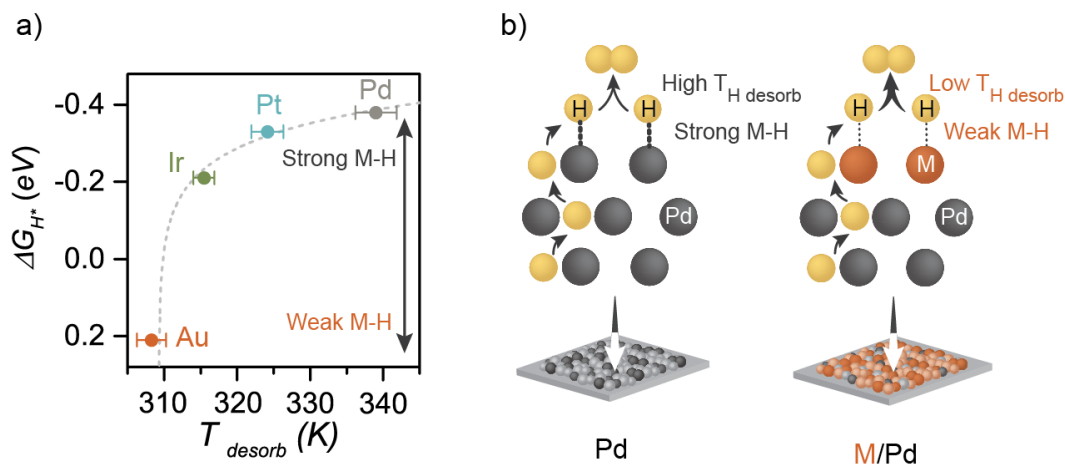


Figure A3.7 Hydrogen desorption temperature correlates the M–H binding energy. a).

Hydrogen adsorption energy (ΔG_{H^*}) as a function of hydrogen desorption temperature of different metal surfaces (Pt, Ir, Au, Pd). The grey dotted line is a monoexponential decay fit of

the experimental data, included as a guide to the eye. b) Schematic representation of desorption of hydrogen from the catalyst-coated membrane surface. Hydrogen desorbs at high temperatures

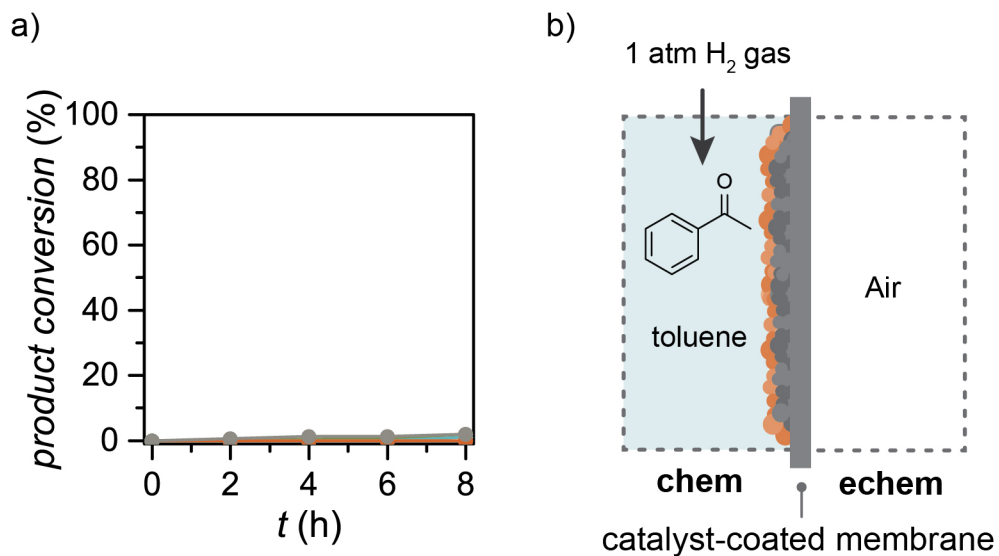


Figure A3.8. Hydrogenation of acetophenone using H₂ gas. (a) Product conversion after 8 h in toluene and with different catalysts. (b) Cell setup for hydrogenation of acetophenone in toluene. The electrochemical cell was left empty and no electrochemical bias was applied.